

APPLIED
COMPUTATIONAL
ELECTROMAGNETICS
SOCIETY
Journal

Winter 1991
Vol. 6 No. 2

ISSN 1054-4887

DISTRIBUTION STATEMENT A
Approved for public release;
Distribution Unlimited

GENERAL PURPOSE AND SCOPE. The Applied Computational Electromagnetics Society Journal hereinafter known as the ACES Journal is devoted to the exchange of information in computational electromagnetics, to the advancement of the state-of-the-art, and to the promotion of related technical activities. A primary objective of the information exchange is the elimination of the need to "re-invent the wheel" to solve a previously-solved computational problem in electrical engineering, physics, or related fields of study. The technical activities promoted by this publication include code validation, performance analysis, and input/output standardization; code or technique optimization and error minimization; innovations in solution technique or in data input/output; identification of new applications for electromagnetics modeling codes and techniques; integration of computational electromagnetics techniques with new computer architectures; and correlation of computational parameters with physical mechanisms.

SUBMISSIONS CONTENT. The ACES Journal welcomes original, previously unpublished papers, relating to applied computational electromagnetics.

Typical papers will represent the computational electromagnetics aspects of research in electrical engineering, physics, or related disciplines. However, papers which represent research in applied computational electromagnetics itself are equally acceptable.

For additional details, see "Information for Authors", elsewhere in this issue.

SUBSCRIPTIONS. All members of the Applied Computational Electromagnetics Society (ACES) who have paid their subscription fees are entitled to receive the ACES Journal with a minimum of two issues per calendar year. Current annual subscription fees are:

U.S. Subscriptions: (\$45.00 personal, \$25.00 full-time student, \$95.00 organizational).

Non-U.S. Subscriptions: (Add \$10.00 to above). (1) BANK DRAFTS (ORIGINATING CHECK MUST HAVE ROUTING NUMBERS, AND MUST BE DRAWN ON U.S. BANK) , (2) INTERNATIONAL MONEY ORDER, or (3) TRAVELERS CHECKS IN U.S. DOLLARS.

Back issues, when available, are \$15.00 each. Subscriptions to ACES, orders for back issues of the ACES Journal and changes of addresses should be sent to:

Dr. Richard Adler
ACES Secretary
Naval Postgraduate School
Code EC/AB
Monterey, CA 93943 USA

Allow four week's advance notice for change of address. Claims for missing issues will not be honored because of insufficient notice or address change or loss in mail unless the secretary is notified within 60 days for USA and Canadian subscribers or 90 days for subscribers in other countries, from the last day of the month of publication. For information regarding reprints of individual papers or other materials, see "Information for Authors".

LIABILITY. Neither ACES or the ACES Journal editors are responsible for any consequence of misinformation or claims, express or implied, in any published material in an ACES Journal issue. This also applies to advertising, for which only camera-ready copies are accepted. Authors are responsible for information contained in their papers. If any material submitted for publication includes material which has already been published elsewhere, it is the author's responsibility to obtain written permission to reproduce such material.

THE APPLIED COMPUTATIONAL ELECTROMAGNETICS

SOCIETY JOURNAL

EDITORS

EDITOR-IN-CHIEF

David E. Stein
Westinghouse Electric Corp.
P.O. Box 169
Linthicum Heights, MD 21090 U.S.A.

MANAGING EDITOR

Richard W. Adler
Naval Postgraduate School
Code EC/AB
Monterey, CA 93943, U.S.A.

EDITOR-IN-CHIEF, EMERITUS

Robert M. Bevensee, U.S.A.

Ruediger Anders
Applied Electromagnetics Engineering
Salem, GERMANY

Tony Fleming
Telecom Australia
Clayton, Victoria, AUSTRALIA

Kenzo Miya
University of Tokyo
Tokyo, JAPAN

Harold W. Askins
The Citadel
Charleston, SC, USA

Pat Foster
Microwave & Antenna Systems
Worcestershire, UK

Giorgio Molinari
University of Genova
Genova, ITALY

Brian A. Austin
University of Liverpool
Liverpool, UK

Gregory R. Haack
DSTO
Salisbury, AUSTRALIA

Frederic A. Molinet
Societe Mothesim
Le Plessis- Robinson, FRANCE

Duncan C. Baker
University of Pretoria
Pretoria, SOUTH AFRICA

Christian Hafner
Swiss Federal Institute of Technology
Zurich, SWITZERLAND

Gerrit Mur
Technische Universiteit Delft
Delft, NETHERLANDS

Fulvio Bessi
Ingegneria dei Sistemi S.p.A.
Pisa, ITALY

Roger Harrington
Syracuse University
Syracuse, NY, USA

Takayoshi Nakata
Okayama University
Okayama, JAPAN

Robert M. Bevensee
Consultant
Alamo, CA, USA

Kiyohiko Itoh
Hokkaido University
Sapporo, JAPAN

Andrew F. Peterson
GA Institute of Technology
Atlanta, GA, USA

John R. Bowler
University of Surrey
Surrey, UK

Adalbert Konrad
University of Toronto
Toronto, Ontario, CANADA

Harold A. Sabbagh
Sabbagh Associates Inc.
Bloomington, IN, USA

James K. Breakall
Pennsylvania State University
University Park, PA, USA

Stanley Kubina
Concordia University
Montreal, Quebec, CANADA

Ted L. Simpson
University of S. Carolina
Columbia, SC, USA

Robert T. Brown
Lockheed Aeronautical Sys. Co.
Valencia, CA, USA

Karl J. Langenberg
Universitat Kassel
Kassel, GERMANY

Chris Smith
Kaman Sciences Corp.
Colorado Springs, CO, USA

Chalmers M. Butler
Clemson University
Clemson, SC, USA

Ray Luebbers
Pennsylvania State University
University Park, PA, USA

C. W. "Bill" Trowbridge
Vector Fields Limited
Oxford, UK

Dawson Coblin
Lockheed Missiles & Space Co.
Sunnyvale, CA, USA

Andrew L. Maffett
Consultant
Dexter, MI, USA

Jean-Claude Verite
Electricite de France
Clamart Cedex, FRANCE

Edgar Coffey
Advanced Electromagnetics
Albuquerque, NM, USA

Ronald Marhefka
Ohio State University
Columbus, OH, USA

John W. Williams
Science Applications Int.
Albuquerque, NM, USA

Peter S. Excell
University of Bradford
West Yorkshire, UK

Edmund K. Miller
Los Alamos National Lab.
Los Alamos, NM, USA

Manfred Wurm
Industrieanlagen-
Betriebsgesellschaft mbH
Ottobrunn, GERMANY

19950630 160

DTIC QUALITY INSPECTED 5

THE APPLIED COMPUTATIONAL ELECTROMAGNETICS SOCIETY

JOURNAL

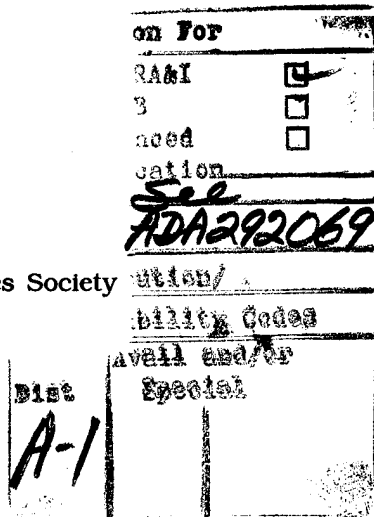
Vol. 6 No. 2

Winter 1991

TABLE OF CONTENTS

"About the Study in the Time Domain of Junctions Between Thin Wires" by A.R. Bretones, A. S. Extremera, R.G. Martin & J.F. Callejon	2
"Optimal Location for Matching Points for Wire Modelling with MMP" by P. Leuchtmann	21
"Surface Modelling For EM Interaction Analysis" by S. Kashyap & A. Louie	38
"On the Functioning of a Helicopter-borne HF Loop Antenna" by D.C. Baker	53
"The Linear-Phase Triangular Facet Approximation in Physical Optics Analysis of Reflector Antennas" by W.A. Imbriale & R.E. Hodges	74
"Simplified 3-D Mesh Generator" by R.K. Najm	86
"The Short Fat Dipole" by D.B. Miron	99
"Analysis of Three Dimensional Dielectric Loaded Cavities" by L. Pichon & A. Razek	133
"Antenna Array Modelling By Parallel Processor Farms" by I. Cramb, D.H. Schaubert, R. Beton, J. Kingdon & C. Upstill	143
Institutional Membership	152

© 1991, The Applied Computational Electromagnetics Society



ABOUT THE STUDY IN THE TIME DOMAIN OF JUNCTIONS BETWEEN THIN WIRES

Amelia Rubio Bretones
Alfonso Salinas Extremera
Rafael Gómez Martín
Jesús Fornieles Callejón

*Dpto. Física Aplicada
Facultad de Ciencias
Universidad de Granada
18071-Granada (SPAIN)*

ABSTRACT

DOTIG1 is a computer code developed for the study of the interaction of arbitrary electromagnetic signals with thin-wire structures, in the time domain. It calculates the current distribution induced on the structure by solving the electric field integral equation using the moment method. The numerical procedure used to develop the program and different possibilities for treating junctions are briefly described.

To obtain an accurate solution for the current induced on the thin-wire structures it is very important to pay attention to the zones at which the wires intersect. Thus, different junction treatments were tested for several simple structures. Following some convergence criteria the current distributions were compared to a reference solution and also, by way of Fourier transform, with results obtained using some well known frequency-domain codes.

1. INTRODUCTION

Recent developments in high-resolution radar and electromagnetic-pulse technology (EMP) have generated interest in their interaction with structures. This can be studied either by using time-harmonic analysis followed by Fourier inversion or solving directly in the time domain using a time-step algorithm [1]. The time domain approach not only offers computational advantages but sheds light on the problem in a way that is not possible using frequency-domain techniques [2].

The first step for such an analysis is to calculate the electric current induced on the

surface of the structures. As they are normally very complex, a common technique is to approximate the surface geometry by a set of joined wires. To obtain an accurate numerical solution for the structure current distribution, particular attention must be paid to the zones at which the wires are joined together [3].

In this paper different treatments for the study of the junctions are presented in order to compare how stable and accurate the solution is obtained. The treatments were applied to: a cross of wires, a stepped-radius wire, a net (Fig. 13) and a dodecahedron (Fig. 16), when illuminated by a transient electromagnetic field. The currents induced on the wires were calculated in the time domain by solving the electric field integral equation (EFIE) using the moment method. The results obtained using the different junction treatments were compared, by Fourier transform, with those obtained from the computer code NEC-2 [4], working in the frequency domain, and for the dodecahedron with the AWAS code [5] as well.

2. NUMERICAL METHOD

DOTIG1 computes, in the time domain, the currents induced on a structure modelled by interconnected wires when it is excited by an arbitrary electromagnetic signal. The method employed consists of resolving the electric field integral equation (EFIE) using the moment method. This equation for a thin wire is [6],[7]:

$$\begin{aligned} \hat{s} \cdot \vec{E}^i(s, t) = & \frac{\hat{s}}{4\pi\epsilon_0} \cdot \int_{C(s')} \left[\frac{\hat{s}'}{c^2 R} \frac{\delta}{\delta t} I(s', t') + \frac{\vec{R}}{cR^2} \frac{\delta}{\delta s} I(s', t') \right. \\ & \left. - \frac{\vec{R}}{R^3} q(s', t') \right] ds' \end{aligned} \quad (1)$$

where \hat{s} and \hat{s}' are tangent vectors to the wire axis of contour $C(s')$ at position $s(r)=s$ and $s(r')=s'$. $I(s', t')$ and $q(s', t')$ are the unknown current and charge distributions at source point s' at retarded time $t'=t-R/c$ and \vec{E}^i is the field applied to the observation point $\vec{R} = |\vec{r}-\vec{r}'|$ (See Fig. 1). The charge $q(s', t')$ can be expressed in terms of $I(s', t')$ by the equation of continuity.

Using the point matching form of the moment method, integral eq. (1) was transformed into the group of equations (in matrix notation) [8],[9]

$$\tilde{E}^s_j + \tilde{E}^i_j = \tilde{Z} \tilde{I}_j \quad (2)$$

which allows us to calculate the current I_j at time t_j from the elements E^s_j of the tangential

electric field scattered by currents of previous times and the elements E_j^i of the tangential applied electric field at the observation point and at time step t_j . Matrix \tilde{Z} is a matrix of interaction, the elements of which are time-independent. They depend on the geometry and on the electromagnetic characteristics of the structure alone [10].

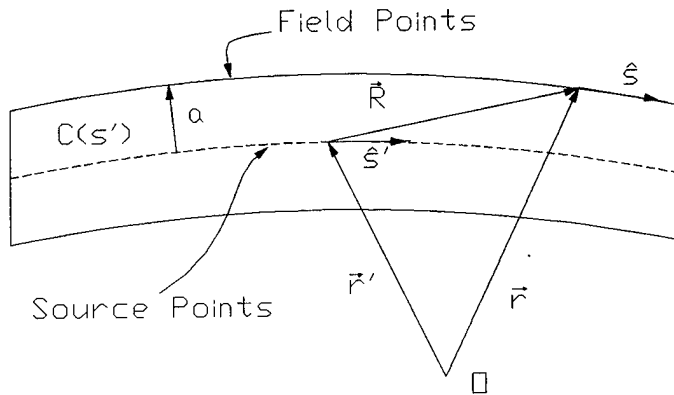


Fig. 1 Geometry of the thin wire

The base function used was a nine-point lagrangian interpolation, which in the case of a single wire can be written

$$I_{i,j}(s', t') = \sum_{l=-1}^{+1} \sum_{m=-1}^{+1} B_{i,j}^{(l,m)} I_{i+l, j+m} \quad (3)$$

where $I_{i,j}(s', t')$ is the value of the intensity current at position s' and time t' inside one of the space-temporal intervals $i-j$ into which the wire was divided. $B_{i,j}^{(l,m)}$ are the coefficients of the interpolation that depend on s' and t' , and $I_{i+l, j+m}$ are the values of the current at the space-temporal interval $i+l-j+m$ nearest to the $i-j$ interval [8],[10]-[11].

Fig. 2 shows how the space interpolation is carried out for an isolated wire. The current at a point s' in the i -segment is interpolated to the values of the currents at the centers of its neighbouring spatial intervals ($i-1$, i and $i+1$) (fig. 2a). The current on the end segments is interpolated to zero just at the wire ends (fig. 2b) [12].

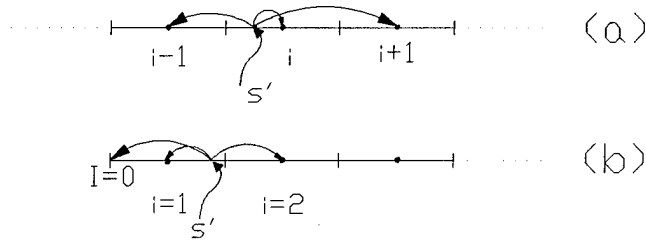


Fig.2

Spatial interpolation for a single wire.
a) Not end segments, b) End segments.

3. DESCRIPTION OF THE DIFFERENT MULTIPLE-JUNCTION TREATMENTS.

When dealing with structures that have several interconnected wires, the assumption that the values of the currents at the ends meeting at the junction are zero is invalid, so the current on the segments closest to the junction point cannot be interpolated to zero and the numerical method described in section 2 cannot be applied [12].

For treating junctions we have modified the method, trying several schemes which are summarized in Fig. 3; the main differences between them are the way of discretizing the wires and how the interpolation function is handled near the junction [13]:

T1: Overlapping-segments treatment:

The first method employed was the translation to the time domain of a technique that had been used successfully in the frequency domain [12]. The method consists of replacing the actual configuration of N wires that meet at the junction (see Fig. 3a) by a set of electrically unjoined but overlapping wires (Fig. 3b). It is easy to prove that the way chosen to represent the overlapping wires satisfies Kirchoff's first law at the junction. This way is that when N wires meet at any junction, wire i overlaps one segment onto wire $i-1$, except that wire 1 is not overlapped

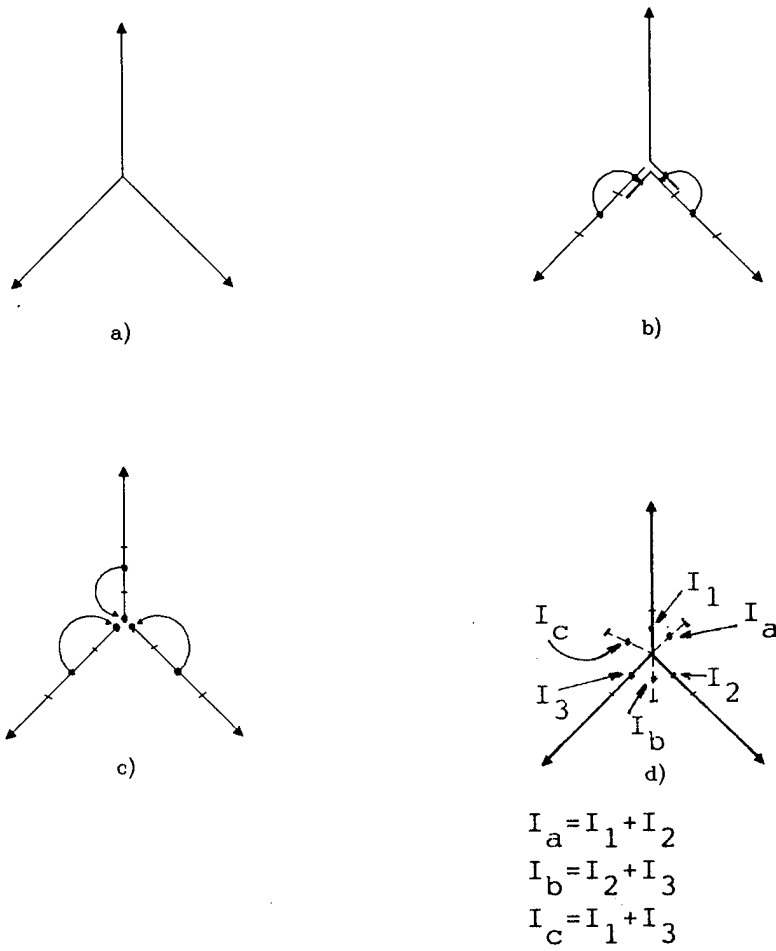


Fig. 3. Different junction treatments. a) Real structure. b) Overlapping-segments treatment. c) Half-segments treatment. d) Sum treatment.

onto wire N. A wire is then considered to end not at a junction but at the end of the overlap, where the current is set to zero. This way each wire can be treated as if it were isolated.

The interpolation of the current on a segment will be to the sum of the current on that segment and the extra overlapping segment if it exists, as shown by the arrows in the diagram (Fig. 3b).

As matrix \tilde{Z} in eq. (2) depends only upon the geometry of the structure, the application of the moment method to a segment and its overlapping segment leads to exactly the same equation. For a junction of N wires the system of equations (2) has N-1 identical equations (the number of overlaps). These extra equations were removed and substituted by the Wu and King condition for the charge at the junction [14], which for thin wires can be expressed as the match of the derivative of the current over space at each wire at the junction. Therefore, a linear system is obtained with the same number of unknowns as equations.

T2. Half-segments treatment (Fig. 3c):

Each wire was discretized, locating at each end, segments of half the length of the other segments of the structure. The current on those half segments is interpolated backwards to the currents on segments of the same wire, as shown in Figure 3c.

The Kirchoff's first law and the Wu and King condition described in the T1 treatment are imposed adding extra equations to the ones that come from the moment method. In this case the method leads to a linear system of equations with one equation more than the number of unknowns. The system is solved by multiplying eq.(2) by Z transpose, which minimizes the square error.

T3. Sum treatment (Fig. 3d):

The multiple junction of N wires is treated by interpolating the current from one segment across the junction to the center of a "ghost segment" with current equal to the sum of the N-1 currents of the other segments at the junction.

It can be seen that the Wu and King condition is implicit in this junction treatment, but not the Kirchoff's first law, which has been imposed by adding an extra equation to eq. (2) and solving as described in T2.

4. RESULTS

The different junction treatments described in section 3 were applied to several simple structures in order to study the accuracy of the solution obtained and the efficiency of the method employed.

The first structure analyzed was a cross-wire structure (see Fig. 4). The currents induced on it were calculated when it was illuminated by a gaussian pulse of the form:

$$\vec{E} = \exp(-g^2(t-t_{\max})^2) \hat{z} \quad (4)$$

with $g=5*10^9 \text{ s}^{-1}$ and $t_{\max}=4.28*10^{-10} \text{ s}$. The radius of all the wires was 0.00222 m .

In Fig. 5 the current distribution is presented versus time at a point on the first wire situated 4.6 mm from the junction point (Point O).

In order to compare how convergent the different junction treatments are with respect to the number of segments in which the structure is divided, two error criteria were calculated: the root mean square current I_{rms} and the normalized root mean square current error e_{rms} [15]. These variables are defined by:

$$I_{rms} = \sqrt{\frac{1}{N_s N_t} \sum_{i=1}^{N_s} \sum_{j=1}^{N_t} |I_{i,j}|^2}$$

$$e_{rms} = \sqrt{\frac{\sum_{i=1}^{N_s} \sum_{j=1}^{N_t} |I_{i,j} - I_{i,j}^r|^2}{\sum_{i=1}^{N_s} \sum_{j=1}^{N_t} |I_{i,j}^r|^2}}$$

where N_s is the number of segments into which the structure was divided and N_t the number of time intervals calculated in each case. N_s^r , N_t^r and $I_{i,j}^r$ correspond to a reference solution that was obtained dividing the wires into a sufficiently large number of segments.

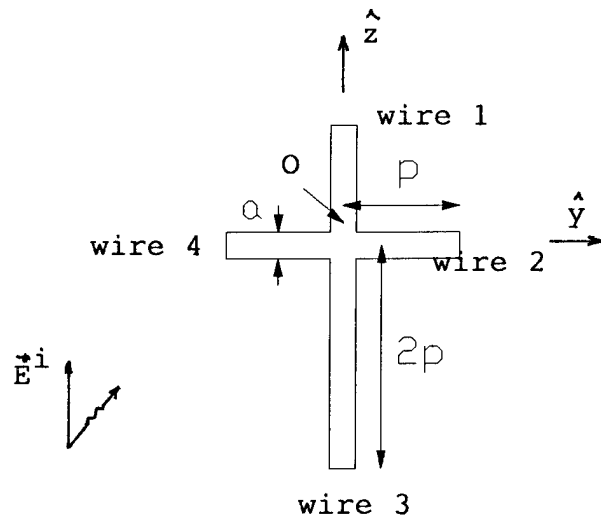


Fig.4 Cross-wire structure. $p=0.11$ m, $a=0.00444$ m.
Length of the wires: (wire 1 = wire 2 = wire 4 = p ;
wire 3 = $2p$).

Figs. 6 and 7 show respectively I_{rms} and e_{rms} versus the number of segments. The rapidity with which a technique leads to a stable solution can be estimated from the I_{rms} plot. It is desirable that the curves should approach a constant as soon as possible. As can be seen in Fig. 6, the I_{rms} obtained using T1 and T3 approach a constant more quickly than T2. The e_{rms} plot in Fig. 7 also shows that T1 and T3 behave better than T2, that is, these approaches need fewer segments than T2 to arrive to solution with $e_{rms} \sim 0$.

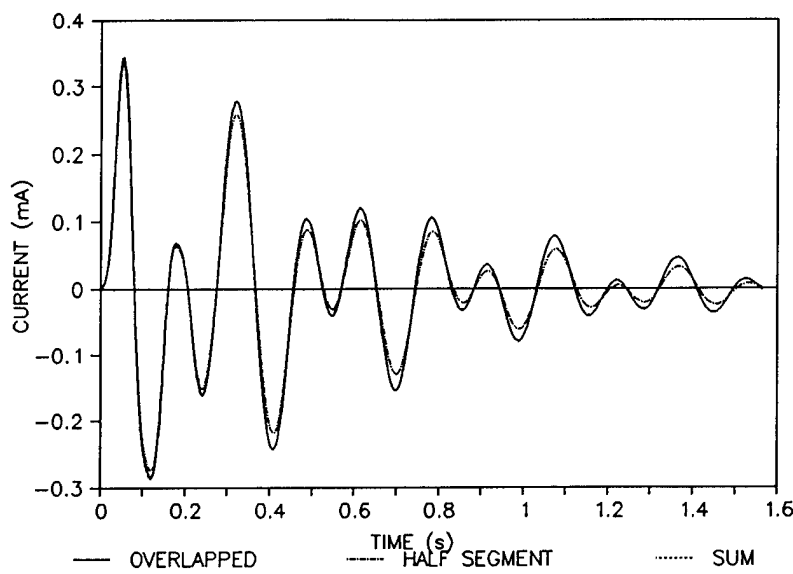


Fig.5. Current distribution versus time at point O on the cross wire structure.
Overlapped and Sum give the same results.

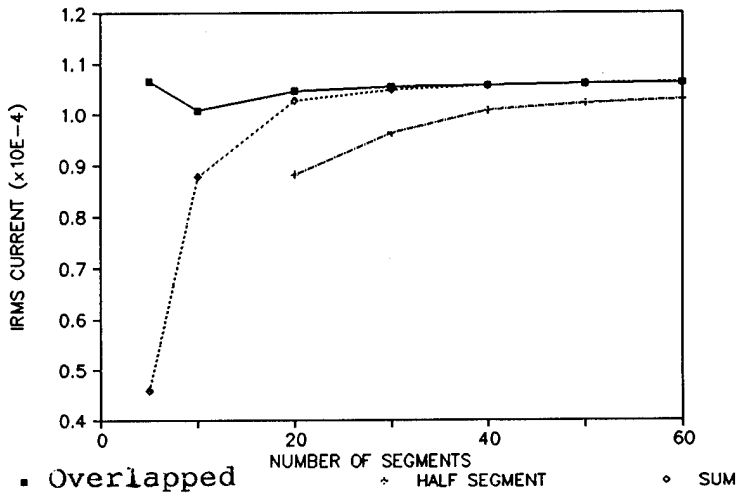


Fig. 6 Root mean square current versus the number of segments into which the cross-wire structure was divided.

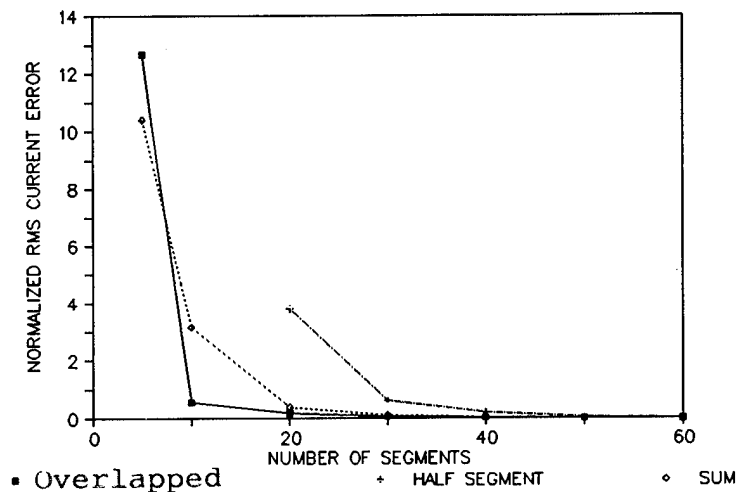


Fig. 7 Normalized root mean square current error versus the number of segments into which the cross structure was divided.

In order to compare our time-domain results with the frequency domain results given by the computer code NEC-2 [4] we Fourier transformed them and divided by the transform of the incident field. Fig. 8 shows the Fourier transformation of the current at a point 4.6 mm from the junction versus frequency. The results obtained with T1 and T3 agree closely with those obtained from NEC.

The same analysis was made for the case of the stepped-radius wire (considering it as a junction of two wires with different radii) drawn in Fig. 9, when illuminated by a gaussian pulse

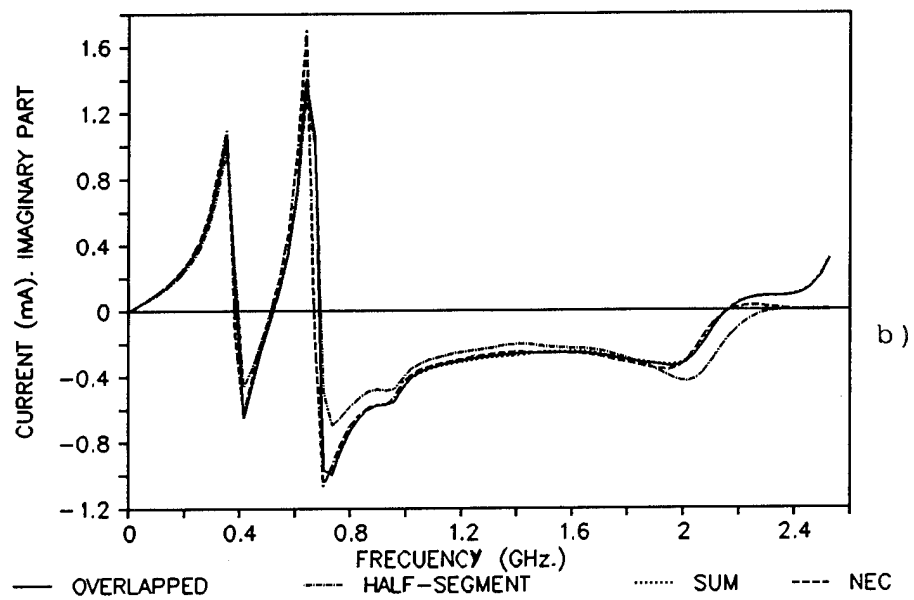
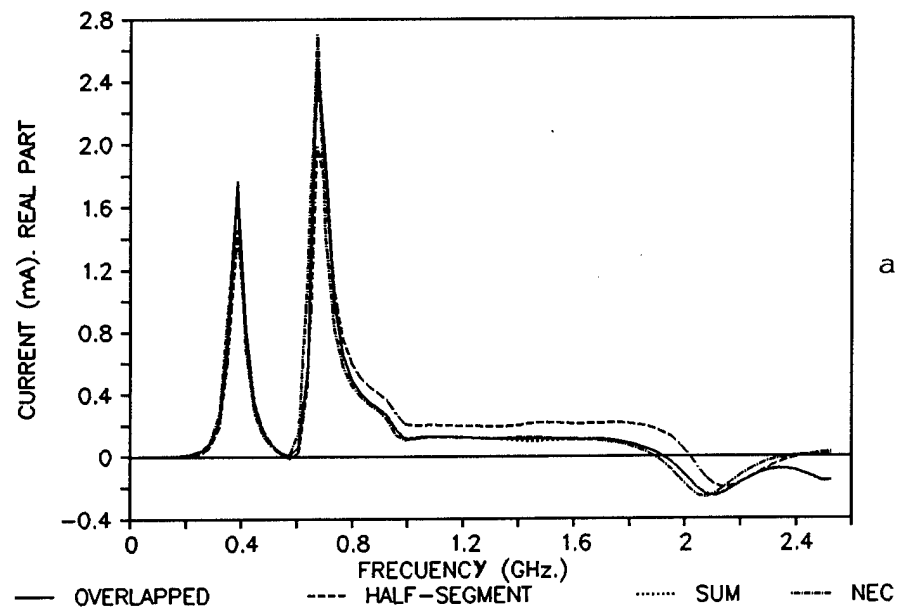


Fig.8 Current at point O on the wire-cross structure versus frequency. a) Real part. b) Imaginary part. (Overlapped and Sum give the same results).

with $g=5*10^9 \text{ s}^{-1}$ and $t_{\max}=9.2*10^{-10} \text{ s}$. Figs. 10, 11 and 12 show respectively the current versus time at point O, the e_{rms} error versus the number of segments and the comparison of the Fourier

transform of the time-domain results with the ones obtained by NEC. As can be seen, in this case all the treatments behaved similarly.

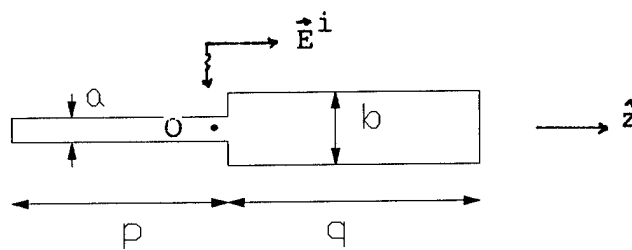


Fig. 9. Stepped-radius wire geometry. $p = 0.3\text{m}$, $q = 0.2\text{m}$, $a = 0.002\text{m}$ and $b = 0.004\text{m}$.

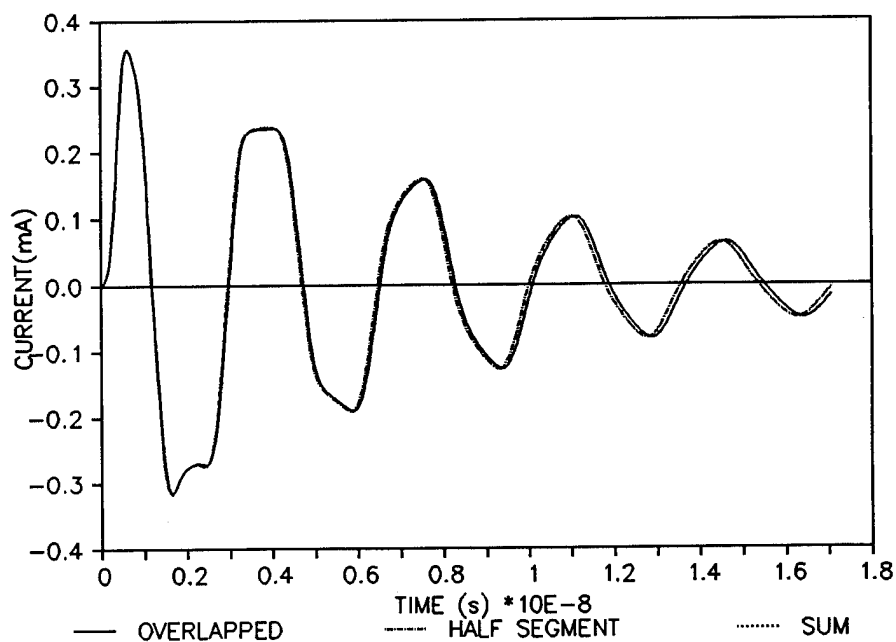


Fig.10 Current distribution versus time at point O on the stepped-radius wire. (Overlapped and Sum give the same results).

The following structures studied were:

- 1.- The net of twelve wires represented in Fig. 13.
- 2.- A dodecahedron structure (Fig. 16).

In both cases the electric field incident was proportional to the temporal derivative of eq. (4) polarized in the x-direction and propagating in the z-direction:

$$\vec{E}^i = 2g(t-t_{\max}) \exp(-g^2(t-t_{\max})^2) \hat{x} \quad (7)$$

with $g=1*10^9 \text{ s}^{-1}$ and $t_{\max}=4.6*10^{-9} \text{ s}$ for the net and $g=8*10^8 \text{ s}^{-1}$ and $t_{\max}=5.7*10^{-9} \text{ s}$ for the dodecahedron. This incident field was chosen because it has not zero-frequency component and, therefore, does not excite the circulating current that would exist on structures with closed-circuit parts [10].

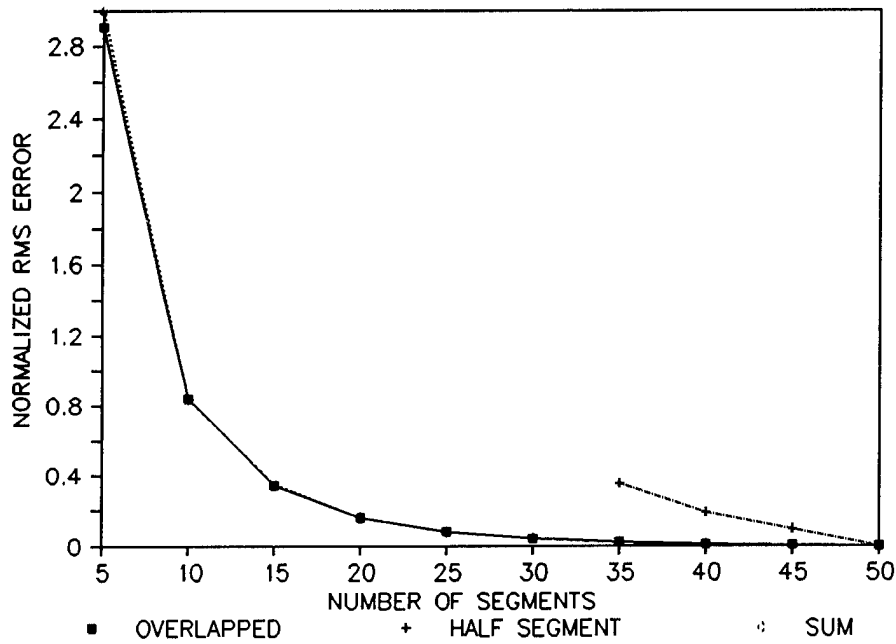


Fig. 11 Normalized root mean square current error versus the number of segments into which the stepped-radius wire was divided. (Overlapped and Sum give the same results)

As the T2 treatment was found to give less accurate results when compared with NEC and to need more segments to arrive at a stabilized solution, for these two more complex structures a comparison was only made between the T1 and T3 treatments.

In Figs. 14 and 17 the current distribution is represented versus time at point O on both structures, and the magnitude of the Fourier transformation of these figures was compared with NEC and plotted in Figs. 15 and 18. The results for the dodecahedron structure were also compared with the ones obtained from the computer code AWAS [5]. In both cases the results arrived at with the T1 treatment (overlapping segments) were found to agree with NEC and

AWAS more closely than the ones resulting from T3.

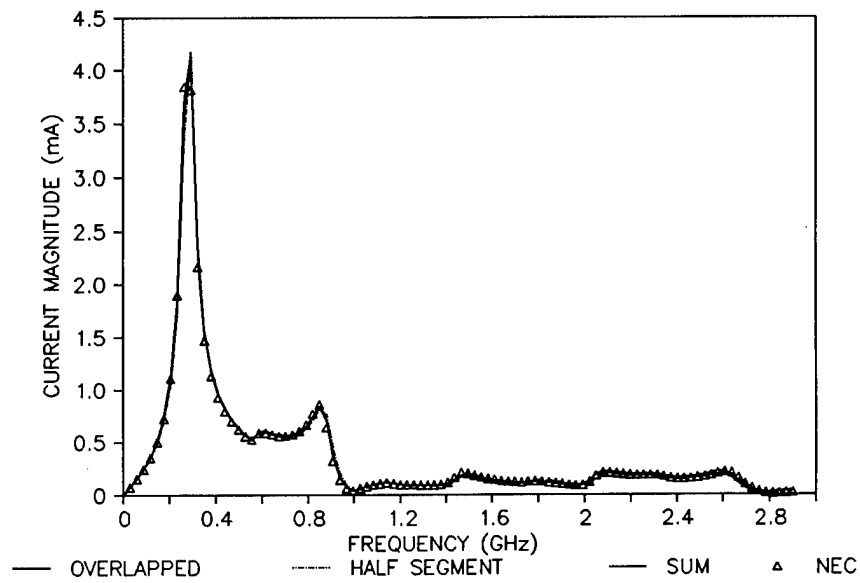


Fig.12 Current magnitude at point O on the stepped-radius wire versus frequency. (All the treatments agree closely).

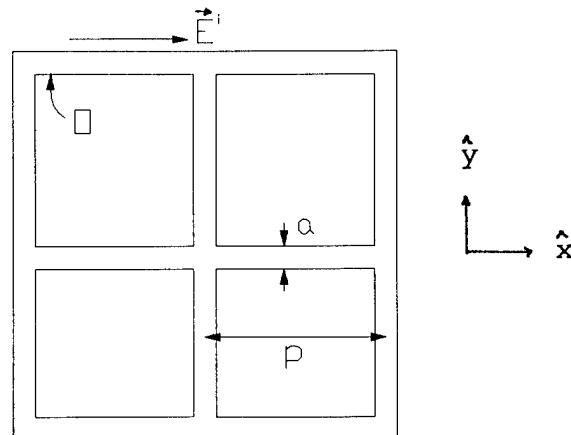


Fig. 13. Geometry of the net structure.
 $p=0.2\text{m}$, $a=13.48\text{mm}$.

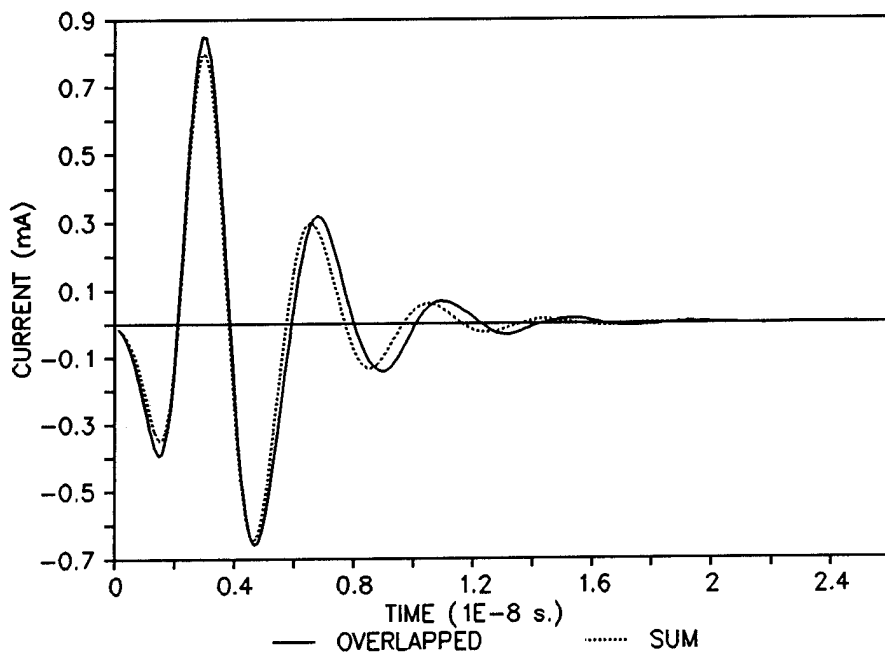


Fig. 14 Current distribution versus time at point O on the net structure.

5. CONCLUSIONS

Different possibilities for treating the multiple junction problem in the time domain have been compared. They have been called:

- T1. Overlapping-segments treatment.
- T2. Half-segments treatment.
- T3. Sum treatment.

The three junction treatments proposed were specifically applied to the study of the interaction of a gaussian pulse with:

- 1.- A cross-wire structure.
- 2.- A junction of two wires with different radii.
- 3.- A net of twelve interconnected wires.
- 4.- A dodecahedron structure.

To analyze the convergence of the method with the number of segments, the root mean square current and the root mean square error of the current induced on a point on the structure

were calculated.

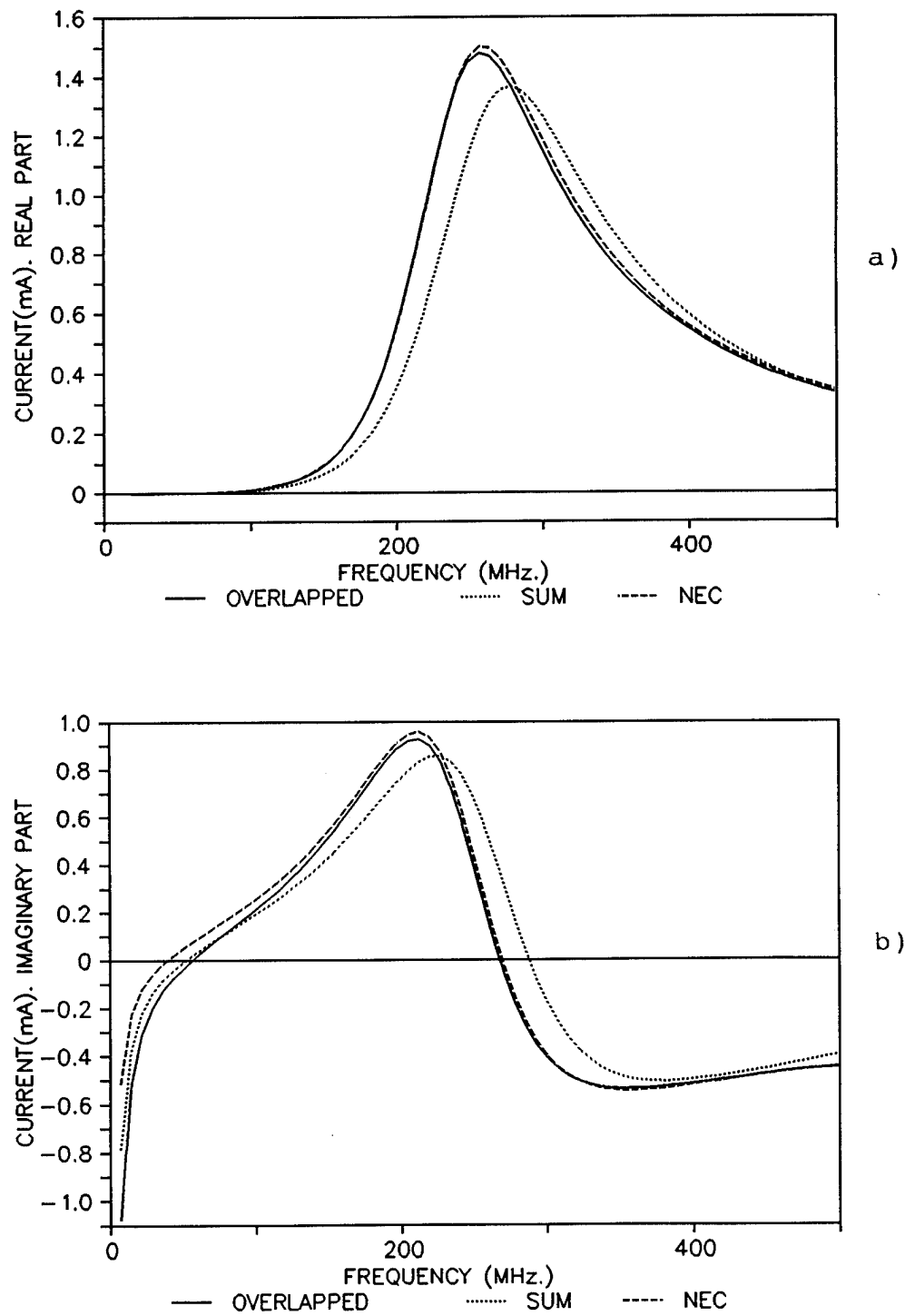


Fig. 15. Current at point O on the net structure versus frequency. a) Real part, b) Imaginary part.

To ascertain their accuracy we applied the Fourier Transform to our time domain results and compared them with some well known codes that work in the frequency domain (NEC and AWAS).

In the light of our criteria, the overlapping procedure seemed to be that which provided the most accurate solution, requiring the structure to be divided into the least number of segments. This treatment was, therefore, the one finally included in the computer program we have developed for studying the interaction of EMP with thin-wire structures, the DOTIG1 code.

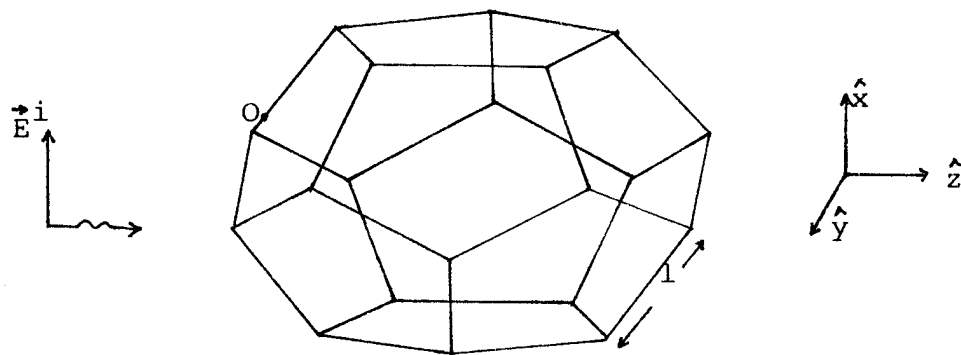


Fig. 16 Geometry of the dodecahedron structure. $l = 0.5\text{m}$. Wire radii = 0.008m.

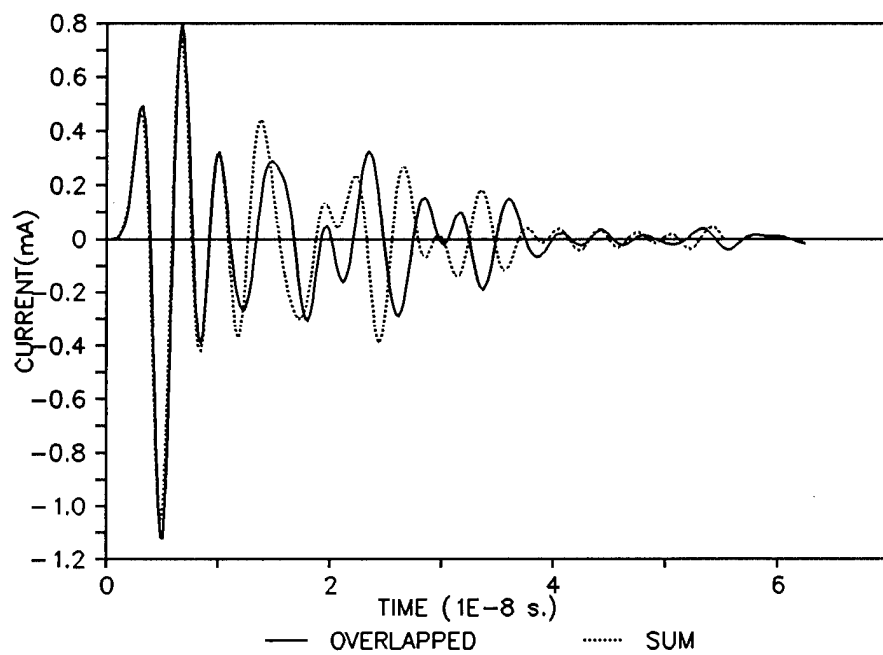


Fig. 17 Current distribution versus time at point O on the dodecahedron.

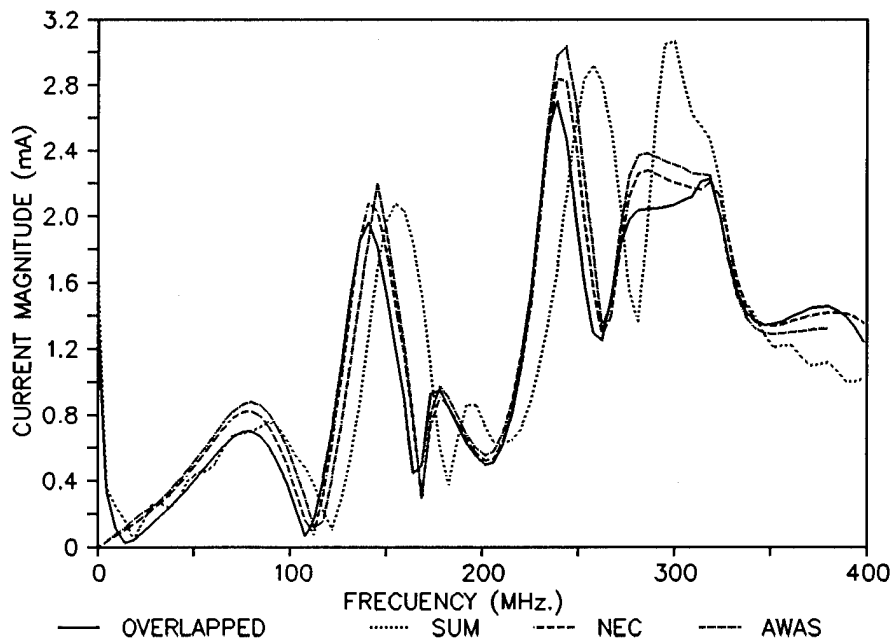


Fig. 18. Current magnitude at point O on the dodecahedron structure versus frequency.

Acknowledgment

This paper was partially supported by D.G.T. (Dirección General de Telecomunicaciones) through PRONTIC 89 0873E.

REFERENCES

- [1] Anton G. Tijhuis, Peng Zhongqiu and A. Rubio Bretones, "Transient excitation of a straight thin-wire segment: A new look at an old problem", To be published in IEEE Trans. Antennas and Propagation.
- [2] E.K. Miller and J.A. Landt, "Direct time-domain techniques for transient radiation and scattering from wires", Proc. of IEEE, vol. 68, p. 1396-1423, 1980.
- [3] A.C. Ludwig, "Wire grid modelling of surfaces", IEEE Trans. Antennas and Propagat., vol.9, p. 1045-1048, 1987.
- [4] G.J. Burke and A.J. Poggio, "Numerical electromagnetics code (NEC)", Lawrence Livermore Laboratory Contract W-7405-Eng-48, U.S.A., 1981.
- [5] A.R. Djordjevic, M.B. Bazdar, G.M. Vitosevic, T.K. Sarkar and R. F. Harrington, Analysis of Wire Antennas and Scatterers, Artech House, 1990.
- [6] A. Rubio Bretones, DOTIG1, un programa para el estudio en el dominio del tiempo de la interacción de ondas electromagnéticas con estructuras de hilo, Ph. D. dissertation, University of Granada 1988.
- [7] E. K. Miller, "An overview of time-domain integral-equation models in electromagnetics", J. Electromag. Waves and Applications, vol.1, p. 269-293, 1987.
- [8] A. Rubio Bretones, R. Gómez Martín and A. Salinas, "DOTIG1, a time-domain numerical code for the study of the interaction of electromagnetic pulses with thin-wire structures", Compel, vol. 8, p. 39-69, 1989.

[9] R. Gómez, A. Salinas, A. Rubio, J. Fornieles and M. Martín, "Time domain integral equations for EMP analysis", International Journal of Numerical Modelling, vol. 4, p. 153-162, 1991.

[10] E. K. Miller, A. J. Poggio and G.J. Burke, "An integro-differential equation technique for the time-domain analysis of thin-wire structures", J. Comput. Phys., vol. 12, p. 24-48, 1973.

[11] A. Rubio Bretones, A. Salinas, R. Gómez and A. Pérez, "The comparison of a time-domain numerical code (DOTIG1) with several frequency-domain codes applied to the case of scattering from a thin-wire cross", Applied Computational Electromagnetic Society (ACES) Journal, Special Issue on Computer Code Validation, p. 121-129, 1989.

[12] J. Moore and R. Pizer, Moment Method in Electromagnetics, Wiley and Sons, U.S.A., 1983.

[13] A. Rubio Bretones, A. Salinas Extremera, J. Fornieles and R. Gómez Martín, "Comparison of different junction treatments in the DOTIG1 code", Seventh Int. Conference on Antennas and Propagat., University of York, U.K., 1991.

[14] T.T. Wu and W. P. King, "The tapered antenna and its application to the junction problem for thin-wires", IEEE Trans. on Antennas and Propagat., vol. AP-24, p.42-45, 1976.

[15] E.K. Miller, R.M. Bevensee, A.J. Poggio R. Adams and F.J. Deadrick, "An evaluation of computer programs using integral equations for the electromagnetic analysis of thin wire structures", Interaction Notes, Lawrence Livermore Laboratory, U.S.A., 1974

Optimal Location for Matching Points for Wire Modelling with MMP

P. Leuchtmann
ETH Zentrum, CH-8092 Zürich, Switzerland

Abstract: *It is a basic premise in electromagnetic field modelling that the tangential electromagnetic field on the surface of ideal conductors must vanish. When point matching is used to impose this condition, the location of the matching points must be chosen. This paper treats the special case of thin wires. It is shown that for common approximations of the wire currents, the optimum locations of the matching points are well defined and that forcing the boundary condition beside these well defined matching points would increase the errors. For both piecewise-linear and staircase approximation of the current, explicit formulae for the optimum location of the matching points are given.*

Introduction

To find the current in a wire one uses an equation of the form

$$E_z = 0, \quad (1)$$

where E_z is the longitudinal tangential component of the electric field on the surface of the wire. If the wire is thin, E_z is small compared to other field components at the same location. Nevertheless it is the only component to be matched. For an approximate solution, E_z will never be zero on the whole surface of the wire, but only in particular points. The most simple procedure for finding an approximate solution of (1) is point-matching, where the wire is segmented and then one matching point is placed in the center of each wire segment. MMP [1] uses an extended point matching technique and lets it up to the user to place any number of matching points. (A minimum of one matching point per segment is necessary.) Equations (1) are then solved in the sense of least squares.

It has been found that the results obtained by the MMP-program are unstable in certain cases. In particular, an increase of the number of matching points did not lead to better results [2]. A closer look at the error of (1) along wires shows a great regularity of the error distribution.

In this paper, we shall show that the behavior of the error of E_z along the wire is well defined. Depending on the expansion functions of the current, there are zeros of E_z at certain points. Besides these points, E_z should never be forced to be zero, since such a forcing would affect the current in a highly unintended manner.

The following scheme gives the principal way to find the results:

- Calculate of E_z of an arbitrary current $I(z)$ on a wire (analytically)
- Approximate $I(z)$ by a staircase function (like MININEC) or a piecewise-linear function (MMP) and calculate \tilde{E}_z of the approximated current (analytically)
- Define the systematic error as the difference $E_z - \tilde{E}_z$
- Use zeros of the systematic error as optimum locations for matching points

The reason why the zeros of the systematic error are optimum locations for matching points is quite obvious: if one would try to push down the error at a location, where the systematic error is nonzero, the error of the solution is increased, since the systematic error cannot be eliminated.

As a principal result, we shall find that these optimum locations are highly independent of the global shape of $I(z)$, but only a consequence of the local ‘misfit’ of the expansion functions vs. the exact field. As a matter of fact, the optimum locations of the matching points depend on both the expansion functions and the unknown field. Therefore, both of them have to be considered to find good rules for the placing of the matching points. To get rid of this highly contradictory situation — the unknown field must be known — we shall consider that class of unknown current distributions which can be represented by a converging Taylor series. It is worth noting that the behavior of the expansion functions alone is not sufficient to find the optimum locations of the matching points.

Taylor-Representation of the Exact Current- and Charge Distribution

Let us consider a straight (thin) z -oriented wire with radius r which is carrying a current $I_{\text{exact}}(z)$. On a piece of finite length L of this wire, the current may be represented by a power series¹

$$I_{\text{exact}}(z) \approx I(z) = \sum_{n=0}^N \alpha_n z^n \quad (2)$$

We assume, that the finite power series (2) is able to represent the function $I_{\text{exact}}(z)$ within the length L so that no further error considerations are necessary. Later on, we shall divide up the length L into segments and we shall focus on the local effects of this segmentation. From this point of view, the assumptions are reasonable.

Due to the charge conservation principle, the current distribution $I(z)$ is accompanied by the charge distribution²

$$q(z) = \frac{1}{i\omega} \frac{\partial I}{\partial z} = \frac{1}{i\omega} \sum_{n=1}^N n \alpha_n z^{n-1} \quad (3)$$

As a further assumption, we state, that L is much smaller than the wavelength λ , so that the electric field \vec{E} may be calculated from $q(z)$ by means of electrostatics. Since we are only interested in local effects, we do not consider the field, which is produced by the currents and charges beyond the length L . This field is not necessarily small but almost constant along L . In particular, it does not vary on a segment of L . For this reason, it has no importance for the location of the matching points relative to the segment.

The z -component of the \vec{E} -field is obtained from $q(z)$ by Coulomb’s integral:

$$E_{z0}(r, z) = \frac{1}{4\pi\epsilon} \int_{-\frac{L}{2}}^{\frac{L}{2}} \frac{q(z')(z - z')}{\sqrt{r^2 + (z - z')^2}^3} dz' = \frac{1}{4\pi i\omega\epsilon} \sum_{n=1}^N n \alpha_n \int_{-\frac{L}{2}}^{\frac{L}{2}} \frac{(z')^{n-1}(z - z')}{\sqrt{r^2 + (z - z')^2}^3} dz' \quad (4)$$

¹ Convergence is given, if L is sufficiently small and $I(z)$ is smooth.

² Time dependency of $e^{-i\omega t}$ is assumed!

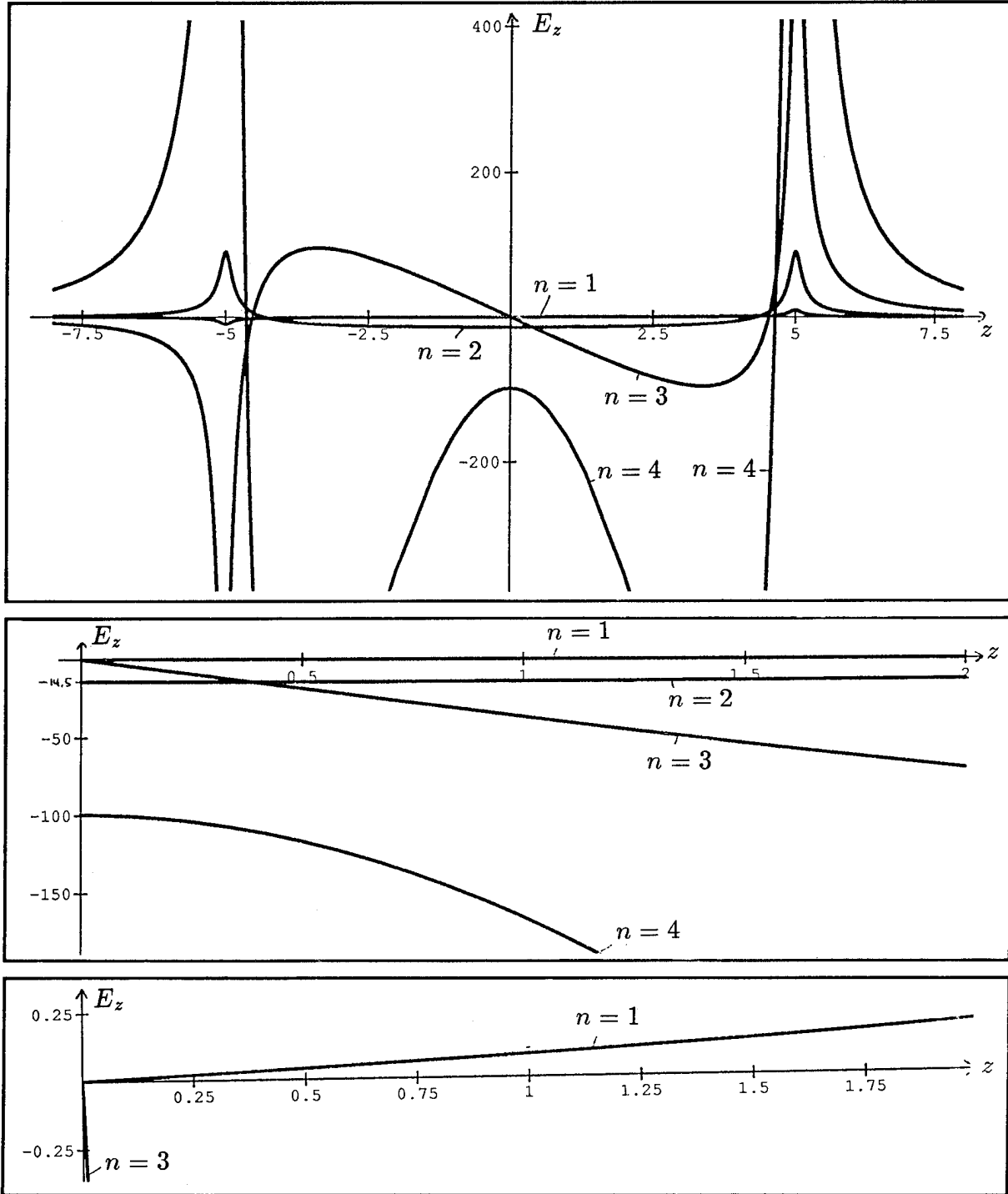


Figure 1 Different current distributions cause different distributions of the z -component of \vec{E} . The pictures show the four parts of E_z for $n = 1 \dots 4$ with $\alpha_n = 1$, $r = 0.1$ and $L = 10$. At the middle and at the bottom, details of the interval $0 \leq z \leq 2$ are shown. The numerical values are obtained from (3), omitting the factor $1/(4\pi i\omega\varepsilon)$. We focus on the area around $z = 0$.

The integral on the right hand side may be solved analytically for any n . These solutions and the plots of these functions have been obtained using Stephen Wolfram's 'mathemat-

ica'. [3] (See fig. 1!)

Due to the superposition principle, each term may be treated alone. Provided that the optimum locations for matching points being the same for each n , these locations are optimum for any $I(z)$. This is exactly what we shall find.

At the ends of L , we assume a constant continuation of the current. Otherwise, the steps in the current distributions would cause point charges at the ends, which would disturb the results in producing an additional large electric field.

Staircase Approximation

The wire of length L is cut into J segments of equal length $l = L/J$. Then the function $I(z)$ is approximated by a staircase. (See fig. 2!) The same approximation is used in MININEC [4]. Note that the point-matching technique which is described in this paper is different to the (more sophisticated) procedure used in MININEC.

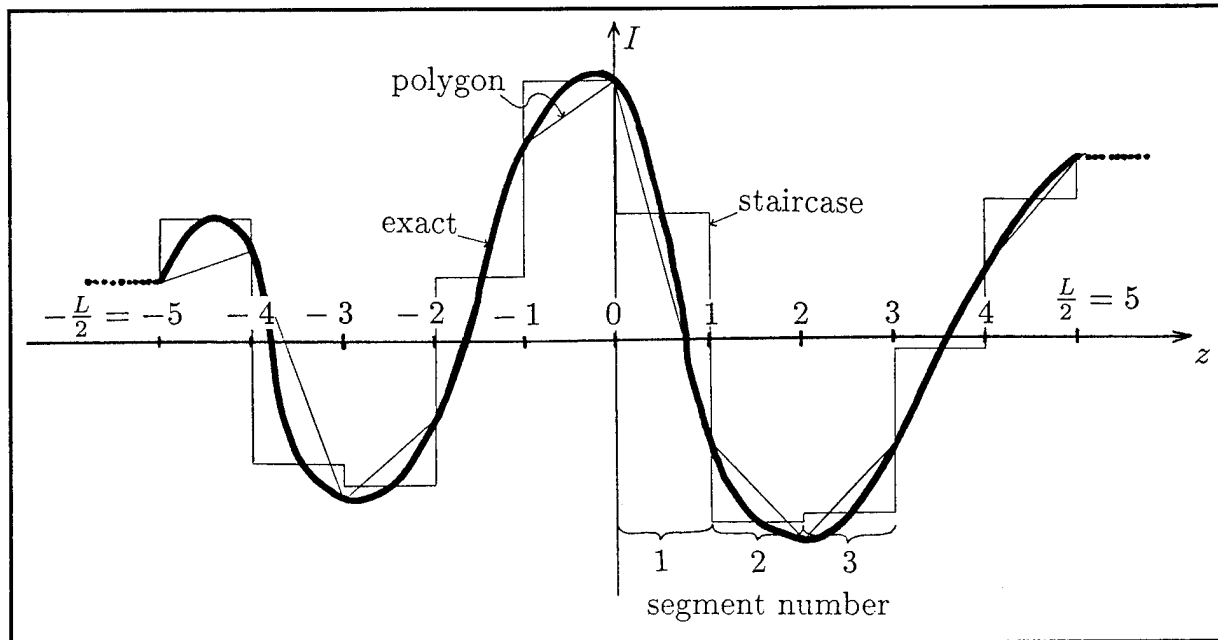


Figure 2 The smooth current $I(z)$ is approximated by staircase (like MININEC) or piecewise-linear functions (MMP). Each type of approximation is accompanied by its typical (erroneous) charge distribution. It is this charge distribution which causes a relatively big error in the local distribution of the longitudinal electric field.

Let³

$$z_j := jl; \quad -\frac{J}{2} \leq j \leq \frac{J}{2} \quad (5)$$

be the z -coordinate of the boundary between the j -th and the $(j+1)$ -th segment. In the

³ For simplicity's sake, J is assumed to be even!

j -th segment the current is constant and equal to

$$I_j := \begin{cases} I(z_j - \frac{l}{2}) & \text{for } -\frac{J}{2} + 1 \leq j \leq \frac{J}{2} \\ I(z_j) & \text{for } j = -\frac{J}{2} \\ I(z_{j-1}) & \text{for } j = \frac{J}{2} + 1 \end{cases} \quad (6)$$

I.e., we assume the approximation being exact *in the center of the segment*. The special definition of the last two currents is due to the constant continuation beyond L . This current distribution leads to *point charges* Q_j located at the segment boundaries z_j . One has

$$Q_j = \frac{1}{i\omega} (I_{j+1} - I_j) \quad (7)$$

From that, we obtain for the z -component of the resulting electric field

$$E_{zs}(r, z) = \frac{1}{4\pi\epsilon} \sum_{j=-\frac{J}{2}}^{\frac{J}{2}} \frac{Q_j \cdot (z - z_j)}{\sqrt{r^2 + (z - z_j)^2}^3} = \frac{1}{4\pi i\omega\epsilon} \sum_{j=-\frac{J}{2}}^{\frac{J}{2}} \frac{(I_{j+1} - I_j)(z - z_j)}{\sqrt{r^2 + (z - z_j)^2}^3} \quad (8)$$

The sum has $J + 1$ terms, because a line of J segments has $J + 1$ boundaries. Figure 3 shows the big variation of E_z along the wire and in particular along a single segment.

Let us define now the *systematic error* F_s^n as the difference between the “exact” result (4) and the approximation (8):

$$F_s^n(r, z) = E_{zs}^n(r, z) - E_{z0}^n(r, z) \quad (9)$$

where the upper index n denotes the power of the current: $I(z) = z^n$. It is clear, that F_s^0 must vanish, since the staircase approximation of a constant function is exact. Figure 4 shows the functions F_s^n along the segments 1 and 2. The values around $z = 0$ are not typical, because of the superimposition of a non local effect due to the symmetrical situation: With *odd* powers of the current distribution (i.e., even powers for the charge distribution), the far action of the discretization errors are cancelled due to symmetry. However, with *even* powers of the current distribution (i.e., odd powers for the charge distribution), these actions add together and cause a vertical shift of the curve. For these reasons, the behavior in the second segment is more typical.

In general we can say that *for all* powers n , the systematic error has a relatively flat zero in the middle of the segment. For that reason, it is optimum to place the matching points in the center of the segment. The second zero (close to the segment boundaries) is not useful for this purpose, because the error function is much too steep in this area. Considering the exact values of E_z (see fig. 1!), we find that the error is not negligible at all.

As a preliminary conclusion we state: For staircase approximation it is optimum to place matching points in the center of the segments — and nowhere else. This is due to the fact that the systematic error *cannot be eliminated*. A placing of a matching point at a position with a high systematic error would increase the global error of the field in such a sense, that the sum of the two vanishes.

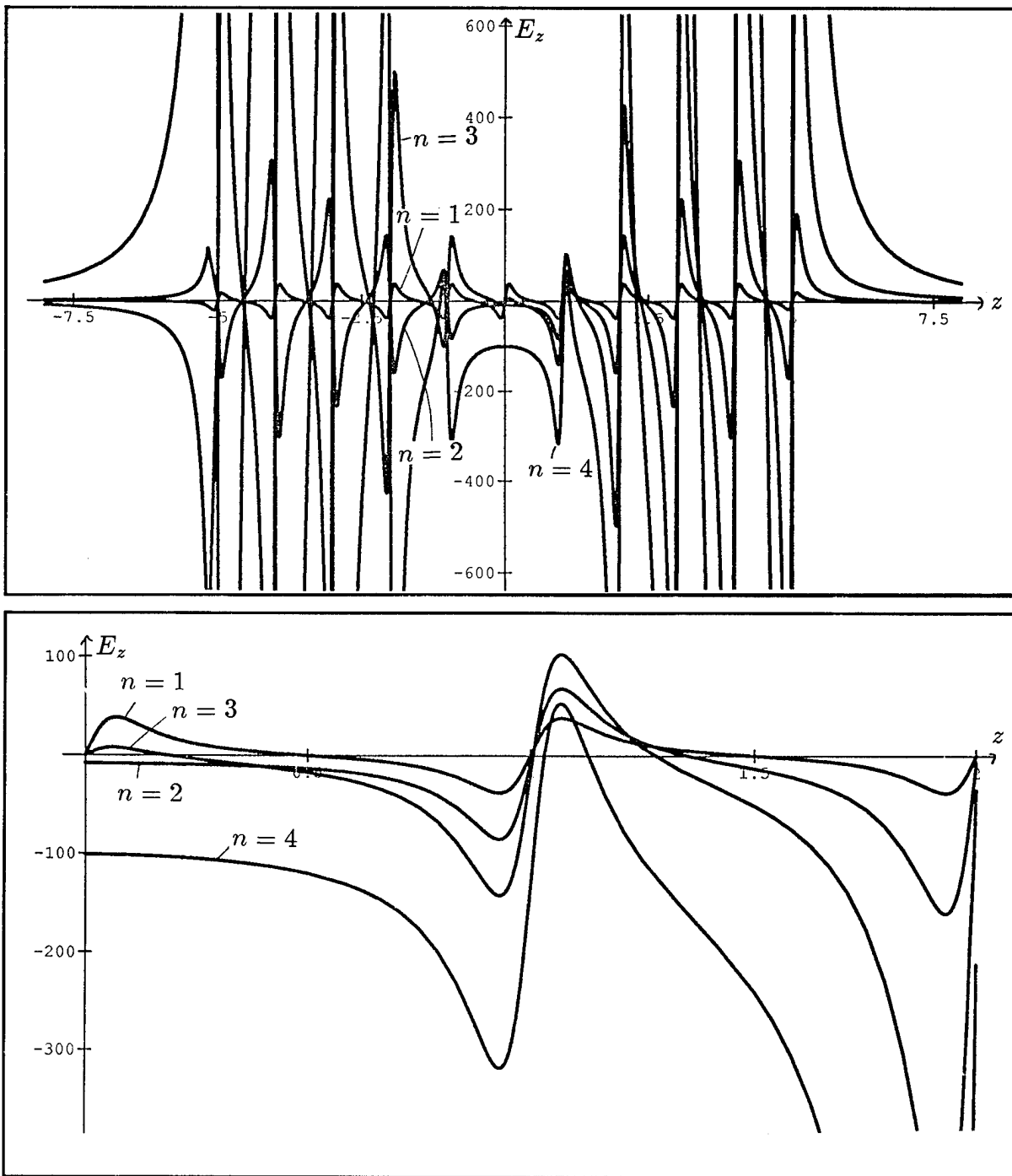


Figure 3 The staircase approximation of the current gives a much less smooth behavior of E_z than the smooth current in fig. 1. See particularly the big values in the center (near $z = 0$)! The picture shows the four parts of E_z for $n = 1 \dots 4$ with $\alpha_n = 1$, $r = 0.1$, $L = 10$ and $J = 10$ (\rightarrow segment length $l = 1$). At the middle and at the bottom, details of the interval $0 \leq z \leq 2$ are shown. The numerical values are obtained from (9), omitting the factor $1/(4\pi i\omega\varepsilon)$.

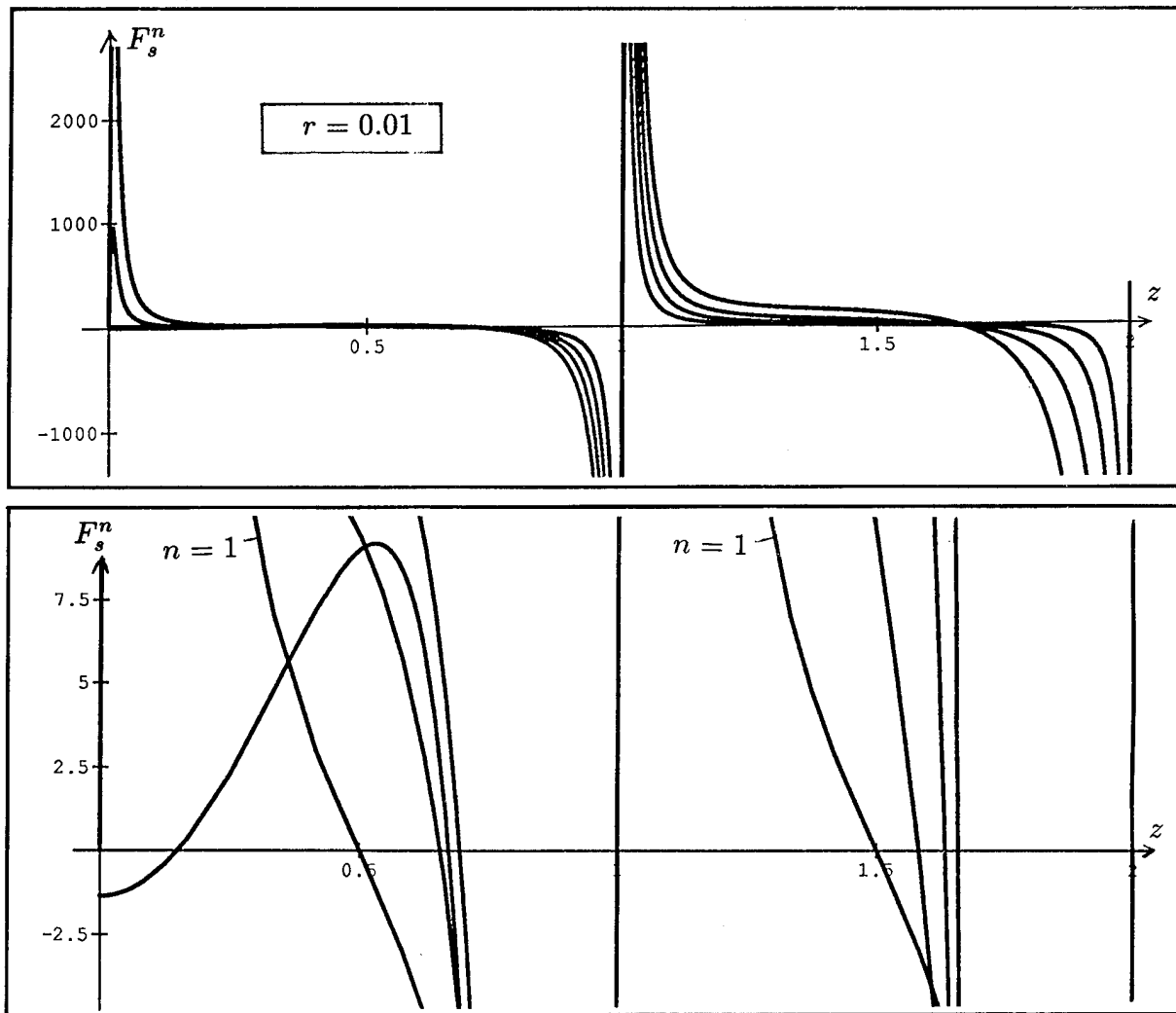


Figure 4 The systematic error F_s^n of E_z (using a staircase approximation of the current) depends on the wire radius r . Since the length of the segments has been kept constant, the ratio length/radius of a segment is actually varied. The change of the vertical scale at the bottom of each picture shows the poor flatness of the zero. As expected, the absolute value of the errors decreases with increasing radius. Note that the numerical values in fig. 1 are related to a wire radius of $r = 0.1$.

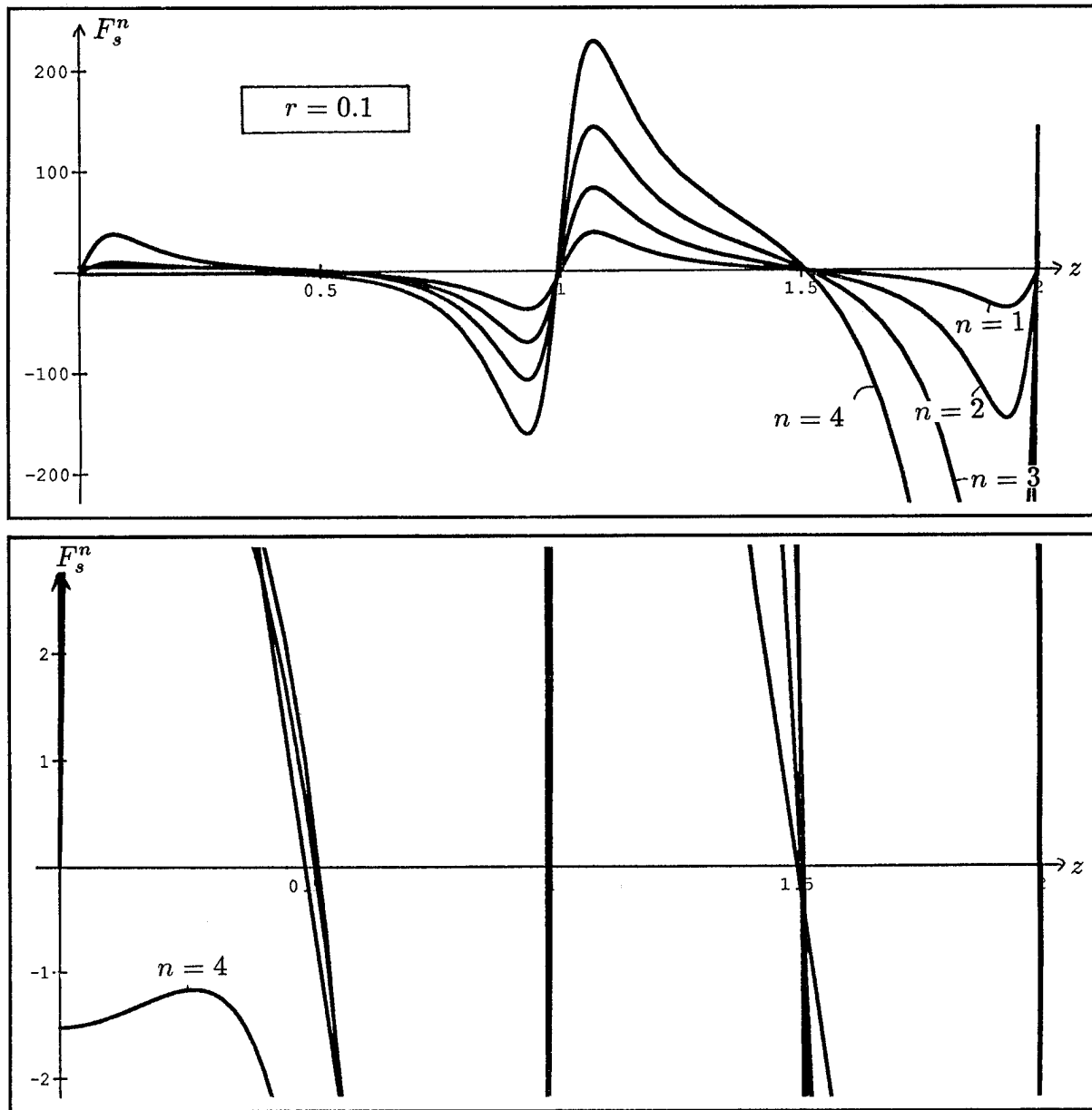


Figure 4 Continued, see above!

Piecewise-linear Approximation (MMP)

As it has been already done in the previous section, the wire of length L is split up into J segments of equal length $l = L/J$. Other than before, the function $I(z)$ is now approximated by a piecewise-linear function⁴. In the j -th segment, the current is a linear function:

$$I_j(z) = I(z_{j-1}) + \frac{I(z_j) - I(z_{j-1})}{l}(z - z_{j-1}) \quad (10)$$

⁴ In the MMP-programs, $I(z)$ is approximated using the functions $\cos kz$ and $\sin kz$, where k is the wave number of the surrounding medium [2]. Since the segments are small compared to wavelength, these two functions tend to 1 and z .

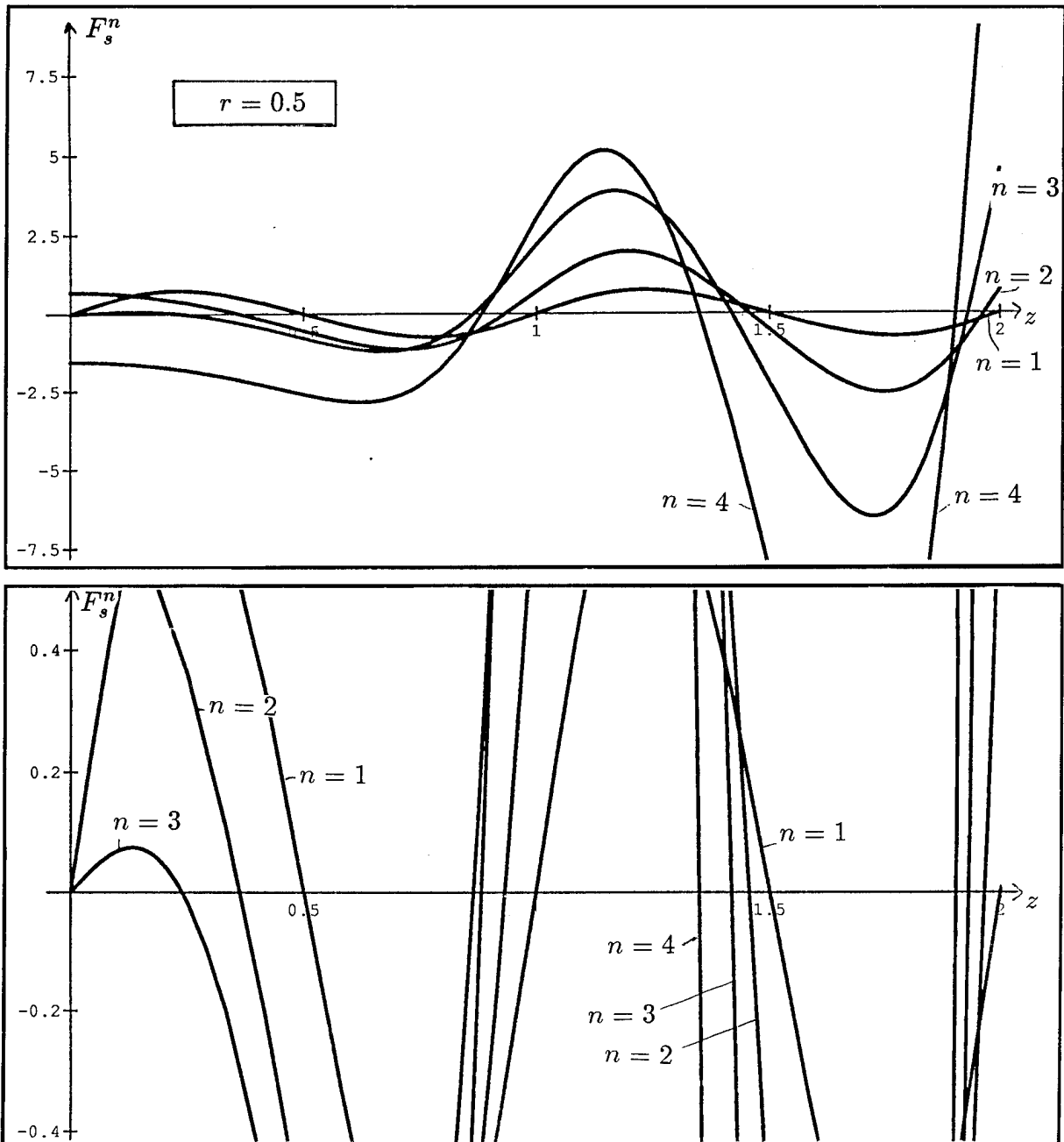


Figure 4 Continued, see above!

i.e., we assume that the approximation is exact at the *segment boundaries*. (See fig. 2!) This approximation of the current distribution leads to a *constant charge distribution* q_j on the j -th segment:

$$q_j = \frac{1}{i\omega} \frac{I(z_j) - I(z_{j-1})}{l} \quad (11)$$

and the z -component of the resulting electric field is

$$E_{zI}(r, z) = \frac{1}{4\pi\epsilon} \sum_{j=-\frac{J}{2}+1}^{\frac{J}{2}} \int_{z_{j-1}}^{z_j} \frac{q_j \cdot (z - z')}{\sqrt{r^2 + (z - z')^2}^3} dz'$$

$$= \frac{1}{4\pi i\omega\varepsilon} \frac{1}{l} \sum_{j=-\frac{l}{2}+1}^{\frac{l}{2}} (I(z_j) - I(z_{j-1})) \int_{z_{j-1}}^{z_j} \frac{z - z'}{\sqrt{r^2 + (z - z')^2}^3} dz' \quad (12)$$

Obviously, this sum has one term less than the one in (8). Figure 5 shows the variation of E_z which is now much smaller than the one shown in fig. 3.

Again, the systematic error F_l^n is defined as the difference between the “exact” result (4) and the approximation (12):

$$F_l^n(r, z) = E_{zl}^n(r, z) - E_{z0}^n(r, z) \quad (13)$$

where the meaning of the upper index is the same as in (9). It is clear, that both F_l^0 and F_l^1 vanish, since the piecewise-linear approximation of a linear function is exact.

Considering the systematic error we find — as in the staircase approximation — a great regularity, which is qualitatively equal for all powers. On the other hand, there is a fundamental difference: The zeros of the systematic error do not occur in the middle of the segments, but more close to the segment’s boundaries. (See figs. 6 and 7!)

Due to the global effect in the middle of L (vertical shift of the even order curves and a zero at $z = 0$ for the odd orders due to symmetry), the first zero after $z = 0$ is not used. (For the numbering of the zeros, see fig. 6 at the bottom.) The exact location of the zeros of the systematic error is a function of the radius r , the order n and the number of the zero. Figure 8 shows this locations as a function of the wire radius r . Note the great regularity!

Due to the fact that the lowest order (here $n = 2$) is most important and, on the other hand, curves for different zero numbers are — at least for small radii, i.e. thin (long) segments — almost equal, it makes sense to use e.g. the third zero of the second order as a reference. The bigger variation at r/l -ratios more than $1/3$ does not matter, since the absolute values of the systematic errors decrease with increasing wire radius.

We conclude: For piecewise-linear approximation, matching points in the center of the segments should be avoided. There are *two optimal locations* for each segment, symmetrically placed at a distance d away from the segment’s boundaries.

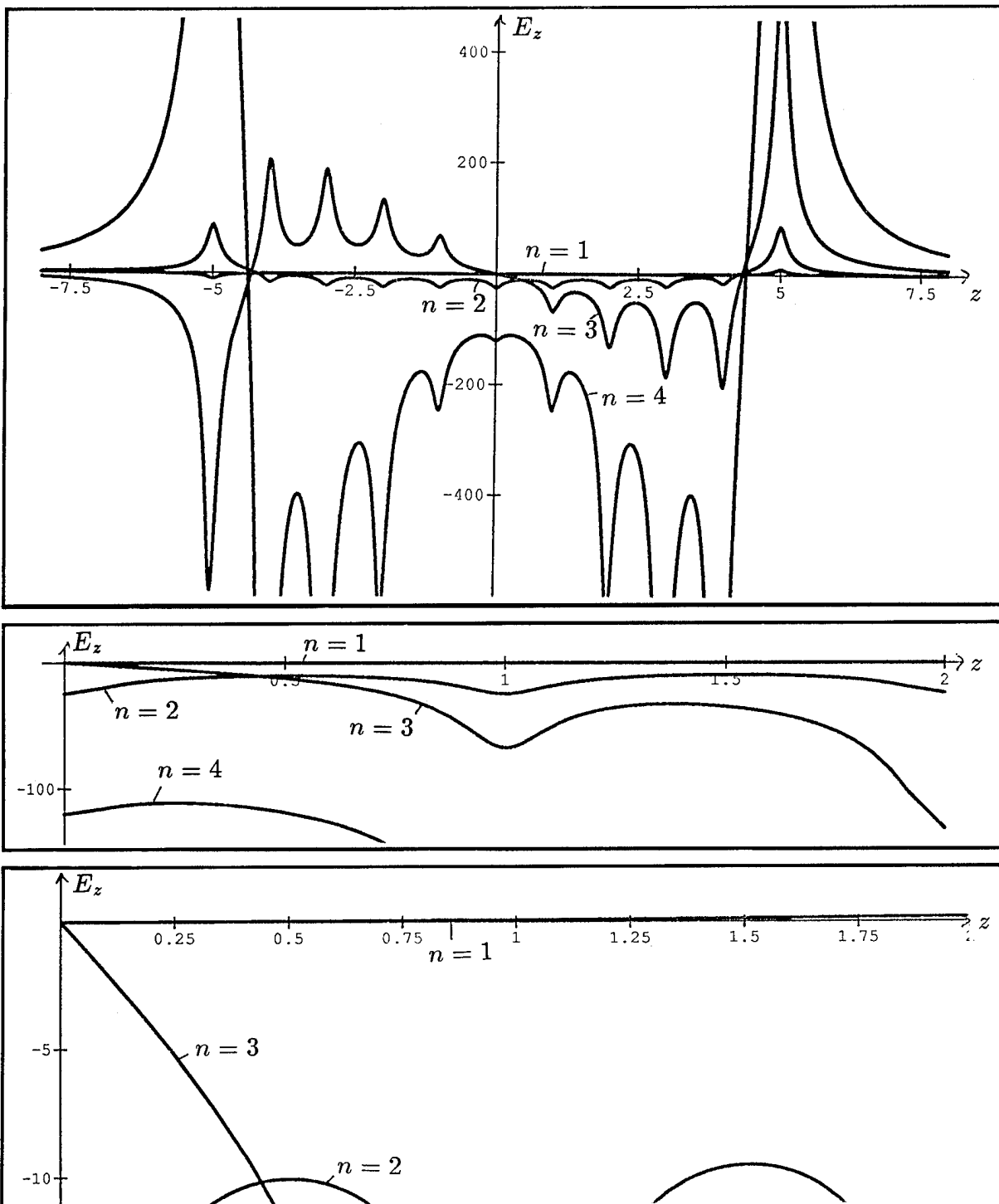


Figure 5 Compared with fig. 1 the piecewise-linear approximation of the current still gives an unquiet behavior of E_z , but the improvement with respect to the staircase approximation (fig. 3) is obvious. The pictures show the four parts of E_z for $n = 1 \dots 4$ with $\alpha_n = 1$, $r = 0.1$, $L = 10$ and $J = 10$ (\rightarrow segment length $l = 1$). At the middle and at the bottom, details of the interval $0 \leq z \leq 2$ are shown. The numerical values are obtained from (12), omitting the factor $1/(4\pi i\omega\epsilon)$.

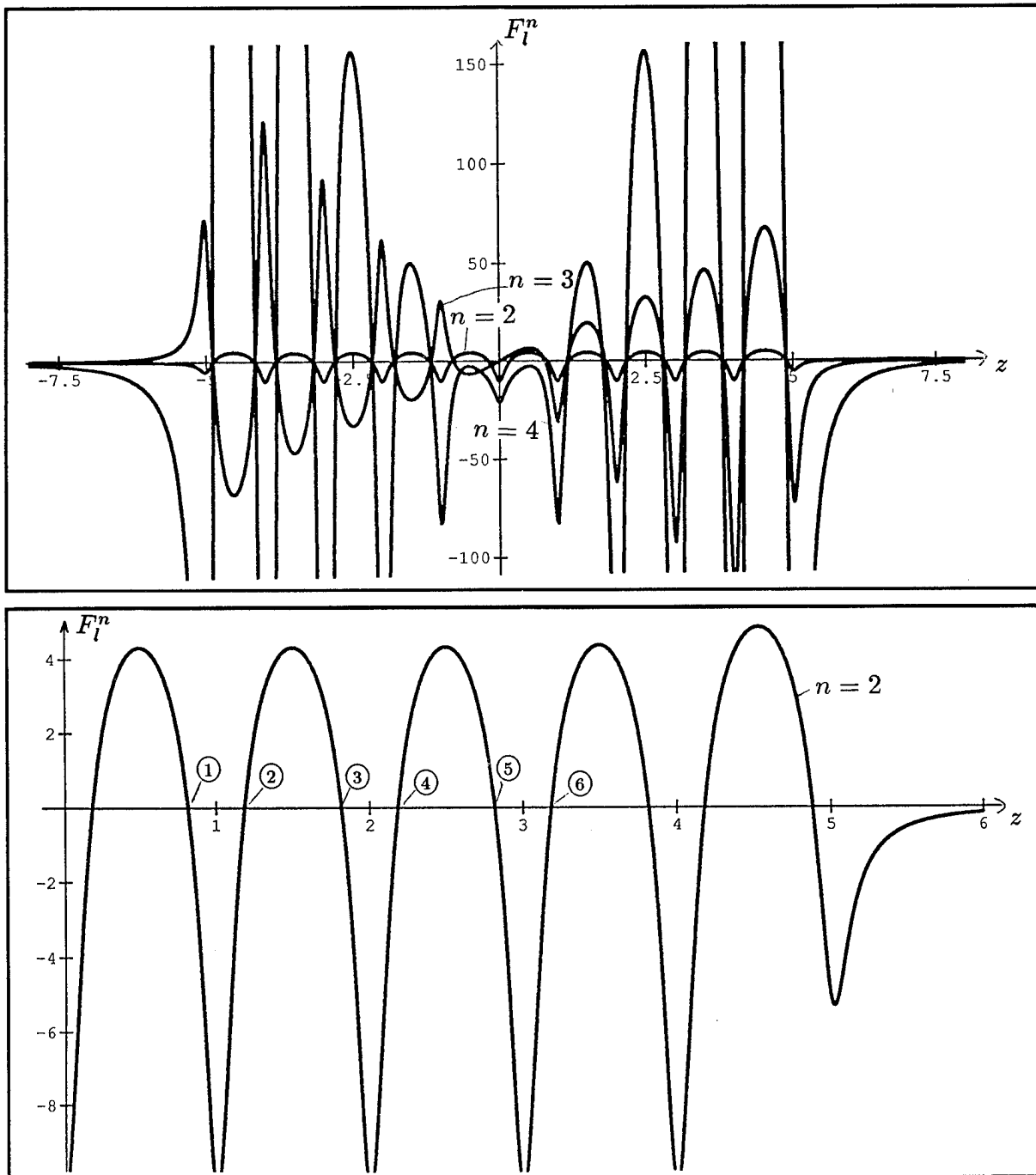


Figure 6 The systematic errors F_l^n (in the case of a piecewise-linear approximation for the current) are very similar for different powers. At the top, the figure shows the systematic errors of the order $n = 2 \dots 4$. At the bottom, the most important order 2 is given individually. The numbering of the zeros (numbers in circles) starts at the second one. This is due to the symmetry caused fact, that the even curves (from 4-th order on) are vertically shifted down around $z = 0$, while odd curves have a zero at $z = 0$. The distance between the zeros and the segment boundaries (here integer valued z 's!) is the important parameter for placing matching points.

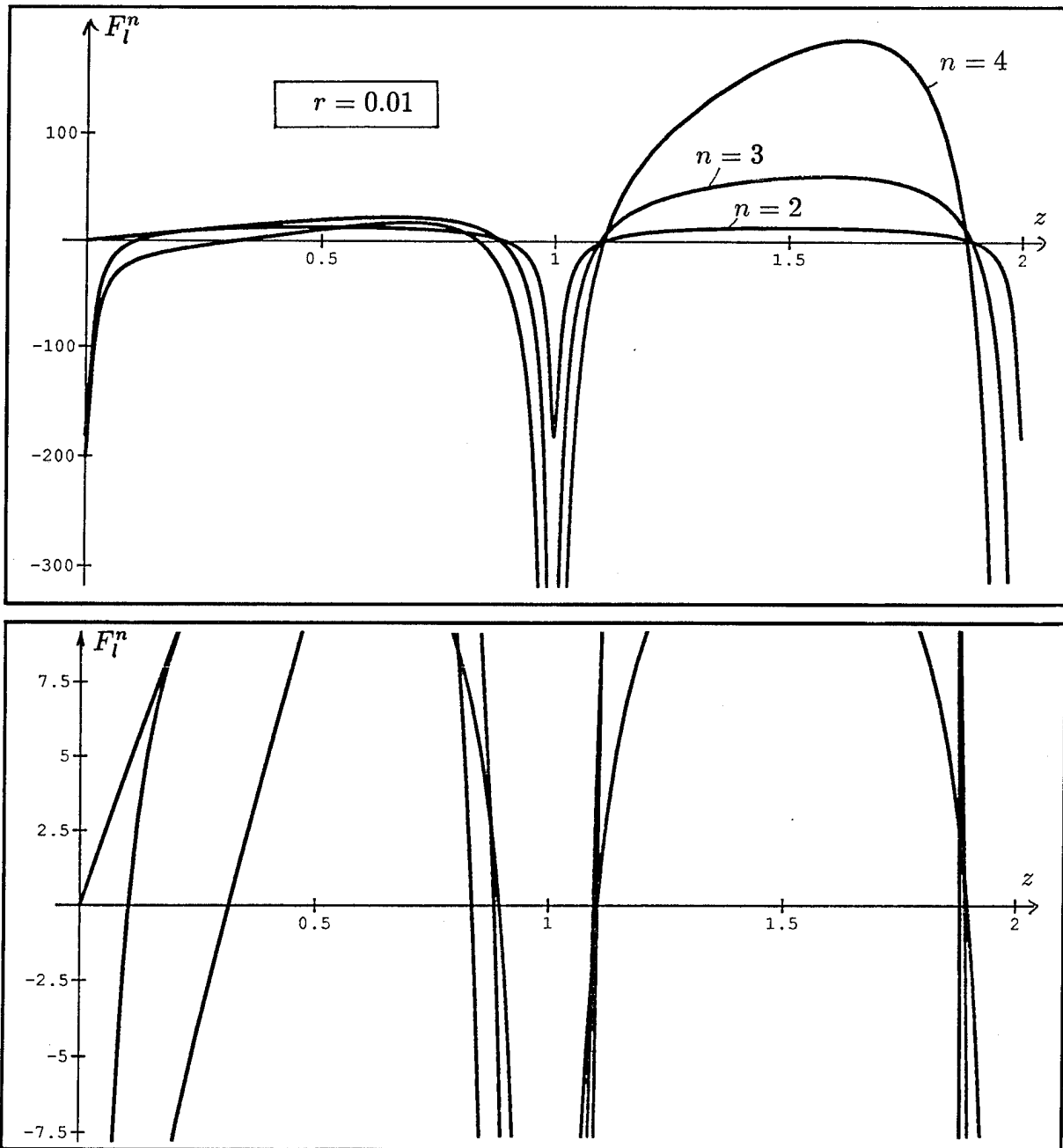


Figure 7 The systematic error F_l^n of E_z when using a piecewise-linear approximation of the current depends on the wire radius r . Since the length of the segments has been kept constant, the ratio length/radius of a segment is actually varied. Note that the numerical values in fig. 1 are related to a wire radius of $r = 0.1$.

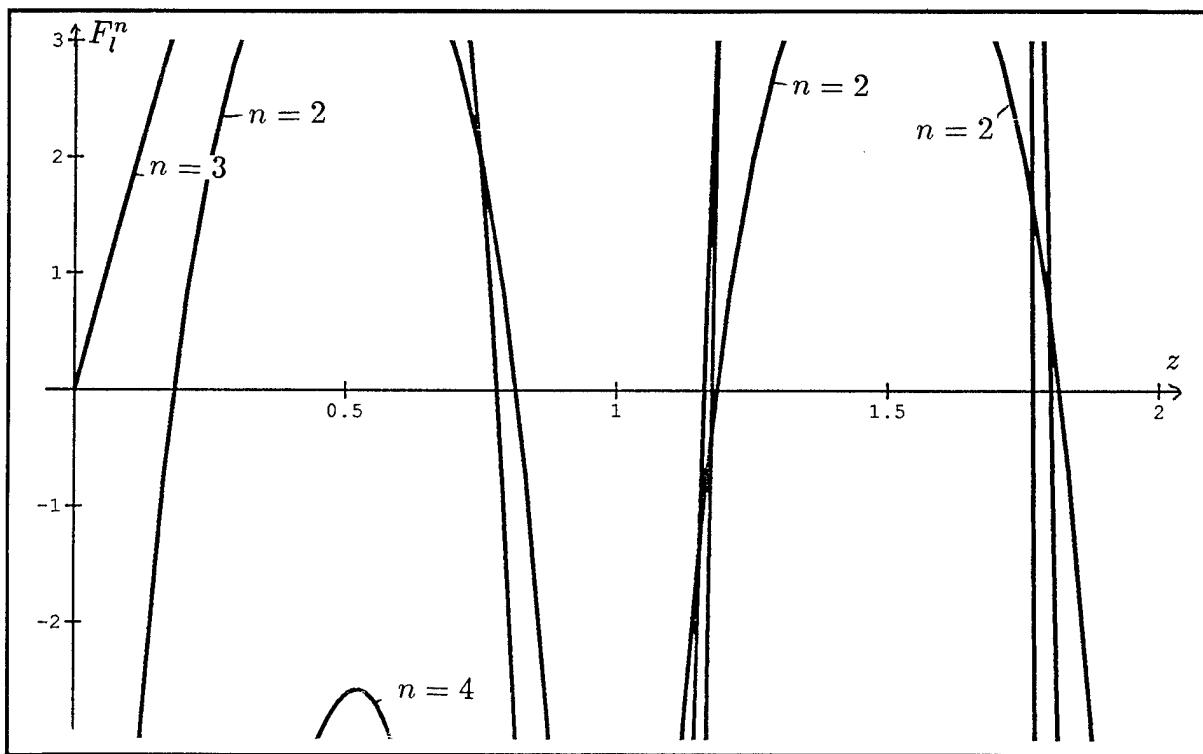
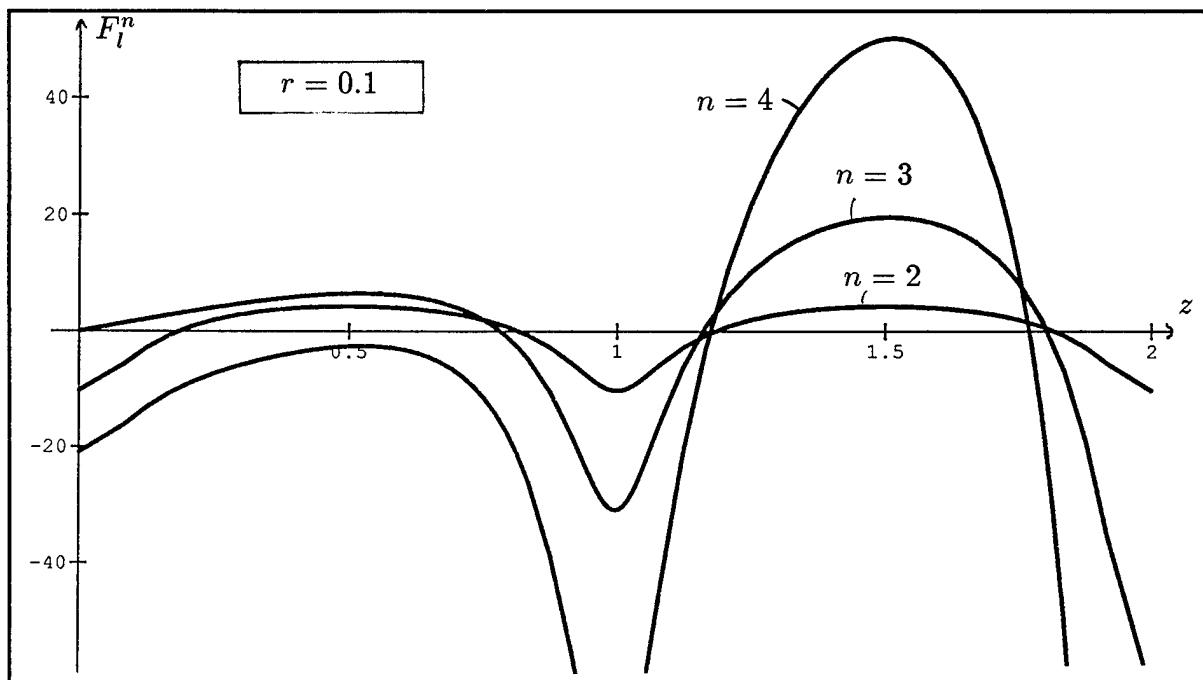


Figure 7 Continued, see above!

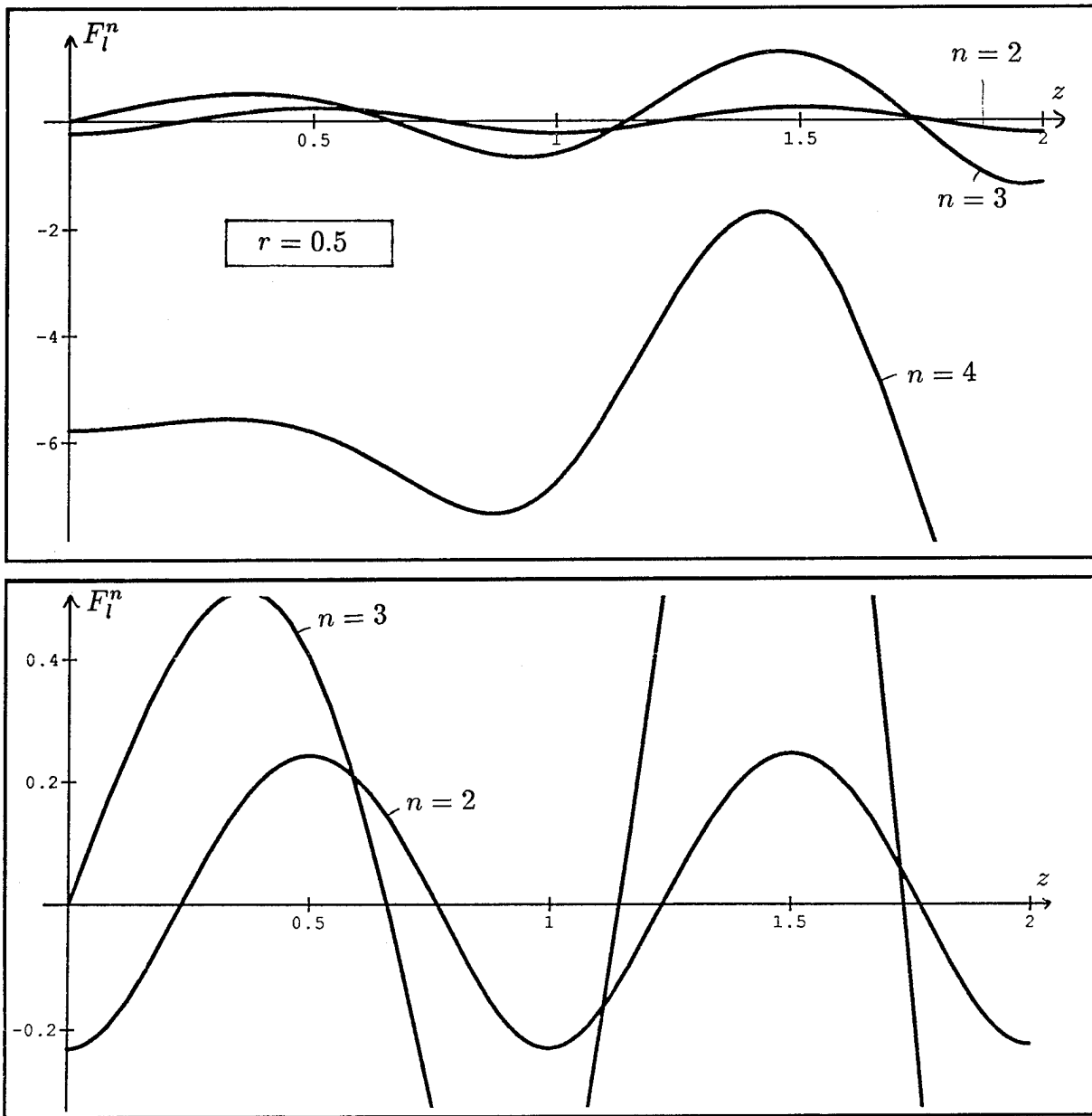


Figure 7 Continued, see above!

Polynomial Approximation of the Zero's Relative Position

We have chosen as a reference the zero number 3 of the quadratic term of the current. It is located at a distance d_3 away from the segment's boundary. This distance d_3 is a function of the wire radius r : $d_3 = d_3(r)$. 'Mathematica' [3] does the job to expand the function $d_3(r)$ into a power series of m -th order. We normalize the segment length to 1 and find:

$$\begin{aligned}
 d_3^2(r) &= 0.1246832 + 0.572177r - 0.7090428r^2 \\
 d_3^3(r) &= 0.1085357 + 0.893254r - 2.043528r^2 + 1.480294r^3 \\
 d_3^4(r) &= 0.0978577 + 1.245951r - 4.679222r^2 + 8.298414r^3 - 5.672312r^4
 \end{aligned} \tag{14}$$

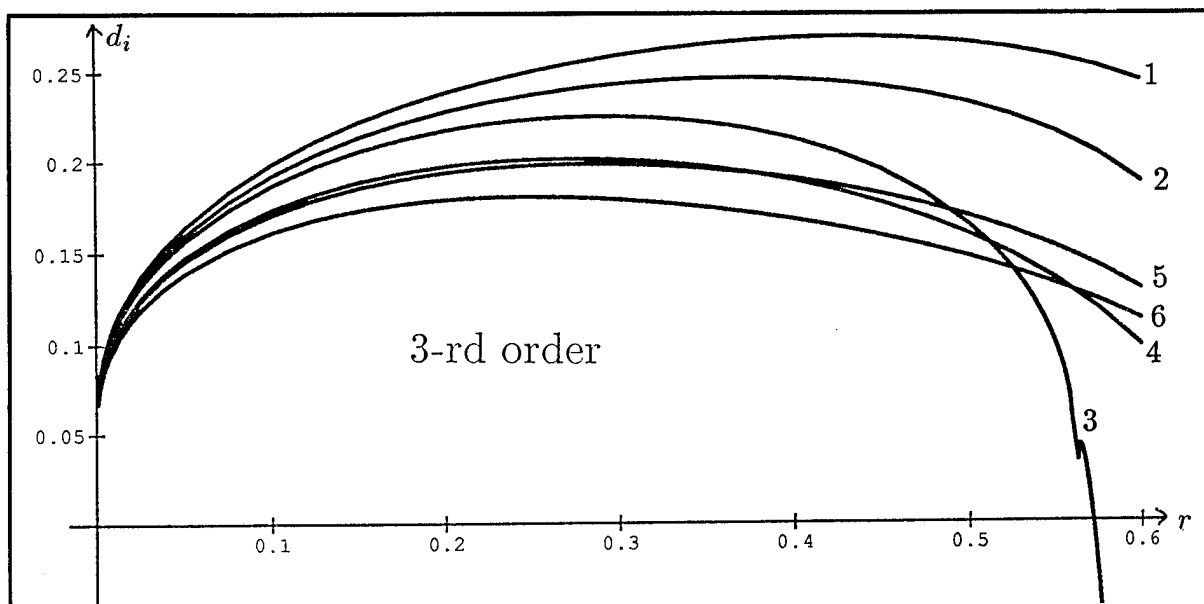
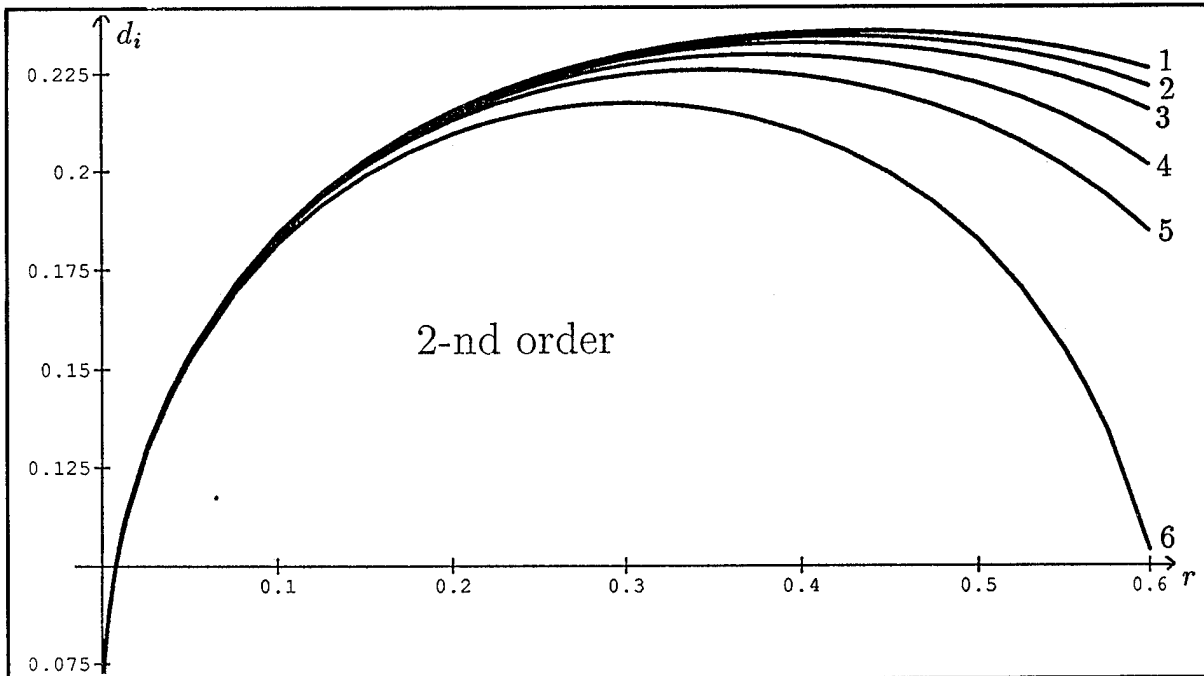


Figure 8 The relative position of the zeros of the systematic error varies only little. The pictures show the distance d_i between the i -th zero and the next segment boundary as a function of the wire radius r . Only the second and the third order is shown. The position of the zeros with higher numbers are inaccurate due to end effects of the model (only 10 segments).

The upper index denotes the order of the approximations, which are valid within the interval $0.001 \leq r \leq 0.6$.

The deviation of the true value is maximum at the border of this interval. We denote the biggest deviation downwards (approximation smaller than true value) with l_m and the biggest deviation upwards (approximation bigger than true value) with u_m . Mathematica

delivers

$$\begin{aligned}
 l_2 &= 0.05406; & u_2 &= 0.00926 \\
 l_3 &= 0.03824; & u_3 &= 0.00634 \\
 l_4 &= 0.02791; & u_4 &= 0.00471 \\
 l_5 &= 0.02208; & u_5 &= 0.00396
 \end{aligned} \tag{15}$$

Comparing these numbers with the true value (≈ 0.2) and considering the variation between the different zeros (see fig. 8!), an approximation of $d_3(r)$ of 4-th order is sufficient.

Summary

We have found that the positions of matching points along thin wires must be chosen carefully. Depending on the segmentation and the type of the approximation of the currents in the wire, optimum matching point positions are different. The results have been found by examining the error produced by a ‘best fit’ of some expansion set (staircase and piecewise-linear expansion functions) to an arbitrary current distribution.

The free choice of matching points in the MMP-code is an error source which could be avoided. Using MMP one should set two matching points for each segment, symmetrically located at a distance d away from the segment’s boundaries (see eq. (14)!). This choice is optimum at all locations where the current $I(z)$ is either concave, convex or linear.

As a further result, we find that the point matching technique is preferred to any other method to satisfy boundary condition (1), as long as the current is a) approximated by fixed functions and b) strictly coupled to the electric field through Maxwell’s equations. This second point is not fulfilled, e.g., by MININEC: it uses a piecewise-constant approximation of the charge distribution, which would be related to a piecewise-linear current distribution.

References

- [1] Ch. Hafner, *The generalized multipole technique for computational electromagnetics*, Artech House Books, 1990.
- [2] P. Leuchtmann, “Thin wire feature for the MMP-code,” in *6th Annual Review of Progress in Applied Computational Electromagnetics (ACES), Conference Proceedings*, (Monterey), Mar. 1990.
- [3] S. Wolfram, *Mathematica*, Addison-Wesley Publishing Company, Inc., 1988.
- [4] *NEEDS, (Numerical Electromagnetic Engineering Design System)*, distributed by the Applied Computational Electromagnetics Society.

SURFACE MODELLING FOR EM INTERACTION ANALYSIS

S. Kashyap and A. Louie
Electronics Division
Defence Research Establishment Ottawa
Ottawa, Ontario
Canada

ABSTRACT

This paper deals with the numerical modelling of the surface of a structure with a wire grid or a surface patch for Electromagnetic (EM) interaction analysis. Surface currents and fields on a wire grid model are computed using the Numerical Electromagnetic Code (NEC). The results are compared with those obtained on a triangular surface patch model using an Electric Field Integral Equation (EFIE) formulation. Simple structures such as a square plate as well as complicated structures such as an aircraft are considered. Good agreement is obtained in most cases.

INTRODUCTION

Numerical modelling of a surface with a wire grid has been used for many electromagnetic antenna radiation and scattering problems [1-4]. It has many attractive features and is capable of giving reliable far-field results if a proper choice of wire diameters and grid size is made [5]. However, some questions have been raised regarding the validity of using wire grid models of a closed surface when calculating electromagnetic pulse (EMP) interactions [6]. These questions arise because, for calculating EMP interaction, one must determine the currents and current densities induced on the surface. In the case of a structure with a closed surface, the field must vanish identically in the interior region, whereas for the wire grid model, there is an evanescent reactive field clinging to both sides of the grid. Even for a structure with an

open surface (e.g. a plate) there are questions regarding the variation of the current around the wire circumference, and regarding the behaviour of the fields between the wires and at the junctions.

There are also questions regarding the choice of the wire diameters in a wire grid representation. There are rules for choosing wire diameters for obtaining reliable results for far field quantities. It is not clear whether the same rules apply for the estimation of currents and current densities induced on a structure exposed to EMP.

This paper attempts to answer some of these questions by comparing wire grid and surface patch modelling for a number of structures. Simple structures such as a square plate as well as complicated structures such as an aircraft are considered. The Numerical Electromagnetic Code (NEC) [1] is used for the wire grid models and the Electric Field Integral Equation (EFIE) [7] is used for the surface patch models. Surface currents and current densities induced on a structure due to an incident electromagnetic wave are computed using the two techniques and compared. Some modifications are required in the existing codes in order to deal with large number of wire or patch segments and to overcome difficulties involved in modelling surfaces where three patches have one common edge. Although the comparison is done in the frequency domain, the time domain behaviour can be obtained using the Fourier transform.

PROCEDURE

A wire grid representation of the surfaces of the body which is to be analyzed is first made following the rules given in the NEC documentation [1]. For a simple structure such as a square plate this is fairly straightforward. However, for a complicated structure the creation of a wire grid model is difficult and one must use specialized software such as DIDECK.DREO [8]. The diameter of the wires is chosen to follow the criterion that the surface area of the wire parallel to one linear polarization should be equal to the surface area of the solid surface being modelled [9]. The NEC is then used to determine currents

at the centre of each wire segment. The induced H-field or surface current density at a point on the equivalent surface represented by the wire is then computed by

$$H_{\text{induced}} = I/2\pi a,$$

where I is the current induced in the wire obtained by NEC computations and a is the radius of the wire.

In order to check the accuracy of the wire grid representation for determining surface current and currents, a surface patch model is created. This surface patch model uses the Electric Field Integral Equation (EFIE) instead of the magnetic field integral equation (MFIE) as proposed in the NEC. The surface of the body is modelled by triangular patches and a modified version of the program EFIE [10] is used to compute the surface current distribution. The modifications to the EFIE include the use of a new matrix LU factorization routine and the addition of a solution polisher. The new matrix factorization routine results in a great reduction in time. The solution polisher gives some extra significant digits whenever the impedance matrix is ill-conditioned. The induced H-field output of the EFIE is available at the edges of every triangular patch and is directed perpendicular to the edge and the normal to the surface.

Since the NEC wire grid modelling computations yield current and induced H-field along the axis of a wire and the EFIE triangular surface patch modelling computations yield induced H-field perpendicular to the triangle edge, care has to be taken in comparing data from the two models. The need for this care is demonstrated in Figures 1a to 1c which show the wire grid and the equivalent surface patch models for a square plate. The Figures show 90 wire rectangles for the wire grid representation and 84 triangular patches for the surface patch representation. This discretization is chosen to allow easy comparison of induced fields or charge densities along two principal cut lines of the square plate. Other discretizations are permitted as long as the rules of EFIE and NEC are not violated. The points along the two axes (XX' and YY') at which the surface fields are evaluated on the wire grid and the surface patch representation are shown in

the Figures. These points are not identical but can be made so if required without much difficulty. It is obvious that making a choice of points for comparison also presents little difficulty in this simple case. However the choice of points for making a proper comparison between two representations is not always straightforward for a complicated structure such as an aircraft.

Figure 2a shows the J_x current density distribution along two principal cut lines (XX' and YY' in Figure 1) on a 1.0 wavelength square plate, illuminated by a plane electromagnetic wave incident normally on the plate. In Figure 2a and the subsequent Figures the induced current density normalized by the incident magnetic field intensity is plotted on the vertical axis. Because of the normalization this quantity has no units. The comparison between the wire grid and triangular surface patch results is very good except at the edges of the plate. The normalized current densities obtained by the wire grid model are smaller at the edges because the equivalent surface area is larger and the "equal-area" rule can no longer be followed.

If the diameter of the wires at the edges is reduced by half (Figure 1c), the wire grid results seem to match very well with the surface patch results even at the edges. This is shown in Figure 2b. The wire grid results at the edges of the plate perpendicular to the y-axis are, however, still not correct. Because of discontinuity, the normalized current density function is singular (i.e. has an infinite value) at these edges [7]. This infinite value can only be approached by the wire grid results in the limit, when the edge wire diameter and the area it represents become infinitesimally small. The surface patch results are not obtained at these edges.

Figure 3b shows the dominant current density distribution along a cut (line XX') through the symmetry plane of a 1.0 wavelength bent square plate (Figure 3a). The distance S shown in Figures 3b and 3c is measured along the plate from point X indicated in Figure 3a. The bend is located at two-third the plate width from this point and is parallel to the plate edge. A plane wave with the E-field parallel to the bend is incident normal to the large section of the plate. The smaller section is bent at an angle of 50° towards the

shadow side of the plate. There are 72 (or 6x6x2) triangular patches for the EFIE solution versus 156 (or 13x12) wire rectangles for the wire gird model NEC solution. The diameter of the wires is chosen to satisfy the equal-area rule discussed earlier (although for simplicity they are not shown in Figure 3a). The comparison of the wire grid and the triangular surface patch models is again very good except close to the edges of the plate.

As discussed before, the discrepancy results from the non-compliance of the equal-area rule at the edges. Again, if the diameter of the wires at the edges is reduced by half, the agreement between the wire grid and the surface patch results is improved. This is shown in Figure 3c. Earlier comments on the singularity of the induced current density at the edges also apply here.

Figure 4a shows an example of a complicated wire grid model of an aircraft that is analyzed here. Figure 4b shows the equivalent surface patch model. The wire grid structure has already been analyzed for scattering and radiation properties [9]. In our case, the wire grid structure consists of 326 wire segments and the surface patch representation consists of 398 triangular patches. A plane wave with the electric field polarized parallel to the long axis of the aircraft is incident normal to the top of the aircraft. The x-axis runs parallel to the length of the aircraft (hence parallel to the incident electric field), with the reference point $x=0$ located in the middle of the attachment of the wings to the fuselage, and with positive x-coordinate values towards the front of the aircraft. Figure 5a compares the normalized current densities of the two models along the top fuselage of the aircraft at 20 MHz. The comparison shows a good agreement between the surface patch and the wire grid models. Figure 5b compares the normalized current density around the circumference of the fuselage at the front of the aircraft at 10 MHz. The agreement between the wire grid and the surface patch models is again quite good.

The discrepancy is partly explained by the fact that the points of observation are not identical in this case. In a complicated structure such as an aircraft, it is difficult to maintain the same observation points for the wire grid and the surface patch models.

Figure 6 shows the wire grid and the triangular surface patch models of a metallic cube with an open top. Each side of the cube is 1.0 wavelength long. The models consist of 405 wire rectangles and 408 triangular surface patches, respectively. A polarized plane wave is incident on the open face as shown. Figure 7 shows the normalized induced current density along the lines XX' and ZZ' on one face of the cube for the two models. The agreement between the models is very good even at the edges of the cube. It is to be noted that the wire diameters at the top edges (only at the open end) parallel to the incident field have been reduced to follow the equal-area rule. The current density at the open edge again exhibits a singular behaviour, and the earlier comments on the wire grid results apply.

EMP INTERACTION ANALYSIS

The above analysis can be performed for a number of frequencies as long as the rules of the wire grid and those of the surface patch representation are followed. Response to a pulse excitation such as the EMP can be obtained by convolution with the EMP spectrum and taking a fast Fourier transform of the response at a proper number of frequencies [11]. The procedure is simple for the cases of the flat square plate, the bent square plate, and the open-topped cube. However, for the case of the aircraft, difficulties arise because of the large number of wire segments or triangular patches required at the upper end of the EMP spectrum. The CPU time required in this case is considerable even for a single frequency.

CONCLUSIONS

We have computed induced surface fields for a number of structures for plane wave incidence. The limited number of examples treated indicate that the results obtained by the wire grid and the triangular surface patch models show good agreement and both models may be used to compute induced surface fields.

REFERENCES

1. G.J. Burke and A.J. Poggio, "Numerical Electromagnetic Code", Technical Document 116, Naval Electronic Systems Command, 18 July 1977.
2. C. W. Trueman, S. R. Mishra and S. J. Kubina, "RCS of Fundamental Scatterers in the HF Band", *1991 Applied Computational Electromagnetics Society Conference Proceedings*, pp. 369-379, 1991.
3. C. W. Trueman and S. J. Kubina, "Automated Radius Calculations for Wire-grid Models", *1991 Applied Computational Electromagnetics Society Conference Proceedings*, pp. 370-388, 1991.
4. L.A Oyekanmi and J. Watkins, "Selecting Wire Radius for Grid/Mesh Models", *Applied Computational Electromagnetics Society Journal*, Vol. 5, No. 2, pp. 43-57, 1990.
5. A.C. Ludwig, "Wire Grid Modelling of Surfaces", *IEEE Transactions on Antennas and Propagation*, Vol. AP-34, No. 9, pp. 1045-1048, 1987.
6. K.H.S. Lee, L. Martin and J.P. Costello, "Limitations on Wire-Grid Modelling of a Closed Surface", *IEEE Transactions on EMC*, Vol EMC-18, NO. 3, pp. 123-129, 1976.
7. S.M. Rao, D.R. Wilton and A.W. Glisson, "Electromagnetic Scattering by Surfaces of Arbitrary Shape", *IEEE Transactions on Antenna and Propagation*, Vol. AP-30, No. 3, pp. 409-419, 1982.
8. S. Kashyap, M. Dion and A. Louie, "An Improved Model-Creation Program for EM Interaction Analysis", *Proceedings of the Canadian Conference on Electrical and*

Computer Engineering, Ottawa, Ontario, Vol. 1, pp. 38.5.1-38.5.3, 1990.

9. S.J. Kubina and C.W. Trueman, "Some Practical Considerations in the Validation of EM Modelling Codes", *Proceedings of 1988 IEEE AP-S International Symposium*, pp. 1351-1354, 1988.
10. M. Burton and S. Kashyap, "Using software to push back the limits of the moment method", *Proceedings of the IEEE/APS Symposium*, London, Ontario, Vol. 3, pp. 1504-1507, 1991.
11. M. Dion and S. Kashyap, "Some Considerations on the Use of NEC for Computing EMP Response", *Applied Computational Electromagnetic Society Journal*, Vol. 4, No. 2, pp. 73-89, 1989.

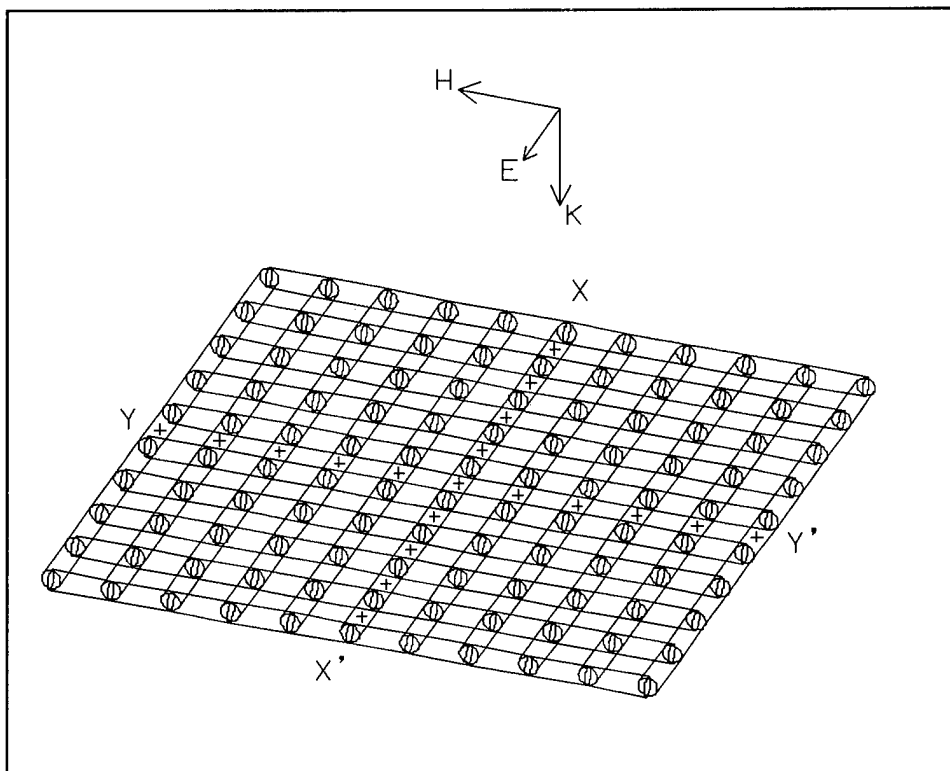


Figure 1a. Wire grid (NEC) model of a flat square plate with equal-area wire diameters.

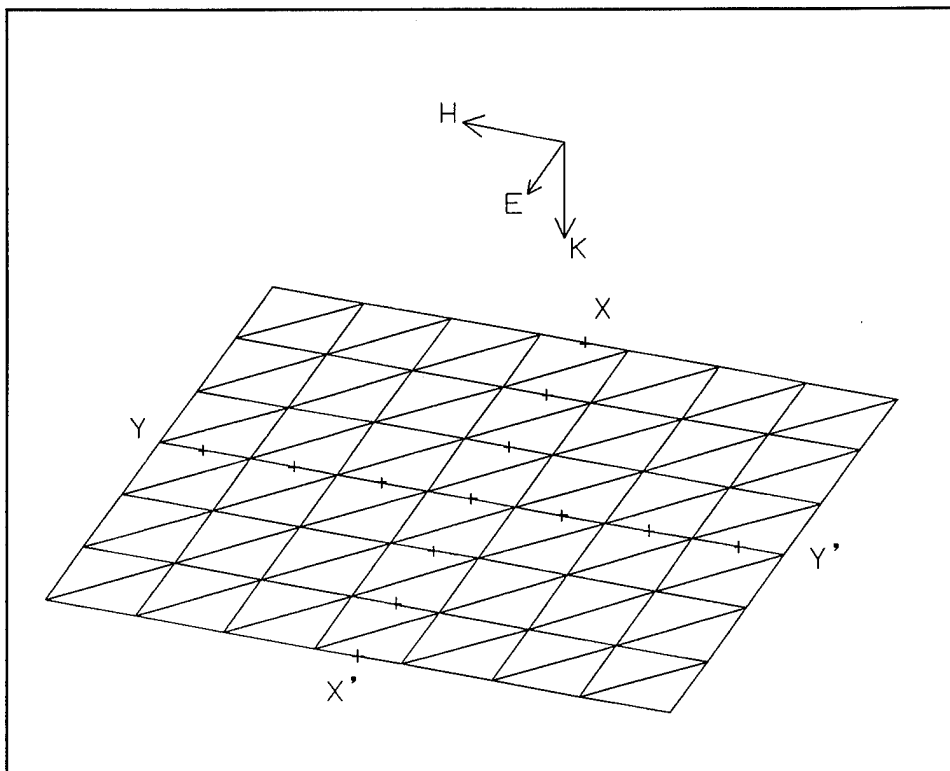


Figure 1b. Surface patch (EFIE) model of the flat square plate, equivalent to the wire grid model of Fig. 1a.

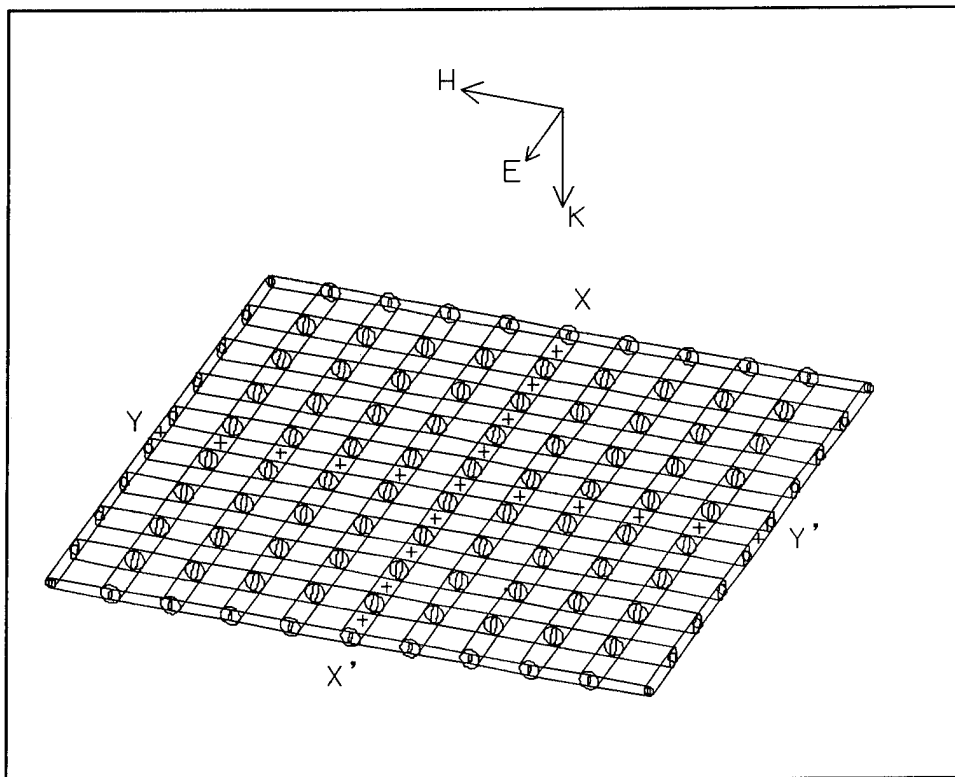


Figure 1c. Wire grid (NEC) model of the flat square plate with edge wire diameters halved.

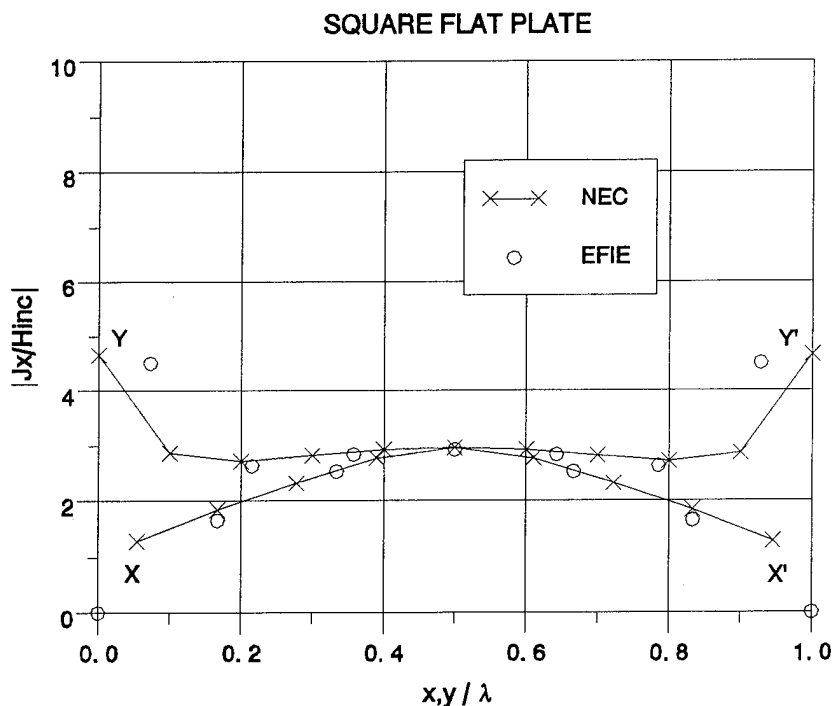


Figure 2a. Distribution of dominant component of current density along XX' and YY' on 1.0 lambda plate; x and solid line = wire grid (NEC) model of Fig. 1a, o = surface patch (EFIE) model of Fig. 1b.

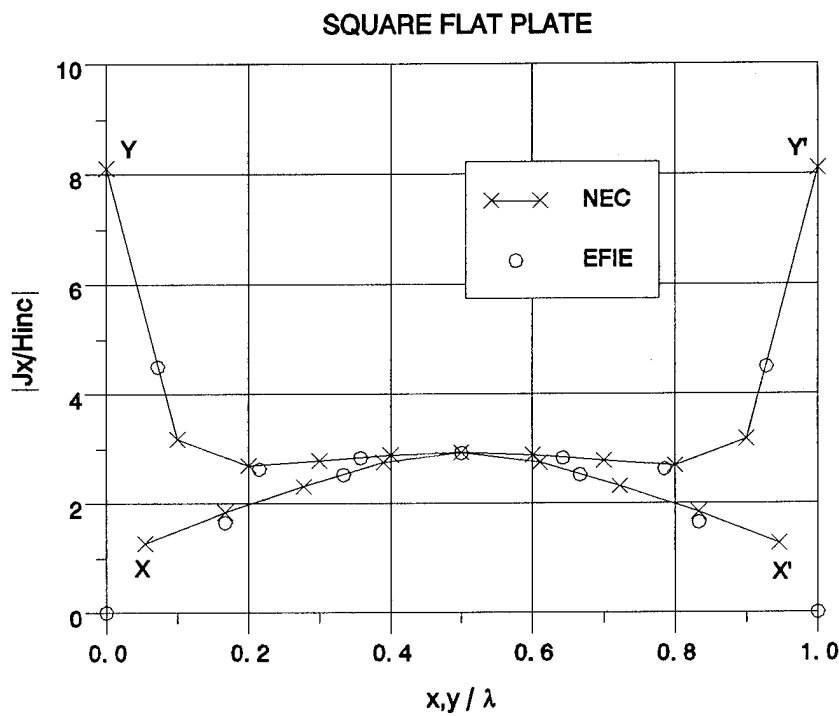


Figure 2b. Same as Fig. 2a, but with the wire grid (NEC) model of Fig. 1c (i.e. with edge wire diameters halved).

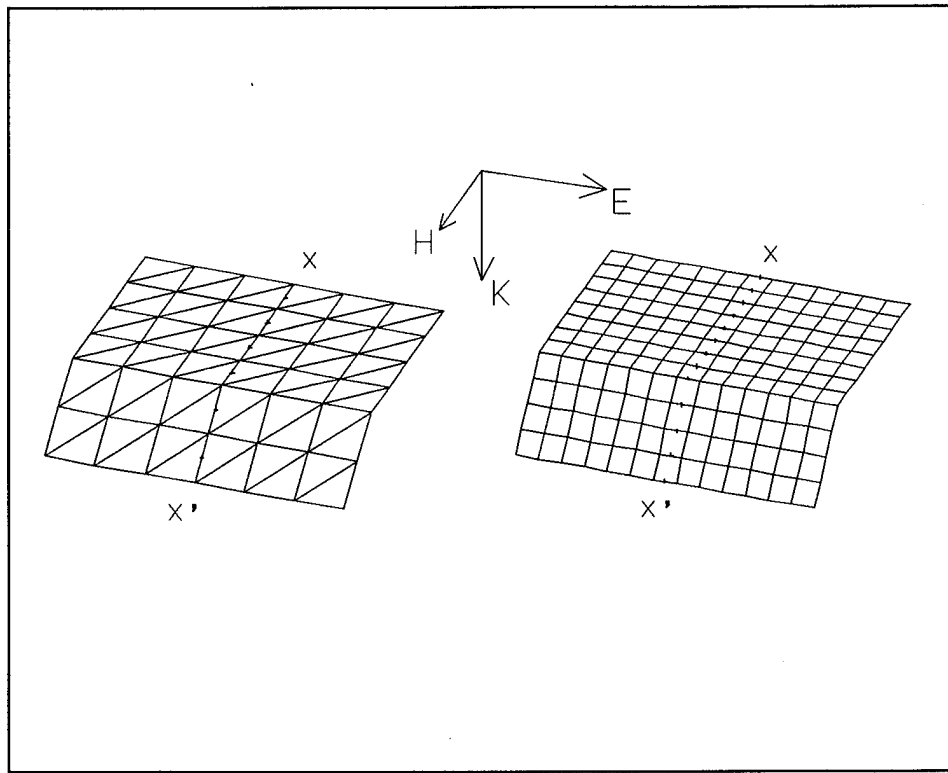


Figure 3a. Surface patch and wire grid models of a bent square plate

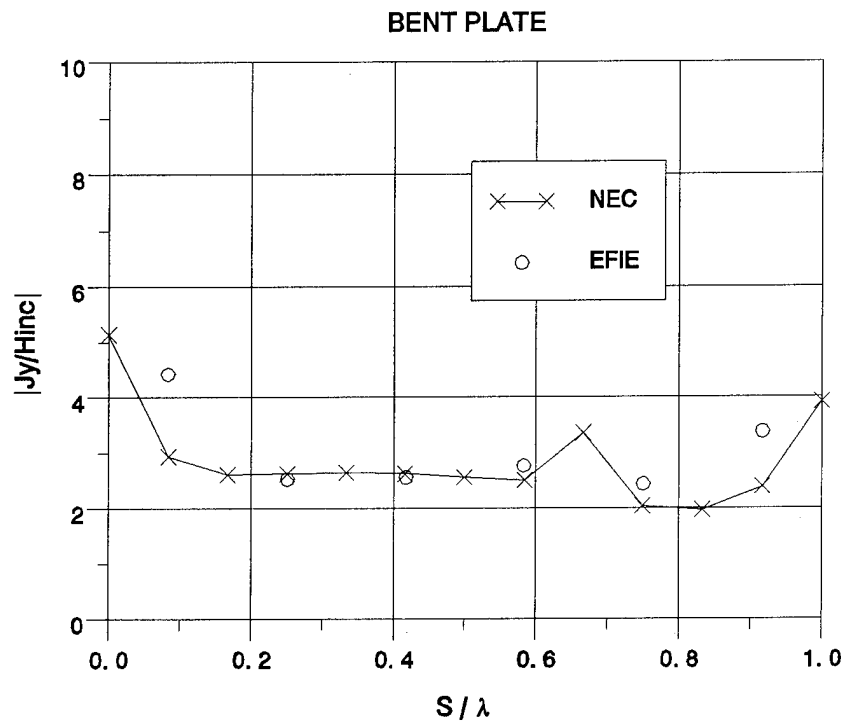


Figure 3b. Distribution of dominant component of current density along XX' on the bent square plate of Fig. 3a; x and solid line = wire grid (with equal-area wire diameters), o = surface patches.

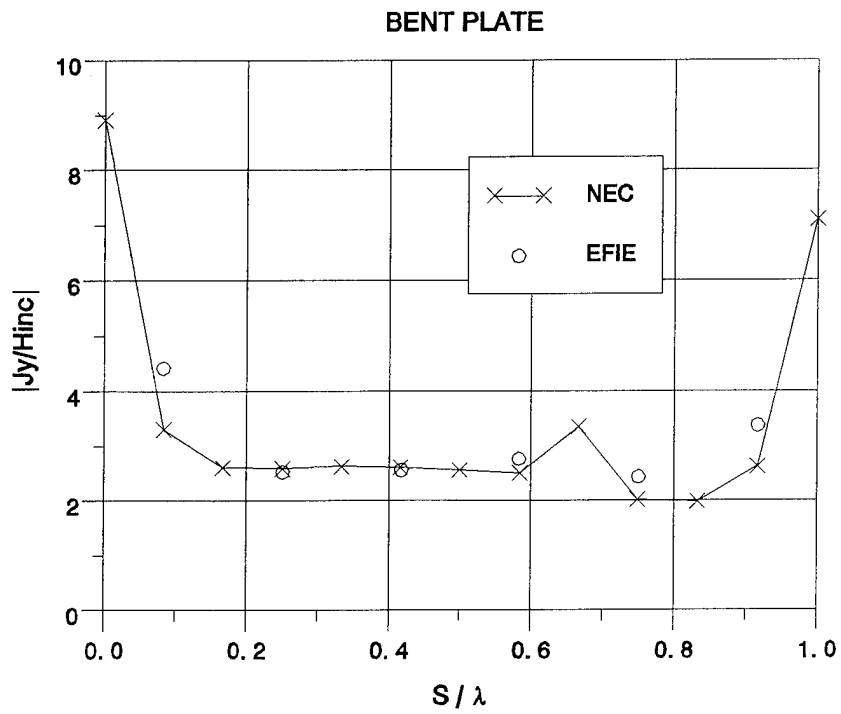


Figure 3c. Same as Fig. 3b, but the wire grid model has edge wire diameters halved.

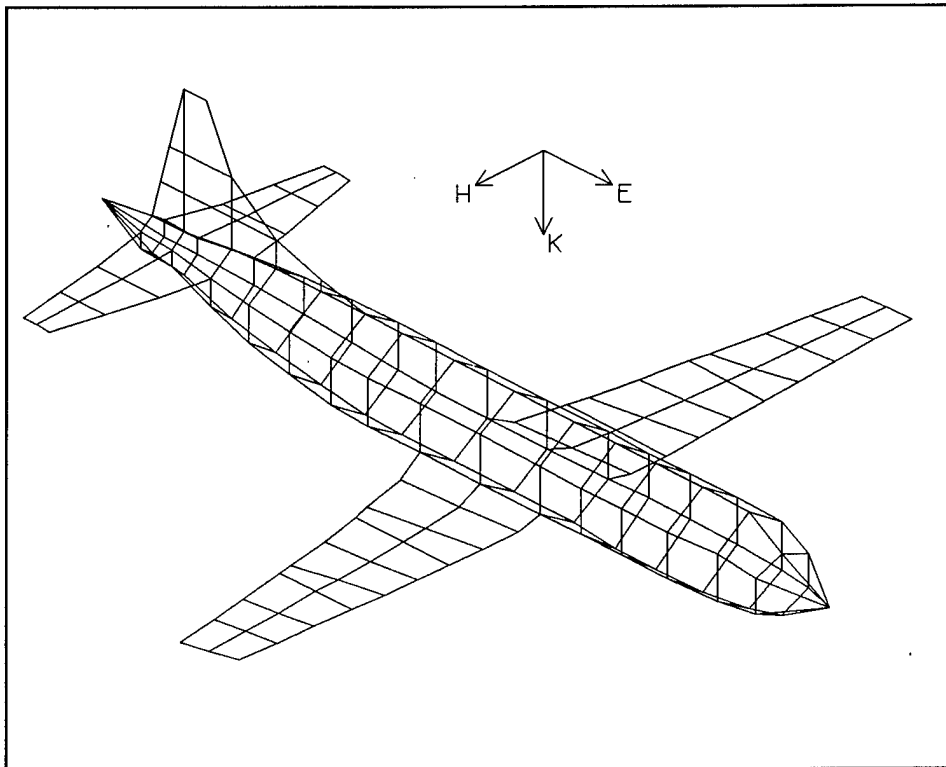


Figure 4a. Wire grid model of an aircraft.

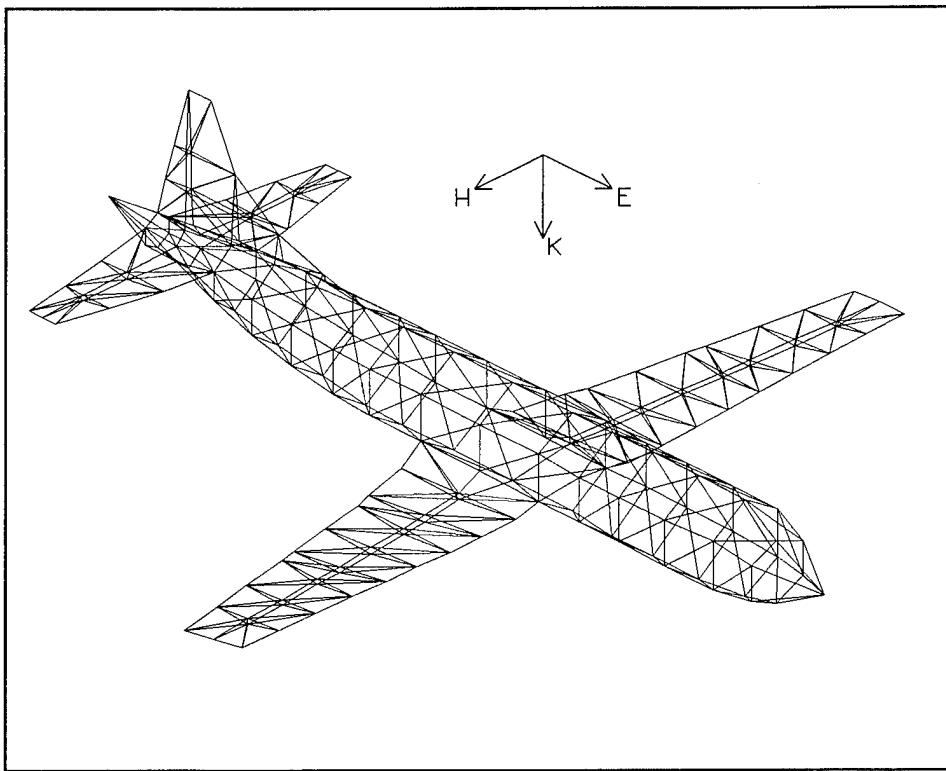


Figure 4b. Equivalent surface patch model of the aircraft in Fig. 4a.

AIRCRAFT TOP FUSELAGE

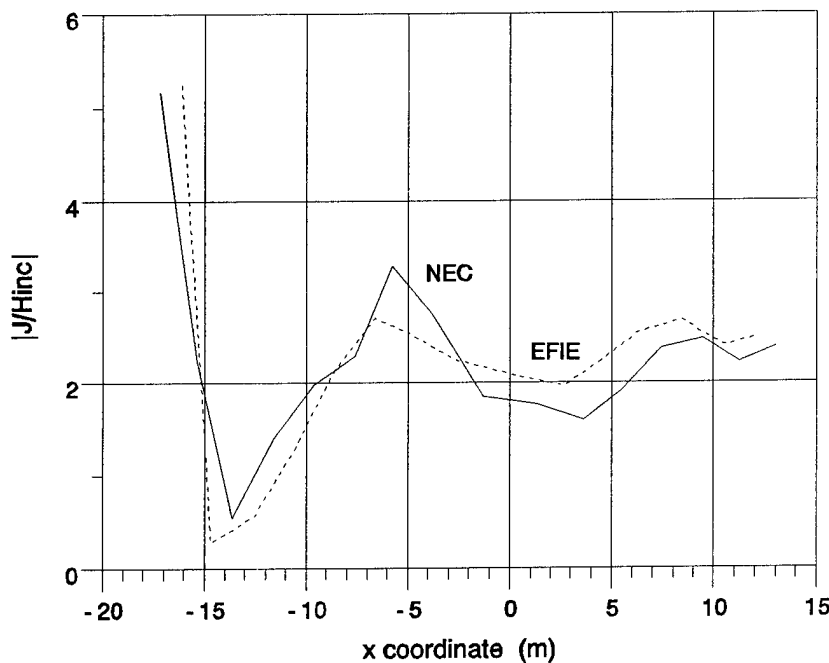


Figure 5a. Normalized current density distribution along the top of the fuselage of the aircraft in Fig. 4 at 20 MHz; solid line = wire grid (NEC), dashed line = equivalent surface patches (EFIE).

AIRCRAFT AROUND FRONT FUSELAGE

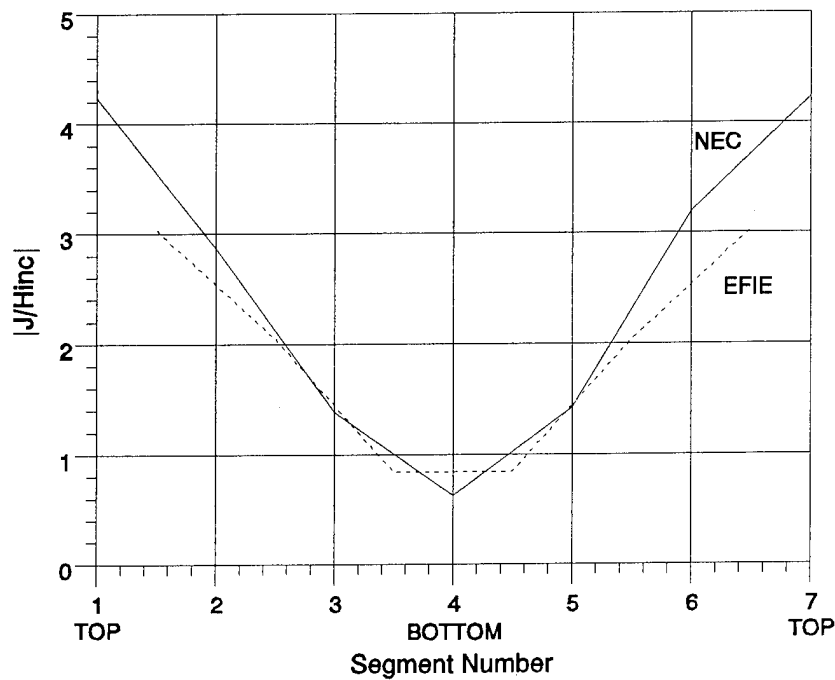


Figure 5b. Normalized current density distribution around the front fuselage of the aircraft in Fig. 4 at 10 MHz; solid line = wire grid (NEC), dashed line = surface patches (EFIE).

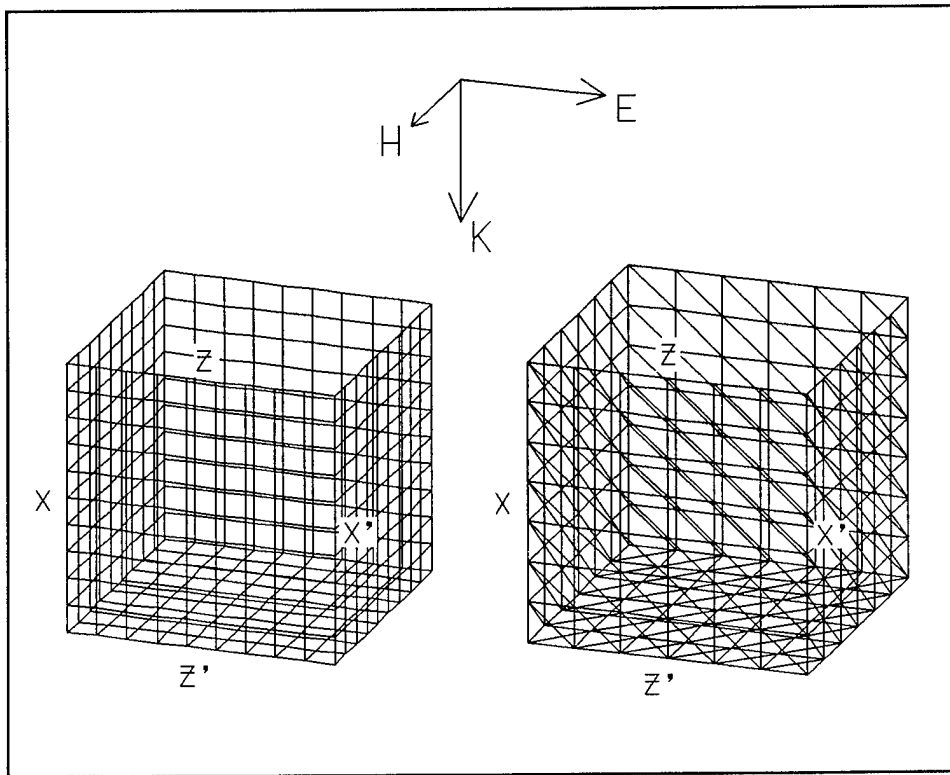


Figure 6. The wire grid and surface patch models of an open-topped cube.

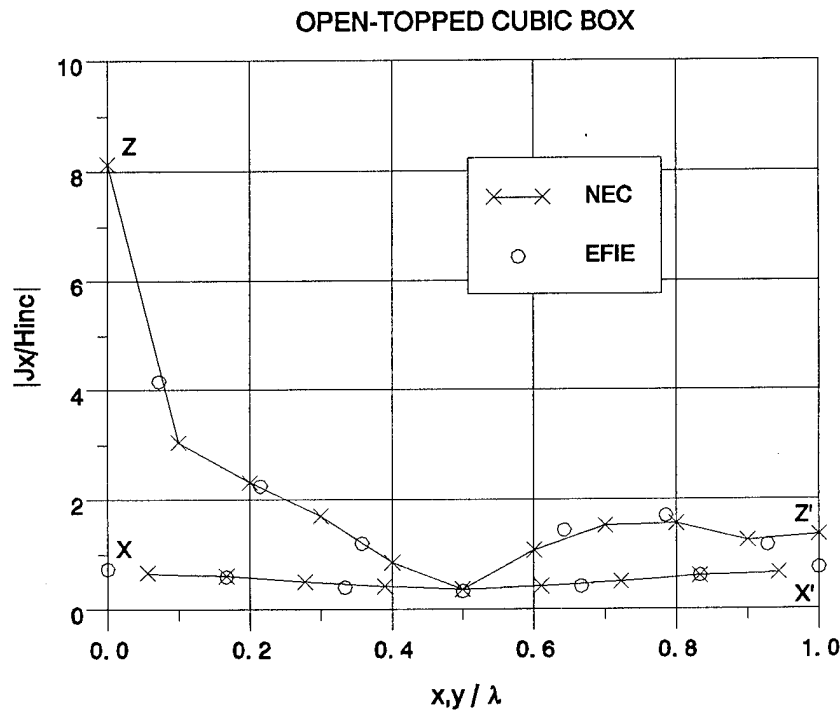


Figure 7. Normalized current density along XX' and ZZ' on the open-topped cube of Fig. 6; x and solid line = wire grid (NEC), o = surface patches (EFIE).

ON THE FUNCTIONING OF A HELICOPTER-BORNE HF LOOP ANTENNA

Duncan C. Baker

Department of Electronics and Computer Engineering,
University of Pretoria, Pretoria, 0002, South Africa.

ABSTRACT: *Numerical techniques allow engineers to evaluate the performance of antennas on complex structures. These techniques can provide valuable physical insights into the overall functional performance of such antennas. This short paper reports on the use of NEC2 to investigate the radiation characteristics of a loop antenna mounted below the tailboom of a helicopter in the frequency band 2-15 MHz. It was concluded that such a loop antenna serves mainly to excite a dominant electrical dipole mode of operation for frequencies less than the lowest natural electrical resonance frequency of the helicopter itself, but greater than some frequency near the low end of the HF band. A limited set of measurements performed on a scale model of a helicopter generally supports the conclusions drawn from the numerical results predicted using NEC2. The reported result is of importance in so-called 'nap of the earth' HF communications from helicopters.*

1. INTRODUCTION

The method of moments [1] is used extensively in the design and analysis of wire antennas as well as the evaluation of the performance of such antennas on a variety of vehicles and structures [2]. The method has proved to be extremely useful for the evaluation of the performance of HF (3-30 MHz) antennas on aircraft, because of problems associated with measuring the overall performance either during flight tests or using scale models. For numerical analysis the aircraft fuselage and wings are modelled as wire-grid structures. The method is useful for examining the detailed performance of aircraft antennas in the HF band and as an engineering tool in designing such antennas.

Kubina [3] presents guidelines for numerically modelling wire grid structures. Along with other examples he also gives predicted and measured radiation patterns for a loop antenna on a CHSS-2/Sea King helicopter at frequencies of 2.6, 4.1, 6.0 and 8.1 MHz. The loop was mounted on the tailboom in the horizontal (x-y) plane. Owen [4] also gives guidelines for numerical modelling and presents measured and predicted radiation patterns for a helicopter mounted loop antenna at a frequency of 8 MHz. In this case the loop antenna was mounted in the vertical (x-z) plane below the tailboom of the helicopter. In [3] and [4] the emphasis appeared to be on the validation of computed results, and how best to achieve good comparisons with the measured results by 'tuning' the numerical model. Neither author examined the various radiation modes which could influence the radiation patterns. Burberry [5] points out that there are two modes of radiation present, that due to the antenna itself, as well as an additional mode due to the currents induced on the airframe by coupling with the antenna. From an examination of the results presented in [3] and [4] this author concluded that a longitudinal electrical dipole mode, corresponding with the

longest dimension of the helicopter fuselage, could at certain frequencies in the HF band be the dominant mode, depending on the mounting and orientation of the loop antenna.¹ A short study, restricted to the 2-15 MHz band which is used for HF communications over distances less than about 600 km, was therefore undertaken to test this hypothesis. It was not the purpose of the study to validate NEC2 for wire-grid models yet again. Consequently no attempt was made to 'tune' the numerical model.

2. DESCRIPTION OF THE NUMERICAL AND SCALE MODELS

In order to investigate the radiation patterns of a loop antenna on a helicopter, a wire grid structure, which can best be described as a generic model of a helicopter, was implemented for use in the Numerical Electromagnetics Code NEC2 [6]. The numerical model was based on top and side view scale model diagrams of an SA330B Puma helicopter available in a 1/32nd scale kit (no. PK-507) produced under the registered trademark 'Matchbox' by Lesney Products, London, England. The full scale dimensions of the helicopter are given in Table 1. Figure 1 shows line drawings of the wiregrid model and a sideview of the Puma helicopter. Also shown is a simple loop/dipole model suggested by Burke [7] for frequencies less than the fundamental electrical resonance frequency.

All wires used in numerically modelling the full scale helicopter fuselage were kept shorter than 1.5 m with a diameter of 0.2 m, except where noted. For the analysis the longer dimension of the helicopter was chosen to lie along the x-axis. The loop was modelled using three straight sections, each with a diameter of 0.03 m. The fourth side of the loop was formed by part of the tailboom, which was modelled as a rectangular grid structure. The overall dimension of the loop was 0.3 x 2.6 m and it was positioned on the starboard side below the tailboom. The longer loop dimension was parallel to the tailboom. The plane of the loop was at an angle of about 30 degrees to the x-z or $\phi = 0$ degrees plane, as defined by the rectangular or spherical coordinate system in the IEEE standard test procedures for antennas [8]. This offset in the plane of the loop was decided on after looking at possible means of attaching the loop to the airframe. The feedpoint was in the centre of the short loop section indicated in Figure 1(b). The shortest segment of length 0.06 m occurred in the feed region, giving a worst case segment length to diameter ratio of 2. Except for the number of main rotor blades this generic model in general resembles that of the Sea King used by Kubina in [3]. The total number of wires and segments used were 206 and 291 respectively. The numerical modelling guidelines of [3] and [4] were used.

Initially a single precision version of NEC2, restricted to a maximum of 300 wire segments, was used in order to speed up computer throughput. This version, however, predicted physically unacceptable negative radiation resistances at frequencies of 2 to 4 MHz as well as different null depths for conducting and perfectly conducting wire grids. Furthermore, scaling of the geometry of the full-scale numerical model at HF to dimensions appropriate for VHF model measurements by using the GS data card in NEC2, did not give the same

¹In a recent paper [11] Cox and Vongas draw attention to the fact that on a helicopter a loop antenna shunt feeds the fuselage/electric dipole, and that the helicopter/loop combination radiates in both loop and dipole modes for frequencies less than the lowest electrical resonance frequency of the helicopter.

results as the unscaled version. The problems were referred to Burke who ascribed them to the use of electrically short segments at the source [7]. At this stage of the investigation, an improved operating system, which was reputed to use more accurate algorithms for evaluating functions, was installed on the computer used. Comparison of outputs run under the two different operating systems, showed that there were considerable differences (6 to 10 dB) in null depths and only marginal differences in peak values for various predicted radiation patterns. A double precision version of NEC2, which also resolved the problem of negative radiation resistances, was therefore implemented.

The numerical modelling was independently checked by a colleague on a VAX computer [9], but with smaller grid spacing and shorter wirelengths. This model used 880 elements. The predicted gain results at 5 MHz were, for practical purposes, identical to those obtained using the single precision version of NEC2 for the model considered in this paper. Two cases were considered in the independent study [9]. These were with a pair of the main rotor blades aligned with the fuselage and then rotated to make an angle of 45 degrees with the 'axis' of the fuselage. The differences in the predictions for these two cases were negligibly small at 5 MHz, suggesting that rotor modulation of the radiation pattern could be small at frequencies below the fundamental resonance frequency. Although this independent analysis indicated that the proposed numerical modelling was probably adequate for the purposes of this study, it was decided to validate the predicted results using a scale model.

A 1/22nd scale model of the helicopter, based on the kit data referred to above, was manufactured from wood. The wooden fuselage was covered with strips of thin brass shimstock. All overlapping joints were soldered to provide electrical continuity in any direction across the interface between strips. This does not necessarily model the expected surface conductivity of the helicopter particularly well because of the use of riveted panels and composite materials and the fact that the metal conductivities cannot always be scaled. No allowance was made in the model for doors or other apertures. The loop antenna on the model was fed via a coaxial cable connection on the inside of the model. The rear rotors as well as the horizontal rear stabiliser were made of metal. All provided good electrical contact with the fuselage. One of the problems which arose at this stage was whether to model the main rotors using carbon fibre composite or metal. Examination of a rotorblade of a Puma at a South African Air Force open day showed that the leading edge was protected by a metal strip which was electrically bonded to the rotor boss and the fuselage. It was concluded that it would be appropriate to treat the main rotors as conductors as had been done in the numerical modelling. This is essentially the same approach as used by Owen [4].

The numerical modelling frequencies for the 22:1 scale model of the helicopter ranged from 44 to 330 MHz in 22 MHz steps. As a check on the accuracy of the computations, gain calculations were made at 5 degree increments in azimuth and elevation and the average gain computed. For perfectly conducting wires the average gain in free space should be 1.0 [6]. The number of segments of the wires in the feed region and other wires connected to these were varied in order to obtain the best overall average gain over the frequency range. The position of the feed segment was also changed to ensure the best overall average gain.

The lowest segment length to diameter ratio of about 2 was in the feed region. The extended thin-wire kernel option of NEC2 was tried but gave no real improvement in the average gain predicted over the frequency range. In general the guidelines for numerical modelling given by [3] and [4] were followed. The segment lengths of all wires connected to the shorter loop sections were made approximately the same length as the segments used in the loop sections. The diameters of these wires were made 0.08 m in order to limit the change in diameter between connected wires to a factor of about 2.5. In this case this was found to give satisfactory results.

Figure 2 shows the predicted average gains, normalisation gain factors and directivities, corrected for the deviation in the average gain from the expected value of 1.0, for the numerical model of the 22:1 helicopter scale model using perfect and brass conductors. The range of modelling frequencies from 44 to 330 MHz corresponds to a full scale frequency range of 2 to 15 MHz. Application of the average gain correction for the brass wire model gives a corrected directivity which agrees to within 0.01 dB with that shown for a perfect conductor in Figure 2(a). Below 200 MHz the directivity is approximately that expected for a dipole. It was concluded that the numerical model would be adequate to test the hypothesis that the dominant radiation mode for frequencies less than the fundamental resonance frequency, is the longitudinal dipole mode.

A limited set of radiation pattern measurements was made on the 22:1 scale model at frequencies of 110 and 220 MHz, corresponding to full-scale frequencies of 5 and 10 MHz respectively. All measurements were performed at the National Antenna Test Facility at Paardfontein, north of Pretoria, South Africa [10]. The choice of frequencies was largely dictated by the level of interference in the FM and TV broadcast bands at the site. The source antenna was a horizontally polarised ground arrayed log-periodic array. A 10 dB attenuator was inserted at the feedpoint of the loop antenna in order to provide a nearly constant load for the receiver. This restricted the overall sensitivity of the system and may have influenced the measured results. The orientation of the model was adjusted depending on the cut and required field component relative to the model's coordinate system.

3. COMPARISON BETWEEN PREDICTED AND MEASURED RESULTS

The maximum path length on the helicopter which could support an electrical dipole-like resonance was estimated to be about 19.2 m. This is measured along the length of a rotor blade, down the drive shaft, back along the tailboom and out to the end of the rear control surface. For an electrical dipole this corresponds to a fundamental resonance frequency of 7.8 MHz, corresponding to a scaled frequency of 172 MHz. For the helicopter this frequency may be reduced because of the diameter to length ratio of the fuselage itself compared with a thin dipole, and possible capacitive loading effects of the main and tail rotors. The selected measurement frequencies of 110 and 220 MHz straddle the fundamental resonance frequency of the model.

Because of the difference in the implementations of the feedpoints in the numerical and physical scale models, it is expected that a comparison of the predicted and measured input impedances for the loop antenna will at best be of a qualitative nature. The feed for the

numerical model was in the centre of the short segment marked as 'feedpoint' in Figure 1(b). In the case of the scaled physical model this loop segment was fed at the junction point at the fuselage. Figure 3 compares the predicted and measured input impedances for the physical scale model. Only half of the Smith chart is shown. The measured results indicate that the real part of the input impedance increases from 1 Ohm to about 60 Ohms over a range of 44 to 242 MHz. Over the same range the inductive part increases from about 4 to 340 Ohms. Figure 4 compares the measured input impedances for the loop antenna with and without the main and tail rotors. The effect of removing the rotors is relatively small, suggesting that rotating rotors will not modulate the loop's input impedance by much. One can see what appears to be a relatively small effect in the measured input impedance for the model due to the fundamental resonance frequency at 176 MHz. In the case of the fuselage with no rotors, the probable effect of a slightly higher fundamental resonance frequency of 220 to 242 MHz can be seen. The length of the full scale fuselage excluding rotors is about 13.8 metres, corresponding to a scaled (model) halfwave resonance frequency of 239 MHz.

Ideally an examination of the relative amplitudes of the theta- and phi- components of the electric field in the x-y plane will show the difference in the relative importance of the loop and electrical dipole fields, $E(\theta)$ and $E(\phi)$ respectively in this case. In retrospect it would have been advisable to mount the loop antenna symmetrically with respect to the tailboom and below it in the x-z plane, instead of at an angle of 30 degrees, in order to enhance the differences in the fields.

For all helicopter radiation patterns shown in the figures one pair of rotors was aligned with the length of the fuselage. Also shown in Figures 5, 6, 8 and 9 are the expected normalised radiation patterns for a dipole placed along the 'axis' of the fuselage. Because of time limitations on the use of the test range no measurements were made in the vertical y-z plane orthogonal to the fuselage 'axis'. The alignment of the rotors in the helicopter schematic in the figures are for illustrative purposes only. The use of symbols to indicate orientation are as follows: F=forward, S=starboard, P=port, T=top, B=bottom and A=aft.

Figures 5 and 6 show normalised comparisons of measured and predicted radiation patterns for a model frequency of 110 MHz, corresponding to a full-scale frequency of 5 MHz, for x-y and x-z planes respectively. In Figure 5 the model's measured and predicted results in the horizontal x-y plane at 110 MHz (5 MHz full-scale) for the $E(\theta)$ and $E(\phi)$ fields are in reasonable agreement. Except for the depth of the nulls, the $E(\phi)$ fields resemble the dipole radiation pattern. The $E(\theta)$ fields can be attributed mainly to the loop antenna with null filling at broadside being caused by vertical currents on the fuselage. Figure 6 shows the model's measured and predicted radiation patterns at 110 MHz for the $E(\theta)$ and $E(\phi)$ fields in the vertical x-z plane. In this case the $E(\theta)$ field can reasonably be expected to be a combination of the loop and dipole modes. The predicted and measured $E(\theta)$ patterns are again in reasonable agreement. However, they tend to resemble only the pattern of an electrical dipole aligned with the fuselage 'axis', with little contribution evident for the loop antenna. Comparison of the measured and predicted $E(\phi)$ fields is however poor. Some of the differences for this field component are probably due to the differences in the feed arrangements for the numerical and physical models referred to earlier. The lack of

measuring sensitivity and stray fields due to scattering from coaxial cables may also have influenced the measurement of the $E(\phi)$ component. The predicted $E(\phi)$ field resembles that of a small loop antenna in the x-y plane. This may be a residual effect of the offset loop antenna which is mainly in a vertical plane.

A residual electrical dipole field, believed to be attributable to the feed arrangement for the numerical model, can be seen in the $E(\theta)$ field illustrated in Figure 7 which shows the predicted fields in the y-z plane. The nulls are approximately aligned with the axis of the short feed section. The $E(\phi)$ component is nearly omni-directional, with a variation of less than 1 dB, as would be expected for a predominantly electrical dipole-like field.

Figures 8 and 9 compare the predicted and measured $E(\theta)$ and $E(\phi)$ fields for the model at 220 MHz (10 MHz full scale) for the x-y and x-z planes respectively. It should be noted that the rotor blades on the full scale helicopter have a diameter of 15 m, corresponding to a resonant halfwave dipole of 10 MHz. In the case of the x-y plane, shown in Figure 8, the agreement is relatively good for the $E(\theta)$ component. The measured $E(\phi)$ component once more tends to resemble the dipole field, but compares relatively poorly with the predicted field. Figure 9 illustrates the case for the x-z plane. Except for the depth of the null the agreement between the measured and predicted $E(\theta)$ fields is reasonable. It is believed that the main rotor blade resonance influenced the predicted depth and position of the null. The effect of changing the frequency to 215 MHz is also shown for comparison. The $E(\phi)$ components resemble each other superficially. Differences are ascribed to problems encountered during the measurements due to low sensitivity and scattering from coaxial cables. The position and depth of null of the predicted $E(\phi)$ component in the x-y plane as shown in Figure 8 was found to be not nearly as sensitive to changes in frequency compared to the $E(\theta)$ field shown in Figure 9.

The results illustrated in Figures 5 and 6 were typical of predictions up to about 176 MHz which was near the fundamental electrical resonance frequency of the model helicopter. However, it was found that as the frequency for the scale model was decreased to 44 MHz (2 MHz full scale), the predicted contribution of the loop antenna to the overall radiation pattern increased steadily until the loop's contribution to the radiated field compared with that of the dipole, as shown in Figure 10. Also shown are the fields computed for the simple electrical dipole/loop antenna combination of Figure 1(c) as suggested by Burke [7]. The dimensions of the electrical dipole/loop combination are similar to the overall helicopter and loop antenna combination. The wire diameters were 0.02m. The null-filling evident in the predicted radiation pattern for the dipole mode for the helicopter model is ascribed to the asymmetric placement of the loop antenna, with resultant circumferential currents on the fuselage in the x-y plane. Above 44 MHz for both the helicopter and simple case, the radiated field due to the electrical dipole mode exceeded that due to the loop. In both cases at 110 MHz (5 MHz full scale) the radiated field due to the electrical dipole mode was predicted to be about 15 dB greater than that due to the loop. At 220 MHz (10 MHz full scale) for the simple model, the electric field due to the loop is predicted to be more than 25 dB less than that due to the electrical dipole.

Examination of the predicted radiation patterns for the model helicopter between the

fundamental resonance frequency of about 176 and 330 MHz (8 MHz and 15 MHz full scale), shows that the electrical dipole field component becomes more distorted. Examples of this effect are shown in Figures 11 to 13 for the principal planes for the model at 330 MHz (15 MHz full scale). Figure 12 shows a similar residual electrical dipole effect, possibly due to the feed segment and also observed in Figure 7. It is believed that the distortion of the electrical dipole field is due to the increasing relative importance of various higher order current modes discussed in [5] as the frequency is increased. It is, however, clear that there is still a substantial contribution from the electrical dipole mode of radiation for the helicopter.

4. DISCUSSION

On the basis of reasonable agreement between measured and predicted results for the largest electrical field components, it is concluded that the dominant radiation mode for a helicopter-borne loop antenna lying in a plane containing the longest dimension of the fuselage, tends to be electrical dipole-like at frequencies below the fundamental resonance frequency but above some frequency at the low end of the HF band. For the full scale example considered here this low end frequency is of the order of 2 MHz. A strong electrical dipole-like component persists up to 15 MHz for the example considered. However, as frequencies increase above the fundamental electrical resonance, the effect of higher order current modes on the fuselage and main rotors on the radiation pattern become increasingly important. The resultant pattern is thus a composite of the electrical dipole-like field, fields due to the higher order current modes and any residual effect due to the loop antenna itself.

'Nap of the earth' (NOE) HF communications is restricted to the lower half of the HF band by ionospheric propagation and require high take-off angles. Most helicopters and aircraft will have fundamental electrical resonances at frequencies in the HF band because of their physical size. For this reason it is important that aircraft antenna engineers concerned with NOE systems consider the entire helicopter as the radiating structure. It is suggested that it could be worthwhile examining ways in which the dipole mode could be directly stimulated in order to improve efficiency and matching.

5. ACKNOWLEDGEMENTS

The author gratefully acknowledges the assistance of the following: Dr. D. E. Baker of EMLab for accommodating the measurements described above in a busy measuring schedule of his own, Mr. B. J. van der Riet of the Division for Microelectronics and Communications Technology, Council for Scientific and Industrial Research for help at the antenna test range, Mr. F. J. van der Walt for the preparation of the polar diagrams and Mr. J. M. Brand for the construction of the helicopter scale model.

6. REFERENCES

- [1] Harrington, R. F.: "Field Computation by Moment Methods". Robert E. Krieger Publishing, Malabor, Florida, 1982
- [2] Miller, E. K.: "Numerical Modelling Techniques for Antennas". The Performance of Antennas in Their Operational Environment, AGARD Lecture Series No. 131, NATO, Neuilly Sur Seine, France, pp. 7-1 to 7-29, 1983.
- [3] Kubina, S. J.: "Numerical Modelling Methods for Predicting Antenna Performance on Aircraft", *ibid.*, pp. 9-1 to 9-38.
- [4] Owen, J. I. R.: "Wire Grid Modelling of Helicopter HF Antennas", IEEE International Antennas and Propagation Symposium Digest, pp. 722 to 725, 1980.
- [5] Burberry, R. A.: "HF Loop Antennas for Air, Land and Sea Mobiles", IEE Second Conference on HF Communication Systems and Techniques, London, pp. 18 to 22, 1982.
- [6] Burke, G. J. and Poggio, A. J.: "Numerical Electromagnetic Code (NEC) - Method of Moments". Technical Document NOSC 116, Naval Electronic Systems Command (ELEX 3041), Naval Ocean Systems Center, San Diego, California, 92152.
- [7] Burke, G. J.: Lawrence Livermore Laboratory, Livermore, California - Private communication.
- [8] IEEE Standard Test Procedures for Antennas, IEEE Std. 149-1979 (IEEE Press, New York, 1979)
- [9] Cloete, J. H.: Department of Electronic and Electrical Engineering, University of Stellenbosch, Stellenbosch, South Africa - Private communication.
- [10] Baker, D. E.: "Development and Evaluation of the 500 M Ground-reflection Antenna Test Range of the CSIR, Pretoria, South Africa", Proceedings of the Annual Conference of the Antenna Measurement Techniques Association, San Diego, California, 2-4 October 1984, pp. 5A4-1 to 5A4-16.
- [11] Cox, J. W. R. and Vongas, G.: "Calculated and Measured Radiation Characteristics of an HF Loop Antenna Mounted on a Helicopter", Fifth International Conference of HF Radio Systems and Techniques, IEE Conference Publication No. 339, July 1991.

Table 1. Dimensions of the Puma SA330 helicopter used in the numerical and scale models.

(1)	diameter of main rotor (4 blades)	15 m
(2)	overall length (rotors turning)	18.15 m
(3)	height	5.14 m
(4)	fuselage length including rear rotors (scaled from kit data)	14.82 m

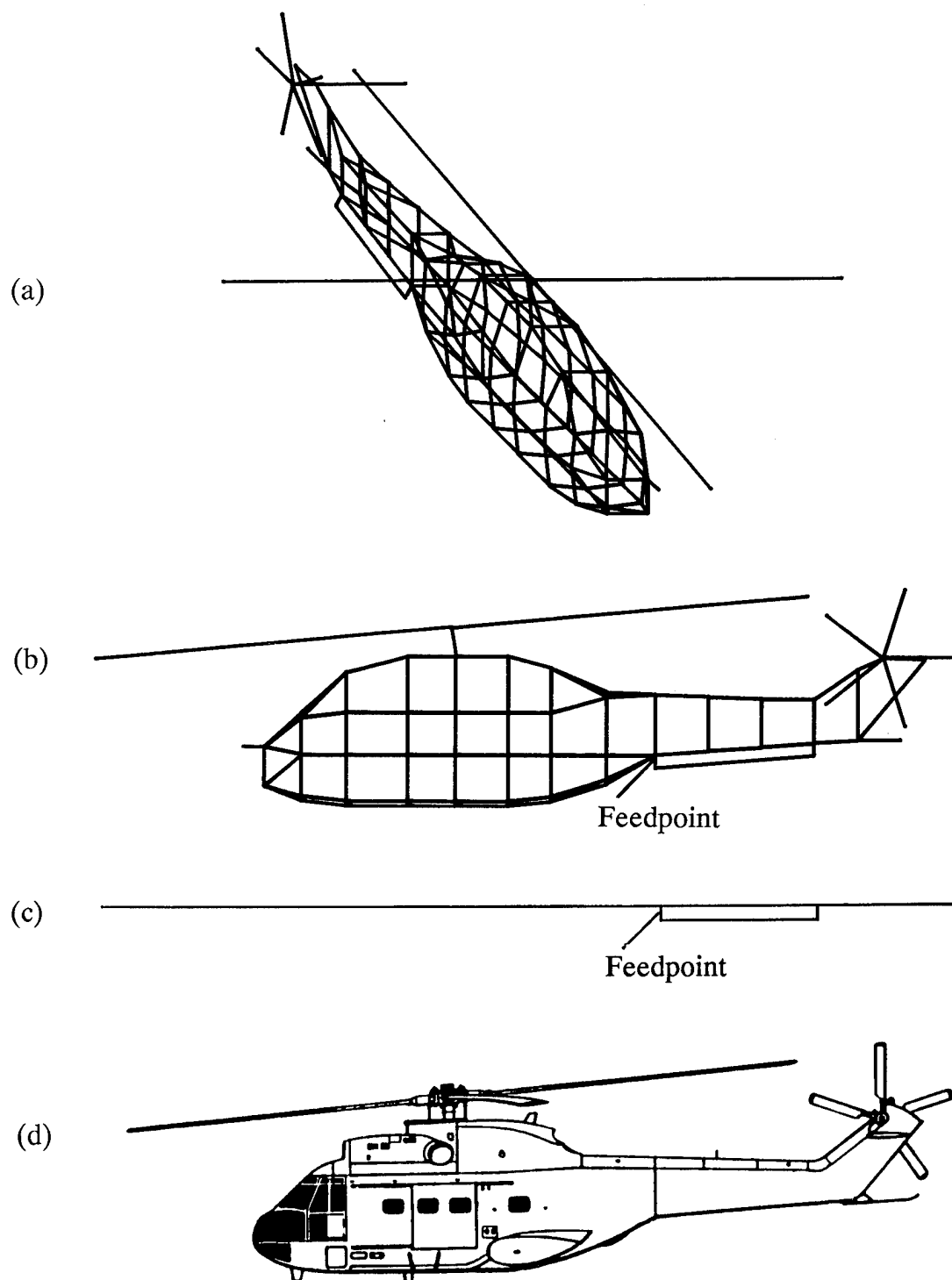


Figure 1. Figures (a) and (b), isometric and side views of the wiregrid model of a SA330 PUMA helicopter; (c), simple low HF loop/dipole model; (d) line drawing of the helicopter.

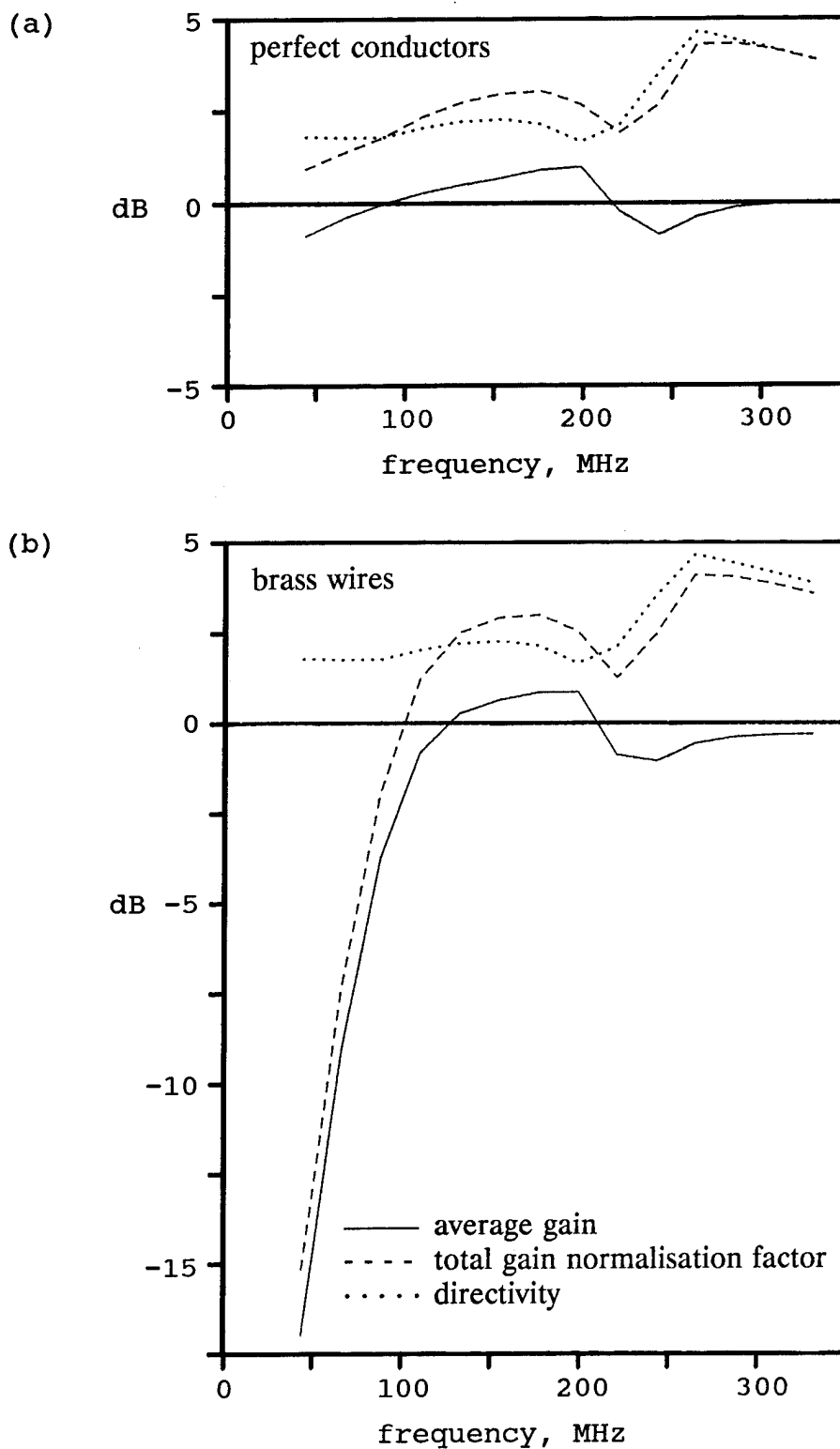


Figure 2. Average gains, predicted total gain normalisation factors and corrected directivities for the helicopter model with (a) perfectly conducting and (b) brass wires.

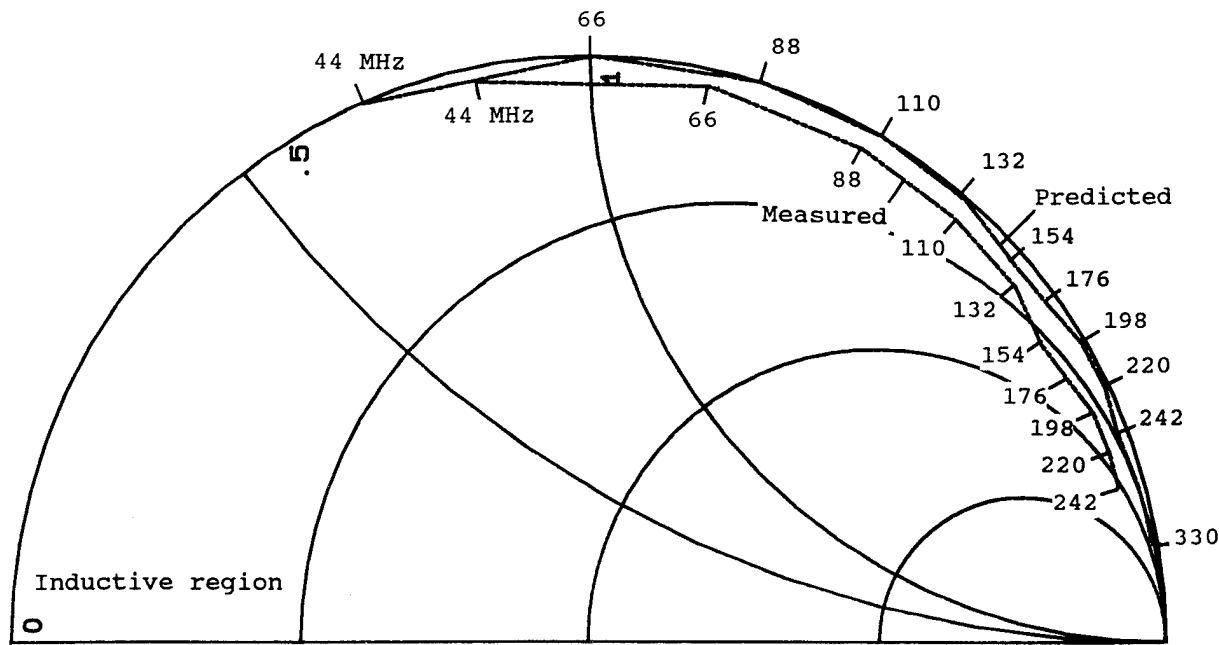


Figure 3. Comparison of predicted and measured antenna input impedances for the complete helicopter scale model. Only the upper half of the Smith chart is shown. (Normalisation - 50 ohms)

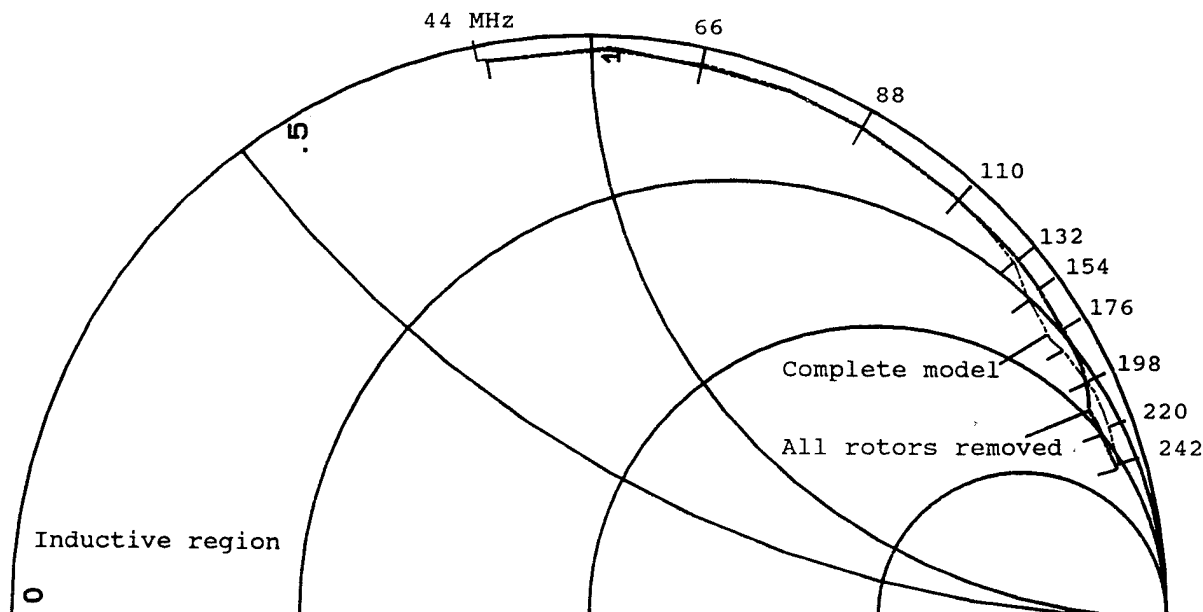


Figure 4. Comparison of measured antenna input impedances for the complete helicopter scale model and the fuselage after removal of all rotors. Only the upper half of the Smith chart is shown. (Normalisation - 50 ohms)

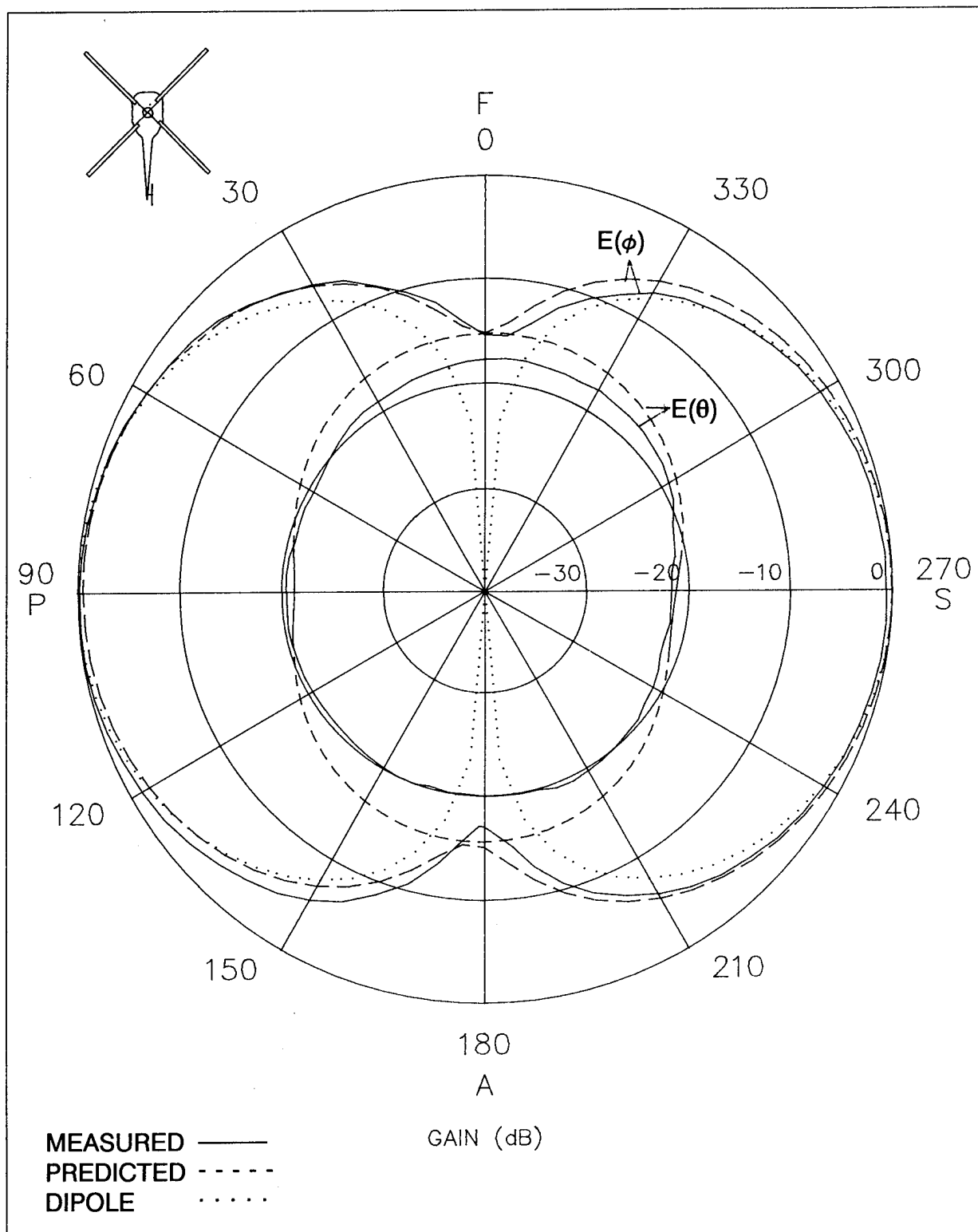


Figure 5. Comparison of normalised measured and predicted radiation patterns at 110 MHz in the x-y plane. Predicted patterns normalised to $E(\phi) = 1.1$ dB. Normalised dipole pattern shown for reference.

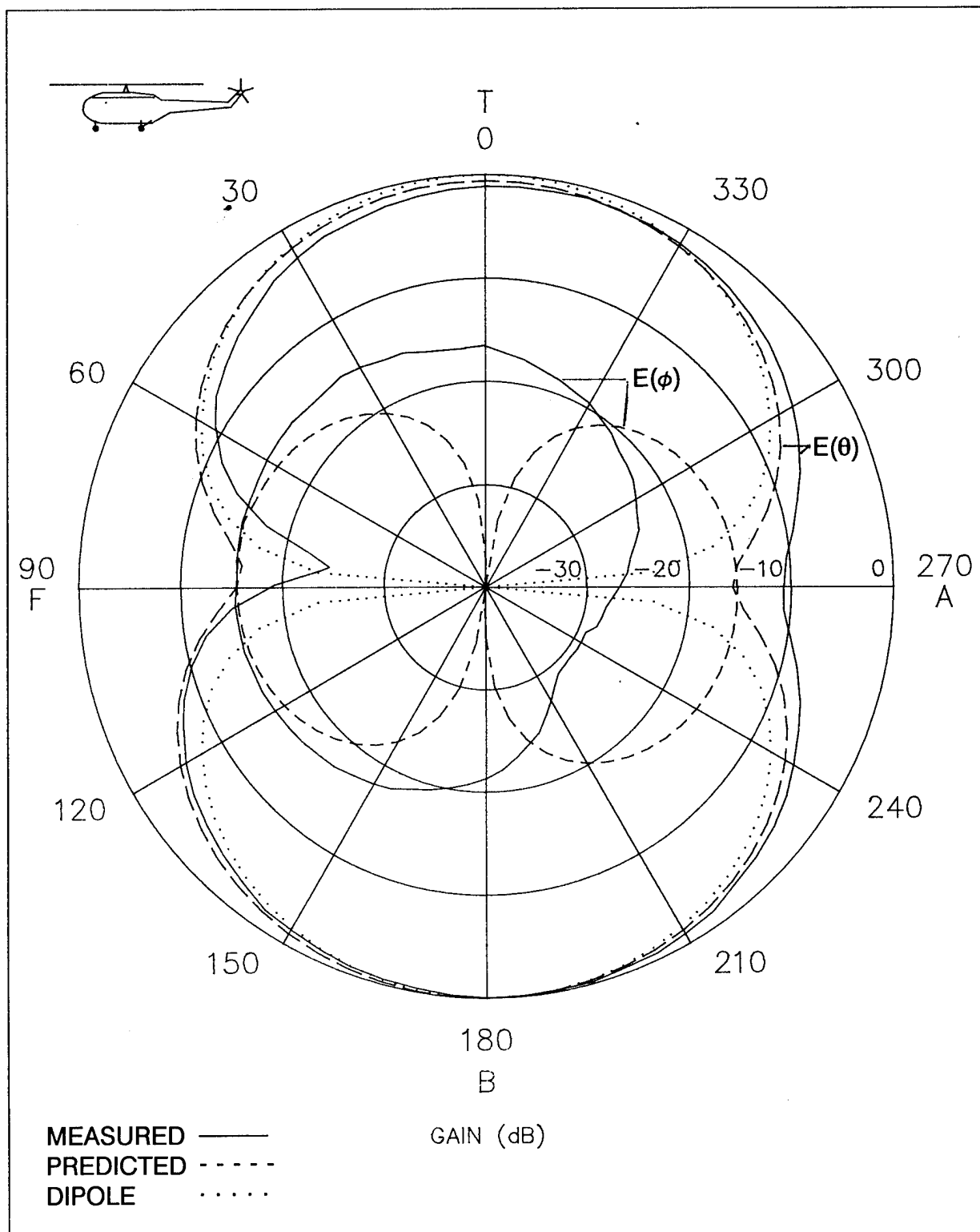


Figure 6. Comparison of normalised measured and predicted radiation patterns at 110 MHz in the x-z plane. Predicted patterns normalised to $E(\theta) = 1.3$ dB. Normalised dipole pattern shown for reference.

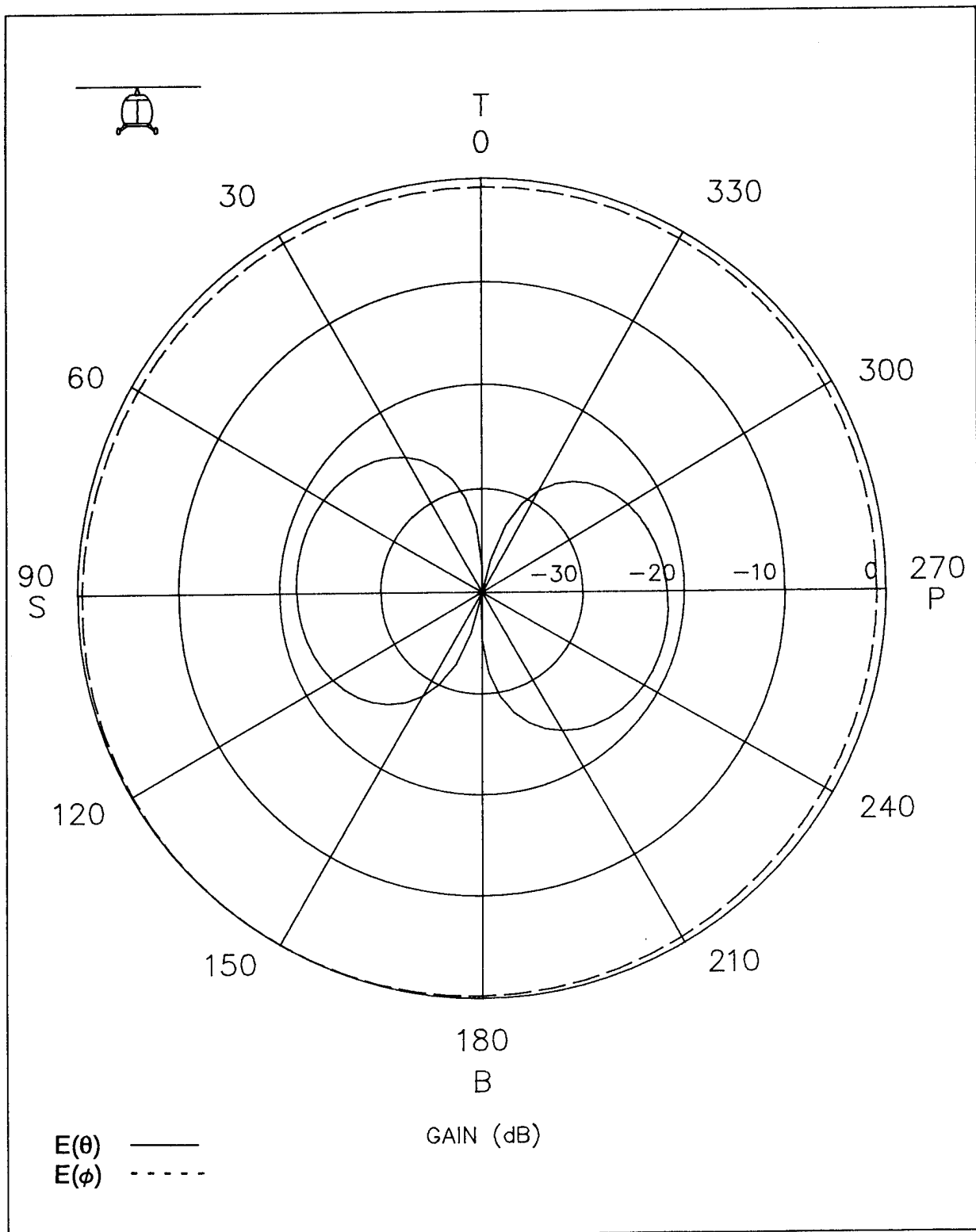


Figure 7. Predicted fields for the helicopter model in the y-z plane at 110 MHz.
Patterns normalised to $E(\phi) = 1.5$ dB.

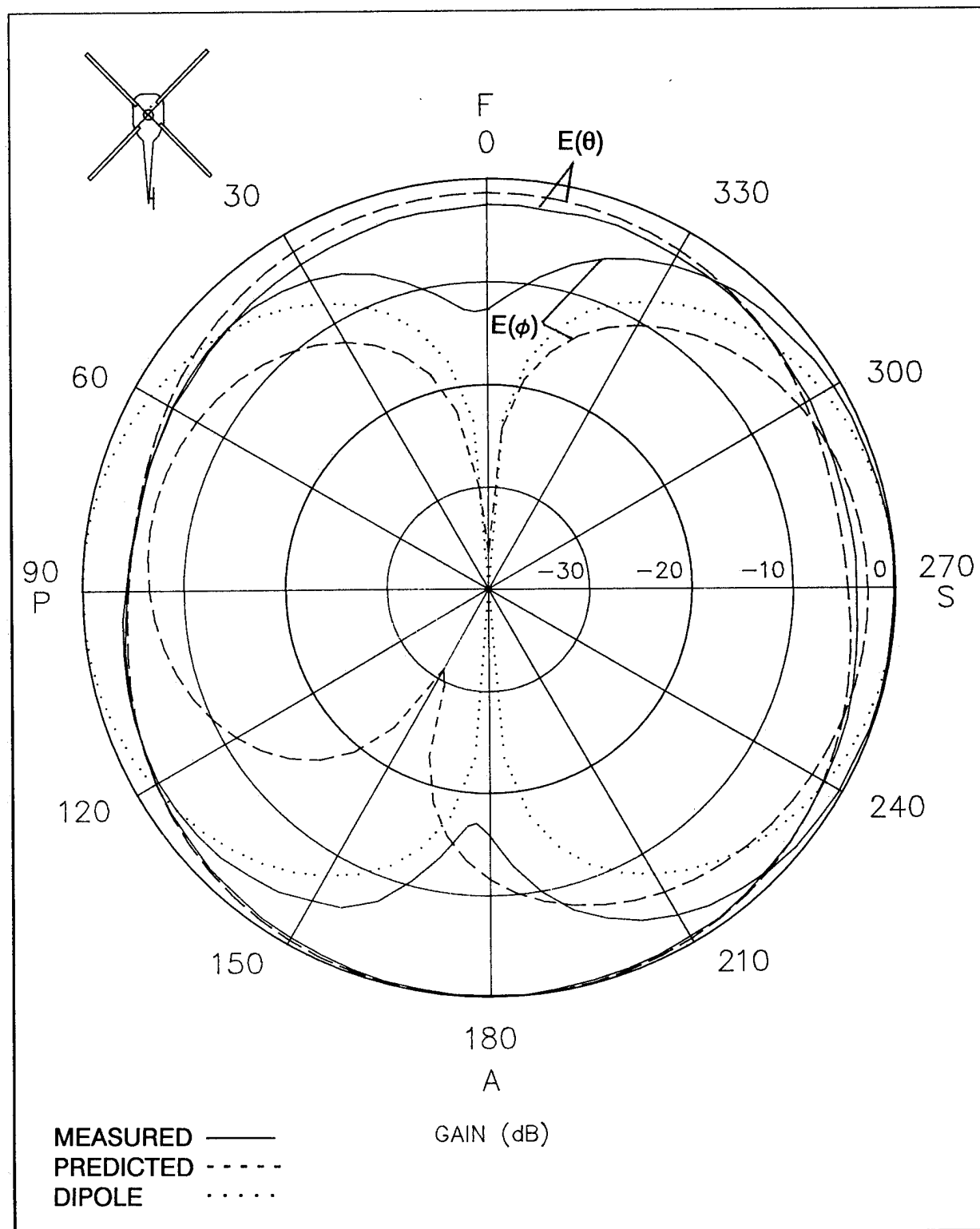


Figure 8. Comparison of normalised measured and predicted radiation patterns at 220 MHz in the x-y plane. Predicted patterns normalised to $E(\theta) = 0.6$ dB. Normalised dipole pattern shown for reference.

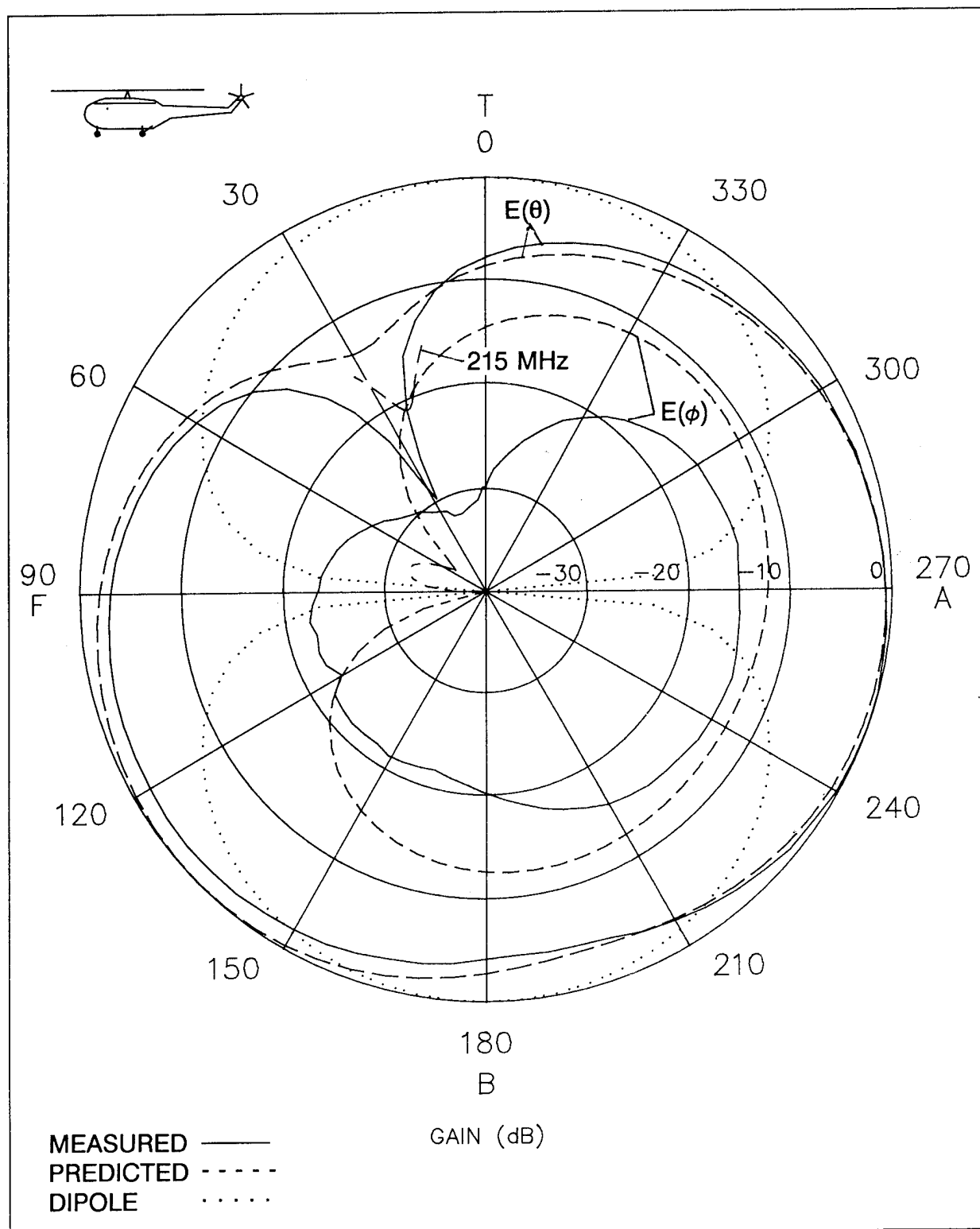


Figure 9. Comparison of normalised measured and predicted radiation patterns at 220 MHz in the x-z plane. Predicted patterns normalised to $E(\theta) = 1.1$ dB. Normalised dipole pattern shown for reference.

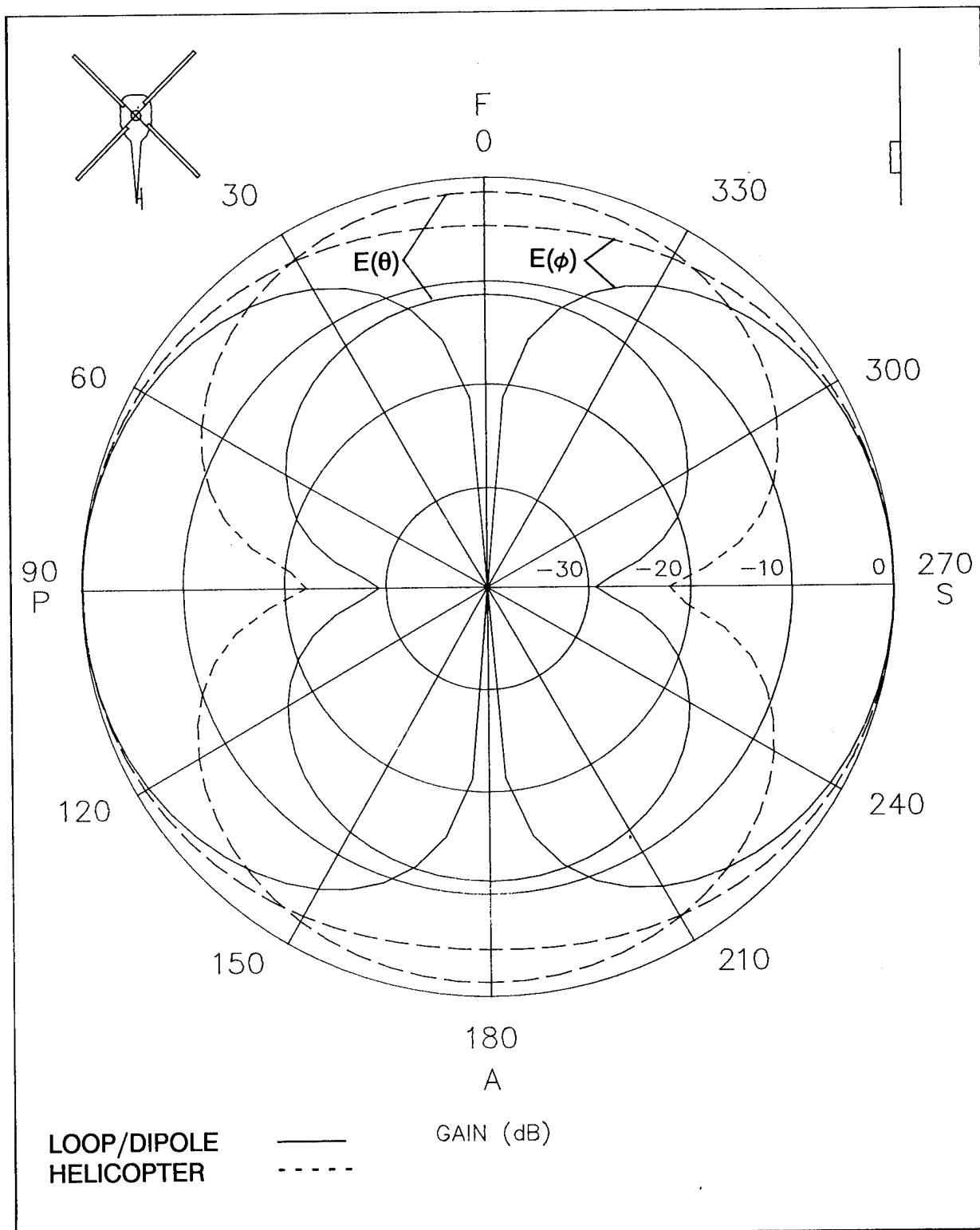


Figure 10. Comparison of predicted radiation patterns at 44 MHz for the scaled helicopter borne loop antenna and the simple loop/dipole model, using brass conductors for both cases. Helicopter patterns normalised to $E(\phi) = -16.5$ dB. Loop/dipole patterns normalised to $E(\phi) = -18.0$ dB. The loop is in the x-z plane. Patterns are for the x-y plane.

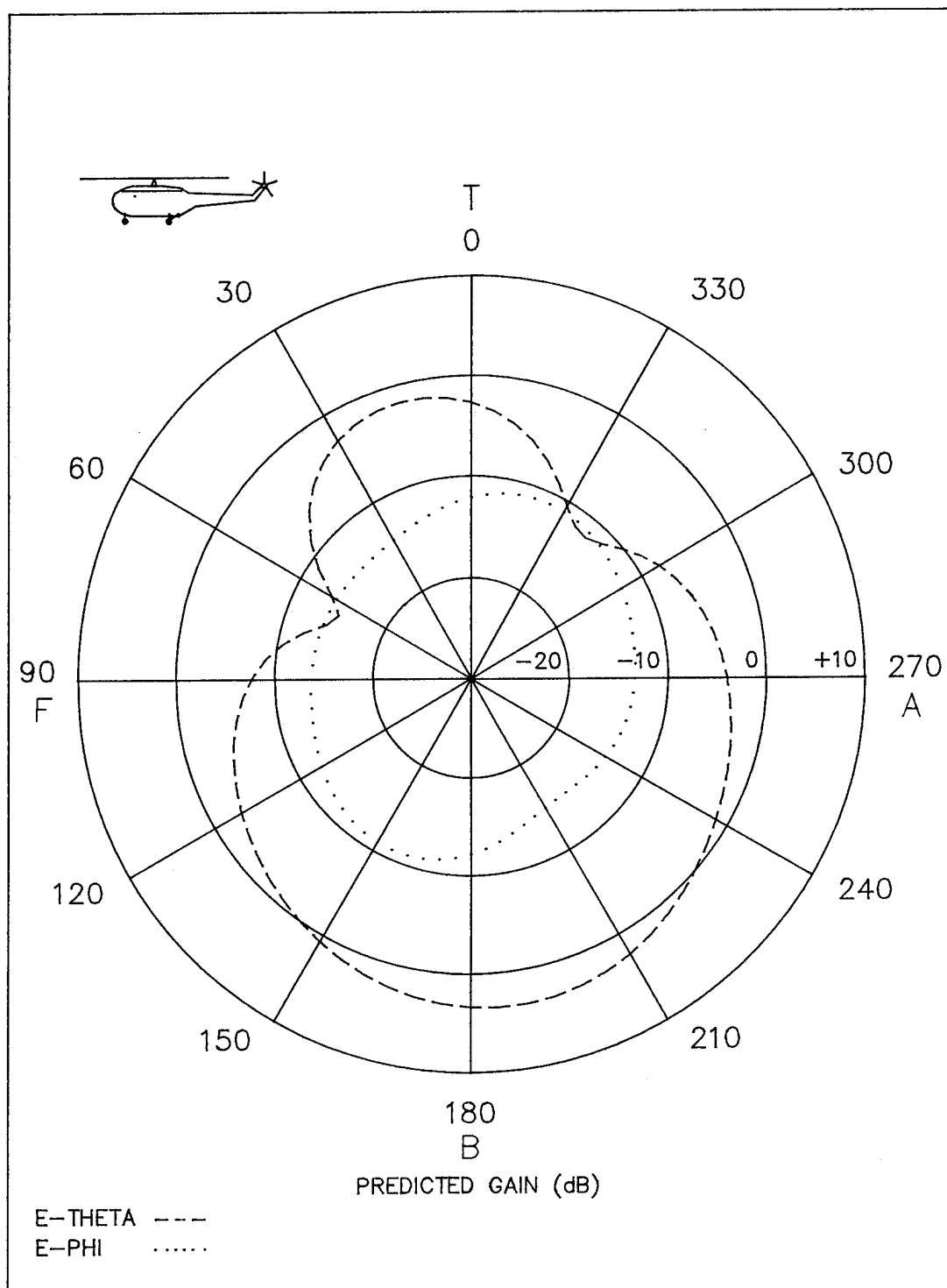


Figure 11. Predicted gains for the helicopter model in the x-z plane at 330 MHz. Brass conductors.

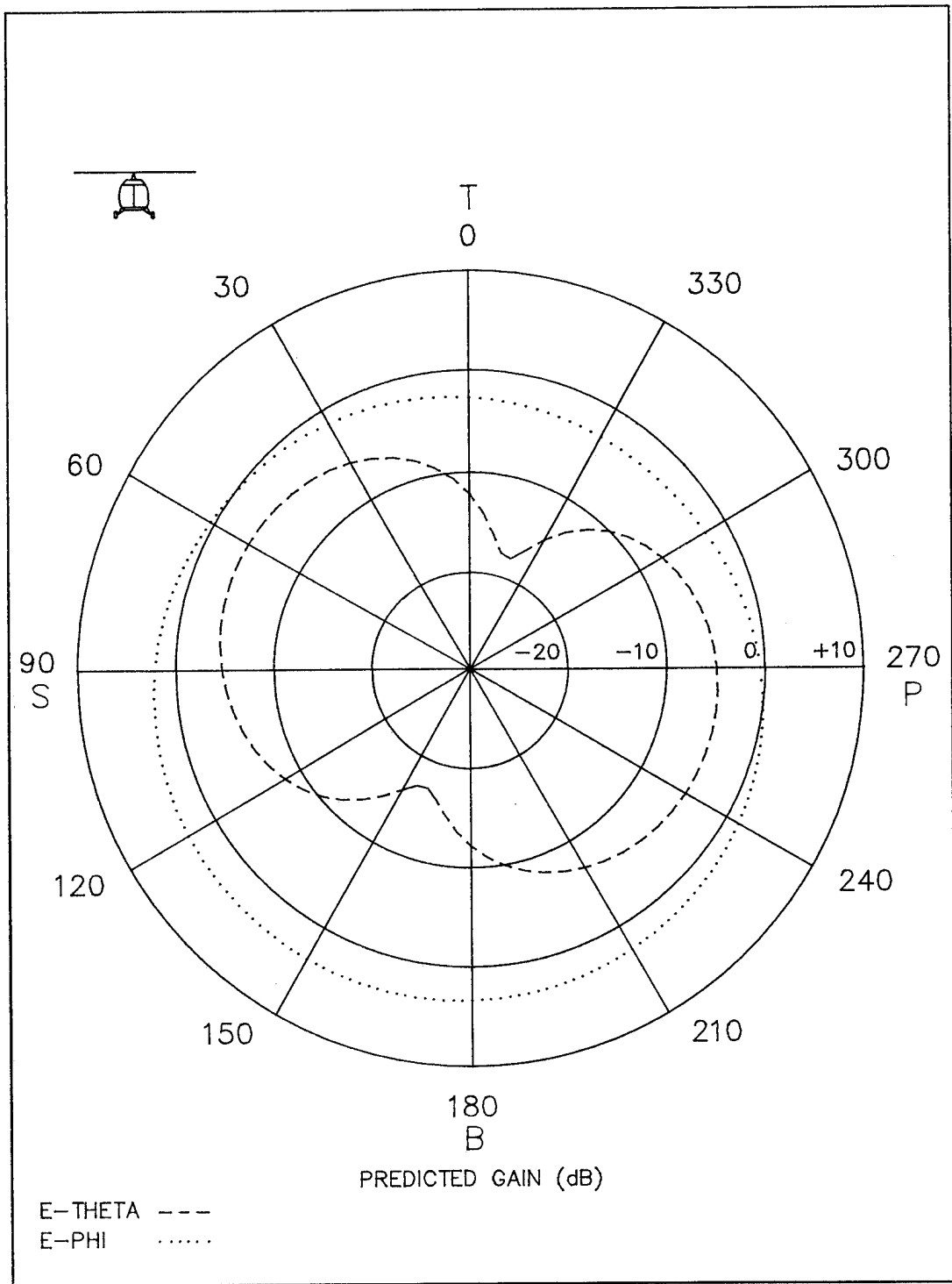


Figure 12. Predicted gains for the helicopter model in the y-z plane at 330 MHz. Brass conductors.

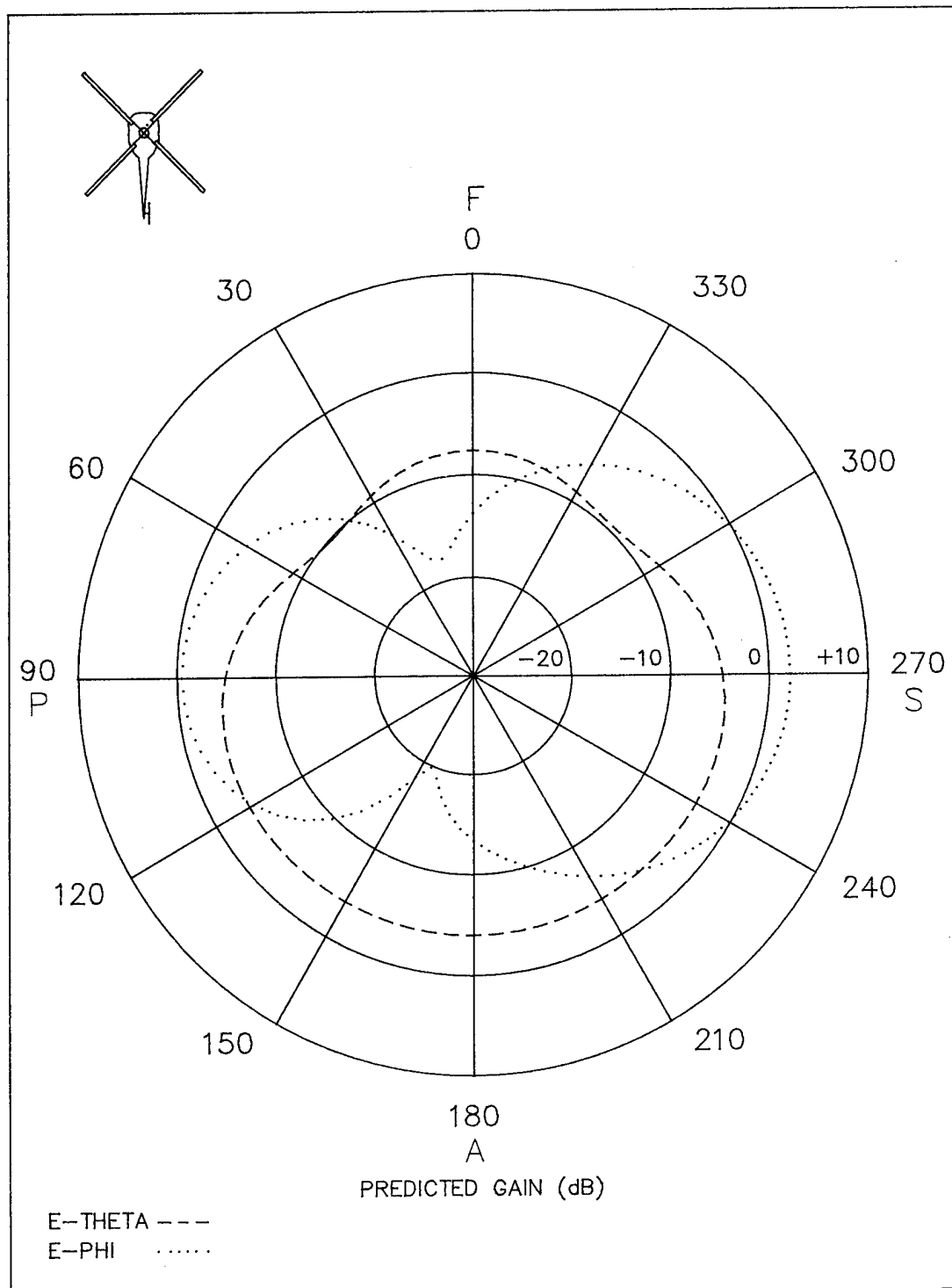


Figure 13. Predicted gains for the helicopter model in the x-y plane at 330 MHz. Brass conductors.

The Linear-Phase Triangular Facet Approximation in Physical Optics Analysis of Reflector Antennas

W. A. Imbriale and R. E. Hodges

Jet Propulsion Laboratory
California Institute of Technology
4800 Oak Grove Drive
Pasadena, California 91109

Numerical analysis of reflector antennas uses a discrete approximation of the radiation integral. The calculation replaces the actual reflector surface with a triangular facet representation. The physical optics current is then approximated within each facet. This paper provides analytical details of the method based on the assumption of a constant magnitude and linear-phase approximation of the physical optics current. Example calculations are provided for parabolic, elliptical, and shaped subreflectors. The computed results are compared with calculations made using a constant-phase approximation. These results show that the linear-phase approximation is a significant improvement over the constant-phase approximation in that the solution converges over a larger angular region of space. This improvement can significantly reduce storage requirements and possibly execution speed.

I. Introduction

One of the simplest numerical techniques for electromagnetic scattering analysis is based on a discrete approximation of the physical optics (PO) radiation integral. The general modeling technique is similar to that employed by Rao et al. [1] for the moment method solution of electromagnetic scattering by surfaces of arbitrary shape. In this paper, we apply the methodology to the problem of shaped reflector antenna analysis. This calculation comprises two distinct approximations. First, the actual reflector surface is replaced by a triangular facet representation so that the reflector resembles a geodesic dome. One then makes an analytic approximation of the PO current within each of the facets. Upon evaluating the PO integral locally over each facet, the radiation integral reduces to a summation over the collection facets that represent the surface.

Several years ago, a computer program was developed at the Jet Propulsion Laboratory (JPL) utilizing the assumption of constant magnitude and phase of the PO current within each facet. This program has proven to be surprisingly robust and useful for the analysis of relatively small shaped reflectors, particularly when the near field is desired and surface derivatives are not known. It is natural to inquire whether a more sophisticated approximation of the PO surface current will yield more accurate results or permit the use of larger facets. In this paper, a linear-phase approximation of the surface currents is made. Within each triangular region, the resulting integral is written as the two-dimensional Fourier transform of the projected triangle. This triangular shape function can be integrated in closed form [2] and the complete PO integral is then a summation of these transforms. Significantly, other authors have developed more general techniques for performing the required integration [3,4,5], which could be very useful for future refinements.

In what follows, the explicit details of the analysis are provided along with example calculations of scattering from parabolic, elliptical, and shaped reflector surfaces. For a given size of triangular facet, two general trends emerge from the calculations. First, the linear-phase approximation takes about three times longer to compute a field point than does the constant-phase approximation. Second, there is an angular region of space over which the solution is valid, and this angular region is significantly larger with the linear-phase approximation than with the constant-phase approximation. Clearly, a trade-off situation exists here.

Since the surface geometry and PO currents must be stored in memory, the linear-phase approximation offers an advantage in terms of storage because fewer triangular facets are needed to reach convergence over a specified angular region. On the other hand, to claim a speed advantage, this method must reduce the required number of facets by at least one-third. This reduction will only be possible for reflectors in which relatively large regions can be adequately approximated by a uniformly illuminated planar surface. It has been found that this is the case for relatively large reflector antennas.

II. Analytical Details

The PO radiation integral over the reflector surface Σ can be expressed [6]

$$\mathbf{H}(\mathbf{r}) = -\frac{1}{4\pi} \int_{\Sigma} \left(jk + \frac{1}{R} \right) \hat{\mathbf{R}} \times \mathbf{J}_s(\mathbf{r}') \frac{e^{-jkR}}{R} ds' \quad (1)$$

in which \mathbf{r} designates the field point, \mathbf{r}' the source point, $R = |\mathbf{r} - \mathbf{r}'|$ is the distance between them, and $\hat{\mathbf{R}} = (\mathbf{r} - \mathbf{r}')/R$ is a unit vector. The PO surface current on the subreflector surface \mathbf{J}_s is expressed

$$\mathbf{J}_s(\mathbf{r}') = 2\hat{\mathbf{n}} \times \mathbf{H}_s(\mathbf{r}') \quad (2)$$

For the purpose of analysis, the true surface Σ is replaced by a contiguous set of N -plane triangular facets. These facets, denoted Δ_i , are chosen to be roughly equal in size with their vertices on the surface Σ . Figure 1 shows a typical facet and its projection onto the x - y plane. Let (x_i, y_i, z_i) represent the *centroid* of each triangle where the subscript $i = 1, \dots, N$ is associated with a triangle. Then, the field obtained by replacing the true surface Σ by the triangular facet approximation is

$$\mathbf{H}(\mathbf{r}) = -\frac{1}{4\pi} \sum_{i=1}^N \int_{\Delta_i} \left(jk + \frac{1}{R} \right) \hat{\mathbf{R}} \times \mathbf{J}(\mathbf{r}') \frac{e^{-jkR}}{R} ds' \quad (3)$$

In Eq. (3), \mathbf{J} is now the equivalent surface current evaluated on the triangular facets. Since the triangles are small, it is expected that $\hat{\mathbf{R}}$ and R do not vary appreciably over the area of a given facet. Thus, let $\hat{\mathbf{R}}_i$ and R_i be the value obtained at the centroid (x_i, y_i, z_i) of each facet and approximate Eq. (3) by

$$\mathbf{H}(\mathbf{r}) = -\frac{1}{4\pi} \sum_{i=1}^N \left(jk + \frac{1}{R_i} \right) \hat{\mathbf{R}}_i \times \mathbf{T}_i(\mathbf{r}) \quad (4)$$

$$\mathbf{T}_i(\mathbf{r}) = \int_{\Delta_i} \mathbf{J}_i(\mathbf{r}') \frac{e^{-jkR}}{R_i} ds' \quad (5)$$

Assume that the necessary transformations have been performed so that the incident field \mathbf{H}_s is given in terms of the reflector coordinate system. Then

$$\mathbf{J}_i(\mathbf{r}') = 2\hat{\mathbf{n}}_i \times \mathbf{H}_s(\mathbf{r}') \quad (6)$$

Next, assume that the incident field can be represented by a function of the form

$$\mathbf{H}_s = \mathbf{h}_s(\mathbf{r}'_i) \frac{e^{-jk r_s}}{4\pi r_{si}} \quad (7)$$

where r_s is the distance to the source point. Also, \mathbf{r}_i and \mathbf{r}_{si} denote the vectors \mathbf{r}' and \mathbf{r}_s evaluated at the centroid of the i th triangular facet and are regarded as constants. Then, Eq. (5) can be written

$$\mathbf{T}_i(\mathbf{r}) = \frac{\hat{\mathbf{n}}_i \times \mathbf{h}_s(\mathbf{r}'_i)}{2\pi R_i r_{si}} \int_{\Delta_i} e^{-jk(R+r_s)} ds' \quad (8)$$

To simplify the form of the integration, the surface Jacobian is introduced within each triangular facet Δ_i . For a planar surface $z_i = f_i(x, y)$, a normal is given by

$$\mathbf{N}_i = -\hat{\mathbf{x}} f_{xi} - \hat{\mathbf{y}} f_{yi} + \hat{\mathbf{z}} \quad (9)$$

where

$$f_{xi} \equiv \frac{\partial f_i}{\partial x} \quad f_{yi} \equiv \frac{\partial f_i}{\partial y}$$

and a unit normal is given by

$$\hat{\mathbf{n}}_i = \frac{\mathbf{N}_i}{|\mathbf{N}_i|} \quad (10)$$

This permits the explicit evaluation of the Jacobian as

$$J_{\Delta_i} = |\mathbf{N}_i| = \left[f_{xi}^2 + f_{yi}^2 + 1 \right]^{1/2} \quad (11)$$

Making use of the Jacobian then allows Eq. (8) to be rewritten as

$$\mathbf{T}_i(\mathbf{r}) = \frac{\hat{\mathbf{n}}_i \times \mathbf{h}_s(\mathbf{r}'_i)}{2\pi R_i r_{si}} J_{\Delta_i} \int_{\Delta'_i} e^{-jk(R+r_s)} dx' dy' \quad (12)$$

in which Δ'_i represents the area of the i th triangular facet projected onto the $z = 0$ plane. Now, make a Taylor-series expansion of the exponent in Eq. (12). Retaining only the first-order terms, one can formally write

$$R(x, y) + r_s(x, y) = \frac{1}{k} (a_i - u_i x - v_i y) \quad (13)$$

in which a_i , u_i , and v_i are constants. This approximation corresponds to a far-field approximation on the i th triangle. With this approximation, Eq. (12) reduces to

$$\mathbf{T}_i(\mathbf{r}) = \frac{\hat{\mathbf{n}}_i \times \mathbf{h}_s(\mathbf{r}'_i)}{2\pi R_i r_{si}} J_{\Delta_i} e^{-jk a_i} \int_{\Delta'_i} e^{j(u_i x' + v_i y')} dx' dy' \quad (14)$$

It may now be observed that this integral is the two-dimensional Fourier transform of the i th projected triangle Δ'_i , expressed as

$$S(u, v) = \int_{\Delta'_i} e^{j(ux+vy)} dx dy \quad (15)$$

In order to explicitly evaluate the constants in Eq. (13), note that the equation of a plane can be expressed as

$$z = (x - x_i)f_{xi} + (y - y_i)f_{yi} + z_i$$

This can be used to obtain

$$a_i = kR(x_i, y_i) + kr_s(x_i, y_i) + u_i x_i + v_i y_i \quad (16)$$

$$\frac{u_i}{k} = \frac{(x_p - x_i) + (z_p - z_i)f_{xi}}{R(x_i, y_i)} + \frac{(x_s - x_i) + (z_s - z_i)f_{xi}}{r_s(x_i, y_i)} \quad (17)$$

$$\frac{v_i}{k} = \frac{(y_p - y_i) + (z_p - z_i)f_{yi}}{R(x_i, y_i)} + \frac{(y_s - y_i) + (z_s - z_i)f_{yi}}{r_s(x_i, y_i)} \quad (18)$$

Placing the result of Eq. (16) into Eq. (14), and recalling Eqs. (6) and (7), yields

$$\mathbf{T}_i(\mathbf{r}) = \mathbf{J}_i(r_i) J_{\Delta_i} e^{-j(u_i x_i + v_i y_i)} S(u_i, v_i) \frac{e^{-jkR_i}}{R_i} \quad (19)$$

This is the final form of the linear-phase approximation over each triangular facet. This expression can be used in Eq. (4) to compute the radiation integral once the Fourier transform of a triangular shape function $S(u, v)$ is known. Fortunately, this transform can be computed in closed form [2] from the expression

$$S(u, v) = \sum_{n=1}^3 e^{j(ux_n + vy_n)} \frac{p_{n-1} - p_n}{(u + p_{n-1}v)(u + p_n v)} \quad (20)$$

in which (x_n, y_n) are the coordinates of the triangle vertices numbered in a clockwise direction. The slope of the n th side (between corners n and $n+1$) is given by

$$p_n = \frac{y_{n+1} - y_n}{x_{n+1} - x_n} \quad (21)$$

Some attention must be given to the following special cases. First, if $u = v = 0$, the transform reduces to the formula for the area of a triangle

$$S(0, 0) = -\frac{1}{2} \left[x_1(y_2 - y_3) + x_2(y_3 - y_1) + x_3(y_1 - y_2) \right] \quad (22)$$

Next, if $u/v \rightarrow -p_n$, then

$$\lim_{u/v \rightarrow -p_n} S(u, v) = \frac{p_{n+1} - p_{n-1}}{v^2(p_{n+1} - p_n)(p_{n-1} - p_n)} \times \left[e^{j(ux_{n-1} + vy_{n-1})} - e^{j(ux_n + vy_n)} \right] + \frac{(x_{n+1} - x_n)}{jv} e^{j(ux_n + vy_n)} \quad (23)$$

III. Numerical Results

A FORTRAN subroutine was written to perform the linear-phase calculations indicated above. Test cases were run for parabolas, ellipses, and shaped subreflectors, and the results were compared with calculations that use a constant magnitude and phase approximation on the triangular facets. A focused parabola is neither an interesting nor a challenging case for the algorithm, since the phase variation over the facet is small. As a simple test case, the far-field pattern and gain of a $1,000\lambda$ -diameter parabolic reflector with a focal length of $F = 400\lambda$ was calculated. The reflector is illuminated by a linearly polarized horn with a $\cos \theta$ pattern function. Figure 2 compares the linear- and constant-phase approximation for a roughly equally spaced 80-by-80 rectangular grid of points divided into triangles over the reflector surface (approximately 10,000 triangles). The running time on a Cray X-MP/18 was less than one minute. Convergence was checked by increasing the number of triangles until the computed solution did not change appreciably over the angular region of interest. It has been previously demonstrated [7,8,9] that, once sufficient triangles to converge the solution have been utilized, the results of the constant-phase algorithm are valid, so only comparisons of the two techniques are presented.

A more interesting example is the ellipse shown in Fig. 3. The projected aperture of the ellipse is about 3 m, illumination function is a $\cos^{42} \theta$ pattern function (22.3-dB gain), and the frequency is 31.4 GHz. The ellipse is about 350λ along the major axis. Figure 4 compares the constant-phase approximation for different grid densities of approximately 4,000, 10,000, and 23,000 triangles, and illustrates a general trend of the method, i.e., depending on the size of the triangles, there is an angular limit over which the solution is valid. Figure 5 compares the linear-phase approximation with the constant-phase approximation for the 4,000-triangle case and demonstrates that the angular range is larger with the linear-phase approximation.

A third example is the shaped subreflector shown in Fig. 6. The diameter is 3.42 m (135 in.), and it is fed with a $\cos^{233} \theta$ pattern function (29.7-dB gain). Figure 7 compares the results of a 4,000- and 10,000-triangle grid constant-phase approximation with a 4,000-triangle linear-phase approximation. The frequency of operation is 2.3 GHz, hence, the subreflector is about 26λ in diameter. The 10,000-triangle constant phase is the converged result and the 4,000-triangle linear case gives the same result. A very good approximation is also obtained with a 1,400-triangle grid for the linear case, but no meaningful results are obtained with the constant-phase case. Figure 8 gives the linear-phase result for 31.4 GHz (360 λ subreflector) using 23,000 triangles. No meaningful result is obtained for the equivalent constant-phase case.

One final example is given by a beam-waveguide system that has recently been built at JPL. The measurement setup consists of a 22-dB-gain feedhorn that is used to illuminate a beam-waveguide system consisting of a pair of parabolic reflectors. The mirrors are arranged to replicate the input feed pattern at the focal point of the second dish. Details of the geometry are given elsewhere [10]. A calculation of this system was made using the triangular facet PO technique by first computing the near-field scattering from the first reflector and using these values to compute the PO current on the second reflector. Subsequently, the triangular facet program is used a second time to compute the field radiated by the second parabolic reflector. In Fig. 9, the results of this calculation are compared with experimental measured data taken at X-band. As can be seen, the computed results compare favorably with the measured data.

Most of the examples given are for large reflectors to illustrate the robust character of the technique. For smaller reflectors ($< 100\lambda$), meaningful results can be obtained on a typical desktop computer in a reasonable time.

IV. Conclusions

The triangular facet approximation technique provides a simple and flexible method of analysis for reflector antennas. We have found that the linear-phase approximation is valid over a larger angular region than is the constant-phase approximation. In applying this method to fairly large (100 to 1000λ) reflectors, the linear-phase approximation provides a significant reduction in the computer storage requirements and can reduce computation time in some cases.

Acknowledgment

The research described in this paper was carried out by the Jet Propulsion Laboratory, California Institute of Technology, under a contract with the National Aeronautics and Space Administration. Reference herein to any specific commercial product, process, or service by trade name, trademark, manufacturer, or otherwise, does not constitute or imply its endorsement by the United States Government or the Jet Propulsion Laboratory, California Institute of Technology.

References

- [1] S. M. Rao, D. R. Wilton, and A. W. Glisson, "Electromagnetic Scattering by Surfaces of Arbitrary Shape," *IEEE Trans. Antennas and Propagation*, vol. AP-30, no. 3, pp. 409-418, May 1982.
- [2] S. W. Lee and R. Mittra, "Fourier Transform of a Polygonal Shape Function and Its Application in Electromagnetics," *IEEE Trans. Antennas and Propagation*, vol. 31, no. 1, pp. 99-103, January 1983.
- [3] W. B. Gordon, "Far-Field Approximations to the Kirchoff-Helmholtz Representation of Scattered Fields," *IEEE Trans. Antennas and Propagation*, vol. 23, no. 4, pp. 590-592, July 1975.
- [4] J. S. Asvestas, "Line Integral and Physical Optics, Part I: The Transformation of the Solid-Angle Surface Integral to a Line Integral," *J. Opt. Soc. A.*, vol. 2, no. 6, pp. 891-895, June 1985.
- [5] J. S. Asvestas, "Line Integral and Physical Optics, Part II: The Conversion of the Kirchoff Surface Integral to a Line Integral," *J. Opt. Soc. A.*, vol. 2, no. 6, pp. 896-902, June 1985.
- [6] A. W. Rudge, K. Milne, A. D. Oliver, and P. Knight, *The Handbook of Antenna Design, Vol. I*, London: Peter Peregrinus, 1982.
- [7] V. Galindo-Israel, T. Veruttipong, and W. Imbriale, "GTD, Physical Optics and Jacobi-Bessel Diffraction Analysis of Beamwaveguide Ellipsoids," *AP-S International Symposium*, Philadelphia, Pennsylvania, pp. 643-646, 1986.

- [8] T. Veruttipong, J. R. Withington, V. Galindo-Israel, W. A. Imbriale, and D. A. Bathker, "Design Considerations for Beamwaveguide in the NASA Deep Space Network," *IEEE Trans. Antennas and Propagation*, vol. AP-36, no. 12, pp. 1779-1787, December 1988.
- [9] A. G. Cha and W. A. Imbriale, "New Analysis of Beamwaveguide Antennas Considering the Presence of the Metallic Tube and Its Experimental Verification," *AP-S International Symposium*, Dallas, Texas, pp. 1506-1509, 1990.
- [10] J. R. Withington, W. A. Imbriale, and P. Withington, *JPL Beam Waveguide Test Facility*, to be presented at the 1991 International IEEE Antennas and Propagation Society Symposium, June 24, 1991.

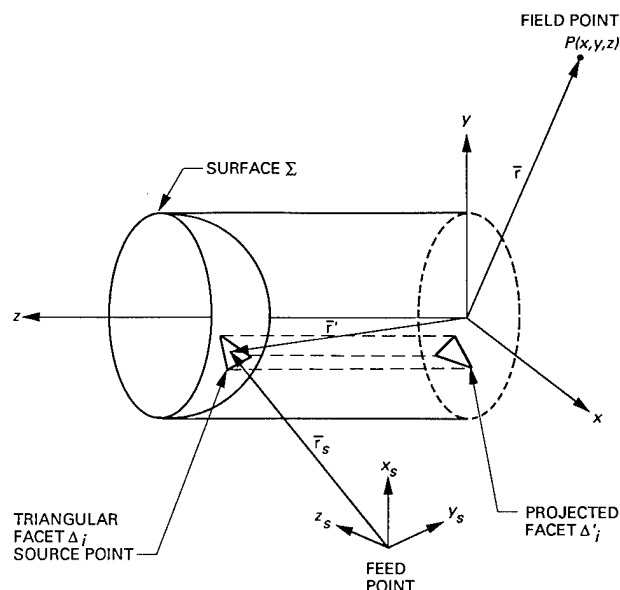


Fig. 1. Reflector analysis coordinate systems and a typical triangular facet.

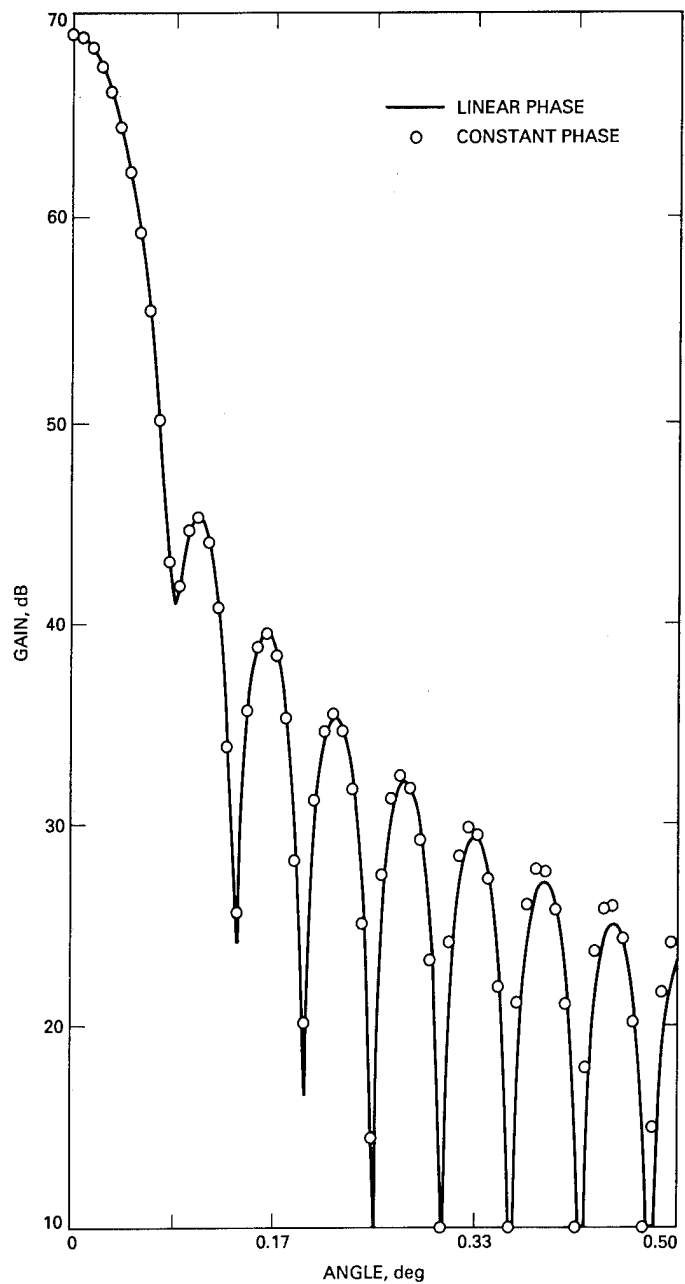


Fig. 2. Parabolic example.

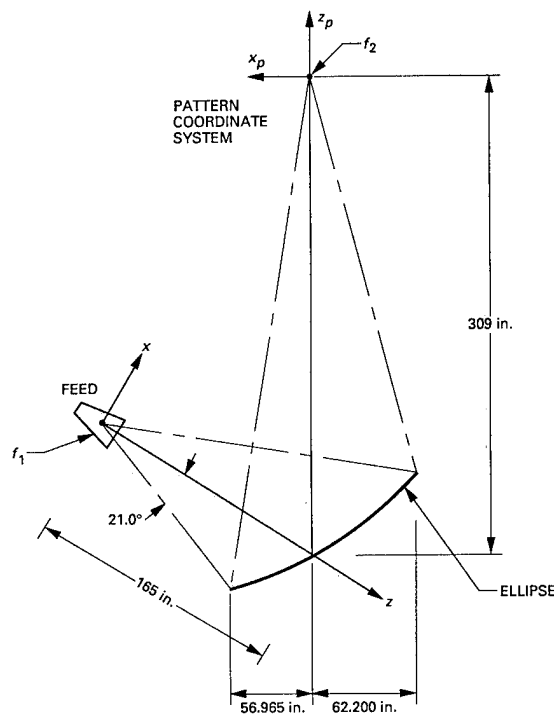


Fig. 3. Ellipse geometry.

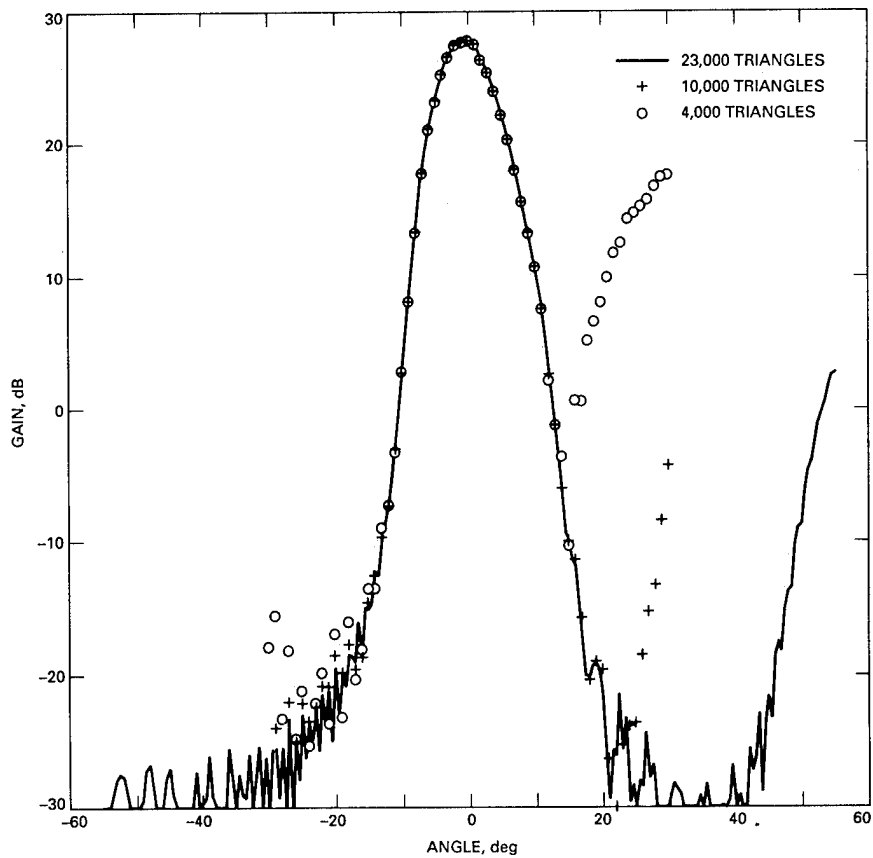


Fig. 4. Ellipse example: constant-phase approximation for offset plane.

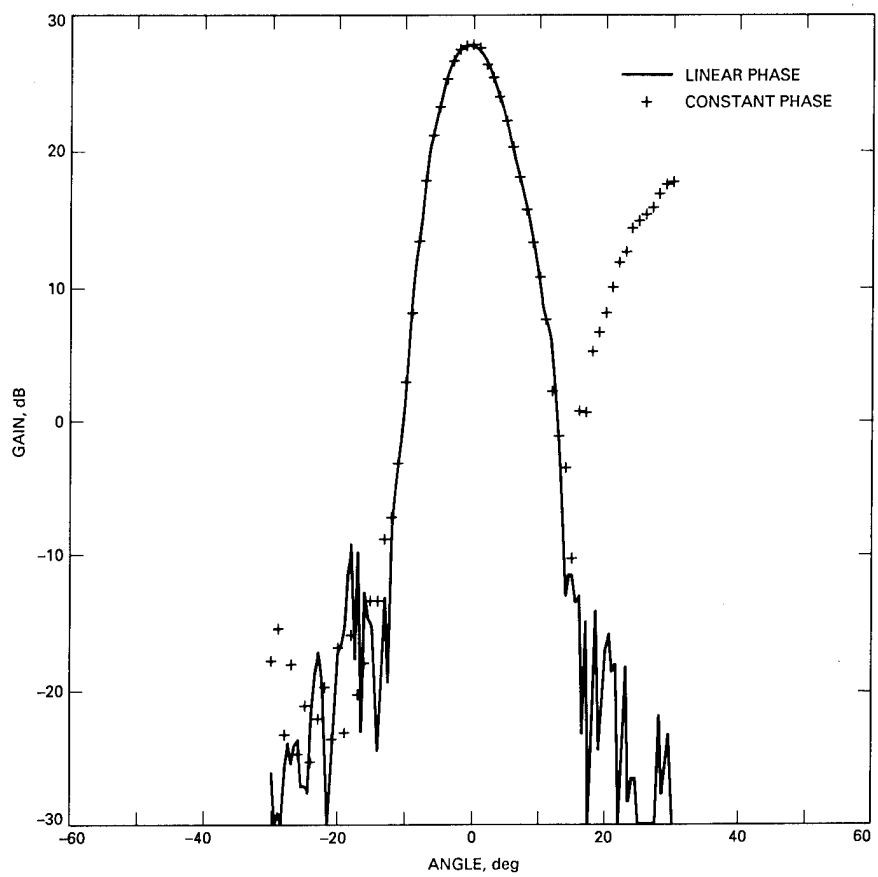


Fig. 5. Ellipse example: constant versus linear phase for offset plane.

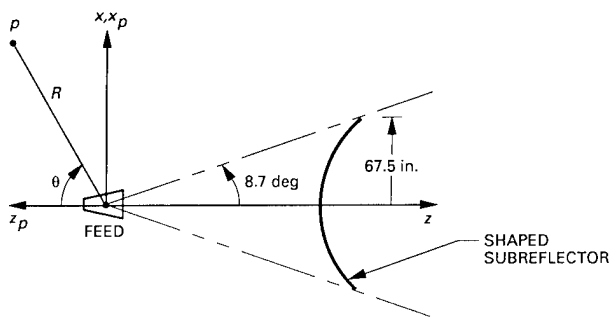


Fig. 6. Shaped subreflector geometry.

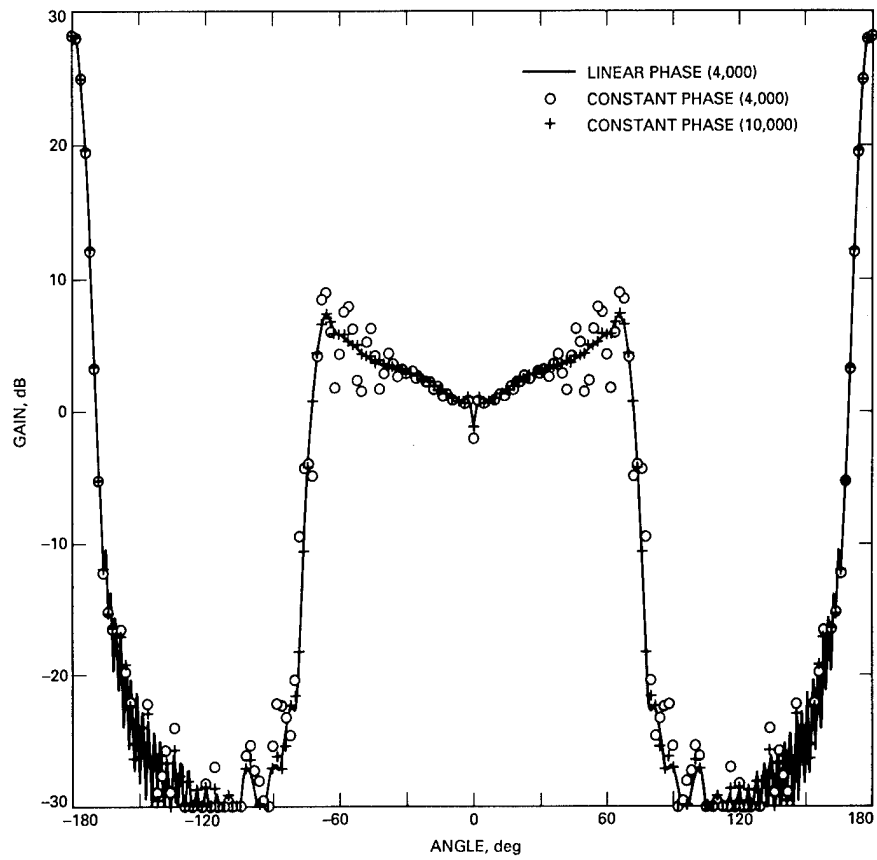


Fig. 7. Shaped subreflector example for H-plane at 2.3 GHz.

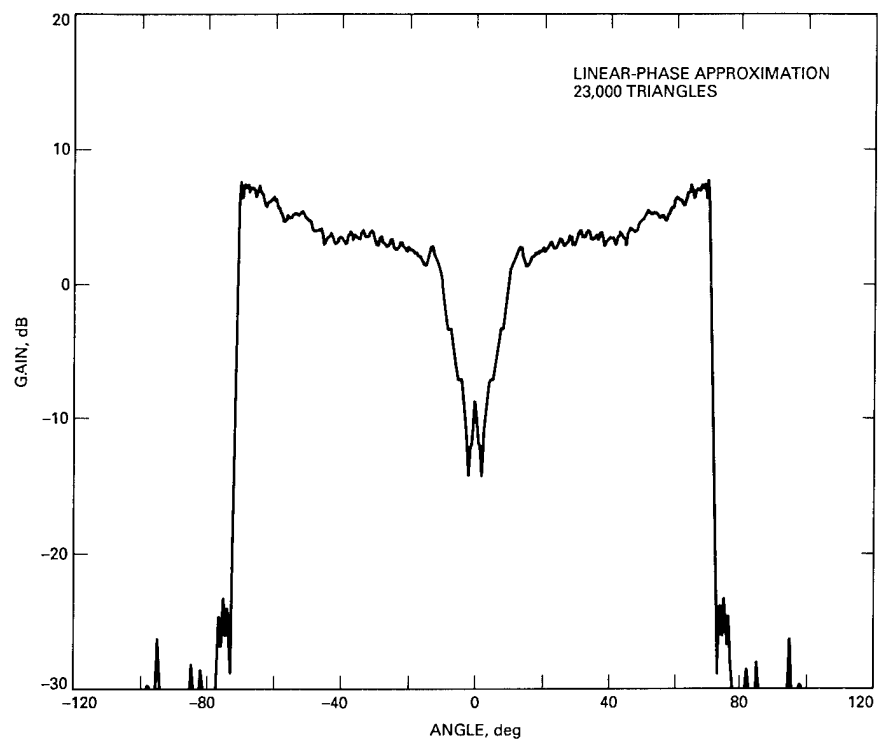


Fig. 8. Shaped subreflector, 31.4 GHz.

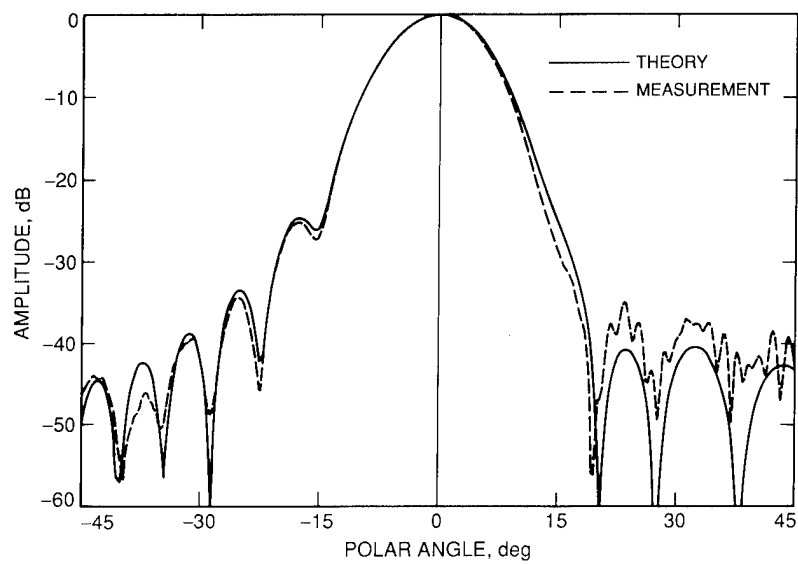


Fig. 9. Two-mirror X-band beam waveguide.

SIMPLIFIED 3-D MESH GENERATOR

Riyadh K. Najm

Department of Electrical Engineering and Electronics
University of Liverpool
Brownlow Hill, P.O. Box 147
Liverpool L69 3BX
United Kingdom

Abstract

Wire-grid modelling of continuous surfaces for structures in three dimensions is a tedious and time consuming process. This paper describes a simplified automatic mesh generator that converts a large class of three-dimensional structures into appropriate wire-grid models. The output of the generator can readily be used as the input to wire antenna Moment Method codes. It is however designed specifically for use with the Numerical Electromagnetics Code (NEC).

1. Introduction

Users of Moment Method codes often require the generation of wire-grid models for three-dimensional structures such as ships, vehicles, aircraft, etc. Producing these models manually usually takes a lot of time and effort. Even when working from the manufacturers CAD drawings the user often needs to eliminate unnecessary details and parts of the structure. Although some sophisticated computer software has been developed for this purpose [1], it is not generally available.

The Mesh Generator developed in this work can produce wire-grid models for these 3-D structures according to the required specifications. The structure needs to be represented by flat surfaces of quadrilateral or triangular shape. The grids produced by the generator are generally quasi-orthogonal wires except near one of the vertices in triangular regions; as will be shown later. Limited modelling errors are checked for by the generator; although not as extensively as described in [2].

The output of the generator can be used as a NEC [3] input data file. External graphics facilities need to be used to view the generated wire-grid.

2. Mesh Generation Guidelines

Wire-grid modelling techniques have been studied extensively by many workers. It is not the intention of this paper to give any recommendations in this regard. However, because of their relevance, mesh generation guidelines will be briefly reviewed here. When modelling a solid surface with a wire-grid, three main factors need to be considered:

- Type of the wire-grid
- Cell size of the grid
- Radii of grid wires

The most widely used type of wire-grid is the rectangular one because it was found to be satisfactory in most cases and it is easier to generate than other types. Also, the rectangular grid makes it easier to decide on the values of wire radii using simple formulas. A triangular mesh on the other hand has the advantage of simulating more realistic currents [4, p.117]. Other types of meshes have also been used. The mesh generator described in this paper can produce rectangular and partly triangular grids.

The grid cell size can either be specified in terms of its area, as in [4], or in terms of the spacing between adjacent elements. Because the rectangular mesh is the one that is most commonly used, it is easier to use the second method. The element spacing (size) will depend on the type of structure being modelled and on the parameters of interest. It must be as small as possible, up to the limitations of the MM code used, if these are near field parameters such as input impedance. The grid element size can range from $\lambda/5$, as suggested in [5], to as little as $\lambda/1500$ as used in [6] near the feed point of the antenna. The generally accepted value for element size is $\lambda/10$.

As for the wire radii of the grid, two basic methods have been discussed in the literature. The first specifies the wire radius of the model as a fraction of the wavelength. Studies that have used this method, such as in [7], set the wire radius empirically at 0.005λ but do not give any reasoning for this choice. The second method is much more widely used and relates the overall surface area of the wires, A_s , to the area of the solid surface that is being modelled, A_r . As has been described in [8], modellers have recommended several criteria for this relation. The following table summarises those most commonly used:¹

Modeller	Criterion
Moore & Pizer	$A_s \geq A_r$ up to $5A_r$
Lee, et al	$A_s \approx 2A_r$
Ludwig	$A_s \approx 2A_r$
Elliott & McBride	$A_s = A_r$ of <u>one</u> side of a closed surface $A_s = A_r$ of <u>both</u> sides of an open surface
Burke & Poggio	A_s of wires in the direction of each current component = A_r . So, for a rectangular mesh, $A_s = 2A_r$

¹ Complete references for these criteria are found in [8].

It is evident that most of these criteria recommend the "twice surface area rule", i.e. $A_s = 2A_r$. If we define the ratio between A_s and A_r to be the overall area factor, AF, then it follows that AF=2 in the general case. It is however useful to keep AF as a variable set by the user according to what is required. This mesh generator uses the given area factor to calculate the wire radius for the mesh of the modelled surface.

3. Description

The program for this mesh generator is written in standard FORTRAN 77. It can run on a mainframe or a microcomputer. The generator is used to model structures in the following manner:

1. The structure is divided into quadrilateral or triangular flat regions of any orientation in space.
2. Knowing the corners co-ordinates of each individual region and the number of sections required on its sides, the region is converted into a wire-grid accordingly.
3. The wire radius for each region is calculated according to the specified area factor as described below.
4. Similar elements at the junctions of regions sides are then eliminated.
5. Parts of the structure that do not form flat surfaces must be added manually.

A quadrilateral region is defined by the co-ordinates of its four corners C1 to C4. There is no restriction on the shape of the quadrilateral region or its orientation in space as long as it is flat. In the special case of the triangular region, the co-ordinates of two consecutive corners are the same. The region is divided into grid elements by specifying the number of elements on two adjacent sides (N1 and N2 in Fig. 1).

The other two opposite sides are assumed to have the same number of elements as those opposite regardless of their lengths. For triangular regions, there are only three corners, so one of the opposite sides will simply be a vertex. To establish a reference, this type of region is defined as one in which corners 3 and 4 have the same co-ordinates. Consequently, there are three alternatives for the mesh of a triangular region as shown in the three schematics of Fig. 2. By changing the numbering order of the region's three corners, the required mesh can be generated. N1 and N2 were kept the same at 4 and 3 respectively, in all the three combinations in order to illustrate the point. In practice they can be changed to suit the model.

The generator will then produce all elements that make up the wire-grid of the region. The sequence of ordering the elements is shown in Fig. 1 for the first four elements (L1 to L4).

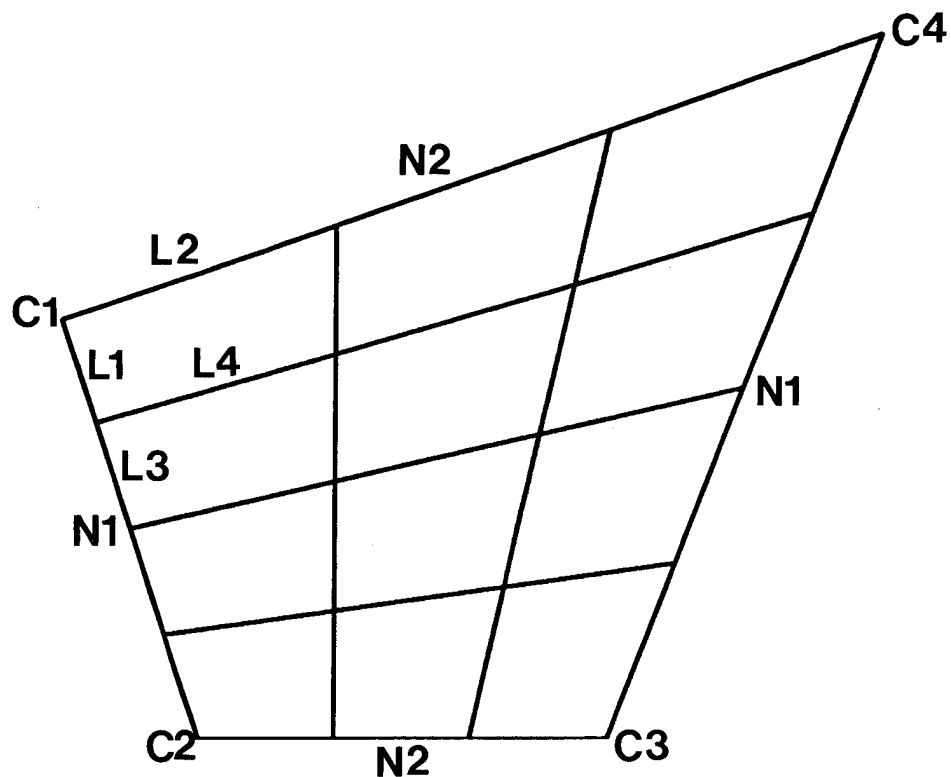


Fig. (1) A schematic of a quadrilateral region and its mesh distribution where $N1 = 4$ and $N2 = 3$.

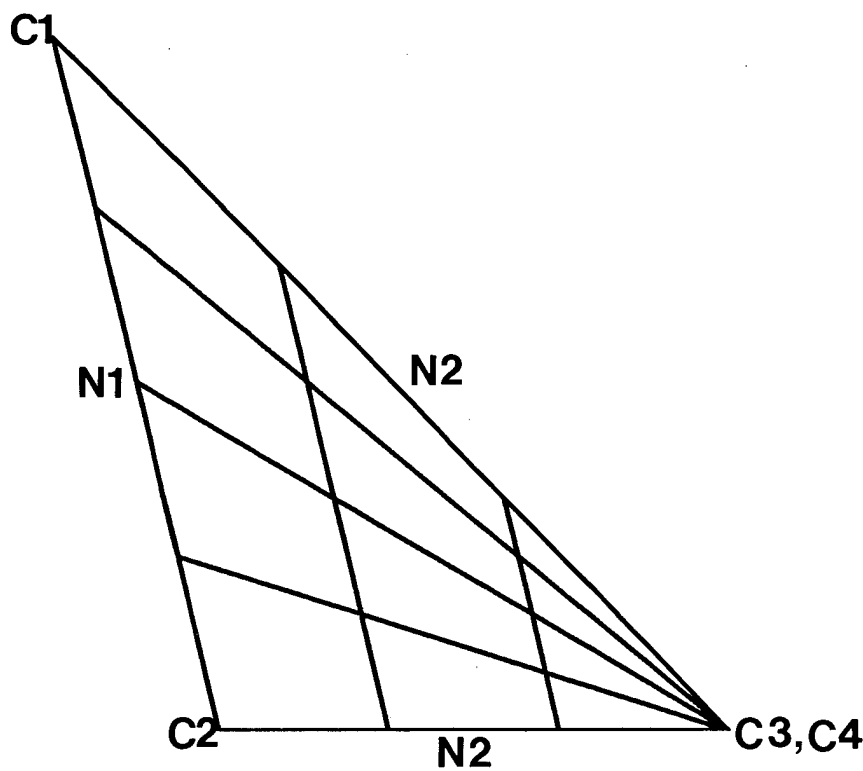


Fig. (2-a) First alternative of a triangular region's mesh.

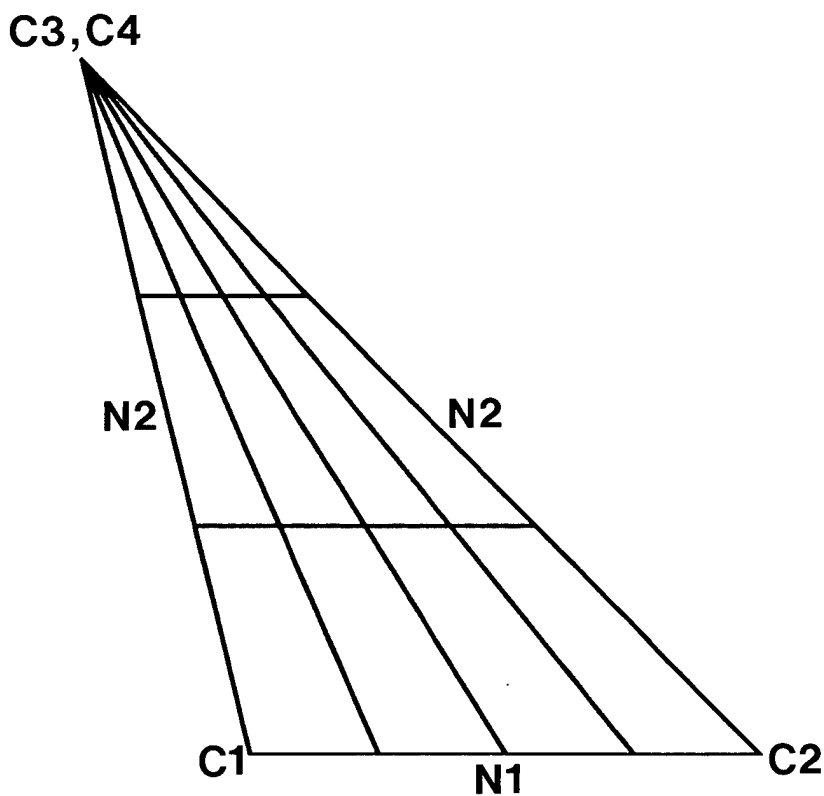


Fig. (2-b) Second alternative mesh of the triangular region in Fig. 2-a

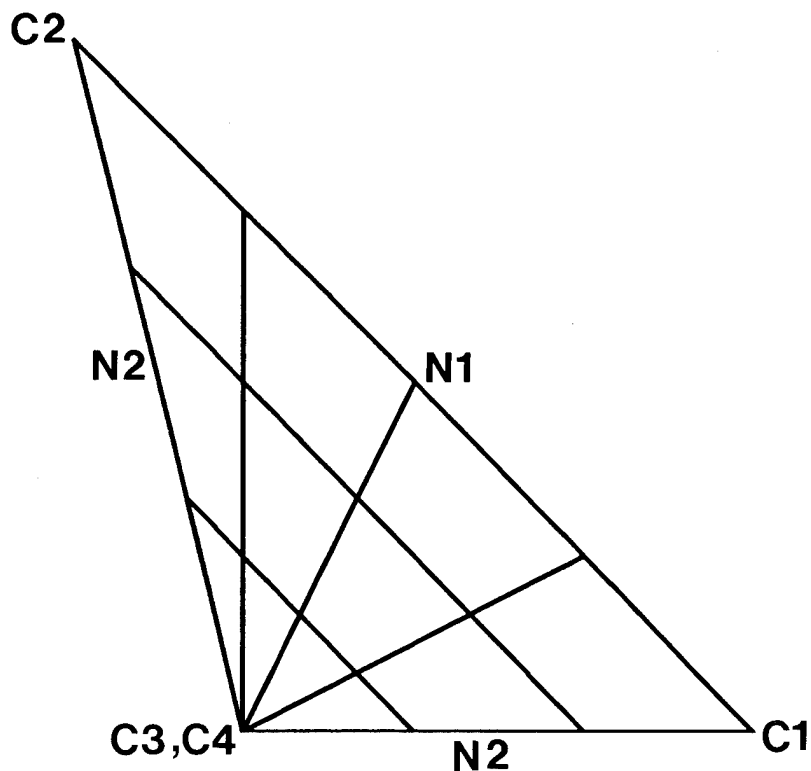


Fig. (2-c) Third alternative mesh of the triangular region in Fig. 2-a

The next step is to calculate the radius of wires in the region using the given area factor. The total surface area of the wires A_s is first calculated by the following formula:

$$A_s = 2\pi a \sum_{i=1}^k l_i$$

where

- l_i : The length of the i th element
- a : The radius of the region's wires
- k : The number of elements in the region

The region's area A_r is then calculated by dividing the region into two triangles whose areas are found using Heron's formula [9, p.7] as follows:

$$A_r = A_1 + A_2$$

$$A_1 = \sqrt{S_1(S_1 - L_{12})(S_1 - L_{23})(S_1 - L_{31})}$$

$$S_1 = \frac{L_{12} + L_{23} + L_{31}}{2}$$

$$A_2 = \sqrt{S_2(S_2 - L_{34})(S_2 - L_{41})(S_2 - L_{13})}$$

$$S_2 = \frac{L_{34} + L_{41} + L_{13}}{2}$$

In the above expressions, L_{mn} refers to the length of the region's side connecting corners m and n . The generator will then determine the wire radius a , which is the same for all the elements of the region, using the expression:

$$a = \frac{AF \times A_r}{2\pi \sum_{i=1}^k l_i}$$

The above process is repeated for each region in the structure. Since common elements exist at the junctions of regions' sides, all are scanned and the duplicated elements are eliminated. The wire radius of the elements at a junction is determined using the parameters of the region listed first in the input file.

At this stage, most of the structure will have been converted automatically to a wire-grid of the required specification. The user only has to add those parts of the structure that could not be represented by flat surfaces. These for example, may include curved surfaces or single wires.

It is important to note that connected regions should have the same number of elements for the sides at the junctions. It is also advisable that they have similar mesh densities so that any change in stepped wire radius between two

connected regions is made as gradual as possible. Different mesh densities for different parts of the structure can be achieved by making a gradual change in the mesh densities of connected regions. After all, the limitations of the Moment Method code that is used will determine the stepped radius factor that it can handle.

In addition, the generator produces some useful information for the different regions of the structure and checks for some of the common modelling errors. The following parameters are produced for each region in the structure:

- Segment length l_s in wavelengths
- Wire radius a in wavelengths
- Ratio of segment length to wire radius l_s/a

The user can specify the error threshold for these parameters or use the default values which are set according to the suggested guidelines in [2]. These are:

$$\begin{aligned} l_s &> \lambda/5 \\ \lambda/a &< 30 \\ l_s/a &< 2 \end{aligned}$$

The threshold for the l_s/a ratio is set at 2 assuming that the extended thin-wire kernel in NEC will not be used.

Note that the information given for individual regions are for all the elements in the region including those that will be eliminated when the regions are joined together.

4. Inputs and Outputs of the Generator

The input data of the generator is read in free format from a file structured as follows:

```

NREG AF FREQ
XX1 XX2 XX3 XX4
YY1 YY2 YY3 YY4
ZZ1 ZZ2 ZZ3 ZZ4
N1 N2

```

where

FREQ	: Frequency of operation in Mega Hertz.
NREG	: The number of regions on the structure.
AF	: The area factor for all the regions.
XX1 ... XX4	: X co-ordinates of the four corners of a region in metres.
YY1 ... YY4	: Y co-ordinates of the four corners of a region in metres.
ZZ1 ... ZZ4	: Z co-ordinates of the four corners of a region in metres.

N1	: Number of elements on the side between corners 1 and 2
N2	: Number of elements on the side between corners 2 and 3

Data for all the regions are input sequentially in the same manner one after the other without leaving spaces. Note that the area factor, AF, is specified only once at the beginning of the file for the entire structure.

Each element generated is simply a one-segment wire. Two output files are produced by the generator:

Geometry output file: which is formatted as a standard NEC geometry file that can be processed using the NEEDS package [10] or a mainframe version of NEC. The file format is accepted by both IGUANA [10] and NECPLOT [3] graphics routines.

Information file: which includes the following:

- The area factor, number of regions, and total number of elements for the structure.
- A_r , A_s , a , and the total length of elements for each region given in metres squared and metres.
- The modelling parameters mentioned in the previous section, grouped for each region separately, and the modelling errors if found.

It was suggested by an anonymous reviewer that one option to this generator would be to specify the number of segments per wavelength between corners of a region and request the wire-grid to be generated accordingly. While this option will be quite useful for the user, its implementation would require substantial review of the software.

5. Examples

To illustrate the usefulness of this mesh generator, three examples will be given. The first is a rectangular box consisting of 6 regions, one for each face, and 104 elements. A monopole is mounted in the middle of its top side. The area factor specified for the box is 2.0 and the frequency of operation is 30 MHz. The input file is listed below for illustration:

```

6 2.0 30.00
0. 2. 2. 0.
0. 0. 0. 0.
0. 0. 3. 3.
2 3
2. 2. 2. 2.
0. 4. 4. 0.
0. 0. 3. 3.
4 3

```

0. 2. 2. 0.
 4. 4. 4. 4.
 0. 0. 3. 3.
 2 3
 0. 0. 0. 0.
 0. 4. 4. 0.
 0. 0. 3. 3.
 4 3
 0. 2. 2. 0.
 0. 0. 4. 4.
 0. 0. 0. 0.
 2 4
 0. 2. 2. 0.
 0. 0. 4. 4.
 3. 3. 3. 3.
 2 4

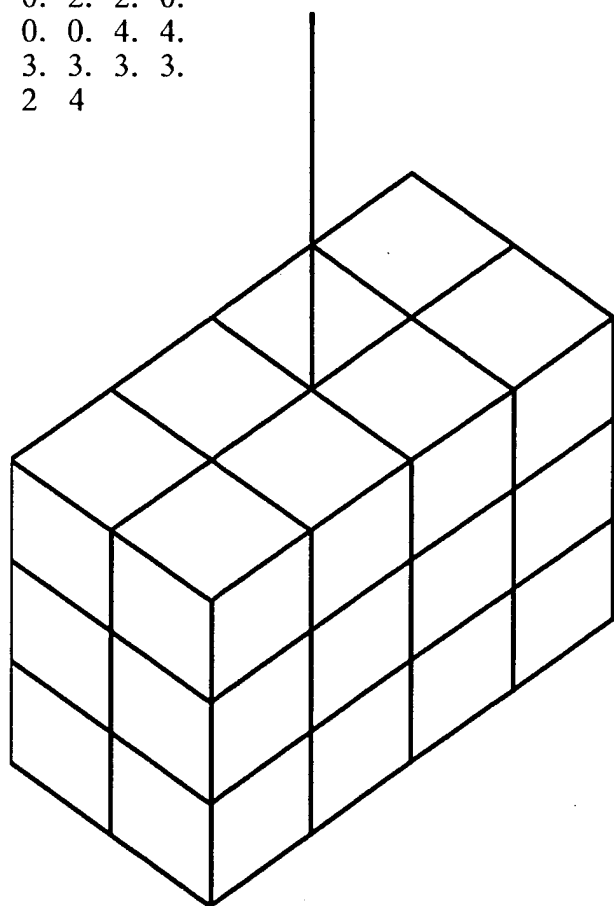


Fig. (3) Wire-grid of a rectangular box consisting of 104 elements and a monopole on top of it.

Only the monopole is added manually after the wire-grid has been generated. Fig. 3 is an isometric view of this simple structure. The second example in Fig. 4, is a pyramid with a trapezoidal base where triangular regions have been used. It consists of 5 regions and 157 elements.

The last example is more practical in that it is a wire-grid of a motor vehicle.

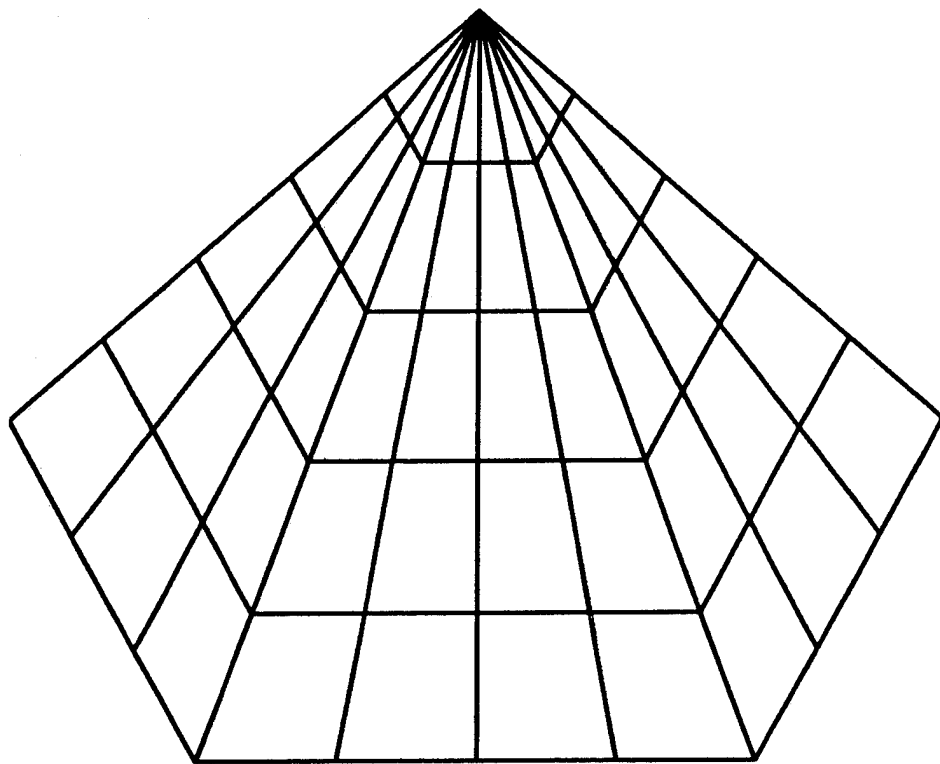


Fig. (4) Wire-grid of a pyramid with a trapezoidal base consisting of 5 regions and 157 elements.

All the body can be represented by flat surfaces except the pillars that support the roof. Because the number of elements where the regions' sides join needs to be the same, 14 regions were used to represent the vehicle body:

- 1 Region for the roof
- 1 Region for the bonnet (hood)
- 1 Region for the boot (trunk) top
- 1 Region for the front side
- 1 Region for the back side
- 3 Regions for the left side
- 3 regions for the right side
- 3 Regions for the bottom.

Fig. 5 shows the wire-grid of 270 elements that was produced by the mesh generator. In order to get the final model of the vehicle, the following steps were done manually:

- On each side of the vehicle, remove the two vertical elements marked x in Fig. 5; extend the wire marked y to the left so that it meets with the wire junction J in the adjacent region; and join the top of these two regions by adding a wire between points p1 and p2.

- Add the wires for the roof pillars.
- Increase the number of segments of the two roof elements marked z from 1 to 2 so that pillars join the roof at segment ends, as required by NEC.

The final model is shown in Fig. 6.

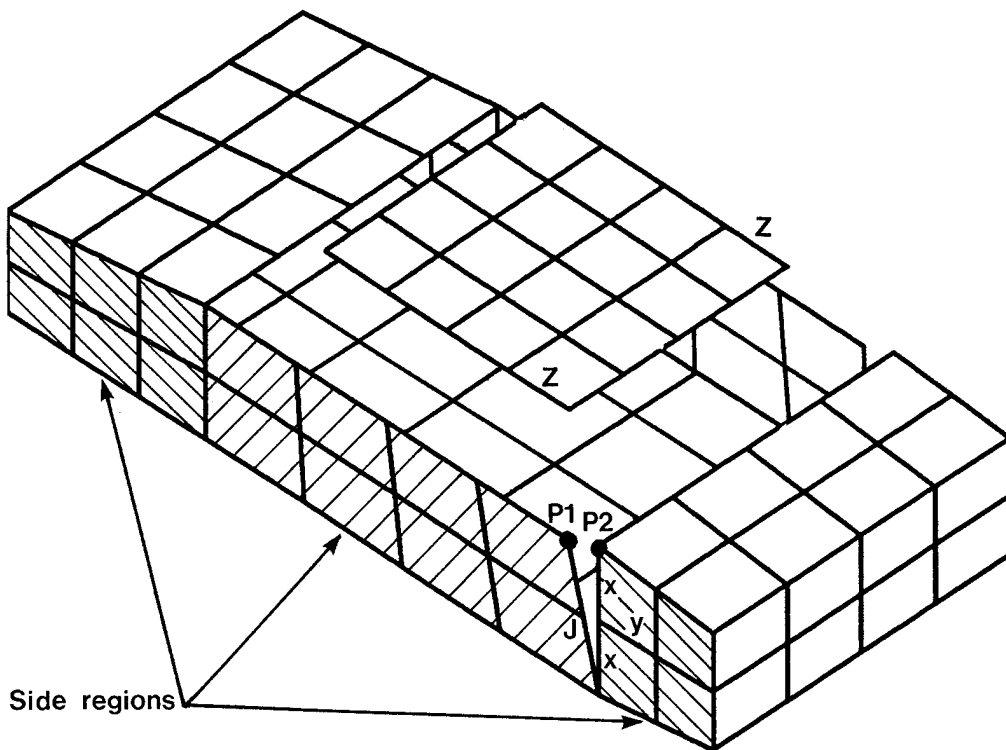


Fig. (5) Wire-grid of a motor vehicle as produced by the mesh generator. It consists of 14 regions and 270 elements.

Typical execution times for these three examples are shown in the table below. They were run using a VAX 11/780 and an 80386 IBM-PC with a coprocessor using the FTN77 compiler. Times shown are those taken to generate the NEC geometry file only without the information file.

Example	Run Time (sec.)	
	VAX	IBM-PC
Box	2.5	3.1
Pyramid	4.3	4.4
Vehicle	10.0	10.4

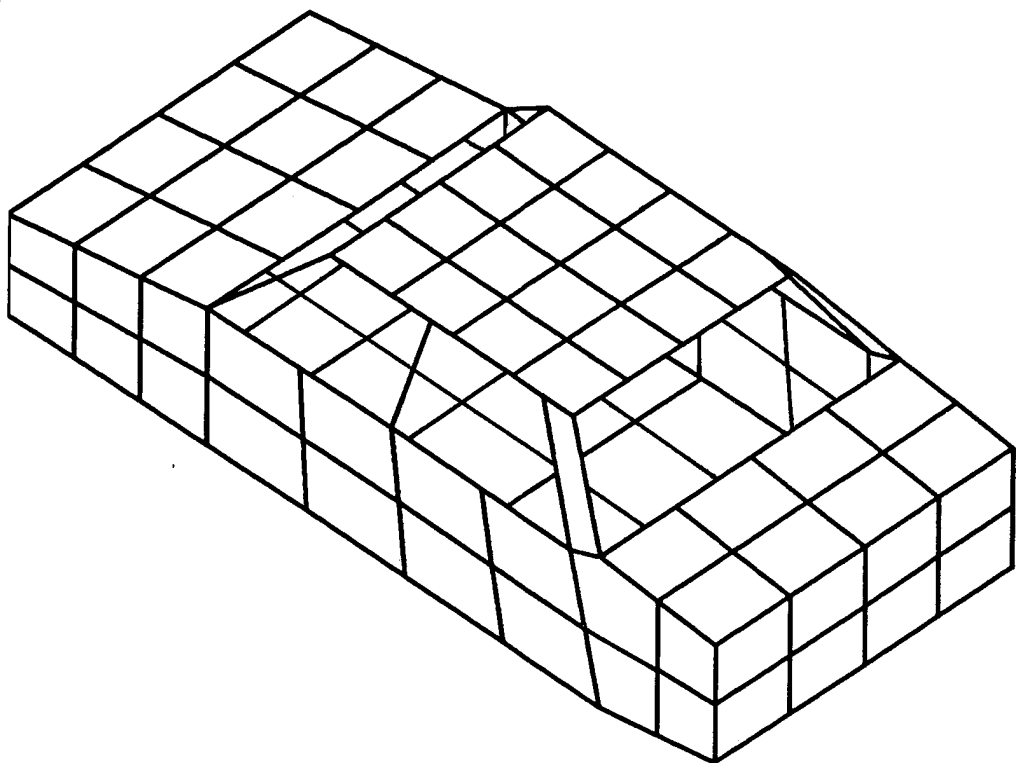


Fig. (6) Wire-grid of the motor vehicle after editing the generated model and adding the roof pillars.

6. Availability of the Software

The software for this mesh generator, including the source code and the input and output files for the examples mentioned above, are available from the author. A nominal fee of £5.00 (or an international money order for US\$10.00) is requested to cover duplication and postage. The software will be provided on a 3.5" MS-DOS 720K floppy disk. Hardcopy supplementary information will also be provided.

Acknowledgements

The author wishes to thank his colleagues M.S. Al-Din and K.P. Murray who have contributed in writing the code for this mesh generator.

References

1. Lochyer, A. and Tulythan, P., "PC Electromagnetic Workstation Good NEWS for ACES' NEEDS", 3rd Annual Review of Progress in ACES, Monterey, Calif., U.S.A., 1987.
2. Trueman, C.W. and Kubina, S.J., "Verifying Wire-Grid Model Integrity with Program 'CHECK'", ACES Journal Vol. 5, No. 2, Winter 1990.
3. Burke, G.J. and Poggio, A.J., "Numerical Electromagnetics Code - Method of Moments", Lawrence Livermore National Laboratory, Technical Document UCID- 18834, Calif., U.S.A., January 1981.
4. Moore, J. and Pizer, R., Moment Methods in Electromagnetics, Research Studies Press, 1986.
5. Ludwig, A.C., "Wire-Grid Modelling of Surfaces", IEEE Trans. on Antennas and Propagation Vol. AP-35, No. 9, Sept. 1987.
6. Cox, J.W.R., "Comparison of Predicted Aircraft Wire Antenna Terminal Impedance (Using NEC) With Measurement in the HF Band", International Conf. on Antennas and Propagation ,ICAP-91, York, U.K., April 1991. IEE Pub. No. 333, Vol. 2, pp. 717-720.
7. Nishikawa, K., "Effect of Automobile Body and Earth on Radiation Patterns of Antennas for FM Radio", Trans. of the IECE of Japan Vol. E-67, No. 10, October 1984.
8. Oyekanmi, L.A. and Watkins, J., "Selecting Wire Radius for Grid/Mesh Models", ACES Journal Vol. 5, No. 2, Winter 1990.
9. Beyer, W.H., ed., Standard Mathematical Tables, 24th Edition, CRC Press, Cleveland, U.S.A., 1976.
10. The Numerical Electromagnetic Engineering Design System, "NEEDS", User's Guide, version 1.0, February 1988. Distributed by ACES.

THE SHORT FAT DIPOLE
Development in APL of a MoM Solution

Douglas B. Miron
EE Dept., Box 2220
South Dakota State University
Brookings, SD 57007

Abstract

This paper describes an effort to find the best profile for a figure-of-revolution, center-fed, electrically-small dipole. It includes presentations on equation development, singularity treatment, code development, verification, and performance.

I. Prologue

The work described in this paper was undertaken to find a minimum-Q shape for an electrically-small dipole to operate over the HF band, 3-30 MHz. The starting point was the 1969 paper by Mautz and Harrington[1] on bodies of revolution. Their formulation for the integral equation and their expansion and testing functions were used without scaling. The dipole is driven only in the tangential direction, so it was assumed there are no ϕ -components to the current density. This simplified the problem considerably. There are numerous ways to handle the potential-function singularity. After trying a couple of others, subtraction of the electrostatic potential from the radiation potential function[2] was chosen. The electrostatic potential function is integratable in ϕ to a known special function, and that function is numerically integratable so that the singularity is expressed in the impedance-matrix elements in a stable way.

This paper is divided into the following sections:

- I. Prologue
- II. Geometry, the Basis Functions, and Counting
- III. The Integral Equation
- IV. Conversion to Discrete Form
- V. Verification
- VI. Impedance and Shape
- VII. Development Time vs. Execution Time
- Appendix APL Syntax, Symbols and Functions

One purpose of this paper is to demonstrate that programming in an interactive array-processing language (APL) makes the most efficient use of professional time. The Appendix briefly describes its basic syntax and lists the definitions of symbols and functions as used in this paper. Specific features are described as they are used in Sections II through IV. In Section V the work is tried by comparison with two classic results. In Section VI a search for a shape that gives an antenna Q close to

the theoretical minimum, $1/(\beta a)^3$ [3], is outlined. In Section VII the hardware-software performance issues are examined.

II. Geometry, the Basis Functions, and Counting

The dipole is symmetric and center-fed. It must fit in a 2 m cube and be easy to manufacture. It would be a good thing then, if its profile were made of connected straight-line segments. Figure 1 shows an example of a simple shape, along with some of the coordinates to be used in the calculations. All prospective shapes are to be figures of revolution about the z axis, with the feed gap at $z=0$. An x axis is necessary from which to define the rotational angle ϕ . Cylindrical radius ρ is used both for the shape description and in the calculations. The fundamental coordinate for integration is the tangential distance t , which runs from $t=0$ at $z=-1$ m to $t=t_m$ at $z=+1$ m, following the antenna's profile.

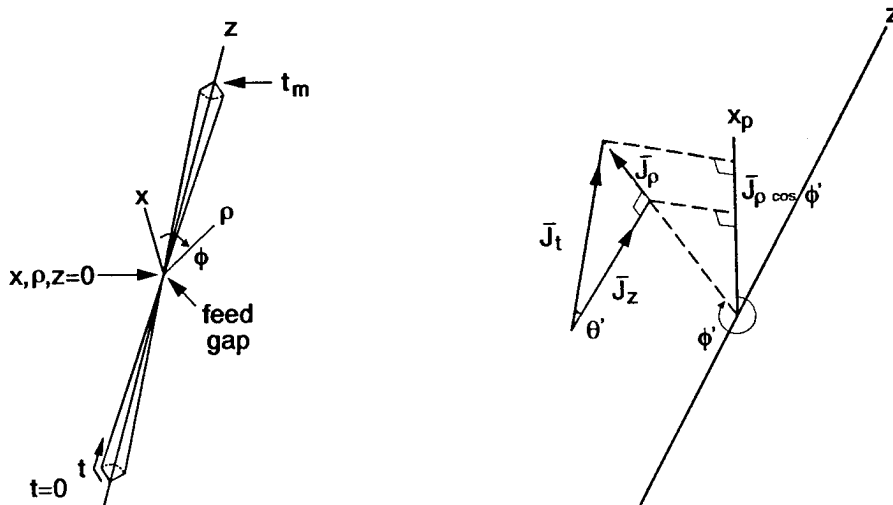


Figure 1. A representative dipole as a figure of revolution about the z axis.

Figure 2. x and z projections of a tangential vector. x_p is parallel to the x axis.

One must know the projection of the current density vector at one place onto the surface at another place, to calculate the vector magnetic potential and surface \vec{E} . Since the applied field is in the z direction, it is assumed there are no ϕ components of current or electric intensity. Figure 2 shows the components of \vec{J}_t projected onto the z and x axes.

$$J_\rho = J_t \sin\theta', J_z = J_t \cos\theta', J_x = J_t \sin\theta' \cos\phi' \quad (1)$$

For the purpose of doing a dot product with a unit tangential vector at the observation point, the last projection should be by way of $\cos(\phi-\phi')$, but the rotational symmetry allows $\phi=0$.

The triangle function was used as the basic element of the current expansion and weighting function series. The triangle, which is shown in Figure 3, was divided by $\rho(t)$ to make the complete scalar function. Since the integrals were discretized it was easier to denote the triangle by a subscript and deal with its relation to t through their counters, which is displayed in Figure 4. However, for the sake of the functional notation used in the next section, one may say that

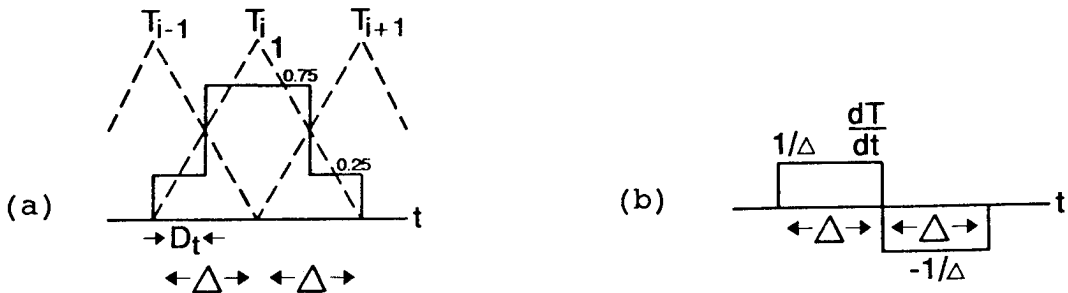


Figure 3. (a) Triangle function and a piecewise-constant approximation. (b) The derivative of a triangle function.

$$\bar{W}_i(t) = \bar{u}_t W_i(t) = \bar{u}_t \frac{T_i(t)}{\rho(t)} \quad (2)$$

where \bar{u}_t is a unit vector, \bar{W}_i are the vector basis functions, and their divergences are

$$\nabla \cdot \bar{W}_i = \frac{1}{\rho} \frac{dT_i}{dt} \quad (3)$$

The dipole can be described by assigning vectors of ρ and z values at the corners in the profile of the half-dipole. For example

RHD \leftarrow 0.01 1 0 \diamond ZD \leftarrow 0 0.9 1

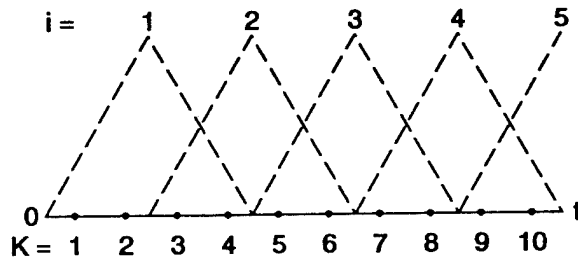


Figure 4. Relationship between the counter for t , $t_k = (k - \frac{1}{2})Dt$, and the triangle counter. T_i spans from $k=2i-1$ to $k=2i+2$.

describes a dipole which has a radius of 0.01 m at the feedpoint, cones out to a 1 m radius at $z=0.9$ m and cones in to a point at $z=1$ m. The full dipole description is formed by reversing ZD and RHD, negating the reversed ZD values, and attaching them to the originals.

$ZV \leftarrow (-\phi ZD), 0, ZD$ (4)

$RHV \leftarrow (\phi RHD), RHD[1], RHD$ (5)

The extra point in the middle is a convenience so the first z point doesn't have to be zero, and a straight pipe may be inserted before the shape takes off.

Figure 5 shows the basis for a scheme to generate the coordinate variables as functions of t . Since the profile is a straight line between corners, the values of ρ and z on a segment are displacements from their corner values which are $\sin\theta$ and $\cos\theta$ times the t displacement from $TC[K]$, where K is a corner counter. The nub of the scheme is to generate the TC vector, and then write a function to find the index of the last corner for a given t . The increase in t between corners is the length of the profile segment.

$TC[K+1] \leftarrow TC[K] + (((RHV[K+1] - RHV[K])^2) + (ZV[K+1] - ZV[K])^2)^{0.5}$

This expression could be put in a loop and stepped through to produce the vector TC . However, APL has a cumulative sum operator, ' $+\backslash$ ', and there are a couple of simple ways to generate the pairwise-difference of a vector. Here is one as a defined function.

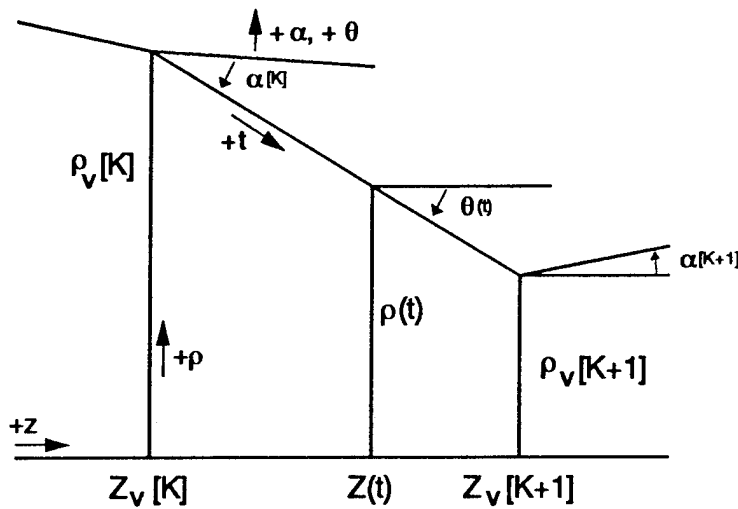


Figure 5. Illustration of a piecewise-linear antenna profile section. z and t increase to the right, ρ increases upward, α and θ are positive ccw.

∇ DIFF[\square] ∇

[0] $Z \leftarrow$ DIFF X
 [1] $Z \leftarrow (1 \downarrow X) - 1 \downarrow X$ (6)

Now the expression for TC is written

$TC \leftarrow 0, +\sqrt{((\text{DIFF RHV})^2 + (\text{DIFF ZV})^2) * 0.5}$ (7)

For a single value of t , one way to find the index of TC just left of t is to compare the value with TC. $TC < T$ will produce a Boolean vector with 1 for each corner up to the nearest one on the left of T , and 0 for the rest. The index value for the corner wanted is the sum of these 1s, $+\text{TC} < T$. To do this for a vector of t values, the outer product operator can be used. $TC^{\circ} \cdot <, T$ takes each value of TC and compares it to all the values in T , producing a row in the result. The result has as many columns as there are elements in T and as many rows as there are elements in TC. The ',' next to T makes a vector of a single-valued T . To get the index values now it is necessary to sum down the columns of the Boolean matrix. These steps are put in a defined function called REGION.

```

VREGION[ ]V
[0] S←REGION T
[1] S←+TC°.<,T

```

(8)

In this function TC is used as a global variable, T and S are local variables through which data is passed into and out of the function.

For the purpose of numerical integration, the profile of the antenna, which is the range of t, is divided into increments of Δ and Dt as in Figure 3. The center of the dipole has to be a center point for an expansion function and a boundary for a Δ segment. Let NP be the number of Δ segments in the half-dipole.

$$DEL←TC[\rho TC]÷2×NP \text{ and } DT←DEL÷2 \quad (9)$$

NP is also the number of unique current coefficients, so it is quite important later on.

Finally, $\beta=2\pi/\lambda$ ($BT←\omega^2÷LAMBDA$) and β^2 ($BS←BT×BT$) are important values in the calculations because β measures the intervals in wavelength. LAMBDA serves as a global variable to hold λ .

III. The Integral Equation

IIIA Field Theory

The antenna is a closed, perfectly-conducting (initial assumption) surface so that the currents flowing on it and the applied voltage must produce tangential E fields that add to zero. The field due to the surface currents is

$$\bar{E}^s(\bar{r}) = -\int_0^{t_m} \int_0^{2\pi} \left[j\omega\mu\bar{J}(t') g(R) - \nabla g(R) \frac{\nabla' \cdot \bar{J}(t')}{j\omega\epsilon} \right] \rho' d\phi' dt' \quad (10)$$

The distance function is

$$R = \sqrt{\rho'^2 - 2\rho\rho' \cos(\phi - \phi') + (z - z')^2} \quad (11)$$

and the propagation function is

$$g(R) = \frac{e^{-j\beta R}}{4\pi R} \quad (12)$$

The δ -gap source model was used so the incident \mathbf{E} is

$$\mathbf{E}^i(\mathbf{r}) = \bar{u}_z V_o \delta(z) \quad (13)$$

and the boundary condition requires that (13) equal the negative of the tangential component of (10). This would be an ill-conditioned integral equation on several counts, but MoM smooths it out somewhat by multiplying both sides by a weighting, or averaging, function and then integrating the products over the surface of the antenna. Using a set of vector weighting functions and the vector dot product (inner product) also picks out the tangential component on each side. Representing a weighting function by

$$\bar{W}(t) = \bar{u}_t W(t) \quad (14)$$

the smoothed equation becomes

$$\int_0^{t_m} \int_0^{2\pi} \bar{W} \cdot \bar{E}^i \rho d\phi dt = \int_0^{t_m} \int_0^{2\pi} \int_0^{t_m} \int_0^{2\pi} j\beta \eta_o \left[\bar{W}(t) \cdot \bar{J}(t') g(R) + \bar{W}(t) \cdot \nabla g(R) \frac{\nabla' \cdot \bar{J}(t')}{\beta^2} \right] \rho' d\phi' dt' \rho d\phi dt \quad (15)$$

Again, from symmetry there are no ϕ -components to the sources or fields, so the left side integrates to

$$2\pi \rho(t_m/2) W(t_m/2) V_o$$

The first dot product on the right can be represented by the unit vectors involved,

$$\bar{u}_t \cdot \bar{u}_{t'} = \cos\theta \cos\theta' + \sin\theta \sin\theta' \cos(\phi - \phi') \quad (16)$$

from Figure 2 and the discussion around equation (1). The second dot product involves the gradient of $g(R)$, which is already a singular function. Although a second-order singularity can be handled [4,5], Harrington and Mautz [1] used the fact that the body is a closed surface to replace the integral of $\bar{W}(t) \cdot \nabla g(R)$ in an integration by parts with $-g(R) \nabla \cdot \bar{W}(t)$.

R and the unit-vector dot product involve $\cos(\phi - \phi')$. These are the only rotational terms, so they were collected and the angle integrals done first. Because the functions really depend on the difference between the two angles, if one integrates with respect to one angle, the dependence on the other disappears. The ϕ -dependent terms can be collected in two integral functions as

$$G_0 = 2\pi \int_0^{2\pi} g(R) d\phi = \int_0^{\pi} \frac{e^{-j\beta R}}{R} d\phi \quad (17)$$

and likewise

$$G_1 = \int_0^{\pi} \cos\phi \frac{e^{-j\beta R}}{R} d\phi \quad (18)$$

Collecting all these substitutions brought the integral equation to

$$\frac{\rho(\frac{t_m}{2})W(\frac{t_m}{2})V_0}{j60\beta} = \int_0^{t_m} \int_0^{t_m} \{W(t)J(t')(\cos\theta(t)\cos\theta(t')G_0 + \sin\theta(t)\sin\theta(t')G_1) - G_0 \nabla \cdot W(t) \nabla' \cdot J(t')/\beta^2\} \rho \rho' dt' dt \quad (19)$$

IIIB The Integrals in ϕ

G_0 and G_1 hold the integrations in ϕ , which must be done before the outer integrals in t and t' . They also hold the $1/R$ singularity. There must be some advantage to the rotational symmetry besides the simplicity of the setup, perhaps it would be in the evaluation of these integrals. At first, writing

$$\beta R = \beta(R - R_0) + \beta R_0, \quad R_0^2 = \rho^2 + (z - z')^2$$

was tried, R_0 being the distance to the axis under the source point. For $\beta(R - R_0) < 1$ a few terms in the exponential series were used, which then led to terms involving elliptic integrals of the three kinds. While this was educational, and some errors in [6] were found, the result was rather complex and slow. An interesting discovery was that, away from the singularity, it is faster to compute the integral by the piecewise-constant series approximation than to use the polynomial-and-log approximation from [7]. The speed crossover was at 20 terms in the series for six-figure accuracy.

The next approach tried was an old one used recently by Simpson, et. al. [2]. They split the exponential instead of βR .

$$\frac{e^{-j\beta R}}{R} = \frac{1}{R} + \frac{e^{-j\beta R} - 1}{R} \quad (20)$$

This method removes the singularity from the propagation function to a static function which integrates to elliptic integrals. These two parts can be thought of as the circuit-element part and the radiation part, concepts which are explored in [2]. Define

$$G_{0E} = \int_0^\pi \frac{1}{R} d\phi \quad (21)$$

$$G_{1E} = \int_0^\pi \frac{\cos\phi}{R} d\phi \quad (22)$$

$$G_{0\omega} = \int_0^\pi \frac{e^{-j\beta R} - 1}{R} d\phi \quad (23)$$

$$G_{1\omega} = \int_0^\pi \frac{e^{-j\beta R} - 1}{R} \cos\phi d\phi \quad (24)$$

One can find the elliptic-function version of G_{0E} either by a succession of substitutions or from [6] as

$$G_{0E} = \frac{2}{\sqrt{a+b}} K(r) \quad (25)$$

with $a = \rho^2 + \rho'^2 + (z-z')^2$, $b = 2\rho\rho'$ and $r^2 = \frac{2b}{a+b}$

$K(r)$ is the complete elliptic integral of the first kind whose defining equation is

$$K(r) = \int_0^{\pi/2} \frac{dx}{\sqrt{1-r^2 \sin^2 x}} \quad (26)$$

Using the same substitutions and the redundancy[8]

$$\sin^2 z = \frac{1}{r^2} - \frac{1}{r^2}(1-r^2 \sin^2 z) \quad (27)$$

provides

$$G_{1E} = \frac{2}{r^2 \sqrt{a+b}} [2K(r) - 2E(r) - r^2 K(r)] \quad (28)$$

$E(r)$ is the complete elliptic integral of the second kind, defined by

$$E(r) = \int_0^{\pi/2} \sqrt{1-r^2 \sin^2 x} dx \quad (29)$$

No closed-form or special-function versions for $G_{0\omega}$ and $G_{1\omega}$ were found, but the integrands are smooth and well-behaved so they were simply approximated by the same piecewise-constant interval integration as used by MoM.

IIIC The Singularity

The development in IIIB moved from the static potential function, which has a $1/R$ singularity through the integration in ϕ to the elliptic integrals. [7] gives a quite accurate approximation which explicitly includes a logarithm which goes to infinity when $r \rightarrow 1$, which occurs when $t' = t$. For $t - t'$ small compared to ρ the argument of the approximation is proportional to $t - t'$, so the approximation can be integrated analytically. However, there are other functions which multiply the G_s , and $t - t'$ is not necessarily small compared to ρ over the interval in the discrete approximation to the integrals.

The basic approach by MoM to solving equation (20) is to break up the integrals into sums, each term of which approximates the integral over a small interval by the product of the interval length and the integrand's value at the center of the interval. This is the piecewise-constant approximation. The question then is, what value should be used to represent the G functions for intervals in which $t' \rightarrow t$? Working the charged-cylinder electrostatic problem[9, 10] showed that displacing the source and observation points by a small amount compared to the interval size gave a result independent of this displacement, once it was small enough, as far as plots of the charge density were concerned. In the present case, the results were poor for small NP , even having sign errors in the terminal impedance. Apparently the singularity was over-represented. The next best choice seemed to be to use the average value of each G function, which means numerically integrating them over the interval since no analytical integration was available. Reference [7] provided some formulas and values for functions with a logarithmic singularity. The numerical approximation has the form

$$\int_0^1 f(x) \log(x) dx \approx \sum w_i f(x_i) \quad (30)$$

where w_i and x_i are given in tables for various numbers of samples per interval. The form needed was

$$IG = \int_{-\delta}^{+\delta} G(y) dy = 2 \int_0^\delta G(y) dy \quad (31)$$

since G is even in y . If $y = \delta x$, then the upper limit becomes 1,

$$IG = 2 \int_0^1 G(\delta x) \delta dx \quad (32)$$

To use (30), $f(x) = G(\delta x)/\log(x)$,

$$IG \approx 2 \delta \sum w_i \frac{G(\delta x_i)}{\log(x_i)} \quad (33)$$

The problem at hand was to integrate over a Dt interval with respect to t' when t is at the interval center. y corresponds to $t'-t$, δ to $Dt/2$. The variables in the G functions were expressed as functions of ρ , ρ' , z and z' , so they were re-expressed in terms of $t'-t$, ρ and $\sin\theta(t)$. This was made possible by assuming t' and t are on the same profile segment. The geometry of this assumption gives

$$(\rho - \rho')^2 + (z - z')^2 = (t' - t)^2 \quad (34)$$

$$\rho' = \rho + (t' - t) \sin\theta \quad (35)$$

so that

$$a = (t' - t)^2 + 2\rho(\rho + (t' - t) \sin\theta) \quad (36)$$

$$b = 2\rho(\rho + (t' - t) \sin\theta) \quad (37)$$

$$a+b = (t' - t)^2 + 4\rho(\rho + (t' - t) \sin\theta) \quad (38)$$

$$a-b = (t' - t)^2 \quad (39)$$

$$m = 1 - r^2 = \frac{a-b}{a+b} = \frac{(t' - t)^2}{a+b} \quad (40)$$

m is the most convenient variable in which to express the elliptic integral approximations.

IV Conversion to Discrete Form

IVA Using MoM

On examining equation (20), one can see that each weighting function is multiplied by a ρ and each occurrence of the current density is multiplied by a ρ' . Furthermore, the first derivative of both functions is required. It makes good sense, in hindsight, that Mautz and Harrington[1] chose to represent both functions as a series of basis functions having a first derivative and being a simple function divided by ρ . The weighting functions are

$$\bar{w}_i(t) = \bar{u}_{ti} \frac{T_i(t)}{\rho(t)}, \quad 1 \leq i \leq N \quad (41)$$

The surface current density is

$$\bar{J}(t') = \sum_{k=1}^N \bar{u}_{t'k} J_{tk} \frac{T_k(t')}{\rho(t')} \quad (42)$$

One can show, by taking the textbook approach of sketching a differential-sized box on the antenna surface and applying the definition of divergence as a Gauss's Law limit, that

$$\nabla \cdot \bar{W}_i = \frac{1}{\rho} \frac{\partial (\rho W_i)}{\partial t} = \frac{1}{\rho} \frac{dT_i}{dt} \quad (43)$$

and

$$\nabla' \cdot \bar{J} = \sum_{k=1}^N J_{tk} \frac{1}{\rho'} \frac{dT_k}{dt'} \quad (44)$$

There can easily be a notation and counting confusion because the value of t at the middle of a triangle is never actually used in the integral computations. It is simpler to express the integrals, though, using this value, so let it be τ_i for triangle T_i . Then, since the triangle functions are nonzero over a 2Δ domain the integrals are shortened up. The application of each weighting function to equation (20) generates a separate equation, the full sequence produces a set of N equations for the $N J_t$ amplitudes.

$$\frac{T_i(\frac{t_m}{2}) V_0}{j60\beta} = \sum_{k=1}^N J_{tk} \int_{\tau_i - \Delta}^{\tau_i + \Delta} \int_{\tau_k - \Delta}^{\tau_k + \Delta} \left\{ T_i(t) T_k(t') (\cos\theta \cos\theta' G_0 + \sin\theta \sin\theta' G_1) \right. \\ \left. - \frac{G_0}{\beta} \frac{dT_i(t)}{dt} \frac{dT_k(t')}{dt'} \right\} dt' dt, \quad 1 \leq i \leq N \quad (45)$$

The left-hand sides of this equation sequence are zero except for $i=NP$ because only that triangle function is nonzero at $t_m/2$. The results of the double integration on the right-hand sides are functions only of i and k , so they can be symbolized by the standard Z_{ik} .

$$V_i = \sum_{k=1}^N J_{tk} Z_{ik}, \quad 1 \leq i \leq N \quad (46)$$

IVB Preparing the Way; Geometry

The function values needed in each Z_{ik} , $\sin\theta$, T_i , etc., are used over and over again, so it doesn't pay to recompute them each time. The basic strategy was to precompute them as vectors and matrices, and call the needed data by their indices during the Z element calculation.

APL provides a function to generate a vector of index values, ' $_i$ '. Any set of values which can be written as a function of an index can be generated as a vector, making a loop, with its repetitive interpretation, unnecessary. One can generate a function of any number of indices by using the outer product operator with the individual index vectors which will produce an array with as many axes as there are index variables. While this is quick to execute, large temporary outer products

can eat up storage to the point where there isn't enough, which will generate a WS FULL (WS for workspace) error message.

The vectors and static G functions are calculated in a function SGENERATE.

```
[0] SGENERATE;K;T;THT;L;T1;N1;N2
```

All the variables in the header are local.

```
[1] T1←0 TS ◇ N1←2×NP ◇ N2←4×NP
```

```
[2] ZT←ZA T←DT×`0.5+LN2 ◇ RHT←RHO T ◇ THT←TH T ◇ COST←2oTHT
    ◇ SINT←1oTHT
```

Remember that the interpreter works from right to left in a statement. The statements in a line are executed starting with the leftmost one. The first statement in line [2] starts by generating a vector of integers from 1 to N2, then adds .5 to these integers, then multiplies them by DT and assigns the result to T, which is the vector of t values used in all subsequent functions. The T is also an input argument to a function ZA which calculates the corresponding vector of z(t) values, ZT. The next two statements in line [2] calculate ρ(t) and θ(t) vectors, RHT and THT. All three of these functions use the simple segment geometry and the function REGION (6). The next two statements in line [2] produce cosθ and sinθ using the circle function with a left argument to indicate which of the 15 transcendental functions is wanted.

```
[3] TRT←(1 3 3 1)÷4 ◇ DTRT←(1 1 `1 `1)÷DEL
```

These are vectors to hold the sample values of the triangle function and its derivative.

```
[4] G0←G1←(N1,N2)ρ0 ◇ K←1
```

G0 and G1 are matrices which hold the static potential integrals G_{0E} and G_{1E} . These matrices must be symmetric about their main diagonal, regardless of the geometry of a problem, and they are also symmetric about a line between rows N1 and N1+1 because of the geometric symmetry of the dipole. Use was not made of the diagonal symmetry because of the complexity of the indexing required. The row symmetry was used.

```
[5] (LN1) REALGREEN LN2 ◇ k←1
```

REALGREEN is a function which calculates the values for the static G functions and puts them in the arrays G0 and G1. Its input arguments are sets of row and column indices. The workings of REALGREEN and IG will be discussed below.

```
[6] GL:L←IG RHT[K],SINT[K] ◇ G0[K;K]←L[1] ◇ G1[K;K]←L[2]
    ◇ →(N1≥K←K+1)/GL
```

This is a one-line loop to replace the diagonal elements of G0 and G1 with the average values of G_{0E} and G_{1E} on the intervals where they are singular. The calculation on these intervals in REALGREEN were prevented from overflow by replacing zeros of m with $1E^{-50}$. It would have been more efficient to send the results directly to G0 and G1 inside IG, but it was left in its development form which gives an explicit result.

```
[7] G0←G0,[1]ΦG0[N1+1-13;] ◇ G1←G1,[1]ΦG1[N1+1-13;]
```

Not all the possible values of G0 and G1 are ever used. Again because of geometric symmetry, there are only NP unique values of J_{tk} , so only NP equations are needed. The expression N1+1-13 generates a vector N1, N1-1, N1-2 which picks these three rows out of the matrix. No column index is specified so the whole row is taken. This three-row block is then reversed end-for-end, and attached to the original matrix under its columns, making the result a 2NP+3 by 4NP array.

```
[8] (+/0 0 0 3600 60 1 1E-3×OTS-T1) 'SEC, STATIC G0 AND G1.'
```

This line calculates and displays the elapsed time in seconds. The mixture of numeric and character data in a vector is a feature of APL2. In standard APL the number would have to be converted to characters to be displayed in the same vector.

```
[9] DSOUND SCALE,[1.5]100
```

This line plays an ascending C major scale to get the user's attention when the function is finished executing.

IVC Preparing the Way; Potential Integrals

REALGREEN is so named because its results are Green's functions of a sort.

```
[0] OX REALGREEN SX;A;B;SQAB;M;K;E
```

OX and SX stand for observation-point indices and source-point indices, respectively. These are the input arguments, the other variables listed in the header are local to the function and named to correspond to variables in (25) and (28). $SQAB=\sqrt{a+b}$.

```
[1] B←2×RHT[OX]°.×RHT[SX] ◇ AB←RHT[OX]°.+RHT[SX]
    ◇ A←ZT[OX]°.-ZT[SX]
```

In each of the statements in line [1] the generalized outer-product operator forms a matrix of all combinations of the left argument elements with the right argument elements, with the arithmetic function placed between them. B has as many rows as there are values in OX and as many columns as values in SX, and each element of B is $2\rho(t_i)\rho(t_k) = 2\rho\rho'$. Each element of AB is $\rho+\rho'$, and each element of A is $z-z'$.

[2] $AB \leftarrow (A \times A) + AB \times AB \quad \diamond \quad A \leftarrow 0\rho 0 \quad \diamond \quad M \leftarrow 1E^{-50} + ZERO \quad 1 - 2 \times B \div AB$

The first statement forms a matrix of $a+b$ values. The second statement reduces A to an empty vector to reduce storage. The third statement calculates an array of m values, defined in (40), as an argument for the elliptic integrals in the next line. The function ZERO replaces each number whose magnitude is less than $1E^{-14}$ by zero.

[3] $K \leftarrow (AE1 \text{ MPOLY } M) - (\text{@M}) \times BE1 \text{ MPOLY } M \quad \diamond \quad E \leftarrow (AE2 \text{ MPOLY } M) - (\text{@M}) \times BE2 \text{ MPOLY } M$

MPOLY is a function whose left argument is a vector of polynomial coefficients. It evaluates the polynomial for each element in M and returns the results in the same shape as M. AE1, BE1, AE2, and BE2 are the coefficients in the polynomial-and-log approximations for the elliptic integrals given in [7 p591-592, 5 terms]. @M gives the natural log of the values in M.

[4] $G0[OX;SX] \leftarrow 2 \times K \div SQAB \leftarrow AB * 0.5$
 $\diamond \quad G1[OX;SX] \leftarrow (2 \div B) \times (K \times (AB - B) \div SQAB) - E \times SQAB$

Line [4] expresses and assigns the blocks of element values to the indexed parts of G0 and G1. The first statement is a direct copy of (25). The second statement is a reworking of (28) to minimize the number of variables holding intermediate data.

REALGREEN called its geometry values by indexing the previously-constructed vectors for ρ and z . The average value for each G function over a singular interval requires that t' values be calculated within the interval for the integration formula, and the G functions evaluated at these t' values. Therefore one can't use REALGREEN and some of the same statements must be rewritten. This is done in the function IG.

[0] $Z \leftarrow IG \ Y; X; K; E; A; B; AB; SQAB; XQ; M$

Z and Y are output and input arguments for the function, each a two-element vector as can be seen from its use in line [6] of SGENERATE. The local variables listed in the header mostly have the same uses as they do in REALGREEN.

```
[1] X←GIX×DT÷2 ◇ XQ←X×X ◇ B←2×Y[1]×Y[1]+X×Y[2]
    ◇ AB←XQ+2×B ◇ A←XQ+B
```

GIX is a vector holding the tabulated x_i values from [7 p920, n=4]. DT÷2 is the half-interval scale factor to convert the x_i to $t'-t$ values. The statement for B is a copy of (37), letting execution order take care of the parentheses. AB is (38). A is (36). These are all four-element vectors.

```
[2] M←XQ÷AB ◇ K←(AE1 MPOLY M)−(0M)×BE1 MPOLY M ◇ SQAB←AB*0.5
```

M is (40) again, and K and SQAB are as in REALGREEN.

```
[3] E←(AE2 MPOLY M)−(0M)×BE2 MPOLY M ◇ Z←2×+/GIW×K÷SQAB×LGX
```

GIW is a vector holding w_i values and LGX is a vector holding $\log(x_i)$ values. '+/' does the summation so now Z holds the average of G_{0E} over a particular interval for which it is singular.

```
[4] Z←Z,2×+/GIW×((A×K÷SQAB)−SQAB×E)÷B×LGX
```

Line [4] calculates the average for G_{1E} and catenates it with Z to form the new Z which the function passes out as the explicit result. The 2δ in (33) doesn't appear in this function because (33) is the integral, not the average. The average is the integral divided by 2δ .

The complex G functions, G_{0w} and G_{1w} (23,24), are initialized, collected and timed in a function WGENERATE which is nearly identical to SGENERATE. The results are held in arrays G0C and G1C. The actual integrations are done by the function CMPLXGREEN.

```
[0] OX CMPLXGREEN SX;N;DA;ANG;R;CR;SR
```

```
[1] N←15 ◇ DA←0÷N ◇ ANG←20DA×0.5+iN
    ◇ R←(RHT[OX]×RHT[OX])°.+RHT[SX]×RHT[SX]
```

The integration in ϕ is done by the piecewise-constant approximation. N is the number of intervals between 0 and π , and DA is the interval length. ANG is the vector of cosine values for the centers of these intervals. R, in this line, is a matrix of all the possible $\rho^2+\rho'^2$ values specified by the OX and SX index vectors.

```
[2] R←R+(ZT[OX]°.-ZT[SX])*2
    ◇ R←(((N,ρR)ρR)-2×ANG°.×RHT[OX]°.×RHT[SX])*0.5
```

The last statement in line [1] and these two statements are a three-step construction of all the possible values of the distance function required by the index vectors OX and SX and the steps in ϕ . Coming into line [2] R has all the $\rho^2 + \rho'^2$ values, and the first statement adds all the $(z-z')^2$ values. Starting at the right of the second statement in line [2], the $()^{*}0.5$ will take the square root of all the elements sent to the outer parentheses. Just inside the right parenthesis $\rho\rho'$ is done as an outer product to form a matrix the same shape as the current value of R. This matrix is then outer-product multiplied by the $\cos\phi$ values in ANG to form a 3-axis array. The first axis corresponds to the steps in ϕ , the other two to the index values in OX and SX. This array is next multiplied by 2 to give the $2\rho\rho'\cos\phi$ part of the distance function. Now a copy of the present value of R needs to be generated for each step in ϕ so the subtraction part can be properly done. $(N, \rho R)\rho R$ makes a 3-axis array out of the $\rho^2 + \rho'^2 + (z-z')^2$ values with N identical copies along the first axis.

```
[3] G0C[;OX;SX]←DA×(+/CR←(`1+2oBT×R)÷R), [0.5]+/SR←(1oBT×R)÷R
[4] ANG←Q((ΦρR)ρANG) ◇ G1C[:OX;SX]←DA×(+/ANG×CR), [0.5]+/ANG×SR
```

$e^{-j\beta R}$ is represented in rectangular form as $\cos(\beta R)$ ($2oBT \times R$) and $-\sin(\beta R)$ ($-1oBT \times R$). The imaginary and real parts are separately formed and summed down the first axis (the ϕ steps) and lastly multiplied by DA to complete the integration. The first statement in line [4] reshapes the $\cos\phi$ vector into a 3-axis array to match the other items in the integrand of $G_{1\omega}$.

The reader may feel that these are compact (a good thing) and formidable bits of code. They are to the developer too. They were developed by using vectors with a few elements each to test the operations and see that they worked out to the shapes needed. If an operation works for little vectors, it will work for any.

IVD Filling the Impedance Matrices

Following Simpson's path, the Z_{ik} matrix was split into circuit-element and radiation parts.

$$Z_{ik} = L_{ik} + \frac{S_{ik}}{\beta^2} + Z_{wik} \quad (47)$$

The L and S matrices depend strictly on geometry with no frequency component, so that once they are computed for a given shape, they need not be recomputed. It actually costs more execution time to compute Z this way most of the time, but it was interesting to see the relative effects of the static and dynamic G functions.

$$L_{ik} = \int_{\tau_i - \Delta}^{\tau_i + \Delta} \int_{\tau_k - \Delta}^{\tau_k + \Delta} T_i T_k (G_{0E} \cos \theta \cos \theta' + G_{1E} \sin \theta \sin \theta') dt' dt \quad (48)$$

$$S_{ik} = - \int_{\tau_i - \Delta}^{\tau_i + \Delta} \int_{\tau_k - \Delta}^{\tau_k + \Delta} \frac{dT_i}{dt} G_{0E} \frac{dT_k}{dt} dt' dt \quad (49)$$

$$Z_{\omega ik} = \int_{\tau_i - \Delta}^{\tau_i + \Delta} \int_{\tau_k - \Delta}^{\tau_k + \Delta} \left\{ T_i T_k (G_{0\omega} \cos \theta \cos \theta' + G_{1\omega} \sin \theta \sin \theta') - \frac{dT_i}{dt} \frac{G_{0\omega}}{\beta^2} \frac{dT_k}{dt'} \right\} dt' dt \quad (50)$$

Again, two kinds of functions were written for these matrices, one to initialize them, set up loops, and time the calculations, and one to do the actual double integration given the i,k values.

[0] REACT;I;K;T1;NC

This function sets up the reactance matrices, L and S. They are called XGL and XGC respectively. The function also finds the terminal (circuit-element) reactance due to the static potentials.

[1] T1 ← TS ◇ I ← 1 ◇ XG ← XGL ← XGC ← (NP, NC ← 1 + 2 × NP) ← 0

[2] IL:K ← 1

These lines initialize the starting time, loop counters, and matrices. NC is the 'N' summation limit in (46), which is the number of equations and unknowns without taking account of the geometric symmetry.

[3] KL:XGL[I;K] ← LIK I, K ◇ XGC[I;K] ← SIK I, K
 $\diamond \rightarrow (NC^2 K^2 K + 1) / KL \diamond \rightarrow (NP^2 I^2 I + 1) / IL$

LIK and SIK are the functions that do the integrations.

[4] XGL ← ((NP, NP) ↑ XGL) + ← 0, (NP, 1-NP) ↑ XGL

[5] XGC ← ((NP, NP) ↑ XGC) + ← 0, (NP, 1-NP) ↑ XGC
 $\diamond XG ← XGL + XGC \div BS$

Here is where the symmetry in t is used to reduce the matrices to NP by NP . Suppose $NP=5$. Then $J_6=J_4$, $J_7=J_3$, $J_8=J_2$ and $J_9=J_1$. This implies that the columns to the right of 5 can be reversed in order and added to those to the left of 5. Only NP rows are calculated, with this reduction in mind. $NP,1-NP$ specifies NP rows and $NP-1$ columns from the right side of the matrix for the take (\uparrow) function. The 0, on the left will put a column of zeros on that side of the NP by $NP-1$ present result. The reverse flips the matrix side-to-side so the column of zeros lines up with column NP and column $NP+1$ of the original matrix lines up with column $NP-1$. The last step in the reduction process is addition to the left NP columns of the original matrix. XG is the total reactance matrix.

[6] $JT \leftarrow ((NP-1)\rho 0), \div 60 \times BT \times DT \times DT) \boxplus XG \diamond XTERM \leftarrow \div 02 \times JT[NP]$

JT is the vector of current density coefficients, J_{tk} . The V_i are $NP-1$ zeros, and a negative imaginary number, $-1 \div (60\rho Dt^2)$. The Dt was put with V_i to reduce the multiplies. Since V_i is imaginary and XG is real, JT is imaginary, as it should be. $V_o=1$, so the terminal reactance is

$$\begin{aligned} X_{term} &= \frac{1}{2\pi\rho \left(\frac{t_m}{2}\right) \frac{T_{NP} \left(\frac{t_m}{2}\right)}{\rho \left(\frac{t_m}{2}\right)} J_{tNP}} \\ &= \frac{1}{2\pi J_{tNP}} \end{aligned} \quad (51)$$

The next two lines of the function print the reactance, the run time, and sound the scale.

The integration functions have the same format, so only the more interesting LIK is described.

[0] $Z \leftarrow LIK\ IK; L; M$
[1] $L \leftarrow P + 2 \times IK[1] \diamond M \leftarrow P + IK[2]$
[2] $Z \leftarrow ((TRT \times SINT[L]) + . \times G1[L; M] + . \times SINT[M] \times TRT) +$
 $(TRT \times COST[L]) + . \times G0[L; M] + . \times COST[M] \times TRT$

P is a global vector whose elements are 1 0 1 2. This makes L and M the set of t and t' indices needed for the four-point integration, as shown in Figure 4. The appropriate portions of the $G0$ and $G1$ matrices are called as 4×4 matrices. Each one is then the center matrix in a vector-matrix-vector multiply (inner product) to do the double sums. That's it.

Another pair of functions, IMP and ZIK, organize and compute the elements for Z_w . The computation principle for the integration is the same as in LIK, but the complex numbers require a little more work in handling the shapes of the vectors and arrays. The reactance and impedance matrices are combined and the net terminal impedance computed in the function TERM.

IVE Current and Dissipation

Once the current density coefficients, J_{tk} , are known, the current at each sample point can be found by adding the appropriately-weighted triangle functions. The values of J_{tk} are held in the variable JTC, but only for half the dipole. To provide plots for the exercise of intuition, the current was extended for the whole dipole. All of the Δ segments have two triangles on them except the starting one at $t=0$ and the ending one at $t=t_m$. The total current is formed by generating a complex vector of coefficient values padded with 0 at the right end (t_m) to multiply by the first half of the triangle function, and another coefficient vector padded with 0 at the left end ($t=0$) to multiply by the second half of the triangle function, and then add the two.

$$ICX \leftarrow (JTC, (\phi \ 0 \ ^1 \downarrow JTC), 0 \ 0)^\circ \cdot x \text{TRT}[1 \ 2] \quad (52)$$

Since JTC is a complex vector (2-row matrix) the outer product produces a two-plate, or 3-axis, result. The first column of the first plate is 0.25 times the real parts, the second column of the first plate is 0.75 times the real parts, and the second plate is the corresponding imaginary parts of the current coefficient times 0.25 and 0.75.

$$RC \leftarrow (, ICX[1;:]), [0.5], ICX[2;:] \quad (53)$$

After extending JTC, there are $2NP$ by 2 elements in each plate of ICX. Raveling each plate takes the plate row-by-row and makes one $4NP$ -element row, every other element is 0.25 times a coefficient and its neighbor to the right is 0.75 times that same coefficient. Thus, each pair in a row is the left half of a triangle function times a current coefficient. The next statement reuses ICX to multiply the current coefficients by the right half of the triangle function, with an extra zero put in at the beginning. In (55) ICX is reformatted as above and the two sets are added.

$$ICX \leftarrow (0 \ 0, JTC, \phi \ 0 \ ^1 \downarrow JTC)^\circ \cdot x \text{TRT}[3 \ 4] \quad (54)$$

$$RC \leftarrow RC + (, ICX[1;:]), [0.5], ICX[2;:] \quad (55)$$

RC holds the surface-current density times the radius, because the complete basis function hasn't been used. To get the total current through a cross-section, just multiply RC by 2π .

$$IT \leftarrow 0.2 \times RC \quad (56)$$

One of the bane's of electrically-small antennas is that loss resistance can be higher than radiation resistance. One of the benefits expected from a thick dipole is a lower loss resistance due to spreading the current out over a large surface. Assuming that which is desired, the dissipation should have little effect on the current distribution, so one can use the current from the lossless equation to calculate the dissipation. The total dissipated power is

$$P = 2\pi \int_0^{\infty} R_s J_t J_t^* \rho dt \quad (57)$$

$$\text{with } R_s = \sqrt{\frac{\omega \mu_0}{2\sigma}} = \sqrt{\frac{360\pi}{\sigma}} \quad (58)$$

At this point in the programming, RC is $J_t \rho$, so magnitude squared of RC divided by RHT (ρ) is used instead of $J_t J_t^* \rho$.

$$P \leftarrow 0.2 \times DT \times ((0.60 \times BT \div SIGMA) * 0.5) \times + / (+ \not\div RC \times RC) \div RHT \quad (59)$$

V Verification

One cannot build a system of APL functions, any more than one can do a long mathematical development, test it only at the end, and hope to live without ulcers. Verification begins by testing the operation of each function on simple cases that can be verified by inspection, by hand calculation, or by looking up results in tables. Also, limiting values for large or small arguments are sometimes useful checks. Both the Green's function matrices and the impedance matrices (before folding) must be symmetrical. In earlier stages of this project, more of the work was done by completely separate functions, and there were more loops in the matrix-generating lines. This allowed easier testing of things like the elliptic integrals and their argument. Once some confidence was developed in results from these simpler functions, these results were kept for comparison, in separate workspaces, against results from more sophisticated versions.

The final tests are overall performance tests. Since we are approximating a continuous current distribution by a finite set of sample values, and using approximate integrations everywhere, we cannot expect perfect accuracy. We have a right to expect that the terminal impedance values will behave smoothly as a function of the number of sample points, and converge to some result. The slow convergence of the impedance values was, at

first, daunting. Reading about the similar experience of others [14, 15] gave a little morale boost. Although quite a number of test shapes were tried, with varying success, two are offered because they are shape extremes and are represented in the literature. These are the very thin wire dipole and the sphere dipole, both operated at half wavelength.

The classical impedance for a thin halfwave dipole is $73+j42.5 \Omega$. To describe this shape to the functions, set $RHD=1E^8 0$, $ZD=0.9999 1$. There was no difference in the results for the radius two orders of magnitude larger. The triangle basis function automatically sets the current at the dipole end to zero, and the difference between the two ZD values is much less than any integration segment used, so the result is a numerical model for a very thin straight wire. The ZD values couldn't be identical because a divide-by-zero error would occur. Because of experience in control systems and broadband rf electronics, convergence was originally tested by doubling NP from one trial to the next, later switching to a 2-5-10 sequence. The largest number which could be run without overfilling the workspace was $NP=150$. This corresponds to 600 sample points. Finally, $NP=5 10 20 50 100$ was settled on as the test values. The admittance values were then fitted by polynomials in $1/NP$. This course was taken because a polynomial in $1/NP$ goes to a constant value as $NP \rightarrow \infty$. Thus, if the solution values do converge, the polynomial-fit constants might be the right values. Table 1 shows the data and results for the thin dipole.

Table 1. Admittances for the Thin Halfwave Dipole, mS

NP	5	10	20	50	100	∞
G	11.05	10.13	9.823	9.709	9.7	9.713
B	-4.548	-5.071	-5.278	-5.42	-5.486	-5.568

$$G = 9.713 - 2.501NP^{-1} + 133NP^{-2} - 889.2NP^{-3} + 2270NP^{-4}$$

$$B = -5.568 + 9.077NP^{-1} - 99.66NP^{-2} + 772NP^{-3} - 1866NP^{-4}$$

$$Z_{\infty} = 77.49 + j44.42 \Omega$$

The spherical dipole profile has to be approximated by a sequence of straight-line segments. A five-segment model with equal subtended angles was chosen for the half-sphere so that the longest Δ value would fit between the corners. The generating statements are $ZD=0,1000.1\times15$ and $RHD=1,2000.1\times15$. The results for the same trial values and curve fitting are given in Table 2.

Table 2. Admittances for the Halfwave Sphere Dipole, mS

NP	5	10	20	50	100	∞
G	17.01	16.71	16.65	16.64	16.64	16.64
B	58.68	71.41	83.78	99.96	112.2	130.1

$$G = 16.64 - 0.1826NP^{-1} + 5.024NP^{-2} + 47.95NP^{-3} - 112.1NP^{-4}$$

$$B = 130.1 - 2119NP^{-1} + 3.592E4NP^{-2} - 2.764E5NP^{-3} + 7.043E5NP^{-4}$$

$$Z_\infty = 0.9673 - j7.563 \Omega$$

The polynomial coefficients give an indication of the rate of convergence, if it exists. The sphere represents two extremes, a case where convergence has already occurred, and a case for which it is doubtful. NP has to go over 2000 to drive the variable terms below 1 mS for B. For the thin dipole, NP=200 drives the variable part of B below 1 % of the constant, and NP=25 will do the same for G.

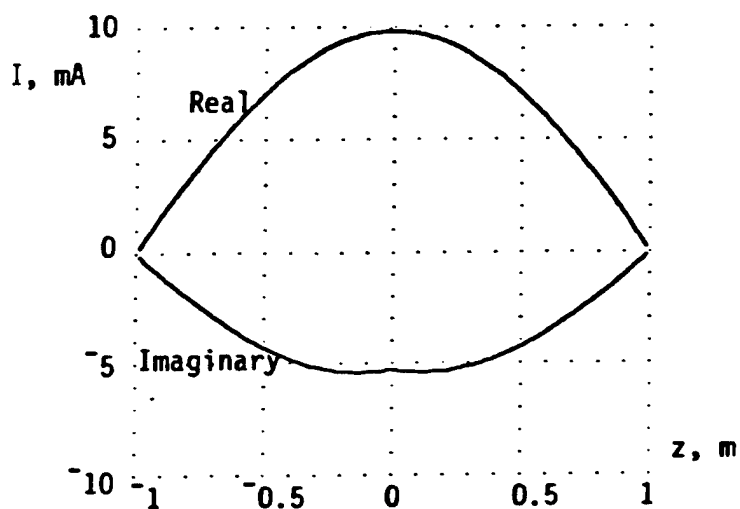


Figure 6. Cross-sectional current along the half-wave thin dipole.

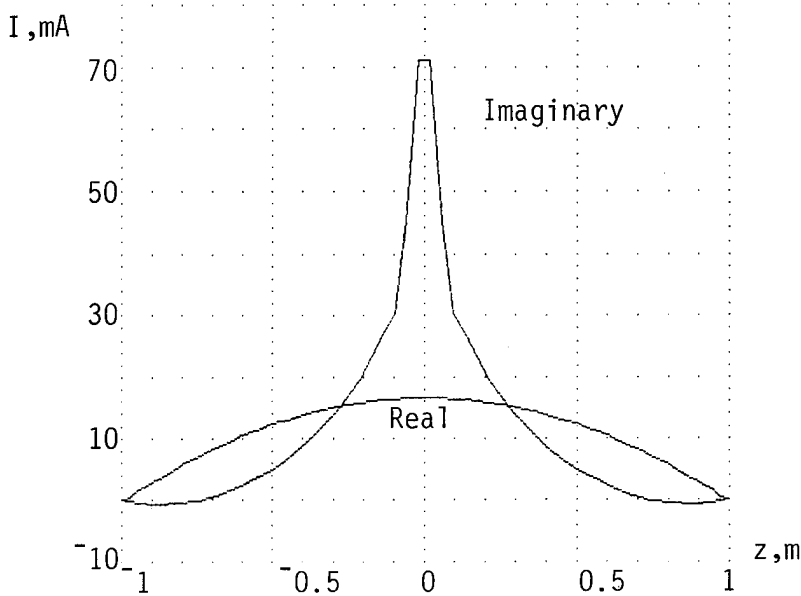


Figure 7. Cross-sectional current along the half-wave sphere.

Forging ahead, the current distributions were plotted for spheroids of various radii from 1 m on down. Figures 6 and 7 show the two extremes. The real parts show a sinusoidal shape as might be expected. The imaginary part of the thin dipole current is negative, necessary for the inductive terminal impedance, and looks sinusoidal except for a tiny upward cusp at the feedpoint. As the dipole is thickened, this cusp grows, the imaginary part of the current changes sign along the z axis, and finally becomes entirely positive. The full sphere shows a large leading current near the feed gap. Since this current is a growing function of the antenna radius, it is presumed that it is bounded as it looks, and the admittance values are reasonable, if not highly accurate.

According to Ramo and Whinnery, Stratton and Chu[11] used spherical-harmonic modes to match the boundary conditions for spheroidal antennas. Their results for the full sphere give a converging series for the conductance, but not for the susceptance. Figure 12.23d, p544, from [12] shows curves for these quantities as functions of βa , 'a' being the sphere radius. The susceptance value for $\beta a = \pi/2$ from this figure is about 27 mS, which was expected to be low, because they stopped arbitrarily at 19 terms. The conductance value is about 17 mS, which matches Table 2 above. A frequency response for βa between 0 and 3 was

VI. Impedance and Shape

For many years it seemed, from [12], that the sphere was a potential broadband antenna, but the recent reexamination of this material and the calculations described in section V show that the large gap perimeter adds too much capacitance to the antenna. At small a/λ the wire dipole has too much series body capacitance and the sphere has too much feed capacitance. A shape with more body than the wire and less gap than the sphere ought to do better than both. From Hansen's paper[3] quoting Chu[13], the minimum Q for an antenna with $\beta a < 1$ is

$$Q_{\min} = \frac{1+3\beta^2 a^2}{\beta^3 a^3 [1+\beta^2 a^2]} \quad (60)$$

At 3 MHz, $\lambda=100$ m, and the antenna size limit is $a=1$ m. This means that $Q_{\min}=4063$. For a simple tuned circuit this means a bandwidth of only about 750 Hz, a little tight even for SSB. This may seem a high value of Q but no reported wire antennas come anywhere near this low. Starting from the sphere, the gap was opened up by using a cone from a small gap as a transition section to a barrel and a capping cone, without good result. Then a biconical half-dipole was explored and showed that the Q improved as the cap cone was flattened. This led to a single cone flaring out from the feed to a plate cap. Is the straight-sided cone the best that can be done? Both convex and concave profiles were tried. Concave was better. Finally, the tube and cone was found to be the best of this shape type. The profile for the best tube-and-cone half-dipole is a tube of 10 cm radius from the feed gap to 0.75 m, then a cone flaring out to 1 m radius at the end, with a plate to close the figure. Table 3 gives descriptions and results for some of the trial shapes.

A basic conclusion one can draw from this work is that both gap and body capacitances need to be kept down. Even with the gap perimeter reduced going from the sphere to the barrel, there's a great deal of charging current. So why isn't a tube out to a plate the best shape? Possibly a little circuit tuning is going on. A frequency-response run for the T-C (tube and cone antenna), shown in Table 4, turned up a series resonance near 17.49 MHz.

Figures 9-12 show the current distributions along the T-C dipole. The real part is nearly flat along the tube below, at, and above resonance, while the imaginary part is closer to flat than anything else below and above the resonance. This is what one would expect from an end-loaded small dipole and supports the idea that the resonance is a circuit phenomenon. The sharp drop in the z components near the dipole ends, shown in Figure 10, are due to the abrupt change in the current's direction going from the tube to the wide-angle cone. The current shifts from axial to almost radially directed.

Table 3. Circuit Properties for Dipole Shapes

$f=3$ MHz, $\lambda=100$ m, dipole length=2 m, NP=20. ρ_d and z_d are the half-dipole profile description in meters. R_{loss} and Z_{in} are series equivalent circuit parameters. $Q=|X|/R$.

Shape Name	ρ_d/z_d				Z_{in} Ω	Q	R_{loss} $m\Omega$	Cu
Thin Spheroid 2 mm feed dia.					0.067-j11,290	168k	44.8	
Full Sphere					0.0142-j267	19k	0.0128	
Barrel	0.01	1	1	0	0.019-j233	12.1k	0.435	
	0	0.2	0.9	1				
Double Cone	0.01	1	0		0.043-j504	11.7k	0.513	
Cone	0	0.5	1					
Cone and Cap	0.01	1	0		0.142-j673	4765	0.672	
	0	0.99	1					
"	0.01	0.5	1	0	0.145-j679	4685	0.677	
	0	0.5	0.999	1				
Concave Cone	0.01	0.5	1	0	0.188-j807	4293	0.895	
Cone	0	0.8	0.999	1				
Tube and Cone (T-C)	0.01	0.01	1	0	0.269-j925	3432	10.4	
	0	0.75	0.999	1				

Table 4. Frequency Response of the T-C Dipole

f , MHz	3	6	10	15
Z_{in} Ω	0.27-j925	1.09-j422	3.1-j195	7.32-j52
f , MHz	17.49	20	30	
Z_{in} Ω	10.28+j0.073	14+j47	39+j215	

run, and Figure 8 shows the plot of conductance for βa between 0 and 2.5. The parameters were $NP=20$ and the half-sphere profile was divided into 20 equal segments. The curve has the same shape as that from [12]. That's nice, but why aren't all the conductance data plotted? Because there's a big wrinkle around $\beta a=2.8$ which would have obscured the shape of the lower-frequency curve. The sphere has a series resonance at about $\beta a=2.752$, $\lambda=2.283$, and a parallel resonance at about $\beta a=2.882$, $\lambda=2.18$ m. Tinkering with NP and segment number did not make the resonances go away so they appear to be real. Fishing for the series resonance λ was interesting because the susceptance behaved reasonably, but the conductance did strange things in magnitude and changed signs close to the resonance. Since the conductance should get large and the susceptance small at series resonance, perhaps the impedance matrix was becoming difficult to invert. The parallel resonance is smoother.

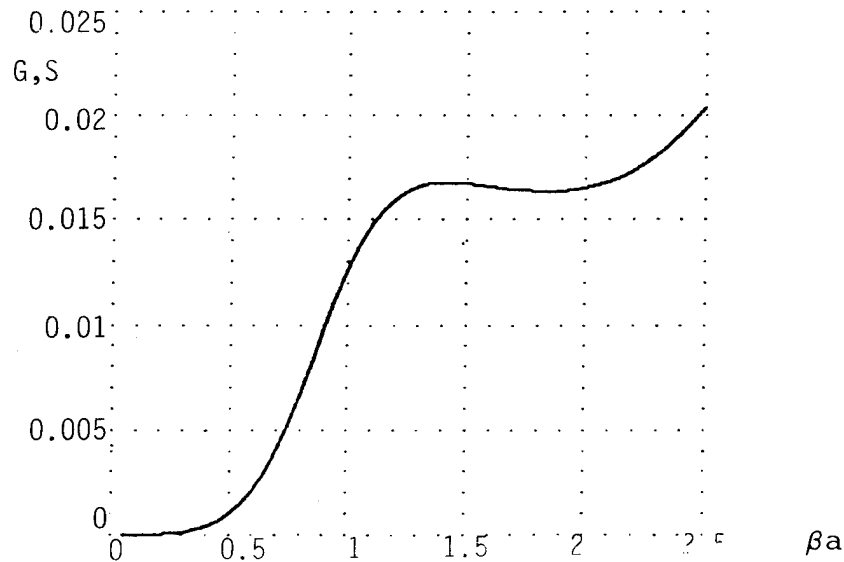


Figure 8. Conductance for a 40-segment sphere dipole.

Since agreement with two classical cases of very different shape is fair, it seems reasonable to gamble that the functions and numerical procedures are generally working and reliable. Ramo and Whinnery[12] said the series for the susceptance doesn't converge for the infinitesimal gap, so the mode analysis has the basic defect that it can't account for the circuit-element behavior of the sphere. This may be why the mode analysis doesn't show up the resonances.

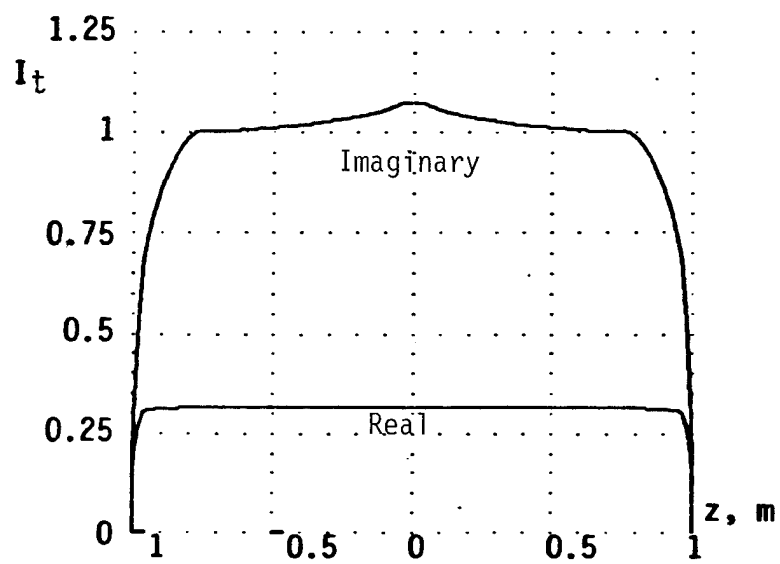


Figure 9. Current on the T-C dipole at 3 MHz. Real part in μ A, imaginary part is mA.

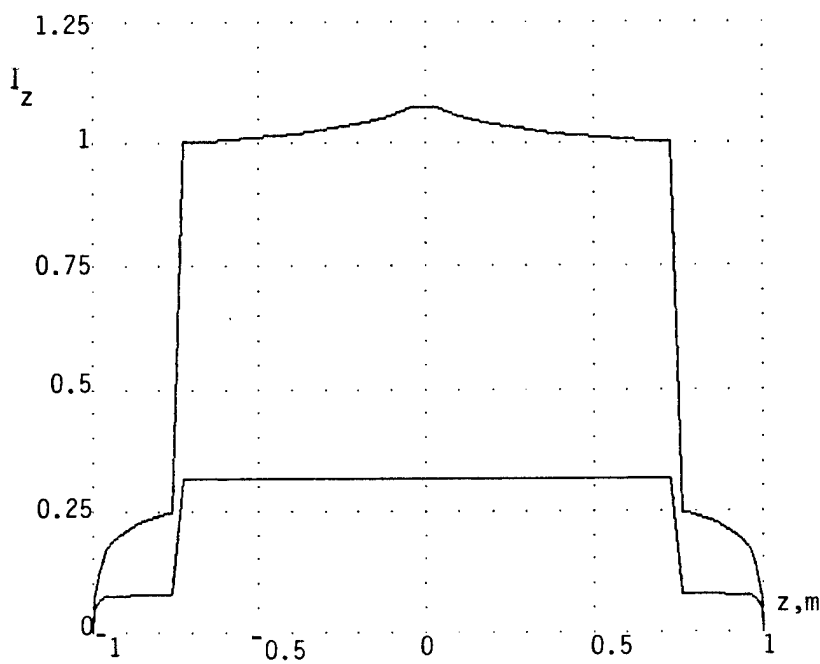


Figure 10. The z components for Figure 9.

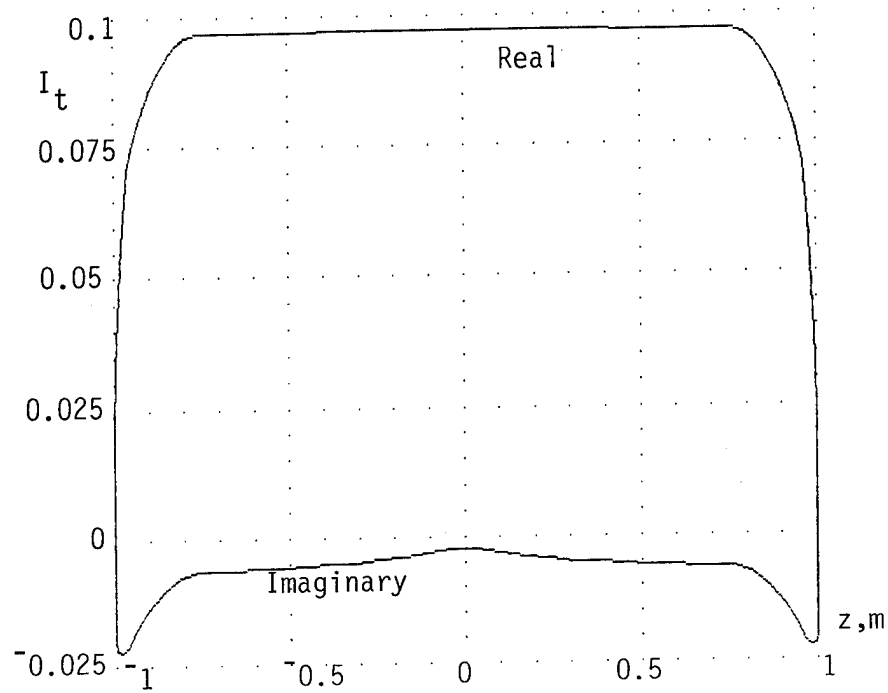


Figure 11. Current on the T-C dipole at 17.49 MHz. Real part in A, imaginary part in dA.

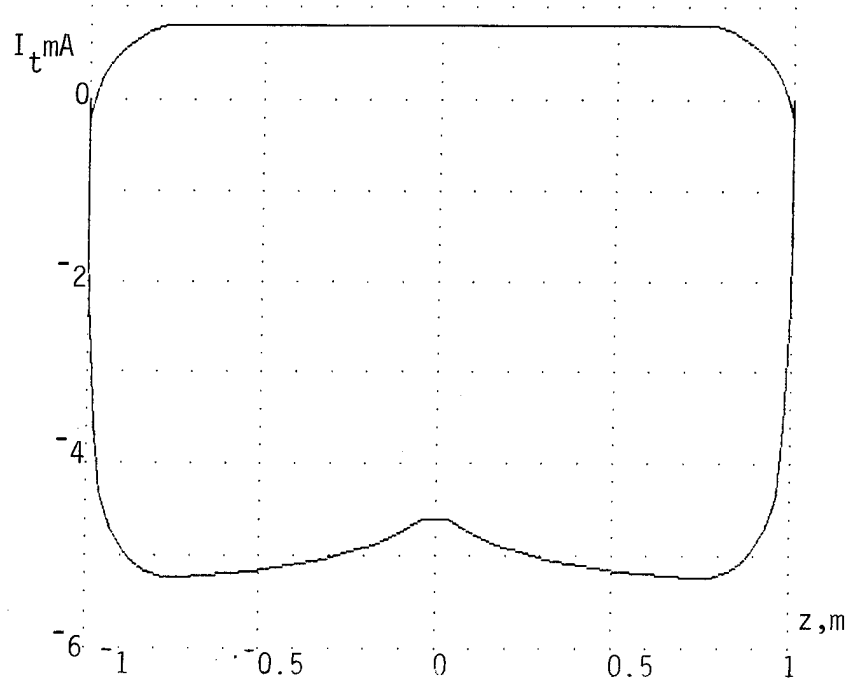


Figure 12. Current on the T-C dipole at 30 MHz.

VII. Development Time vs. Execution Time

This project was spread over a year and a half beginning in January, 1989. Too much time was spent in the first quarter of 1990 in sorting out hardware and software problems in a move to a 32-bit pc and a 32-bit APL interpreter. Writing this paper has taken three 7-day weeks. By comparison, the time spent in the code development seems only a brief pleasant memory. The reader has seen almost all the code written for this project in this paper. Think about that. Realize how closely the code mirrors the mathematics and how little overhead there is. In 1989, an 8 MHz 286/287 system with 2.7 Mb of RAM was being used for this project. A few times cases were run that took about 5 hours. With the move to the 20 MHz, 8 Mb, 32-bit system, the longest case took about an hour. The 100-point admittance calculation for Figure 8 took about 2 hours, during which markup on a student's thesis draft was started. Now this project, which is part of a larger one, is over. This code may never run again. From this perspective, even if the execution time of a compiled program was zero, it would not compensate for the excess time spent in coding and debugging the constituent functions in a scalar programming language. Human time is too precious.

Table 5 shows the execution times for various parts of a case computation. The blank entries are for cases that won't fit in 8 Mb. While these times are for a particular case, a simple shape and long wavelength, there is considerable variation from case to case. Shorter wavelengths seem to take longer, as much as 10 % on the dynamic calculations. This effect has not been investigated. The array sizes don't depend on wavelength, nor are there any loops which test on relative size for termination. The maximum problem that will fit with row looping is NP=150 (600 samples), and looping on ten-element bites out of a row allows the problem to run on a 640 kb machine with the 16-bit interpreter. The times for the G functions with ten-element-bite loops are double those for no loops on the same machine. One can see that the times generally follow an NP^2 law. The difference between total case time and time for a new frequency is a little deceiving, if one is considering whether to fill a separate static matrix or not. If the static and dynamic G functions are added and then used to fill only one impedance matrix, the time to fill that matrix would be only slightly longer than the times given for the dynamic matrix fill. In such a scheme, the time for a new frequency point in a response run would be the same, and the saving per frequency would be the time to compute the static G functions. The circuit-element reactance was calculated separately, for cases with new geometry or number of samples, for interest. The utility of this data is unclear, so it wasn't included in this paper.

Table 5. Execution Times

All times are in seconds. Cases were run on an ATronics 386B/20 (20 MHz clock) w. 64k cache card, 8 Mb RAM, Intel '387. The interpreter is STSC's APL*PLUS II, release 2.

Sample point, 4xNP.	20	40	80	200	400
Static G_0 and G_1 without loops.	1.16	3.4	11.3	63.5	
Static G_0 and G_1 with row loop.	1.49	4.12	13.5	66.8	249
Static matrix fill and invert.	1	4	16.2	103	426
Dynamic G_0 and G_1 without loops.	2.9	11.4	45		
Dynamic G_0 and G_1 with row loop.	3.1	12	47.4	284	1140
Dynamic matrix fill and invert.	1.4	5.1	22.2	157	789
Total, without G loops.	6.5	24	95		
Total, with G loops.	7	25	100	511	2704
Time for a new frequency.	4.5	17	70	441	1929

Appendix: APL Syntax, Symbols and Functions

This appendix will present only as much APL as is used in the paper. APL is fundamentally an interactive array-processing language. To be interactive, it must be an interpreter. It is economical of time in development and execution because it uses an extended symbol set from which over 80 functions and operators can be called by one or two keystrokes each. There are no data type statements, a variable is given its type by the way the user assigns data to it, and the interpreter keeps track of the type, not the user. Arithmetic is double-precision, or better. A variable may be a scalar, a vector, or an array of any number of axes (dimensions). Execution of a statement proceeds from right to left, except when interrupted by parentheses. $A \times B + C$ is not equal to $C + A \times B$. Thus, a typical statement execution begins with the interpreter reading data (explicitly or in a variable name) at the right end and finishing either with a screen display or an assignment to a variable at the left end. Customarily, only uppercase letters are used in names for variables and user-defined functions, but the interpreter is case-sensitive so that lowercase letters can also be used. The \diamond is a statement separator, so that more than one statement can be placed on the same line. The interpreter passes from one statement to the next in the usual left-to-right manner, as if the successive statements did have line numbers. Multiple-statement lines is a feature of STSC's APL*PLUS systems, but it is not standard. In the following listing, related symbols are grouped together to save space. S is a scalar, N is an integer, V is a vector, M is a matrix, f and g represent any built-in (primitive) function. Primitive scalar functions operate on a variable in an element-by-element manner, fM does f to each element in M and the result has the same shape as M . There are also array functions which rearrange arrays or extract blocks of data from them. Operators modify the way functions are applied to data.

APL Symbols	Meanings
+ - × ÷	Basic arithmetic functions.
*X X*Y ⋀X	e^X , X^Y , $\ln(X)$.
X←Y	X is assigned the shape and values of Y.
∇	Open or close (toggle) function-definition mode.
1N	A vector of integers from 1 to N.
→	Go to. $\rightarrow(\text{test})/\text{line_label}$. If 'test' is true control passes to the statement line beginning with 'line_label'.
LABEL:	A line label is identified by the colon.
oX	π times X.
NoX	$N=1$ is $\sin X$, $=2$ is $\cos X$, etc.
V←ρX A←VρX	Shape is the number of elements along each axis of an array. ρX gives the shape of X, a vector. With a vector left argument the function ρ reshapes the data in X, taking it row by row, to the shape specified by the vector.
X ×X	Magnitude of, sign of, each element in X.
V⊖M ⊕M	$M^{-1}V$, M^{-1} .
,X V1,V2	Make X a vector, make V1 and V2 a vector.
V1,[0.5]V2	Place V1 over V2 in a two-row matrix.
⊖ φ ↷	Matrix rearrange. Transpose, reverse left to right, reverse top to bottom.
V↑M V↓M	Take and Drop. V specifies how many rows and columns of M are affected.
f/M f↗M	Reduction. Apply f between the elements of each row (column) of M.
M1f.gM2	Inner product. $f/M1gM2$.
X1°.fx2	Outer product. f is applied between each element of X1 and every element of X2. The shape equals the joining of the shapes of X1 and X2.

References

- [1] Mautz, J. R. and R. F. Harrington, "Radiation and Scattering from Bodies of Revolution", Applied Scientific Research vol. 20, June 1969.
- [2] Simpson, T. L, J. C. Logan, and J. W. Rockway, "Equivalent Circuits for Electrically Small Antennas Using LS-Decomposition with the Method of Moments", IEEE Trans. Ant. and Prop. vol. 37, no. 12, December 1989.
- [3] Hansen, R. C., "Fundamental Limitations in Antennas", Proc. IEEE vol. 69, no. 2, February 1981.
- [4] Miron, D. B. "Survey of Recent Results for the Singularity Problem in the Electromagnetic Integral Equation", Proc. North Dakota Acad. Sci., vol.38, p30, April 1984.
- [5] Mahadevan, K. and H. A. Auda, "Electromagnetic Field of a Rectangular Patch of Uniform and Linear Distributions of Current", IEEE Trans. Ant. and Prop. vol.37, no. 12, December 1989
- [6] Gradshteyn, I. S. and I. M. Ryzhik, Table of Integrals, Sums, and Products, Academic Press, New York, 1965, p153-154.
- [7] Abramowitz, M. and I. A. Stegun, Handbook of Mathematical Functions, Dover, New York, 1972(?), p591-592.
- [8] Pierce, B. O. and R. M. Foster, A Short Table of Integrals, 4th ed., p72, Ginn, New York, 1956.
- [9] Neff, H. P. jr., Basic Electromagnetic Fields, 2nd ed., Harper and Row, 1987, p154-159.
- [10] Miron, D. B., "The Conducting Cylinder Problem", an unpublished handout, available from the author.
- [11] Stratton, J. A. and L. J. Chu, J. Appl. Physics, no. 12, pp230-248, March 1941.
- [12] Ramo, S. and J. R. Whinnery, Fields and Waves in Modern Radio, 2nd ed., Wiley, New York, 1960.
- [13] Chu, L. J. "Physical Limitations of Omnidirectional Antennas", J. Appl. Phys. no. 19, pp1163-1175, Dec. 1948.
- [14] Sarkar, T. K., A. R. Djordjevic, and E. Arvas, "On the Choice of Expansion and Weighting Function in the Numerical Solution of Operator Equations", IEEE Trans. Ant. and Prop. vol. AP-33, no. 9, p988, September 1985.
- [15] Petersen, A. F., "Difficulties Encountered When Attempting to Validate Thin-Wire Formulations for Linear Dipole Antennas", Applied Computational Electromagnetics Society Journal, Special Issue on Code Validation, p41, 1989.

ANALYSIS OF THREE DIMENSIONAL
DIELECTRIC LOADED CAVITIES
WITH EDGE ELEMENTS

L. Pichon A. Razek
Laboratoire de Génie Electrique de Paris
Ecole Supérieure d'Electricité
U.R.A. D0127 CNRS
Universités Paris 6 et Paris 11
91 192 Gif sur Yvette Cédex
France

ABSTRACT

In this paper we show that edge elements (a class of mixed finite elements) provide an efficient numerical approach in the determination of resonant modes in three dimensional high frequency cavities. These finite elements avoid "spurious modes", the non-physical numerical fields obtained from the solution of eigenvalue problems.

Here, empty cavities as well as dielectric loaded cavities are analyzed: no "spurious mode" was observed. Moreover, comparisons with analytical results and previously published ones show the great accuracy of the numerical technique.

INTRODUCTION

Electromagnetic resonance is important in the design of particle accelerators, microwave ovens and resonant cavities. For such analysis, numerical techniques including the finite element method have been developed.

The well known finite element method seems very attractive since for several years it has been found to be an efficient tool in low frequency electromagnetic field computations. In high frequency applications, finite elements were used for cavity resonances analysis [1]-[5]; resonant modes and resonant frequencies are obtained as solutions from an eigenvalue problem.

The main serious drawback in these studies is that the computed solutions are plagued by non-physical (or "spurious") solutions: solutions which do not satisfy the divergence free condition implied by the Maxwell's equations. Many attempts were performed to circumvent these unwanted numerical fields (enforcing the divergence

condition with a global penalty term [1],[5], reducing the number of unknowns by taking locally into account the divergence condition [3] , using divergence free trial functions ...). It has been observed that discretized fields with continuous tangential components suppress the "spurious modes" (the problem was solved for a scalar function in two dimensions [5] and for the magnetic vector potential [4] in three dimensions); nevertheless no precise argument was put forward to explain the importance of this kind of approximation.

However the choice of finite elements for electromagnetic field computations is essential: A. Bossavit showed that "edge elements" are well adapted for the representation of vector fields since they allow their possible discontinuities [6]. These "edge elements" are also a class of the mixed finite element proposed by J.C. Nedelec [7]. Such elements were successfully used in eddy currents problems [8]-[10] and are well adapted for the approximation of scattering and resonance problems [11] [12] ; the reason for which they would not generate "spurious modes" is explained in [12].

We have developed and applied such a numerical approach for empty and dielectric loaded cavities. In this paper, we present first the variational formulation of the Maxwell's equations in terms of electric field and the reason of the occurrence of "spurious modes". Then we detail the numerical discretization and explain the interest of "edge elements". Finally we present the analysis of three dimensional cavities .

VARIATIONAL FORMULATION

We deal with the Maxwell's time-harmonic equations in a bounded region Ω surrounded by a perfect conductor and containing lossless materials :

$$\text{rot } \mathbf{e} = - i\omega \mu_0 \mathbf{h} \quad (1)$$

$$\text{rot } \mathbf{h} = i\omega \epsilon_0 \epsilon_r \mathbf{e} \quad (2)$$

where \mathbf{e} and \mathbf{h} are the complex electric and magnetic fields, ϵ_0 and μ_0 are respectively the permittivity and permeability of vacuum, ϵ_r is the relative permittivity and ω is the angular frequency.

The conditions on the boundary Γ of Ω are those of a perfect conductor:

$$\mathbf{n} \wedge \mathbf{e} = 0 \quad (3) \qquad \mathbf{n} \cdot \mathbf{h} = 0 \quad (4)$$

where n is the outward normal vector.

Substituting (1) into (2), we deduce the following eigenvalue problem expressed in terms of the electric field

$$\left\{ \begin{array}{l} \operatorname{rot}(\operatorname{rot} \mathbf{e}) - \epsilon_r \epsilon_0 \mu_0 \omega^2 \mathbf{e} = 0 \quad \text{in } \Omega \\ \mathbf{n} \cdot \mathbf{e} = 0 \end{array} \right. \quad (5)$$

$$\left\{ \begin{array}{l} \operatorname{rot}(\operatorname{rot} \mathbf{e}) - \epsilon_r \epsilon_0 \mu_0 \omega^2 \mathbf{e} = 0 \quad \text{in } \Omega \\ \mathbf{n} \cdot \mathbf{e} = 0 \end{array} \right. \quad (6)$$

A weak formulation of (5)-(6) holds in E_0 [11]:

$$\int_{\Omega} \operatorname{rot} \mathbf{e} \cdot \operatorname{rot} \mathbf{e}' \, d\Omega - k^2 \int_{\Omega} \epsilon_r \mathbf{e} \cdot \mathbf{e}' \, d\Omega = 0 \quad \forall \mathbf{e}' \in E_0 \quad (7)$$

where

$$E_0 = \left\{ \mathbf{e} \in [L^2(\Omega)]^3, \operatorname{rot} \mathbf{e} \in [L^2(\Omega)]^3, \mathbf{n} \cdot \mathbf{e}|_{\Gamma} = 0 \right\}$$

and where the values of k ($k^2 = \omega^2 \epsilon_0 \mu_0$) are the wavenumbers.

SPURIOUS MODES

The searched resonant fields ($\omega > 0$) are theoretically divergence free since from (5) it follows:

$$\operatorname{div} \epsilon_r \mathbf{e} = \frac{1}{k^2} \operatorname{div}(\operatorname{rot}(\operatorname{rot} \mathbf{e})) = 0 \quad (8)$$

Moreover, for a simply-connected region Ω , the only field corresponding to $\omega=0$ (static field) satisfying equations (1), (3) and the condition $\operatorname{div} \epsilon_r \mathbf{e}=0$ is $\mathbf{e}=0$.

The trouble arises when discretizing (7) with classical finite elements (for example nodal vector elements) : a matrix with many eigenvalues being zero is obtained (0 is a highly degenerate eigenvalue) [3] [5]. The numerical approximations of this value $k^2=0$ are difficult to isolate from the meaningful lowest non-zero eigenvalues ($k^2 > 0$); especially when the number of degrees of freedom increases. Most of them do not satisfy $\operatorname{div} \epsilon_r \mathbf{e}=0$ and then are unacceptable as solutions of Maxwell's equations. The resulting set of solutions is a mixture of physical modes and numerical spurious ones.

With edge elements, as we shall see in the next section such a situation doesn't occur.

FINITE ELEMENT DISCRETIZATION

Mixed finite elements [7] are used for the numerical approximation of (7). Let Ω_h (with boundary Γ_h) be the discretization of Ω with tetrahedra. The "edge elements" have the following properties:

The degrees of freedom e_a and the trial functions w_a are associated with the mesh edges. For every edge "a" containing the nodes "i" and "j" :

- e_a is the circulation of e along "a".

$$e_a = \int_a e \cdot t \, d\gamma \quad (9)$$

- w_a can be expressed in terms of the barycentric functions λ_i and λ_j as :

$$w_a = \lambda_i \operatorname{grad} \lambda_j - \lambda_j \operatorname{grad} \lambda_i \quad (10)$$

In each tetrahedron e is :

$$e(r) = \alpha + \beta \wedge r \quad (11)$$

where α and β are three-components constant vectors and r is the vector (x, y, z) .

We introduce the space E_{0h} :

$$E_{0h} = \left\{ e \mid e = \sum e_a w_a, n \wedge e \mid_{\Gamma} = 0 \right\} \quad (12)$$

For every e in E_{0h} the tangential part of e is continuous across tetrahedra interfaces. The approached problem is to find e in E_{0h} so that :

$$\int_{\Omega_h} \operatorname{rot} e \cdot \operatorname{rot} e' \, d\Omega_h - k^2 \int_{\Omega_h} e \cdot e' \, d\Omega_h = 0 \quad \forall e' \in E_{0h} \quad (13)$$

Finally, we have to solve a generalized algebraic eigenvalue problem of the form :

$$A u = k^2 B u \quad (14)$$

A ("stiffness matrix") and B ("mass matrix") have dimensions $n_a \times n_a$ where n_a is the number of edges in the finite element mesh.

Remark: with "edge elements" all the numerical solutions corresponding to $k^2 > 0$ are "weakly divergence free" : no spurious mode occur. The reason is the following :

Let φ be any linear combination of the barycentric functions λ_i (φ piecewise affine) and $\varphi = 0$ on Γ ; it can be showed that all the fields e' of the form $e' = \operatorname{grad} \varphi$ are in E_{0h} [11] [12]. Then they can be chosen as admissible test fields in (13). Rewriting $e' = \operatorname{grad} \varphi$ in (13) leads to :

$$k^2 \int_{\Omega_h} \epsilon_r \cdot \mathbf{e} \cdot \operatorname{grad} \varphi \, d\Omega_h = 0 \quad (15)$$

Equation (15) is equivalent to say that for every $k^2 > 0$ the solution $\operatorname{div} \epsilon_r \mathbf{e} = 0$ is verified in the distribution sense. An integration by parts of (15) shows that for every inner node "i" of Ω_h , an integral involving the sum of jumps of $\epsilon_r \mathbf{e} \cdot \mathbf{n}$ through facets of tetrahedra having node "i" in common is zero. This property is important since it gives an average local divergence condition. Such result does not exist in case of classical finite elements (nodal ones) since the fields of the form $\mathbf{e}' = \operatorname{grad} \varphi$ are not in the space of the test functions E_{0h} .

NUMERICAL RESULTS

a. Empty rectangular cavity.

An empty rectangular cavity with perfectly conducting walls was modelled with the above developed technique. The cavity has dimensions: $a = 0.4 \text{ m}$, $b = 0.3 \text{ m}$, $c = 1. \text{ m}$ (figure 1-a). A quarter of the cavity (figure 1-b) was analyzed using 220 tetrahedra. Symmetry conditions were prescribed on faces $x = 0$ and $z = 0$.

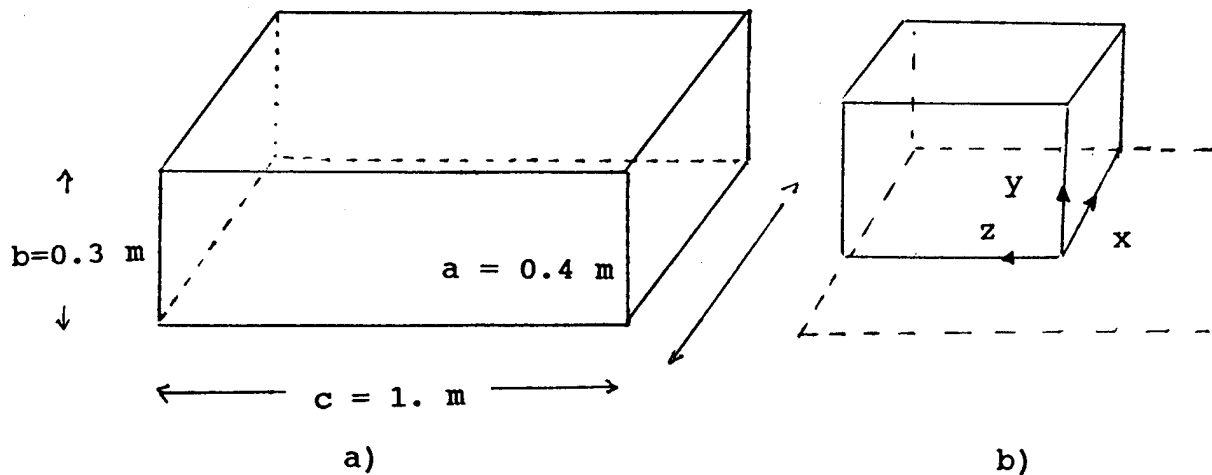


Figure 1 Studied air-filled cavity

The problem is symmetrical in x, y, z ; so the fields can be expressed as TE (transverse electric) or TM (transverse magnetic) to any one of these coordinates [13]. It is conventional to choose the longer dimension along the z direction. Analytical solutions are then labelled TE_{mp} (modes whose electric field has no z -component) and TM_{mp} (modes whose magnetic field has no z -component). The corresponding resonant wave numbers are :

$$k^2 = \pi^2 \left(\frac{m^2}{a^2} + \frac{n^2}{b^2} + \frac{p^2}{c^2} \right)$$

The algorithm for solving the matricial eigenvalue problem is based on the classical QR method.

Computations were performed on a DN4000 Apollo workstation; about 10 minutes are necessary to solve the entire problem. The six lowest computed modes are shown on Table 1.

Mode	Wavenumber k computed	Wavenumber k analytical	Error (%)
TE ₁₀₁	8.365	8.458	1.
TE ₁₁₁ (TM ₁₁₁)	13.243	13.461	1.6
	13.488	13.461	0.2
TE ₁₀₃	12.327	12.268	0.5
TE ₁₁₃ (TM ₃₁₁)	16.273	16.129	0.9
	16.356	16.129	1.4

Table 1
Numerical Results

This simple case is known to give spurious solutions when solved with classical finite elements [2] [14]. Here no spurious mode is observed. Moreover the relative error never exceeds 2%.

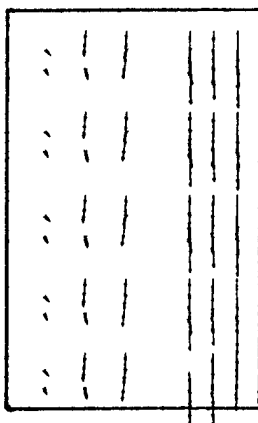


Figure 2
Electric field (TE₁₀₁ mode
in (x,y) plane for z=0.5 m)

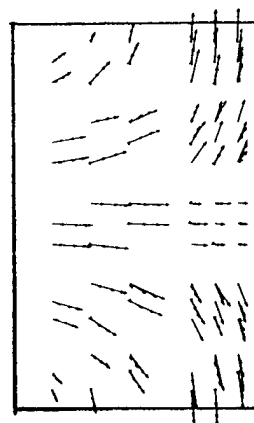


Figure 3
Electric field (TE₁₁₁ mode
in (x,y) plane for z=0.5 m)

Figures 2 and 3 show, in the quarter of the cavity, the distribution of vector fields for the TE₁₀₁ mode and the TE₁₁₁ mode respectively. The plane of symmetry is on the right of the figures. On this plane e is tangential and

on the others e is normal. In each tetrahedron e is represented with an arrow in the centre of gravity and the length of the arrow is proportional to the magnitude.

b. Inhomogeneous dielectric loaded cavities

Two examples of inhomogeneous loaded cavities were analyzed.

The first one (figure 4) is the preceding cavity with dielectric discontinuities in one direction only. The relative permittivity ϵ_r of the dielectric material is $\epsilon_r = 16$. For a quarter of the cavity 230 tetrahedra were used. The theoretical eigenvalue for the dominant mode (lowest eigenvalue) is known [15] : $k = 2.5829$. An error of 0.4% was found.

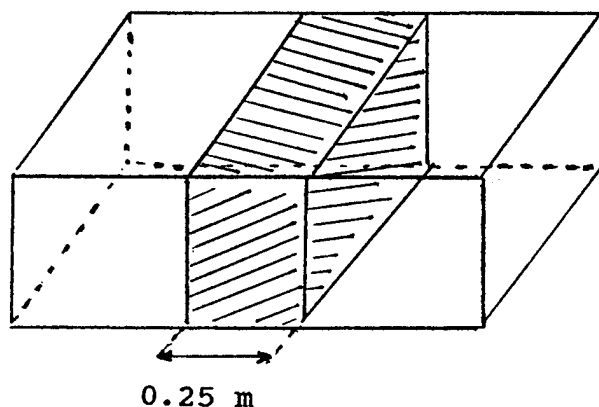
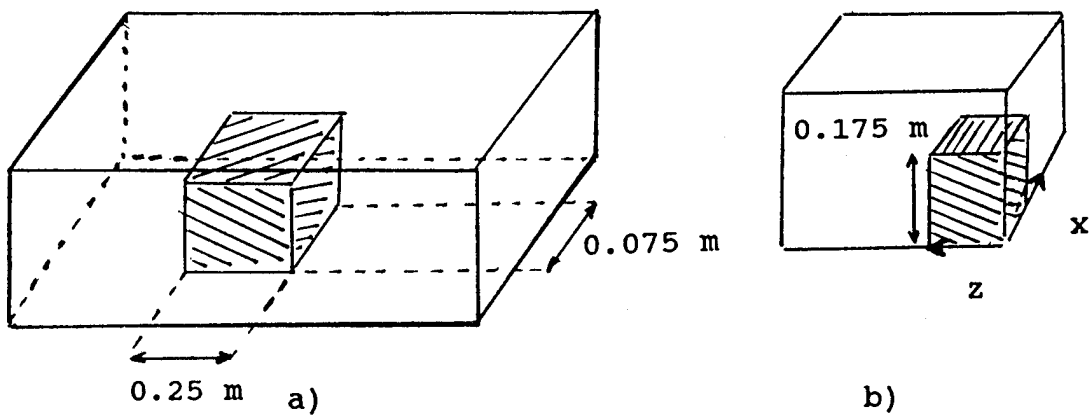
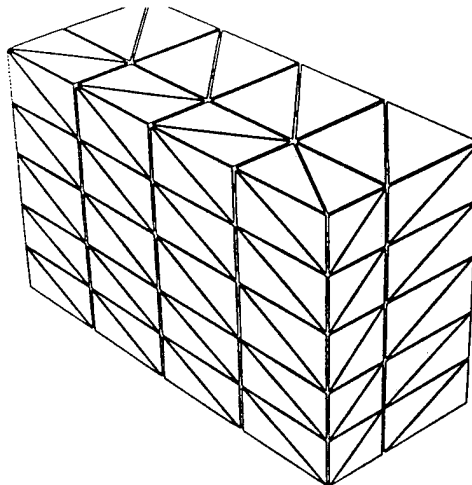


Figure 4
Cavity with dielectric block (example 1)

The second cavity (figure 5-a) is the cavity of a. with dielectric discontinuities in three dimensions ($\epsilon_r = 16$). The quarter (figure 5-b) was modelled with 240 tetrahedra (figure 5-c). Computing time is about 15 minutes.





c)

Figure 5
Cavity with dielectric block (example 2)

No analytical result is available but comparison with already published computed values is possible; results for the dominant mode are the following:

Source	k (computed)
Ref [1]	5.60
Ref [15]	5.529
Ref [16]	4.907
Presented Method	5.102

All these results agree within roughly 10%. Some others structures should be modelled in order to make a comparison more satisfactory between all the methods. However the mixed finite elements used here are well adapted in case of dielectric materials because they imply the tangential continuity of the electric field across interfaces and take account of the discontinuity of the normal component.

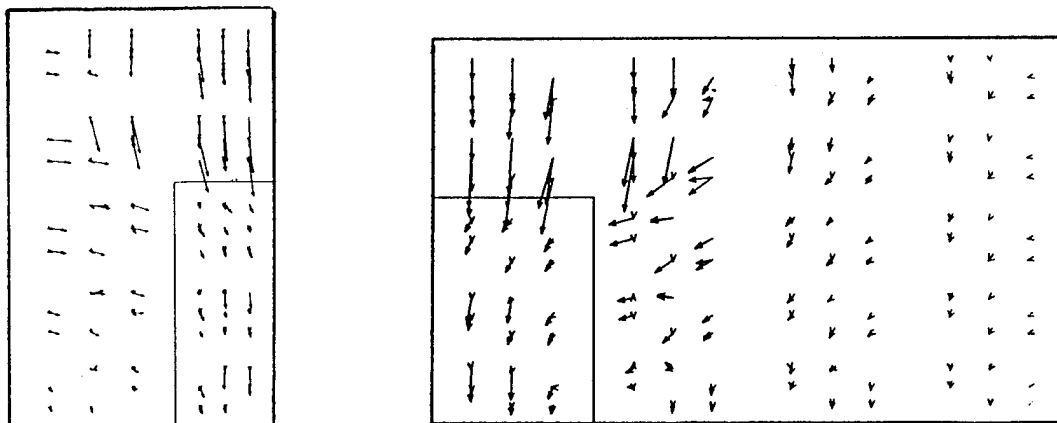


Figure 6
Electric field (dominant mode)
In the (x,y) plane
for $z=0.5$ m
In the (y,z) plane
for $x=0.2$ m

No spurious mode occurred; all the computed field correspond to resonant fields. Figure 6 shows electric vector fields in the quarter of the cavity.

CONCLUSION

"Edge elements" (a class of mixed finite element) have been used to model empty and dielectric loaded cavities. The first resonant frequencies were computed; comparison with analytical values or results published in previous papers shows the efficiency of the method.

These elements avoid all the well known "spurious modes" and seem very promising for the study of more complicated problems in high frequency applications

REFERENCES

1. J.P. Webb, "Efficient Generation of Divergence-free Fields for the Finite Element Analysis of 3D Cavity Resonances", IEEE Transactions on Magnetics, 33, No. 1, 1988, pp 162-165.
2. A. Konrad, "On the Reduction of the Number of Spurious Modes in the Vectorial Finite-element solution of Three Dimensional Dimensional Cavities and Wave Guides", IEEE Transactions on Microwave Theory and Techniques, 34, No. 2, 1982, pp 224-227
3. K. Hayata, M. Koshiba, M. Eguchi and M. Suzuki, "Vectorial Finite Element Method Without any Spurious Solutions for Dielectric Waveguiding Problems Using Transverse Magnetic Field Component", IEEE Transactions on Microwave Theory and Techniques, 34, No. 11, 1986, pp. 1120-1124.
4. M. Hano, "Frequency-free Analysis of Three Dimensional Electromagnetic Problems by the Finite Element Method", Compumag, Tokyo, 1989.
5. F. Kikuchi, "Mixed and Penalty Formulations for Finite Elements Analysis of an Eigenvalue Problem in Electromagnetism", Comp. Meth. Appl. Mech. Engng., 64, 1986, pp 569-570.
6. A. Bossavit, "A Rationale for "Edge-elements" in 3-D Fields Computations", IEEE Transactions on Magnetics, 24, No. 1, 1988, pp. 74-79.
7. J.C. Nedelec, "Mixed Finite Elements in R^3 ", Numer. Math., 35, 1980, pp. 315-341.

8. A. Bossavit and J.C. Verite, "The "Trifou" Code: Solving the 3-D Eddy-currents problem by Using H as State Variable", IEEE Transactions on Magnetics, 19, No. 6, 1983, pp. 2465-2470.
9. Z. Ren, F. Bouillault, A. Razek, A. Bossavit, and J.C. Verite, "A New Hybrid Model Using Electric Field Formulation For 3-D Eddy Current Problems", IEEE Transactions on Magnetics, 26, No. 2, 1990, pp. 470-473.
10. Z. Ren and A. Razek, "New Technique for Solving Three-dimensional Multiply Connected eddy-current problems", Proc. IEE, Pt. A, 137, No. 3, 1990, pp. 135-140
11. A. Bossavit, "Simplicial Finite Elements for Scattering Problems in Electromagnetism", Comp. Meth. Appl. Mech. Engng., 76, 1989.
12. A. Bossavit, "Solving Maxwell Equations in a Closed Cavity and the Question of Spurious Modes", IEEE Transactions on Magnetics, March 1990.
13. F. Gardiol, Hyperfrequencies, Dunod, 1987.
14. J.P. Webb, "The Finite-element Method for Finding Modes of Dielectric-loaded Cavities", IEEE Transactions on Microwave Theory and Techniques, 33, No. 7, 1985, pp. 635-649.
15. S. Akhtarzad and P.B. Johns, "Solution of Maxwell's Equations in Three Space Dimensions and Time by the T.L.M. Method of Numerical Analysis", Proc. IEE, 122, No. 12, 1975, pp. 1344-1348.
16. M. Albani and P. Bernadi, "A Numerical Method Based on the Discretization of Maxwell Equations in Integral Form", IEEE Transactions on Magnetics, 22, 1974, pp. 446-450.

ANTENNA ARRAY MODELLING BY PARALLEL PROCESSOR FARMS

Iain Cramb, Daniel H. Schaubert*, Richard Beton, James Kingdon, and Colin Upstill

Roke Manor Research Limited,

Roke Manor, Romsey, Hampshire, SO51 0ZN, UK

ABSTRACT

The fast concurrent implementation of a FORTRAN method of moments analysis of the electromagnetic properties of an array of tapered slot antennae is discussed. Decomposition of an existing FORTRAN algorithm for calculation of the currents induced by an incident radiation field in an infinite array of tapered slot antennae is described. The problem was distributed across an array of INMOS transputers, yielding significant speed-up over a single CPU. This decomposition was relatively simple to implement, can readily be scaled to larger processor arrays virtually indefinitely, and promises linear speed-up with the number of processors in the array.

1. INTRODUCTION

A growing number of electromagnetic analysis problems are being formulated for processing on parallel processing computers, and transputer arrays represent one of the least costly parallel computer systems available to the EM analyst. Recently, tutorial papers have appeared to describe the successes and difficulties one may encounter in solving various types of problems [1, 2]. The objective of this paper is to describe the way in which a FORTRAN moment method analysis was converted from a code for a single CPU to a code that utilises several cpus with very high efficiency.

The particular analysis that was converted is for infinite arrays of endfire, tapered slot antennas [3]-[5]. The currents flowing on the metallic fins that comprise an infinite array of tapered slot antennae (figure 1) are determined by using the method of moments to solve the electric field integral equation. Floquet's theorem is used so that only a unit cell of the structure must be considered, and the version of the analysis being performed here uses piecewise sinusoidal *rooftop* basis and testing functions. Most (over 95%) of the time taken to calculate the currents induced in the antennae is spent filling the impedance matrix for the 50 to 200 unknowns that are used to model the current. Since this particular analysis is not the main topic of the paper, only a few sample results are included.

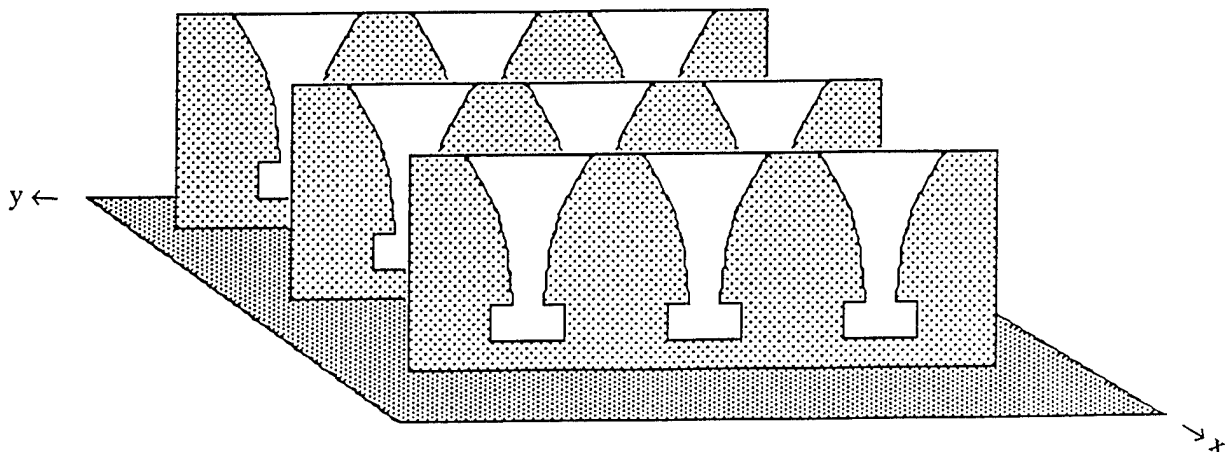


Figure 1 Tapered slot antennae

Use of the numerical model for antenna design and development requires computing the antenna currents for many scan angles and frequencies of operation. Computations for each set of parameters

* This work was performed while D.H. Schaubert was on leave from:
University of Massachusetts at Amherst,
Department of Electrical and Computer Engineering,
Amherst, MA 01003.

are lengthy but tractable with modest CPUs; typical cases require several minutes to a few hours on a 25-MHz 80386/80387 PC. However, typical applications require that dozens, or perhaps hundreds, of parameter sets be analyzed. It is the objective of this paper to demonstrate that EM analysts can readily decompose a FORTRAN algorithm of this type to be distributed to an economical transputer array. The decomposition maintains the input and output features familiar to the user while distributing the computations for each parameter set to a different processor via a "general purpose" communications harness that is easily adapted to different FORTRAN algorithms. A request-driven transputer farming paradigm is used, which provides efficient utilization of the transputer array for this type of computation. Thus, we demonstrate how easily the total processing speed of the transputer array can be used to the benefit of EM analysis codes that were not originally intended for parallel processing as well as to the benefit of new codes that may be written specifically to exploit the parallelism in computations for a single parameter set. The controller/worker model is described in detail in the implementation section below.

2. PARALLEL IMPLEMENTATION

2.1. Paradigms for Parallelism

Parallel systems may be described at various levels of abstraction, and it proves convenient to use the subclasses *conceptual*, *physical*, and *logical* architectures to describe more accurately what is meant by 'parallel architectures'. This is more than mere taxonomy: understanding parallel processing and effectively managing parallel systems design and implementation requires different views to be taken for different purposes, and thinking in terms of these architectural subclasses has been found very useful in practice.

Conceptual architectures involve the most abstract aspects of parallel processing systems, in particular the type of computation being undertaken. Most conceptual architectures fall into one of four classes: control-driven, data-flow, object-based, and logic-based.

Physical architectures deal with the actual physical implementation of such systems. The categorisation of physical architectures preferred is that introduced by Flynn [6]. It is a classification which distinguishes four basic combinations of instruction streams and data streams (SISD, SIMD, MISD, and MIMD). Flynn's scheme is simpler than most, and is very useful for classifying machines which are clearly different. This work uses a machine in the last of the above four categories - a transputer array.

The *logical architecture* of a system is the architecture seen by applications software designers and programmers. There are three main types of logical architecture appropriate to MIMD machines - *farming*, *geometric* and *algorithmic* [7,8].

Farming is a controller/worker paradigm in which an overall problem is split into conveniently sized work packets which are distributed over a number of worker processors in such a way as to *dynamically balance* the work load across the processors in the farm. The controller knows about the work that has to be done, and the worker knows how to do it - each worker has an identical copy of the code. The controller sends batches of work to each worker; the latter executes its algorithm on a batch of data then returns the results, starting to work on the next batch pending any message transmission. The primary advantage of the task farm is the fact that it dynamically balances the loading of an overall problem across a network of processors. A potential disadvantage is that each worker has to have a copy of the complete code, which can lead to problems if memory is limited.

An architecture of this type is most appropriate to an application in which firstly, the work packets may require different amounts of processing - that is to say the amount of work for each is packet-dependent. Secondly, and perhaps more obviously, the overall task should naturally lend itself to temporal concurrency. This means that as far as is possible, the processing of any individual packet should not depend upon the processing of any other packet. Complete independence may not actually be possible; packets may have some positional or other relationship to each other. However, such an architecture does demand that the final result does not depend upon the order in which the packets are processed.

In contrast with the automatic run-time load-balancing in a farm, geometric and algorithmic architectures, which exploit data concurrency and algorithm concurrency respectively, have to be load-balanced at design time.

In *geometric parallelism*, the parallelism inherent in the data is exploited. The problem will generally have an underlying geometrical structure (this is often very similar to SIMD array processing), and when this is the case, the array topology reflects the data topology. In geometric parallelism, as in farming, each processor has an identical copy of the complete code for the whole program, but each works on separate pre-defined portions of the data space, i.e., each processor is responsible for a specific area or volume of the data set.

Algorithmic parallelism is the case in which the parallelism inherent in the algorithm is exploited, e.g. with a pipeline. In a distributed memory machine, each processor has its own segment of the code, and this is different from processor to processor. The topology of the machine typically reflects the topology of the data flow graph on which the algorithm is based.

Many architectures are, in fact, hybrids of two or all three types, but our decomposition is purely a farm. The logical architecture is described in more detail a little later. Before giving the description we present a brief summary of the various techniques used in implementation of parallel software.

2.2. Implementing Parallel Software

There are several distinct approaches to implementing parallel software. The quickest, and the one used in this case, is to use existing codes within a specially created communication harness. Possible parallelism is identified at the procedure level, separate code segments are isolated, and then a communication harness is constructed. Slight modifications may be needed to the existing code - the extent of this depends on the manner in which the original code was written. According to how well the existing code is written, this approach usually requires less effort than either implementing the same algorithm in a more appropriate language (e.g., Occam) or than making a completely fresh start with respect to algorithm and language, and provides a significant return.

2.3. Transputers and Parallelism

Confusion is often caused in discussions of transputer-based software by the ambiguous use of the term parallelism. Three distinct forms of parallelism may be observed in a multi-transputer implementation.

Firstly there is the case of separate transputers running separate processes. This is genuine simultaneous operation of concurrent or parallel processes, similar to having two or more independent computers running side by side.

Secondly, a single transputer may be running several processes in a time-sliced mode. This is analogous to the forms of pseudo-parallelism performed on many conventional machines, e.g., those running processes under an operating system such as Unix or VAX VMS. Time slicing is performed on a time scale which is short compared to the process lifetimes. It should be remembered that each of the parallel processes on a single transputer is competing for cpu time, and in the same way that another user on a VAX makes operation seem slower, every extra process will slow down the operation of those already there.

The time-slice mechanism of the transputer is implemented in hardware, and is particularly efficient compared to many similar systems. In particular, processes waiting for communication are removed from the active process list (descheduled) and incur no cpu overheads.

The third form of parallelism concerns the hardware of the transputer. The T800 contains a fixed-point cpu, a floating-point processor, and four bidirectional serial communications link engines; all of these elements can function simultaneously and independently. This is particularly important in relation to communications. If the time required to pass a message is less than the processing time required to do the work generated by the previous message, then the communications can be done in the background with little impact on the time required to generate the desired results.

The link engines operate by DMA. For a message to pass between two processors, the cpu must provide the link engine with a start address and a byte count. This cpu overhead for communications means that it is more efficient to pass long messages (e.g., a few kbytes) than short ones (e.g., single bytes).

In this paper we are primarily concerned with the exploitation of the genuine parallelism of running separate processes on separate processors.

3. ALGORITHM FOR THE CPU

The analysis was originally coded in FORTRAN for implementation on a single CPU. The code is comprised of a main program which performs data input and output, and controls the computations by calling subroutines that fill the impedance matrix and solve the system of equations. A typical matrix element is obtained by evaluating an expression of the form [9]:

$$Z_{pq} = \sum_{n=1}^N \sum_{m=-M}^M K_{mn} B_{mn}^q T_{mn}^p$$

$$K_{mn} = \frac{(n\Delta V_m) \sin(\beta_{mn}a)}{(\beta_{mn}a) [\cos(U_0a) - \cos \beta_{mn}a]}$$

$$B_{mn}^q = \frac{\sin(V_m W_q) \cos(n\Delta Z_q) [\cos(n\Delta h_q) - \cos(kh_q)]}{V_m (k^2 - n^2 \Delta^2) \sin(k h_q)} e^{j V_m y_q}$$

$$T_{mn}^p = \frac{\sin(n\Delta z_p) \sin(n\Delta W_p) [\cos(V_m h_p) - \cos(k h_p)]}{(n\Delta)(k^2 - V_m^2) \sin(k h_p)} e^{j V_m y_p}$$

$$\beta_{mn} = \sqrt{k^2 - V_m^2 - n^2 \Delta^2}, \quad \text{Im}\{\beta_{mn}\} \leq 0$$

$$V_m = k \sin \theta_0 \sin \phi_0 + m \frac{2\pi}{b}$$

$$U_0 = k \sin \theta_0 \cos \phi_0$$

$$k = \omega \sqrt{\mu_0 \epsilon_0}$$

θ_0, ϕ_0 = main beam direction

a, b = array grid spacings in x and y directions

Δ = increment of the spectral variable

y_q, z_q = coordinates of center of basis function q

y_p, z_p = coordinates of the center of testing function p

h_q, W_q = half-length and half-width of basis function q

h_p, W_p = half-length and half-width of testing function p

The upper limits of the summations required for convergence are typically +/- 15 for m and 500-1500 for n. The large range of the upper limit for n is due to this parameter being sensitive to the antenna geometry. The FORTRAN code uses the common practice of storing various terms that comprise K_{mn} , B_{mn}^q and T_{mn}^p so that they are not recomputed when needed for successive sets of the indices.

Total storage requirements are kept to a reasonable level (1-3 MBytes) by proper nesting of the loops on m, n, p and q. The problem possesses an inherent parallelism because the computations are usually performed for several scan angles, which provides a simple way to divide it up into independent subproblems. Except for a few initialising calculations, the various scan angles do not share any common data, but the code that is executed for each angle is identical.

4. THE FORTRAN FARM

4.1. Toplevel architecture

The architecture used in this case is shown in figure 2 - a ring. Data and work packets pass round the farm in the same direction. All file access and control is provided by the driver and the calculations are performed by the worker processors. The communications harness was written in the parallel processing language Occam, and all the original file access, control and calculation code was retained. The result is about 600-700 lines of Occam and about 2000 lines of FORTRAN. Occam was chosen for the communications harness because it is a natural language for describing parallel communications within a computer program and it was the quickest means available at the time of creating an efficient communications harness. Further data on the transputer system are contained in table 1.

Table 1 System characteristics

<u>Hardware</u>	<u>Compliers</u>
Meiko M10 computing surface	Inmos Occam compiler for the communications harness
T800 transputers (20 MHz, 4 cycle RAM)	
T800 maximum computing power \approx 1Mflop	
VAX3800 maximum computing power \approx 3-4 Mflops	Meiko Fortran 77 compiler for the main program

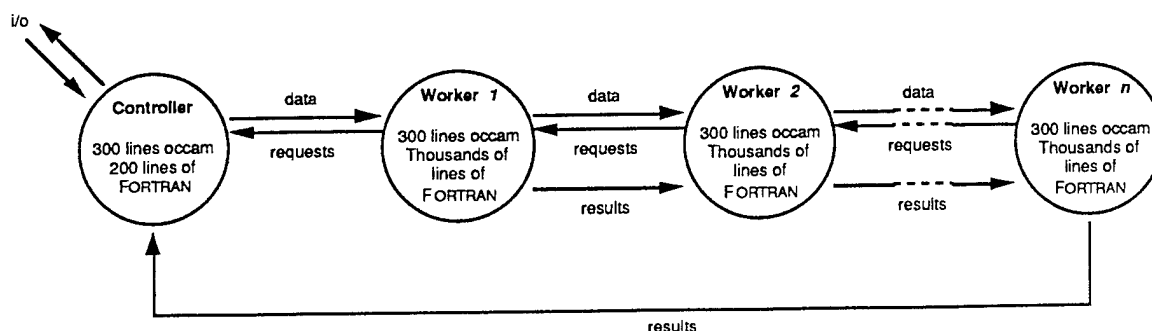


figure 2 Toplevel architecture

In this case the most convenient decomposition was to perform the calculations for different scan angles on different processors. This is the simplest approach possible, and is also the one which yields the highest ratio of computation load to communications load. The work packets passed out to the farm consist of little more than the scan angle at which the calculations are to be performed - a few bytes of data at most, whereas the calculations for each angle require between one and two hours of T800 cpu time.

4.2. Communications paradigm

The simplest type of communications harness for a farming decomposition is one in which the driver processor passes work packets out to the farm as quickly as possible, and each worker processor accepts data if it is free to do some work, or passes it on if not. This flood-fill approach to supplying the workers with data for processing is not appropriate in this case, because it is necessary for each worker to have buffer processes in which work packets must be stored temporarily whilst the processor decides whether to pass on the data or accept it for processing - the minimum possible

number of buffers is one. This is not usually a problem for decompositions in which the number of processors in the farm is one or two orders of magnitude *less* than the total number of work packets. However, in a case where the total number of work packets to be processed is only twice or three times the number of processors in the farm, the flood-fill approach can have very serious disadvantages. Work packets are often left stranded in buffers in such a way that at the end of a processing run the last two or three packets are processed one after the other by the same processor. This is not noticeable in cases where there are hundreds, or even thousands, of individual work packets, each of which takes a few milliseconds to process. If there are only a few tens of packets and a similar number of processors, as there are in this particular decomposition, then the total compute time can be significantly greater than if the farm were used with the maximum possible efficiency.

We have adopted an approach which removes the necessity for any buffering on the worker processors - the farm is request driven. The driver only passes work packets out to the workers when they specifically request it. Each packet is tagged with the address of the requesting worker and no other processor may accept that packet. This approach can reduce farm efficiency if the work packets are large because there is then a significant delay between a worker sending out a request and receiving its work package, during which time the processor stands idle; but for this problem the work packets are at most ten bytes, and for a transmission time around ten microseconds per processor the communications delay is insignificant.

4.3. Performance

Typical processing runs were over 20 to 55 scan angles with 10 to 20 worker processors available. The results below are for a particular example of 52 scan angles ($\theta = 0^\circ$ to 85° in 5° steps and $\phi = 0^\circ$ to 90° in 45° steps) distributed over 17 processors: the time taken for the processing run was 7.61 hours. The same processing run on a VAX 3800 with a floating point accelerator took 37.32 hours: even without the benefit of the extremely efficient FORTRAN compiler available on the VAX, the transputer system is four times as fast. This increase in compute power allowed overnight production of results which would otherwise have taken two days of dedicated VAX 3800 cpu time.

The VAX 3800 is chosen for comparison because its characteristics are widely publicized and these machines, or similar ones, are often available to EM analysts. Obviously, newer workstations could outperform the VAX 3800, but newer transputers also could outperform the T800.

4.4. Sample Computed Results

Typical results for the input impedance of the antenna depicted in figure 3 are shown in figures 4 and 5. These curves are similar to those one might obtain for any well-behaved phased array antenna. The resistance versus scan is reasonably constant near broadside and then drops to zero at endfire. In the H-plane ($\phi = 0$) and the E-plane ($\phi = 90$), the reactance changes are opposite. The same array, operating at 3.725 GHz, exhibits a grating lobe at 54.9° in the principal planes. The reflection coefficient for this case is shown in Figure 6. The data in Figures 4, 5 and 6 were computed by using 77 rooftop-like current modes on the metal fin. These modes and a closely related formulation of the electromagnetic problem are described in [9], as are issues related to convergence and validation of the analysis. To summarize those findings, the summation limits mentioned above are adequate for computing the impedance to an accuracy that agrees within 1 or 2 ohms with published data for test cases, such as dipoles and monopoles, and also agrees well with waveguide simulators for other cases.

5. CONCLUSIONS

We calculate that the ratio of communications to compute load for this particular application is so small (a few milliseconds versus half an hour) that the farm size could easily be increased to several hundred processors without significant (or even visible) degradation of efficiency. This implies linear speed-up. This assumes either that a more finely grained decomposition for this algorithm could be found without excessively increasing the communications load on the farm, or that one would desire to compute the antenna response either for many thousands of scan angles, or for several tens of scan

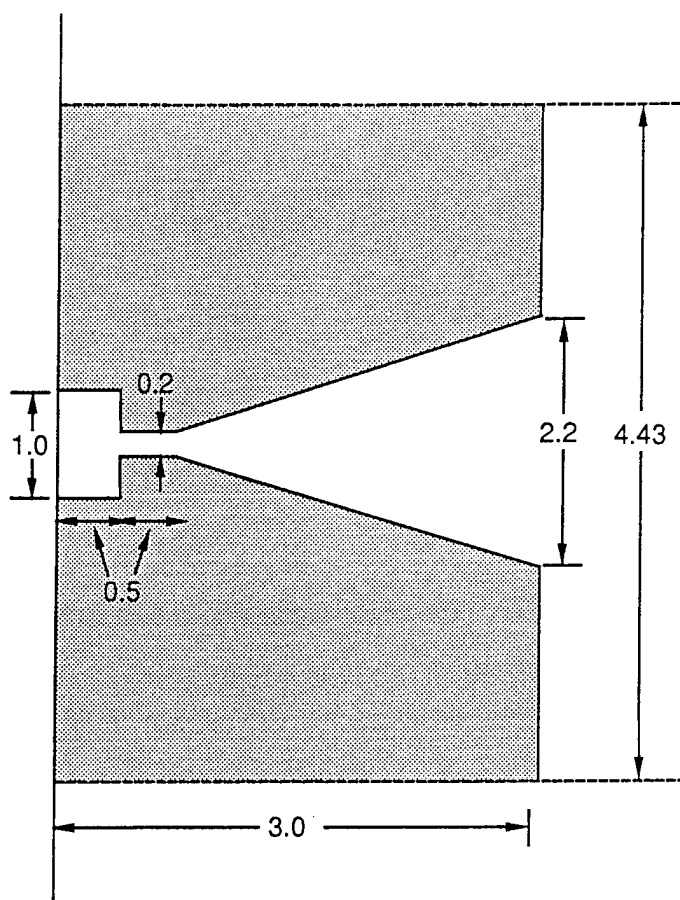


figure 3 Unit cell of linearly tapered slot antenna. Dimensions in cm and H-plane spacing = 4.43 cm.

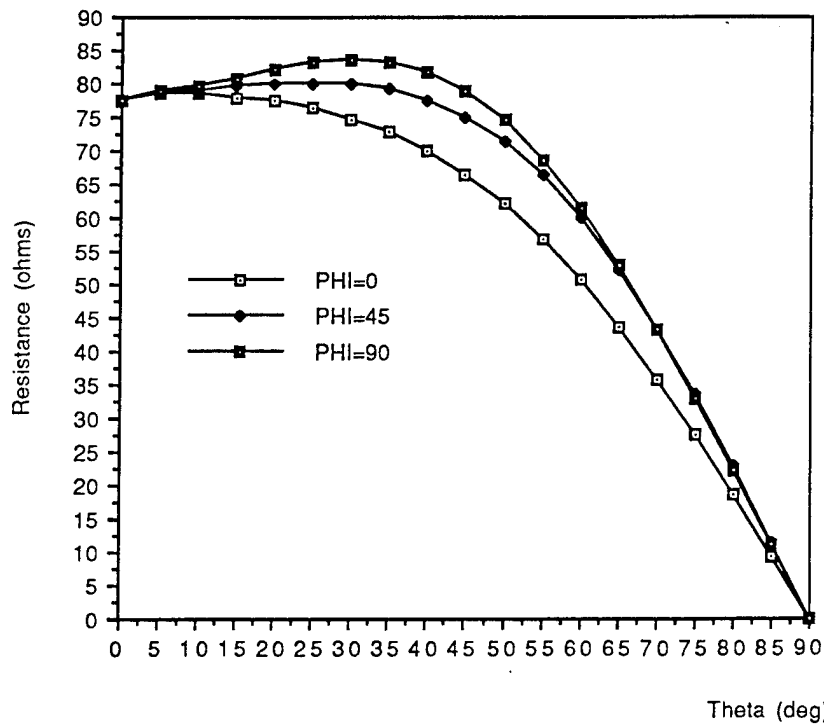


figure 4 Resistance against scan angle for three values of phi. Phi = 0 is H-plane and frequency = 2.54GHz.

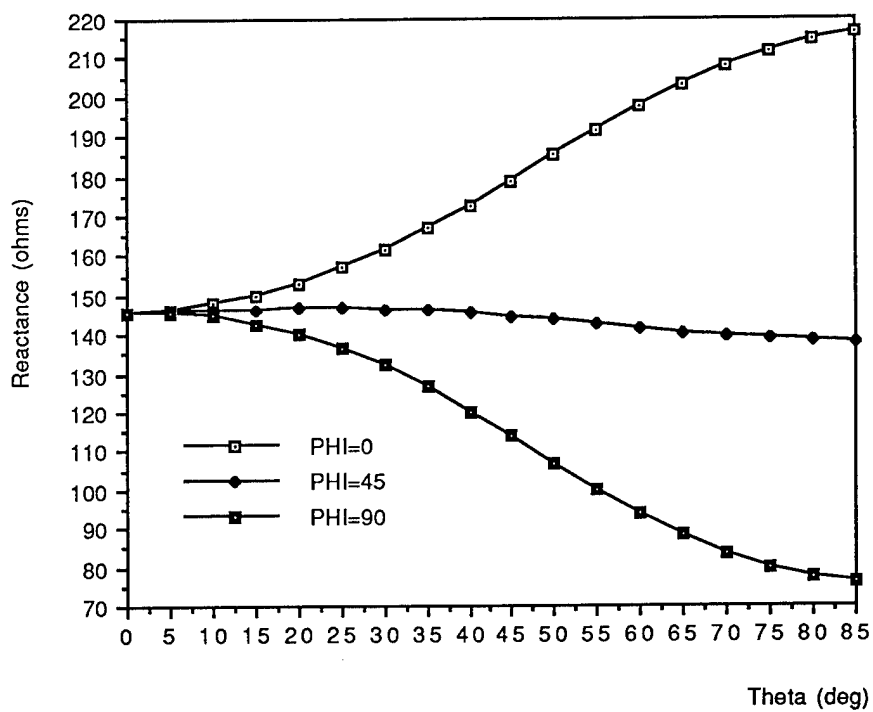


figure 5 Reactance against scan angle for three values of phi.

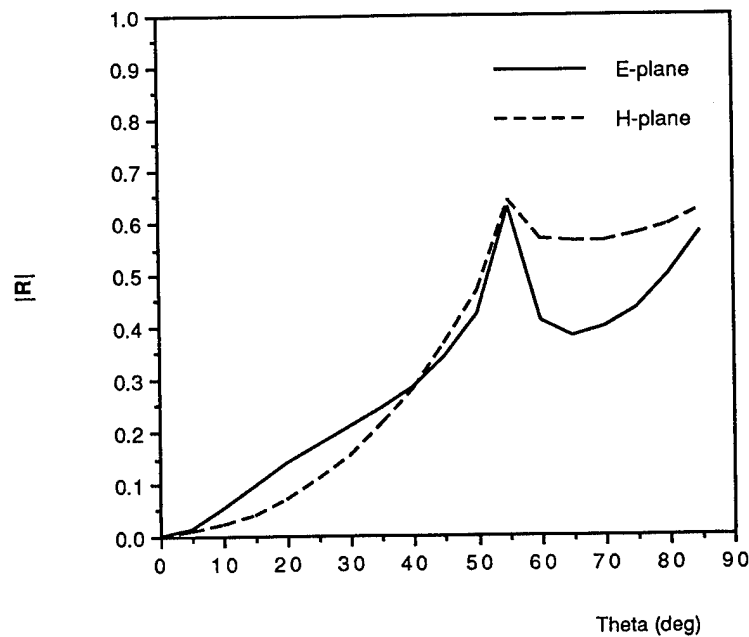


figure 6 Magnitude of reflection coefficient for array of figure 5 operated at 3.725 GHz.

angles at many different frequencies. Increasing the number of processors is easy, finances permitting - in the software, a single constant defining the number of workers is changed and the communications harness is recompiled - the FORTRAN is completely unaffected. We estimate that a 32 processor system, offering an order of magnitude speed-up over a VAX 3800, complete with all necessary software and additional hardware could be purchased for less than half the price of the VAX.

An alternative to increasing the number of processors, or redesigning and recoding the algorithm to suit a finer grained decomposition, is to use different hardware. Examples of high performance cpus available, or soon to be available, are the INTEL i860 and the INMOS T9000 transputer. These would both offer performance improvements over the T800 of at least a factor of ten - the i860 is already available (with communications handled by transputers), and the T9000 is expected to be available late in 1991. The i860-transputer hardware can be obtained for around £10,000 per i860; as yet the truly exceptional performance of this chip (upto 60Mflops - 60 x T800 transputer power) is only available to those who are willing to hand craft their algorithms in the appropriate assembler. Currently available compilers achieve between 5 and 10 Mflops. Between the times of writing the original manuscript and the revisions, the cost of i860 boards has been reduced more than 50 percent. However, at present, it appears that the 30 Mflops/£20,000 cost effectiveness of the transputer farm employing T800's is superior to that of multiple i860's that would be required to achieve 30 Mflops with currently available compilers. This means that the i860 is, as yet, no more cost effective than the transputer - we are not yet able to comment on the T9000.

6. REFERENCES

- [1] Hafner, C., 1989, "Parallel Computation of Electromagnetic Fields on Transputers", *IEEE Ant. Prop. Soc. Newsletter*, **31**, no 5, 6-12.
- [2] Davidson, D.B., 1990, "A Parallel Processing Tutorial", *IEEE Ant. Prop. Soc. Magazine*, **32**, no 2, 6-19.
- [3] Lewis, L.R., Fasset, M., and Hunt, J., 1974, "A Broadband Stripline Array Element", *Digest of 1974 IEEE Symp. Ant. Prop.*, 335-337, Atlanta, GA.
- [4] Gibson, P.J., 1979, "The Vivaldi Aerial", *Digest of 9th Eur. Microw. Conf.*, 120-124, Brighton, UK.
- [5] Yngvesson, K.S., Korzeniowski, T.L., Kim, Y.S., Kollbert, E.L., and Johansson, J., 1989, "The Tapered Slot Antenna - A New Integrated Element for Millimeter Wave Applications", *IEEE Trans. Microw. Th. Tech.*, **MTT-37**, 365-374.
- [6] Flynn, M.J., 1966, "Very high speed computing systems", *Proc IEEE*, **54**, No 12, 1901-1909.
- [7] Pritchard, D.J., 1987 "PARLE Vol 1", *Lecture Notes in Comp. Sci.* No. 258, Springer-Verlag.
- [8] Beton, R.D., Turner, S.P., Upstill, C., 1989, "Hybrid Architecture Paradigms in a Radar ESM Data Processing Application", *Microprocessors and Microsystems*, **13**, No. 3, 160-164.
- [9] Cooley, M.E., Schaubert, D.H., Buris, N.E. and Urbanik, E.A., 1991, "Radiation and Scattering Analysis of Infinite Arrays of Endfire Slot Antennas with a Ground Plane", to appear in *IEEE Trans. Ant. Prop.*, AP-39, No. 11.

1991 INSTITUTIONAL MEMBERS

ANDREW CORPORATION 10500 W. 153rd St. Orland Park, IL 60462	ARC, INC. 8201 Corporate Dr. Landover, MD 20785	ARRL 225 Main St. Newington, CT 06111
ASELSAN PO Box 101 Yenimahalle, Ankara, TURKEY	B.M.S. COMPUTER SYSTEMS Sproughton House Ipswich, Suffolk, UK IP8 3AW	BBC Research Kingswood Warren Tadworth, Surrey, UK K2TO 6NP
BNR EUROPE LTD. London Rd. Harlow, Essex, UK CM17 9NA	BOEING CO. PO Box 3707 Seattle, WA 98124-2207	BOFORS ELECTRONICS J-17588 Jarfalla, SWEDEN S-17588
BOMBARDIER INC.-CANADAIR Cargo Rd. A-4 CANADA J7N 1C7	BRITISH AEROSPACE MILITARY AIRCRAFT Warton Aerodrome Preston, Lanc, UK PR4 1AX	BRITISH AEROSPACE FPC 267 PO Box Filton, Bristol, UK BS12 7QW
BRITISH TELECOM RESEARCH LABS Martlesham Heath Ipswich, UK IP5 7RE	COLLEGE OF TECHNOLOGY Kevin St. Dublin, IRELAND 8	COMPAQ COMPUTER CORPORATION PO Box 692000 Houston, TX 77269-2000
CSELT-RADIO, ANTENNA Via Guglielmo Reiss Romoli, 274 Turin, ITALY 10148	CSIRO PO Box 76 Epping, NSW, AUSTRALIA 2121	CULHAM LAB UK Atomic Energy Authority Abingdon, Oxfordsh, UK OX14 3DB
DAWSON SUBSCRIPTION SERVICE PO Box 191 Mt. Morris, IL 61054-0191	DEFENSE RESEARCH EST. OTTAWA 3701 Carling Ave/Shirley Bay Ottawa, ON, CANADA K1A 024	DYNETICS INC. PO Drawer B Huntsville, AL 35814
ELECTRONICS RESEARCH INC. 108 Market St. PO Box 275 Newburg, IN 47630	ERIM INFORMATION CENTER PO Box 134001 EE Ann Arbor, MI 48113	FGAN/FHP Neuenahrer Strabe 20 Wachtberg-Werthoven, GERMANY D-5307
FOKKER AIRCRAFT B.V. Postbus 7600 Schiphol, NETHERLANDS, 1117 ZJ	GEORGIA TECH RESEARCH INSTITUTE E ³ Lab, ERB 242D Atlanta, GA 30332	GL/LID Hanscom Departments Local Hanscom AFB, MA 01731
GRUMMAN AEROSPACE MS C50-05/Dept 0589 Bethpage, NY 11714	HALLIBURTON LOGGING SERVICES PO Box 42800 Houston, TX 77242	HATFIELD & DAWSON 4226 Sixth Ave, NW Seattle, WA 98107
HELSINKI UNIV OF TECHNOLOGY Otakaari 1 Espoo, FINLAND 02150	HUNTING ENGINEERING LTD. Reddings Wood Amphill, Bedford, UK MK45 2HD	IABG Einsteinstr,20 Ottobrunn, Bavaria, GERMANY D-8012
ITT AEROSPACE/OPT DIV. 7310 Innovation Blvd. Box 731 Ft. Wayne, IN 46801	JAMPRO ANTENNAS, INC. 6939 Power Inn Rd. Box 28425 Sacramento, CA 95828	KATHREIN-WERKE KG Postfach 260 Rosenheim 2, GERMANY D-8200
KERSHNER, WRIGHT & HAGAMAN 5730 Gen. Washington Dr. Alexandria, VA 22312	LAB SIGNAUX & SYSTEM Plateau Du Moulon Gif-Sur-Yvette, Cedex, FRANCE 91192	MCDONNELL DOUGLAS CORP. Box 516 St. Louis, MO 63166-0516
MCDONNELL DOUGLAS TECH INC. 16761 Via Del Campo Ct. San Diego, CA 92127-1713	MIT LINCOLN LABORATORY LIBRARY 244 Wood St. Lexington, MA 02173-0073	MONASH UNIV/CAULFIELD CAMPUS PO Box 197/Caulfield East Melbourne, VIC, AUSTRALIA 3145
MOTOROLA INC. 1301 E. Algonquin Rd. Schamburg, IL 60196	MPB TECHNOLOGIES 151 Hymus Blvd. Pointe-Claire, QC, CANADA H9R 1E9	NATIONAL RES. COUNCIL OF CANADA Bldg. M50, Montreal Rd. Labs Ottawa, ON, CANADA K1A 0R8
NAVAL AIR TEST CENTER Bldg. 1703 Patuxent River, MD 20670	NAVAL SURFACE WARFARE CENTER 10901 New Hampshire Ave. Silver Spring, MD 20903-5000	NAVAL WEAPONS CENTER Code 3951 China Lake, CA 93555
NOVATEL COMMUNICATIONS 1020-64 Ave NE Calgary, ALTA, CANADA T2E 7V8	NTL Crawley Ct. Winchester, Hants, UK SO21 2QA	OCEAN APPLIED RESEARCH CORP. 10447 Roselle St. San Diego, CA 92121
OHIO UNIVERSITY 325 Stocker Center Athens, OH 45701	PETERS, ARTHUR K, CONSULTING 7020 NW 11th Pl. Gainesville, FL 32605	RACAL/REDAK GROUP LTD Newton Tewkesbury, Glos, UK L20 8HE

1991 INSTITUTIONAL MEMBERS (CONT.)

RACAL/DECCA CANADA LTD. 71 Selby Rd. Brampton, ON, CANADA L6W 1K5	RADIO FREQUENCY SYSTEMS Box 191 Roydon, VIC, AUSTRALIA 3136	ROCKWELL INTERNATIONAL 1745 Jefferson Davis Hwy SW 1100 Arlington, VA 22202
ROLM SYSTEMS INC. 4900 Old Ironsides Dr. Santa Clara, CA 95052-8075	ROYAL AIRCRAFT ESTABLISHMENT Main Library Building Q4 Farnborough, HANTS, UK GU14 6TD	SAAB MISSILES Dept. TUSTAS Linkoping, SWEDEN S58188
SAIC 255 Hudson Rd. Stow, MA 01775	SFA, INC. 1401 McCormick Dr. Landover, MD 20785	STG NATIONAL LUCHT-EM Ruimtevvard Lab. Amsterdam, NETHERLANDS 1059
SYRACUSE RESEARCH CORPORATION Merrill Lane Syracuse, NY 13210-4080	TASC 8601 E Cornhusker Highway Lincoln, NE 68505	TECHNICAL RESEARCH CENTRE Otakaari 7B Espoo, FINLAND SF-01250
TELECOM AUSTRALIA 770 Blackburn Rd. Clayton, VIC, AUSTRALIA 31686	UNIVERSITY OF BUNDESWEHR Werner Heisenberg Weg 39 Neubiberg, GERMANY D 8014	UNIVERSITY OF CANTERBURY Private Bag Christchurch, NEW ZEALAND
UNIVERSITY OF NSW/UNIV COLLEGE Northcott Dr. Campbell, ACT, AUSTRALIA 2600	VISTA RESEARCH INC. 100 View St. #202 Box 998 Mountain View, CA 94042	XETRON CORPORATION 40 W. Crescentville Rd. Cincinnati, OH 45246--1286

ACES COPYRIGHT FORM

This form is intended for original, previously unpublished manuscripts submitted to ACES periodicals and conference publications. The signed form, appropriately completed, MUST ACCOMPANY any paper in order to be published by ACES. PLEASE READ REVERSE SIDE OF THIS FORM FOR FURTHER DETAILS.

TITLE OF PAPER:

RETURN FORM TO:

Dr. Richard W. Adler
Naval Postgraduate School
Code EC/AB
Monterey, CA 93943

AUTHORS(S)

PUBLICATION TITLE/DATE:

PART A - COPYRIGHT TRANSFER FORM

(NOTE: Company or other forms may not be substituted for this form. U.S. Government employees whose work is not subject to copyright may so certify by signing Part B below. Authors whose work is subject to Crown Copyright may sign Part C overleaf).

The undersigned, desiring to publish the above paper in a publication of ACES, hereby transfer their copyrights in the above paper to The Applied Computational Electromagnetics Society (ACES). The undersigned hereby represents and warrants that the paper is original and that he/she is the author of the paper or otherwise has the power and authority to make and execute this assignment.

Returned Rights: In return for these rights, ACES hereby grants to the above authors, and the employers for whom the work was performed, royalty-free permission to:

1. Retain all proprietary rights other than copyright, such as patent rights.
2. Reuse all or portions of the above paper in other works.
3. Reproduce, or have reproduced, the above paper for the author's personal use or for internal company use provided that (a) the source and ACES copyright are indicated, (b) the copies are not used in a way that implies ACES endorsement of a product or service of an employer, and (c) the copies per se are not offered for sale.
4. Make limited distribution of all or portions of the above paper prior to publication.
5. In the case of work performed under U.S. Government contract, ACES grants the U.S. Government royalty-free permission to reproduce all or portions of the above paper, and to authorize others to do so, for U.S. Government purposes only.

ACES Obligations: In exercising its rights under copyright, ACES will make all reasonable efforts to act in the interests of the authors and employers as well as in its own interest. In particular, ACES REQUIRES that:

1. The consent of the first-named author be sought as a condition in granting re-publication permission to others.
2. The consent of the undersigned employer be obtained as a condition in granting permission to others to reuse all or portions of the paper for promotion or marketing purposes.

In the event the above paper is not accepted and published by ACES or is withdrawn by the author(s) before acceptance by ACES, this agreement becomes null and void.

AUTHORIZED SIGNATURE

TITLE (IF NOT AUTHOR)

EMPLOYER FOR WHOM WORK WAS PERFORMED

DATE FORM SIGNED

PART B - U.S. GOVERNMENT EMPLOYEE CERTIFICATION

(NOTE: If your work was performed under Government contract but you are not a Government employee, sign transfer form above and see item 5 under Returned Rights).

This certifies that all authors of the above paper are employees of the U.S. Government and performed this work as part of their employment and that the paper is therefore not subject to U.S. copyright protection.

AUTHORIZED SIGNATURE

TITLE (IF NOT AUTHOR)

NAME OF GOVERNMENT ORGANIZATION

DATE FORM SIGNED

PART C - CROWN COPYRIGHT

(Note: ACES recognizes and will honor Crown Copyright as it does U.S. Copyright. It is understood that, in asserting Crown Copyright, ACES in no way diminishes its rights as publisher. Sign only if ALL authors are subject to Crown Copyright.)

This certifies that all authors of the above Paper are subject to Crown Copyright. (Appropriate documentation and instructions regarding form of Crown Copyright notice may be attached).

AUTHORIZED SIGNATURE

TITLE OF SIGNEE

NAME OF GOVERNMENT BRANCH

DATE FORM SIGNED

Information to Authors

ACES POLICY

ACES distributes its technical publications throughout the world, and it may be necessary to translate and abstract its publications, and articles contained therein, for inclusion in various compendiums and similar publications, etc. When an article is submitted for publication by ACES, acceptance of the article implies that ACES has the rights to do all of the things it normally does with such an article.

In connection with its publishing activities, it is the policy of ACES to own the copyrights in its technical publications, and to the contributions contained therein, in order to protect the interests of ACES, its authors and their employers, and at the same time to facilitate the appropriate re-use of this material by others.

The new United States copyright law requires that the transfer of copyrights in each contribution from the author to ACES be confirmed in writing. It is therefore necessary that you execute either Part A-Copyright Transfer Form or Part B-U.S. Government Employee Certification or Part C-Crown Copyright on this sheet and return it to the Managing Editor (or person who supplied this sheet) as promptly as possible.

CLEARANCE OF PAPERS

ACES must of necessity assume that materials presented at its meetings or submitted to its publications is properly available for general dissemination to the audiences these activities are organized to serve. It is the responsibility of the authors, not ACES, to determine whether disclosure of their material requires the prior consent of other parties and if so, to obtain it. Furthermore, ACES must assume that, if an author uses within his/her article previously published and/or copyrighted material that permission has been obtained for such use and that any required credit lines, copyright notices, etc. are duly noted.

AUTHOR/COMPANY RIGHTS

If you are employed and you prepared your paper as a part of your job, the rights to your paper initially rest with your employer. In that case, when you sign the copyright form, we assume you are authorized to do so by your employer and that your employer has consented to all of the terms and conditions of this form. If not, it should be signed by someone so authorized.

NOTE RE RETURNED RIGHTS: Just as ACES now requires a signed copyright transfer form in order to do "business as usual", it is the intent of this form to return rights to the author and employer so that they too may do "business as usual". If further clarification is required, please contact: The Managing Editor, R.W. Adler, Naval Postgraduate School, Code EC/AB, Monterey, CA, 93943, USA (408)646-2352.

Please note that, although authors are permitted to re-use all or portions of their ACES copyrighted material in other works, this does not include granting third party requests for reprinting, republishing, or other types of re-use.

JOINT AUTHORSHIP

For jointly authored papers, only one signature is required, but we assume all authors have been advised and have consented to the terms of this form.

U.S. GOVERNMENT EMPLOYEES

Authors who are U.S. Government employees are not required to sign the Copyright Transfer Form (Part A), but any co-authors outside the Government are.

Part B of the form is to be used instead of Part A only if all authors are U.S. Government employees and prepared the paper as part of their job.

NOTE RE GOVERNMENT CONTRACT WORK: Authors whose work was performed under a U.S. Government contract but who are not Government employees are required to sign Part A-Copyright Transfer Form. However, item 5 of the form returns reproduction rights to the U.S. Government when required, even though ACES copyright policy is in effect with respect to the reuse of material by the general public.

INFORMATION FOR AUTHORS

PUBLICATION CRITERIA

Each paper is required to manifest some relation to applied computational electromagnetics. Papers may address general issues in applied computational electromagnetics, or they may focus on specific applications, techniques, codes, or computational issues. While the following list is not exhaustive, each paper will generally relate to at least one of these areas:

1. Code validation. This is done using internal checks or experimental, analytical or other computational data. Measured data of potential utility to code validation efforts will also be considered for publication.

2. Code performance analysis. This usually involves identification of numerical accuracy or other limitations, solution convergence, numerical and physical modeling error, and parameter tradeoffs. However, it is also permissible to address issues such as ease-of-use, set-up time, run time, special outputs, or other special features.

3. Computational studies of basic physics. This involves using a code, algorithm, or computational technique to simulate reality in such a way that better or new physical insight or understanding is achieved.

4. New computational techniques, or new applications for existing computational techniques or codes.

5. "Tricks of the trade" in selecting and applying codes and techniques.

6. New codes, algorithms, code enhancement, and code fixes. This category is self-explanatory but includes significant changes to existing codes, such as applicability extensions, algorithm optimization, problem correction, limitation removal, or other performance improvement. NOTE: CODE (OR ALGORITHM) CAPABILITY DESCRIPTIONS ARE NOT ACCEPTABLE, UNLESS THEY CONTAIN SUFFICIENT TECHNICAL MATERIAL TO JUSTIFY CONSIDERATION.

7. Code input/output issues. This normally involves innovations in input (such as input geometry standardization, automatic mesh generation, or computer-aided design) or in output (whether it be tabular, graphical, statistical, Fourier-transformed, or otherwise signal-processed). Material dealing with input/output data base management, output interpretation, or other input/output issues will also be considered for publication.

8. Computer hardware issues. This is the category for analysis of hardware capabilities and limitations in meeting various types of electromagnetics computational requirements. Vector and parallel computational techniques and implementation are of particular interest.

Applications of interest include, but are not limited to, antennas (and their electromagnetic environments), networks, static fields, radar cross section, shielding, radiation hazards, biological effects, electromagnetic pulse (EMP), electromagnetic interference (EMI), electromagnetic compatibility, power transmission, charge transport, dielectric and magnetic materials, microwave components, MMIC technology, remote sensing and geophysics, communications systems, fiber optics, plasmas, particle accelerators, generators and motors, electromagnetic wave propagation, non-destructive evaluation, eddy currents, and inverse scattering.

Techniques of interest include frequency-domain and time-domain techniques, integral equation and differential equation techniques, diffraction theories, physical optics, moment methods, finite differences and finite element techniques, modal expansions, perturbation methods, and hybrid methods. This list is not exhaustive.

A unique feature of the Journal is the publication of unsuccessful efforts in applied computational electromagnetics. Publication of such material provides a means to discuss problem areas in electromagnetic modeling. Material representing an unsuccessful application or negative results in computational electromagnetics will be considered for publication only if a reasonable expectation of success (and a reasonable effort) are reflected. Moreover, such material must represent a problem area of potential interest to the ACES membership.

EDITORIAL REVIEW

In order to ensure an appropriate level of quality control, papers are refereed. They are reviewed both for technical correctness and for adherence to the listed guidelines regarding information content. Authors should submit the initial manuscript in draft form so that any suggested changes can be made before the photo-ready copy is prepared.

STYLE

The ACES Journal is flexible, within reason, in regard to style. However, a few requirements are in effect:

1. Do NOT place the paper title on a separate page. The title, author(s), abstract, and (space permitting) beginning of the paper itself should all be on the first page. The title, author(s), and author affiliations should be centered (center-justified) on the first page.
2. Place the figure captions directly on the figures. Do NOT submit a separate page of figure captions.
3. Either British English or American English spellings may be used. However, do NOT spell any word two or more different ways in a single paper.
4. Any commonly-accepted format for referencing is permitted, provided that internal consistency of format is maintained. As a guideline for authors who have no other preference, we recommend that references be given by author(s) name and year in the body of the paper (with alphabetical listing of all references at the end of the paper).
5. Internal consistency shall also be maintained for other elements of style, such as equation numbering. As a guideline for authors who have no other preference, we suggest that equation numbers be placed in parentheses at the right column margin.
6. The intent and meaning of all text must be clear. For authors who are NOT masters of the English language, the ACES Editorial Staff will provide assistance with grammar (subject to clarity of intent and meaning).

MATERIAL SUBMITTAL FORMAT AND PROCEDURE

Only camera-ready copies are accepted for publication, although authors may submit other copies for publication review. The term "camera-ready" means that the material is neat, legible, and reproducible. There is NO requirement for India ink or for special paper; any plain white paper may be used. However, faded lines on figures and white streaks along fold lines should be avoided. Original figures — even paste-ups — are preferred over "nth-generation" photocopies. These original figures will be returned if you so request.

While ACES reserves the right to re-type any submitted material, this is not generally done.

All submissions should be sent in triplicate to the Editor-in-Chief. Each submission should be accompanied by a cover letter. The cover letter should include the name, address, and telephone of at least one of the authors.

PUBLICATION CHARGES

At the present time, there are no page charges for camera-ready articles. Authors are entitled to 20 free reprints of their articles and must request these from the Managing Editor. Additional reprints are available to authors, and reprints available to non-authors, for a nominal fee.

COPYRIGHTS AND RELEASES

Each author must sign a copyright form and obtain a release from his organization vesting the copyright with ACES. Both forms will be provided by ACES and allow both the author and his organization to use the copyrighted material freely for their own private purposes.

Permission is granted to quote short passages and reproduce figures and tables from an ACES Journal issue provided the source is cited. Copies of ACES Journal articles may be made in accordance with usage permitted by Sections 107 or 108 of the U.S. Copyright Law. This consent does not extend to other kinds of copying, such as for general distribution, for advertising or promotional purposes, for creating new collective works, or for resale. The reproduction of multiple copies and the use of articles or extracts for commercial purposes require the consent of the author and specific permission from ACES. Institutional members are allowed to copy any ACES Journal issue for their internal distribution only.